Vol. 10 No. 1
April 2026

ISSN 2579-5821
e-ISSN 2579-5546

S3
sinta
Science and Technology Index

Jurnal Geocelebes

Published by:
Geophysics Department
Hasanuddin University
Makassar, Indonesia

JURNAL GEOCELEBES

Geophysics Department | Faculty of Mathematics and Natural Sciences | Hasanuddin University

Volume 10 Number 1, April 2026

P-ISSN: 2579-5821
E-ISSN: 2579-5546

Published by:
Geophysics Department, Math and Natural Science Faculty
Hasanuddin University

JURNAL GEOCELEBES
Volume 10 Number 1, April 2026

ISSN: 2579 – 5821 (Print)
ISSN: 2579 – 5546 (Online)
URL address: http://journal.unhas.ac.id/index.php/geocelebes

Diterbitkan berkala dua kali setahun oleh/ **Published periodically two times annually by**
Dept. Geofisika Universitas Hasanuddin/ **Geophysics Dept., Hasanuddin University**

Dewan Redaksi/ Editor Board

Sekretariat/ Secretariat:
Departemen Geofisika, FMIPA Universitas Hasanuddin
Gedung MIPA, Kampus Unhas Tamalanrea - Jalan Perintis Kemerdekaan, Makassar, Sulawesi Selatan, 90245.
E-mail: geocelebes@sci.unhas.ac.id

Jurnal Geocelebes is a scientific journal published by the Department of Geophysics, Hasanuddin University. This journal is intended as a means of scientific publication in the field of geophysics ranging from theoretical topics to geophysical applications in various fields topics. The articles are original research results, reviews of recent advances in a particular topic, case studies of geophysical applications or reviews of software related to geophysics. Papers should be sent to the editorial website in softcopy using the template provided. Each accepted paper will be reviewed for eligibility through a rigorous reviewing process by the Editorial Board.

Contents

JURNAL GEOCELEBES

Volume 10, Number 1, April 2026

ISSN: 2579 – 5821 (Print)
ISSN: 2579 – 5546 (Online)

URL: http://journal.unhas.ac.id/index.php/geocelebes

Preface

Jurnal Geocelebes managed by the Department of Geophysics, Faculty of Mathematics and Natural Sciences, Hasanuddin University Makassar has entered its tenth year. The Editorial Board expresses gratitude to God Almighty for this achievement and expresses gratitude for the commitment of the Editorial Board, in carrying out this mandate. In particular, the Editorial Board expresses its gratitude and highest appreciation to all authors who have submitted their scientific works and to the Reviewers who have been willing to take the time to provide constructive suggestions and corrections to each article in each issue of the Jurnal Geocelebes.

In the edition of Volume 10 Number 1 April 2026 there are nine articles. The articles published generally discuss the implementation of the role of geosciences, especially geophysics in natural resource exploration and other fields that are in accordance with the focus and scope of the field published by the Jurnal Geocelebes. The language used in this volume is English, which shows that Jurnal Geocelebes deserves to be an international journal in the future. With deep gratitude, we announce that based on the assessment conducted by Arjuna DIKTI, Jurnal Geocelebes has successfully obtained SINTA 2 accreditation rating based on the Keputusan Direktur Jenderal Riset dan Pengembangan Kementerian Pendidikan Tinggi, Sains dan Teknologi number 295/C/C3/KPT/2026 dated 2 January 2026. The official accreditation certificate is currently still in the process of being issued by the Arjuna DIKTI. We will provide further information as soon as we receive the certificate. Jurnal Geocelebes welcomes participation from academics, researchers, industry practitioners, students, and others in the field of geosciences in both theoretical and application perspectives, both related to the subsurface (lithosphere) and above the surface (atmosphere), which of course will go through a series of processes namely submitting, editing, and reviewing.

The Editorial Board of Jurnal Geocelebes is open to suggestions and constructive criticism for future improvements. All suggestions and criticisms can be sent via email geocelebes@sci.unhas.ac.id

Makassar, April 2026

The Editorial Board of Jurnal Geocelebes

ISSN: 2579-5821 (Print)
ISSN: 2579-5546 (Online)
URL address: http://journal.unhas.ac.id/index.php/geocelebes
DOI: 10.70561/geocelebes.v10i1.42958

Jurnal Geocelebes Vol. 10 No. 1, April 2026, 1 – 11

The Earthquake Prediction in the Southern Part of Sumatra Using Deep Learning (Long Short-Term Memory) Models

Ainul Lisa[1], Refrizon[1,2*], Rida Samdara[1]

[1]Department of Physics, Faculty of Mathematics and Natural Sciences, Bengkulu University, Bengkulu, 38371, Indonesia
[2]Department of Geophysics, Faculty of Mathematics and Natural Sciences, Bengkulu University, Bengkulu, 38371, Indonesia

*Corresponding author. Email: refrizon@unib.ac.id

Manuscript received: 20 January 2025; Received in revised form: 4 February 2025; Accepted: 5 February 2025

Abstract

The Southern part of Sumatra is highly vulnerable to earthquakes due to its location in the subduction zone between the Indo-Australian plate and the Sunda plate. The Southern part of Sumatra's vulnerability to earthquakes poses significant risks. This research aims at predicting the Earthquakes in the Southern part of Sumatra Using Deep Learning (Long Short-Term Memory) Models, a deep learning method designed to analyze sequential data. The model utilized 20 years of historical earthquake data from 2004 to 2024, with parameters including magnitude, epicenter location, depth, and event time. Data were preprocessed using Min-Max Scaling normalization and split into training data (70%) and testing data (30%). The model was trained over 150 epochs with a batch size of 32. Evaluation results showed a Mean Absolute Error (MAE) of 0.28 and a Root Mean Squared Error (RMSE) of 0.39, indicating high prediction accuracy. The distribution of prediction results confirmed previous studies indicating that earthquakes in Southern part of Sumatra frequently occur in Bengkulu, western South Sumatra, and Southwestern Lampung. These findings underscore the importance of ongoing seismic hazard mitigation efforts and sustainable development planning in earthquake-prone areas.

Keywords: Earthquake; Historical Data; LSTM; Southern part of Sumatra.

Citation: Lisa, A., Refrizon, R., & Samdara, R. (2026). The Earthquake Prediction in the Southern Part of Sumatra Using Deep Learning (Long Short-Term Memory) Models. *Jurnal Geocelebes*, 10(1): 1–11, doi: 10.70561/geocelebes.v10i1.42958

Introduction

The Southern part of Sumatra, encompassing South Sumatra, Lampung, Jambi, and Bengkulu, plays a strategic role in supporting national development. This region is known for its abundant natural resources, including mining products, oil, gas, and plantations. Additionally, the presence of major infrastructure such as the Trans-Sumatra Highway, key ports, and ambitious projects like the Trans-Sumatra Toll Road has positioned this region as a growing economic hub (Al-Faridzi & Kurniasari, 2024).

However, alongside its economic potential, Southern part of Sumatra faces significant challenges, primarily in the form of earthquake risks. This area lies in an active subduction zone, where the Indo-Australian and Sunda plates converge, recognized as one of the most seismically active zones globally (Sukrungsri et al., 2024). Furthermore, the Sumatra Fault, which extends longitudinally from the island's north to south, exacerbates the risk of tectonic earthquakes. Historical records highlight major earthquakes, such as the 2007 Bengkulu earthquake with a magnitude of 8.4 (Mase, 2021), which caused extensive damage, and the 2010 Mentawai earthquake (Marzuki et al.,

2022), which triggered a tsunami. These vulnerabilities necessitate special attention, particularly in disaster mitigation efforts.

Ongoing development in the region increases the risks associated with earthquakes, potentially leading to significant material and non-material losses. Damaged infrastructure, disrupted economic activities, and widespread social impacts are some of the serious consequences that need to be anticipated. Furthermore, the region has experienced a significant population increase, particularly in earthquake-prone areas, amplifying the potential for disaster-related losses. Damage to vital facilities such as roads, bridges, and healthcare centers can impede evacuation processes and emergency responses, ultimately worsening the disaster's impact on communities (Yang et al., 2024).

In addition to these issues, the potential disruption of economic activities must also be considered. Southern part of Sumatra, which serves as a center for resource-based economic activities such as plantations, mining, and logistical transportation, heavily relies on robust and operational infrastructure. Without adequate mitigation measures, earthquake-induced damage could hinder the distribution of goods, trade activities, and regional economic stability (Samudra et al., 2024). Therefore, disaster mitigation must be comprehensively designed, encompassing infrastructure strengthening, region-based risk management, and spatial planning that considers earthquake risks. This approach should not only be reactive but also proactive, aiming to minimize future losses, one of which is through more accurate earthquake predictions.

Advancements in technology in the modern era provide significant opportunities for disaster risk management. Artificial intelligence-based technologies, such as Long Short-Term Memory (LSTM), offer innovative solutions to predict earthquake patterns using historical data (Mer et al., 2024). LSTM is a deep learning method designed to analyze sequential data while retaining relevant temporal information. Previous research has demonstrated this method's effectiveness in predicting time-based events, particularly for problems involving long-term patterns (Lin et al., 2024).

This study aims to develop an LSTM-based earthquake prediction model using historical earthquake data from Southern part of Sumatra over the past two decades. By considering parameters such as magnitude, depth, epicenter location, and event time, this research is expected to provide more accurate prediction results. These findings are hoped to support disaster mitigation efforts, strengthen resilient development planning, and enhance community preparedness against potential future earthquakes.

Artificial intelligence-based technologies, such as LSTM, offer innovative solutions to predict earthquake patterns using historical data (Mer et al., 2024). Several studies have shown that LSTM can effectively capture spatial and temporal patterns in seismic records, making it a valuable tool for earthquake forecasting.

For instance, Sonthalia et al. (2023) developed an LSTM-based model capable of predicting earthquake magnitude occurrences with higher accuracy compared to traditional statistical methods. Similarly, Kavianpour et al. (2024) introduced a hybrid CNN-BiLSTM model with an attention mechanism, which significantly enhanced the accuracy of magnitude predictions. Additionally, Berhich et al. (2020) applied LSTM to spatiotemporal earthquake data, demonstrating that the model performed well in forecasting both earthquake locations and magnitudes. These findings underscore the increasing role of deep

learning, particularly LSTM, in improving the effectiveness of earthquake prediction models. Therefore, in this study, the LSTM method is applied to develop an earthquake prediction model for the Southern part of Sumatra.

Long Short-Term Memory (LSTM)

Deep Learning is a branch of Artificial Intelligence (AI) that focuses on the use of artificial neural networks with multiple layers to process data (Nurhakiki & Yahfizham, 2024). One of the popular models for sequential data applications is LSTM, a type of Recurrent Neural Network (RNN) designed to retain information over long periods (Adherda et al., 2023). LSTM is particularly useful in analyzing time-series data containing temporal patterns, such as seismic data related to earthquakes.

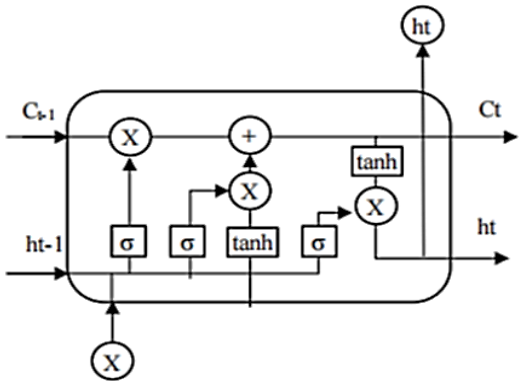

Figure 1. LSTM Architecture (Sianturi et al., 2023).

LSTM has the capability to learn from more than 1000 previous time steps (Verianto, 2024), depending on the complexity of the network. The core concept of LSTM lies in the Cell State, which is controlled by a gating mechanism within a single LSTM unit and passed on to the next unit through the following main gates: Forget Gate, Input Gate, and Output Gate (Fig. 1).

Materials and Methods

The steps involved in this research are illustrated in Fig. 2, which presents the research framework. The explanation of each step is as follows:

1. Load Data

The data loaded into the system consisted of historical earthquake records from the Southern part of Sumatra region spanning the years 2004 to 2024. The data were sourced from the official IRIS Wilber 3 website, with constraints set for magnitudes ranging from 5 to 10 and depths between 10 and 60 km.

2. Pre-Processing Data

a) Resampling Data

The earthquake data spans a 20-year period with varying time intervals, requiring resampling techniques to adjust the recording frequency. Resampling ensured that the data intervals were consistent and met the requirements of the LSTM model, which is sensitive to temporal irregularities. For instance, earthquake recordings may not have been conducted uniformly on a daily basis. Through resampling, the data was transformed into fixed intervals, such as daily or monthly, making temporal patterns easier to identify and analyze by the LSTM. Additionally, methods like down-sampling were employed to simplify the data by removing redundant information that was irrelevant to the main patterns, thereby enhancing the model's efficiency (Gerlach et al., 2024).

b) Data Normalization

Normalization was performed to prevent issues during model training due to scale discrepancies among features. A commonly used technique is Min-Max Scaling, which transforms data values into a range of 0 to 1 (Ma, 2024). In the LSTM model, normalization was applied prior to data utilization to ensure that all features were within a consistent scale, thus preventing the dominance of specific features. After predictions were generated, denormalization was applied to facilitate easier interpretation of the results.

$$x' = \frac{x - \min(x)}{\max(x) - \min(x)} \qquad (1)$$

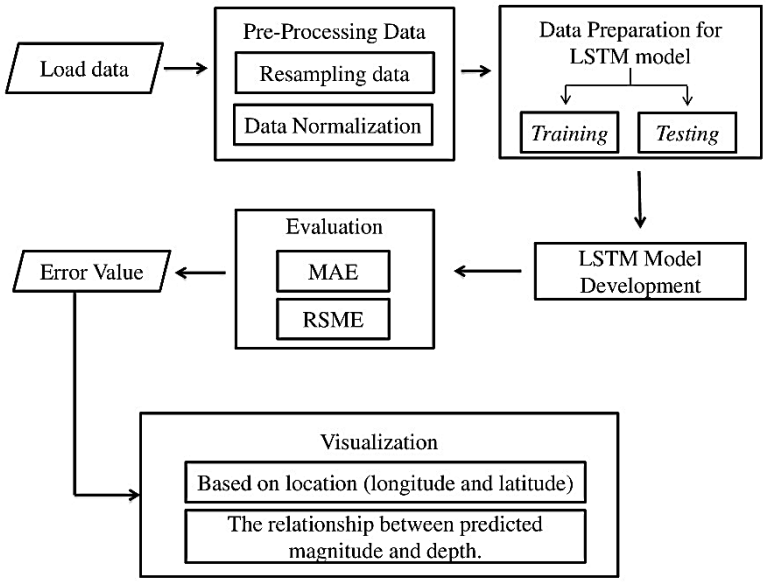

Figure 2. Research methodology diagram.

3. Data Preparation

Before being input into the LSTM model, the data were prepared in a format suitable for time-series input. The dataset was divided into training data (70%) and testing data (30%).

4. LSTM Model Development

Traditional Recurrent Neural Networks (RNN) often suffer from the vanishing gradient problem, limiting their effectiveness in processing long sequences. According to Bellamkonda et al. (2021), LSTM mitigates this issue by employing memory cells and gating mechanisms, enabling it to retain significant patterns in seismic activity over extended periods. This capability allows LSTM to establish complex temporal relationships within earthquake datasets, making it a more suitable choice compared to conventional RNN and Feedforward Neural Networks (FNN).

To standardize data distributions and facilitate stable training, Min-Max Scaling was applied to normalize input values, ensuring that all features operated within a consistent numerical range. By integrating these preprocessing techniques, the model aimed to optimize earthquake prediction accuracy and mitigate overfitting issues associated with deep learning models.

5. Evaluation

The model was trained over 150 epochs with a batch size of 32 samples per iteration. Testing was conducted using the testing dataset. The evaluation metrics used were MAE and RMSE. Low error values indicated the effectiveness of the developed model.

a) Mean Absolute Error (MAE)

MAE calculates the average absolute difference between predicted values (y-pred) and actual values (y-true), indicating the magnitude of the model's average error without considering the direction of the error. The formula is (Scott & Willmott, 2023):

$$\text{MAE} = \frac{1}{n}\sum_{i=1}^{n}\left|y_{pred,i} - y_{true,i}\right| \quad (2)$$

where:

- n is the number of data points
- $y_{pred,i}$ is the predicted value for the i-th data point
- $y_{true,i}$is the actual value for the i-th data point

b) Root Mean Squared Error (RMSE)

RMSE is the square root of the average squared differences between predicted values (y-pred) and actual values (y-true). This metric measures the average error while giving greater weight to larger errors compared to MAE. Some characteristics of RMSE include: its scale being the same as the original data, a significant influence of large errors due to the squaring process, and higher sensitivity to outliers compared to MAE. The formula is (Hodson, 2022):

$$RMSE = \sqrt{\frac{1}{n}\sum_{i=1}^{n}(y_{pred,i} - y_{true,i})^2} \quad (3)$$

6. Visualization

The final stage involved visualizing the earthquake prediction results. The first visualization, based on location (longitude and latitude), was implemented using libraries such as Matplotlib or Folium. The second visualization, a graphical representation, was used to analyze the relationship between predicted magnitude and depth.

Results and Discussion

All data loaded into the system were formatted using a datetime structure, as shown in Table 1, before undergoing the data preprocessing stage.

Table 1. Historical earthquake data with datetime format.

Date	Latitude	Longitude	Depth	Magnitude
8-2-2004	-5.4608	102.6564	42.800	5.5
10-24-2004	-4.8658	101.8926	28.100	5.3
10-28-2004	-4.9375	103.2393	41.500	5.3
10-28-2004	-4.9000	103.2507	58.100	5.0
12-26-2004	-3.3512	101.6312	53.000	5.0
…	…	…	…	…
10-29-2023	-4.3162	102.0295	58.539	5.1
2-5-2024	-2.1520	100.4749	51.246	5.0
3-4-2024	-5.7671	102.2524	10.000	5.2
6-5-2024	-3.5277	100.7812	30.666	5.0

Table 2. Results of normalization or scaling.

Latitude	Longitude	Depth	Magnitude
0.142	0.095	0.627	0.658
0.085	0.200	0.461	0.363
0.085	0.187	0.754	0.632
0.000	0.194	0.757	0.965
0.000	0.468	0.404	0.862

Next, the data were normalized to ensure that all features contributed equally during the training process. This step mapped data with initially varying ranges into a uniform scale between 0 and 1. Examples of normalized data for features such as magnitude, latitude, longitude, and depth are presented in Table 2.

Subsequently, sequential data were prepared by utilizing the previous 30 data points to predict target values. The data were then split into training and testing sets, allowing input into the LSTM multiple-output sequential model. The model, detailed in Table 3, consists of LSTM layers for extracting temporal patterns from sequential data, dropout layers to mitigate overfitting, and dense layers for generating four output values. The evaluation results, summarized in Table 4, indicate small error values, demonstrating the strong performance of the earthquake prediction model.

Table 3. LSTM model.

Layer (type)	**Output Shape**	**Params**
LSTM	(None, 50)	11
Dropout	(None, 50)	0
Dense	(None, 4)	0.204

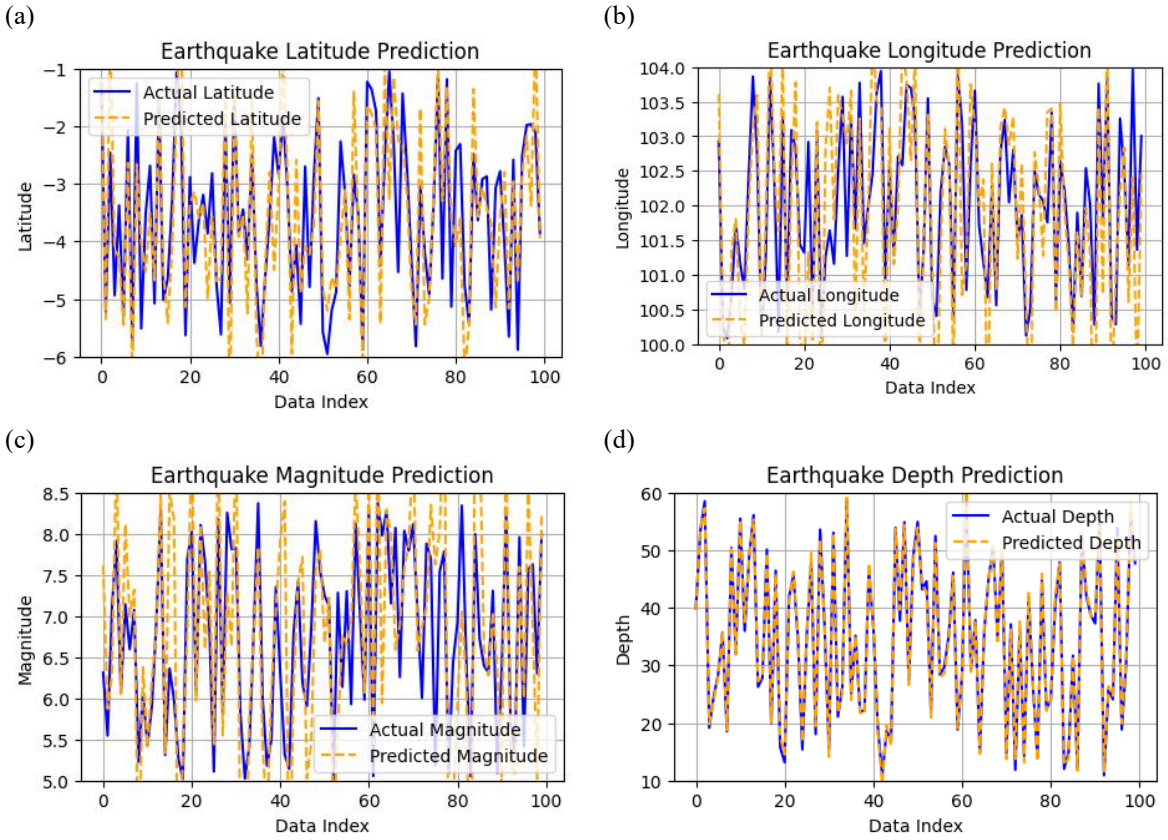

Figure 3. Comparison curve between actual data and prediction results: (a) Earthquake latitude prediction, (b) Earthquake longitude prediction, (c) Earthquake magnitude prediction, (d) Earthquake depth prediction.

Table 4. Error metrics.

Metrics	Predicted Values
MAE	0.283
MSE	0.156
RMSE	0.395

The model contains a total params: 11.204 (43.77 KB), trainable params: 11.204 (43.77 KB), non-trainable params: 0 (0.00 KB).

Fig. 3 illustrates the earthquake prediction curve generated by the LSTM model. It compares predicted values with actual values based on parameters such as magnitude, latitude, longitude, and depth. Additionally, two plots were generated from this curve to analyze the distribution of predicted earthquakes. The first plot (Fig. 4) shows the distribution based on latitude and longitude, while the second plot (Fig. 5) focuses on the distribution based on magnitude and depth.

Fig. 3 illustrates the comparison between actual values (solid blue line) and predicted results (dotted orange line) generated by the prediction model. From the graph, it can be observed that the prediction pattern closely resembles the actual data. This visualization demonstrates that the gap between the predicted and actual lines is relatively small for most data points.

This indicates that the model performs well in predicting earthquakes. The MAE and RMSE error values presented in Table 4 are also low, further confirming that the LSTM model can produce predictions with minimal errors, thereby validating the model's effectiveness in capturing patterns in historical data.

The earthquake prediction modeling results indicated that earthquakes frequently occurred in the Southern part of Sumatra region with magnitudes ranging

from 5.0 to 6.0 and depths between 20 and 60 km. Based on Fig. 4, the coordinates revealed that earthquakes commonly occurred at latitudes between -2° and -6°, representing areas south of the equator, and longitudes between 100°E and 104°E, encompassing the western part of Sumatra. Most of these earthquake occurrences were concentrated in the Southern part of Sumatra region, including Bengkulu Province, western South Sumatra, and southwestern Lampung. This area is part of an active subduction zone, making it highly prone to seismic activity. Furthermore, high-magnitude earthquakes (7.0–8.5) at depths between 20 and 37 km were found to occur near the western coastline of Sumatra Island, specifically within coordinates of longitudes 100°–102° and latitudes -2° to -5°. This region forms part of the megathrust zone along the convergence boundary of the Indo-Australian and Sunda plates (Azmiyati, 2021).

These findings align with the geological characteristics of Sumatra, which is dominated by the subduction of the Indo-Australian plate beneath the Sunda plate, resulting in frequent seismic activities. The zone along the western coastline, extending from Aceh in the north to Lampung in the south, is known to generate significant earthquakes with the potential for triggering tsunamis. This makes the region a critical area for disaster preparedness and mitigation efforts (Firmansyah et al., 2022).

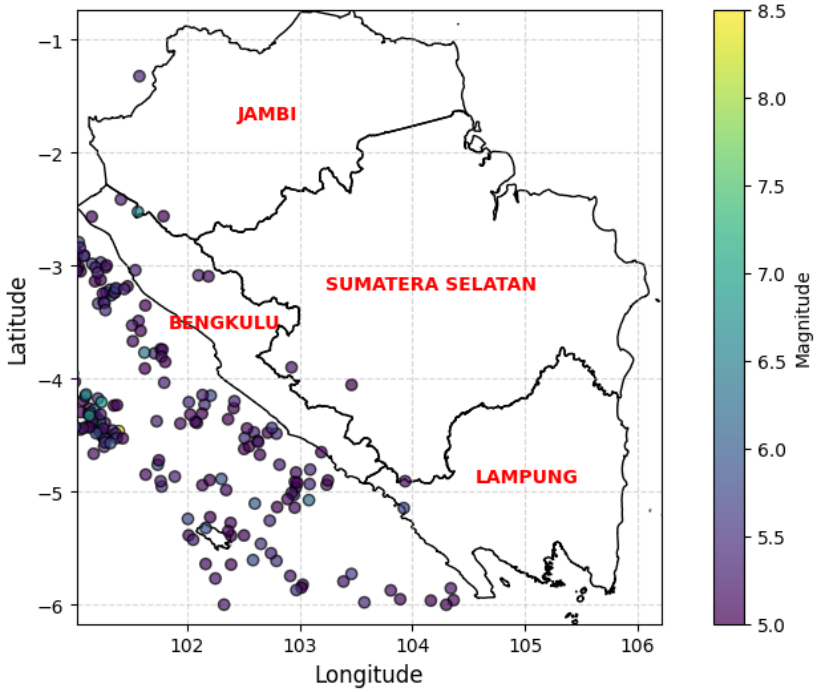

Figure 4. Earthquake distribution based on longitude and latitude.

The earthquake prediction model also highlighted patterns in the temporal distribution of seismic events. Most earthquakes occurred during specific periods, indicating potential seasonal or temporal trends influenced by tectonic stress accumulation and release in the subduction zone. These temporal patterns can be further studied to enhance the predictive accuracy of seismic models and improve early warning systems for high-risk areas.

Additionally, the results emphasized the importance of region-specific mitigation strategies, particularly in densely populated and economically vital areas like Bengkulu, South Sumatra, and Lampung. Infrastructure in these regions, including transportation networks,

industrial facilities, and residential areas, must be designed and retrofitted to withstand seismic impacts. The study also underscores the potential of advanced machine learning models, such as LSTM, in contributing to disaster risk management. By incorporating historical seismic data and leveraging the model's capability to identify long-term dependencies, LSTM-based predictions offer valuable insights for policymakers, urban planners, and disaster management agencies. These predictions can support the development of targeted risk reduction measures, such as optimized evacuation plans, improved land-use planning, and enhanced public awareness campaigns.

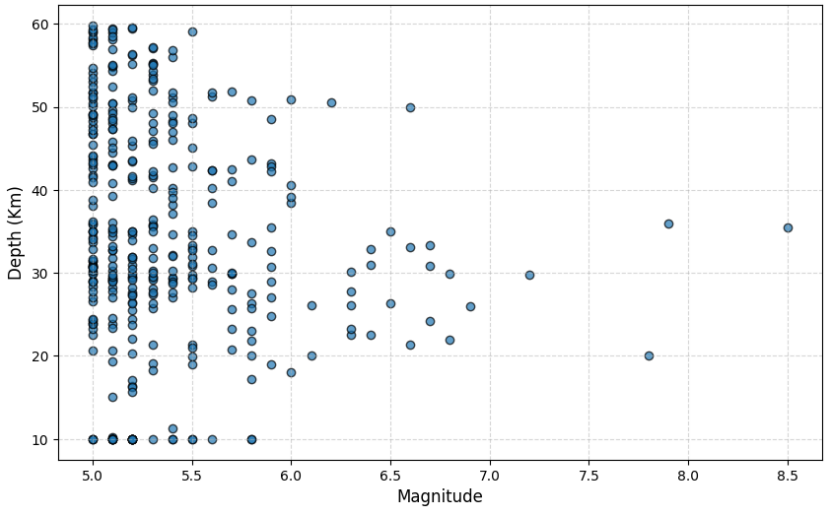

Figure 5. Earthquake distribution based on magnitude and depth.

Future research could further refine the model by integrating additional parameters, such as soil type, fault activity, and energy distribution during seismic events, to improve prediction accuracy. Moreover, the inclusion of real-time seismic monitoring data and the expansion of the dataset to include other regions in Indonesia could make the model more robust and broadly applicable. This would support a more comprehensive approach to earthquake disaster mitigation across the archipelago, ultimately reducing the social and economic impacts of seismic events.

Conclusion

This study successfully developed an LSTM-based earthquake prediction model using historical data from Southern Sumatra (2004–2024). The model demonstrated reliable performance in predicting earthquake parameters, with a MAE of 0.28 and RMSE of 0.39, indicating good accuracy. High-risk areas were identified around Bengkulu, western South Sumatra, and southwestern Lampung, with most predicted earthquakes ranging from magnitudes 5.0–6.0 at depths of 20–60 km, aligning with active subduction zone characteristics.

These findings contribute to disaster mitigation by aiding government and stakeholders in preparedness and infrastructure planning. Future enhancements could integrate real-time data, such as satellite and GPS observations, to improve accuracy. This model offers a scalable framework for earthquake prediction in other seismically active regions, supporting global disaster risk reduction.

Acknowledgements

The authors would like to express their heartfelt gratitude to the editors, reviewers,

and proofreaders for their constructive feedback and assistance in refining this manuscript.

Special thanks are extended to the technical staff and colleagues at the Physics and Geophysics Departments, Faculty of Mathematics and Natural Sciences, Universitas Bengkulu, for their support in equipment preparation and data analysis. The authors also acknowledge those who contributed to the survey and data collection, which were essential for developing the Long Short-Term Memory (LSTM) models for earthquake prediction in Southern part of Sumatra.

Author Contribution

Ainul Lisa: Conceptualization, Methodology, Data Analysis, Writing – Original Draft. **Refrizon**: Supervision, Validation, Writing – Review & Editing. **Rida Samdara**: Data Collection, Resources, Visualization.

Conflict of Interest

The authors declare that they have no conflict of interest. There are no financial or personal relationships with any individuals or organizations that could inappropriately influence (bias) the work presented in this study.

References

Adherda, D. T., Hikmatyar, M., & Ruuhwan, R. (2023). Gender classification based on voice using recurrent neural network (RNN). *Antivirus: Jurnal Ilmiah Teknik Informatika*, 17(1), 111–122. https://doi.org/10.35457/antivirus.v17i1.3049

Al-Faridzi, A., & Kurniasari, N. (2024). Perancangan kawasan perdagangan dan jasa koridor Jalan Sultan Agung Bandar Lampung. *Jurnal Riset Perencanaan Wilayah dan Kota*, 4(1), 51–58. https://doi.org/10.29313/jrpwk.v4i1.3614

Azmiyati, U. (2021). Analisis percepatan getaran tanah maksimum akibat gempabumi di wilayah Nusa Tenggara dengan metode probabilistic seismic hazard analysis (PSHA). *JISIP (Jurnal Ilmu Sosial dan Pendidikan)*, 5(1), 331–339. http://dx.doi.org/10.58258/jisip.v5i1.1709

Bellamkonda, S., Settipalli, L., Vedantham, R., & Vemula, M. K. (2021). An enhanced earthquake prediction model using long short-term memory. *Turkish Journal of Computer and Mathematics Education (TURCOMAT)*, 12(14), 2397–2403. https://turcomat.org/index.php/turkbilmat/article/view/10665

Berhich, A., Belouadha, F. Z., & Kabbaj, M. I. (2020). LSTM-based models for earthquake prediction. *The ACM International Conference Proceeding Series*, pp. 1–7. https://doi.org/10.1145/3386723.3387865

Firmansyah, A., Wandono, W., & Ramdhan, M. (2022). Tectonic pattern imaging of southern Sumatra region using double difference seismic tomography. *EKSPLORIUM*, 43(1), 29–40. https://ejournal.brin.go.id/eksplorium/article/view/8135

Gerlach, L., Gu, W., Nayak, N., Qian, X., & Viren, B. (2024). Waveform resampling with LMN method. *Journal of Instrumentation*, 19(10), P10029. https://doi.org/10.1088/1748-0221/19/10/p10029

Hodson, T. O. (2022). Root-mean-square error (RMSE) or mean absolute error (MAE): When to use them or not. *Geoscientific Model Development*, 15, 5481–5487. https://doi.org/10.5194/gmd-15-5481-2022

Kavianpour, P., Kavianpour, M., Jahani, E., & Ramezani, A. (2023). A CNN-

BiLSTM model with attention mechanism for earthquake prediction. *The Journal of Supercomputing*, 79(17), 19194–19226. https://doi.org/10.1007/s11227-023-05369-y

Lin, L., Tan, Y., Zeng, G., Zhou, M., & Zhou, W. (2024). Research on prediction model based on improved LSTM. Proceedings of CISCE 2024, pp. 1171–1174. https://doi.org/10.1109/cisce62493.2024.10653120

Ma, X. (2024). The investigation of LSTM-random search with various standardization and normalization technologies. Highlights in Science, Engineering and Technology, 85, 1087–1094. https://doi.org/10.54097/xgeyhr93

Marzuki, M., Ramadhan, R., Friska, V., Primadona, H., Ramadhan, R. A., Monica, F., Arisa, D., & Namigo, E. L. (2022). Dynamics of West Coast of Sumatra and island arc Mentawai during the coseismic phase of the Mentawai Mw7.8 25 October 2010 earthquake. *Journal of Physics: Conference Series*, 2309(1), 012030. https://doi.org/10.1088/1742-6596/2309/1/012030

Mase, L. Z. (2021). A note of ground motion interpretation and site response analysis during the 2007 Bengkulu–Mentawai earthquakes, Indonesia. *Arabian Journal of Geosciences*, 14, 99. https://doi.org/10.1007/s12517-020-06344-0

Mer, S., Saxena, S., & Pundir, A. S. (2024). Unveiling earthquake dynamics: A comprehensive data analytics and LSTM-based prediction model for enhanced seismic forecasting. *Proceedings of 2024 IEEE 5th India Council International Subsections Conference (INDISCON) 2024*, pp. 1–6. https://doi.org/10.1109/indiscon62179.2024.10744325

Nurhakiki, J., & Yahfizham, Y. (2024). Studi kepustakaan: Pengenalan 4 algoritma pada pembelajaran deep learning beserta implikasinya. *Pendekar: Jurnal Pendidikan Berkarakter*, 2(1), 270–281. https://journal.politeknik-pratama.ac.id/index.php/Pendekar/article/view/598

Samudra, A. A., Juhad, M., & Dewi, M. P. (2024). Mitigation strategies and policy recommendations for the economic impact of the Sunda Strait Megathrust: Seismic risk probability assessment and cost-loss estimates. *Journal of Infrastructure, Policy and Development*, 8(11), 9023. http://dx.doi.org/10.24294/jipd.v8i11.9023

Scott, M. R., & Willmott, C. J. (2023). Decomposition of the mean absolute error (MAE) into systematic and unsystematic components. *PLoS ONE*, 18(20, e0279774. https://doi.org/10.1371/journal.pone.0279774

Sianturi, T. B., Cholissodin, I., & Yudistira, N. (2023). Penerapan algoritma long short-term memory (LSTM) berbasis multi fungsi aktivasi terbobot dalam prediksi harga Ethereum. Jurnal Pengembangan Teknologi Informasi dan Ilmu Komputer, 7(3), 1101–1107. https://j-ptiik.ub.ac.id/index.php/j-ptiik/article/view/12384

Sonthalia, A., Pasari, S., & Devi, S. (2023). Earthquake prediction using long short-term memory on spatio-temporally segmented data. *2023 Third International Conference on Artificial Intelligence and Smart Energy (ICAIS)*, pp. 1378–1382. https://doi.org/10.1109/ICAIS56108.2023.10073687.

Sukrungsri, S., Khamsiri, S., & Pailoplee, S. (2024). Investigation of co-seismic stress and aftershock distribution along the Sumatra–Andaman subduction zone. *Geoscience Letters*,

11, 48. https://doi.org/10.1186/s40562-024-00366-2

Verianto, E. (2024). Penerapan LSTM dengan regularisasi untuk mencegah overfitting pada model prediksi tingkat inflasi di Indonesia. *Jurnal Sistem Informasi dan Sistem Komputer*, 9(2), 195–204. https://doi.org/10.51717/simkom.v9i2.460

Yang, Y., Liu, H., Mostafavi, A., & Tatano, H. (2024). Review on modeling the societal impact of infrastructure disruptions due to disasters. *arXiv*. https://doi.org/10.48550/arxiv.2405.12732

ISSN: 2579-5821 (Print)
ISSN: 2579-5546 (Online)
URL address: http://journal.unhas.ac.id/index.php/geocelebes
DOI: 10.70561/geocelebes.v10i1.48347

Jurnal Geocelebes Vol. 10 No. 1, April 2026, 12 – 33

Analysis of Flood Vulnerability and Rainfall Changes in the Angke-Pesanggrahan Watershed using Spatial Mapping

Ratu Kenanga Fitria*, Yayat Ruhiat, Yuvita Oktarisa

Physics Education, Sultan Ageng Tirtayasa University, Serang, 42117, Indonesia.

*Corresponding author. Email: 2280220023@untirta.ac.id

Manuscript received: 16 November 2025; Received in revised form: 31 December 2025; Accepted: 31 Januari 2026

Abstract

This study analyzes flood vulnerability in the Angke-Pesanggrahan Watershed, Jakarta, which faces increased risks due to land-use changes. The study aims to calculate the 50-year return period flood discharge, map flood-prone zones, and formulate mitigation recommendations using spatial mapping. A quantitative approach was employed, analyzing 15 years of rainfall data from five stations. Methodology included data consistency testing, Spearman's correlation, stationarity, and outlier identification, followed by regional rainfall analysis using Thiessen Polygons. The Log Pearson Type III distribution was applied for frequency analysis, and the Nakayasu Synthetic Unit Hydrograph method estimated flood discharge. Flood-prone zones were mapped using scoring and overlay techniques in a Geographic Information System (GIS). Results show that the 50-year flood discharge reaches 1.128 m^3/s, exceeding existing river capacity. Mapping simulations identified flood depths of 3–6 meters in downstream areas, with high-risk zones concentrated in Northern Kembangan, Kedaung Kali Angke, Kapuk Muara, Kamal Muara, Eastern Cengkareng, and Northern Kedoya, where surface runoff contributes up to 90%. Spatial analysis categorized 257.18 km^2 as non-prone, 92.14 km^2 as moderately prone, 75.75 km^2 as prone, and 58.57 km^2 as highly prone. This study concludes that the Angke-Pesanggrahan Watershed, particularly the Cengkareng Drain section, requires urgent technical intervention, including river normalization and catchment area optimization. These findings provide a crucial spatial database for sustainable flood mitigation and risk-based decision-making in urban planning.

Keywords: Angke-Pesanggrahan Watershed; Disaster Mitigation; Nakayasu HSS; Q50 Flood Discharge; Spatial Mapping.

Citation: Fitria, R. K., Ruhiat, Y., & Oktarisa, Y. (2026). Analysis of Flood Vulnerability and Rainfall Changes in the Angke-Pesanggrahan Watersheds using Spatial Mapping. *Jurnal Geocelebes*, 10(1): 12–33, doi: 10.70561/geocelebes.v10i1.48347

Introduction

Flood vulnerability in the Angke-Pesanggrahan River Basin, particularly in Jakarta, has increased in line with population growth and massive land use changes (Habibi & Darmawan, 2024). Land conversion reduces soil absorption and river retention capacity, causing frequent surface runoff and annual flooding in downstream areas such as North Kembangan-Kamal Muara (Ignes & Arbaningrum, 2021). BNPB data from 2015 recorded 93 flood points in Jakarta (Novarini et al., 2024), while regional development has significantly altered the land cover in the Pesanggrahan watershed, leading to a substantial increase in surface runoff where urbanized areas now contribute to a higher percentage of immediate flood discharge rather than natural infiltration (Taki & Wartaman, 2022). As a result, a 3.5 meter flood hit Pesanggrahan in 2025, causing hundreds of residents to evacuate (Abdolazimi et al., 2025; Noviansah, 2025) and blocking several roads in Kembangan, West Jakarta (Syukur, 2025).

A review of previous studies shows significant developments in flood modelling, but there is still room for further discussion and exploration. Habibi & Darmawan (2024), Mitu et al. (2025) and Limeria & Saputra (2024) have successfully applied the HEC-RAS model (1D and 2D) to predict peak discharge and inundation area at various return periods, but their analysis tends to focus on hydraulic dynamics within river channels without integrating broad physical land variables. On the other hand, Fox et al. (2024) and Sinurat et al. (2022) have gone further by converting HEC-RAS output into spatial format using QGIS and InaSAFE for economic loss analysis, but the vulnerability parameters used do not yet cover detailed biophysical characteristics of the soil. A research gap exists in the lack of integration between design discharge (Q_{50}) and multifactorial geospatial parameters that determine water retention capacity outside the river channel. This study aims to fill this gap by developing a more comprehensive flood vulnerability mapping approach through scoring and overlay techniques on seven key parameters, which are rainfall intensity, administrative boundaries, soil infiltration, land slope, elevation, land use, and soil texture. The strength of this study lies in the cross-validation between Nakayasu's Synthetic Unit Hydrograph (HSS) hydrological modelling, HEC-RAS 6.7 hydraulic simulation, and geospatial mapping from the Geospatial Information Agency, in order to map hotspots of vulnerability in the Angke-Pesanggrahan watershed more precisely amid massive trends in climate change and land use. The study was conducted in the Angke-Pesanggrahan watershed, Jakarta, as shown in the location map in Figure 1.

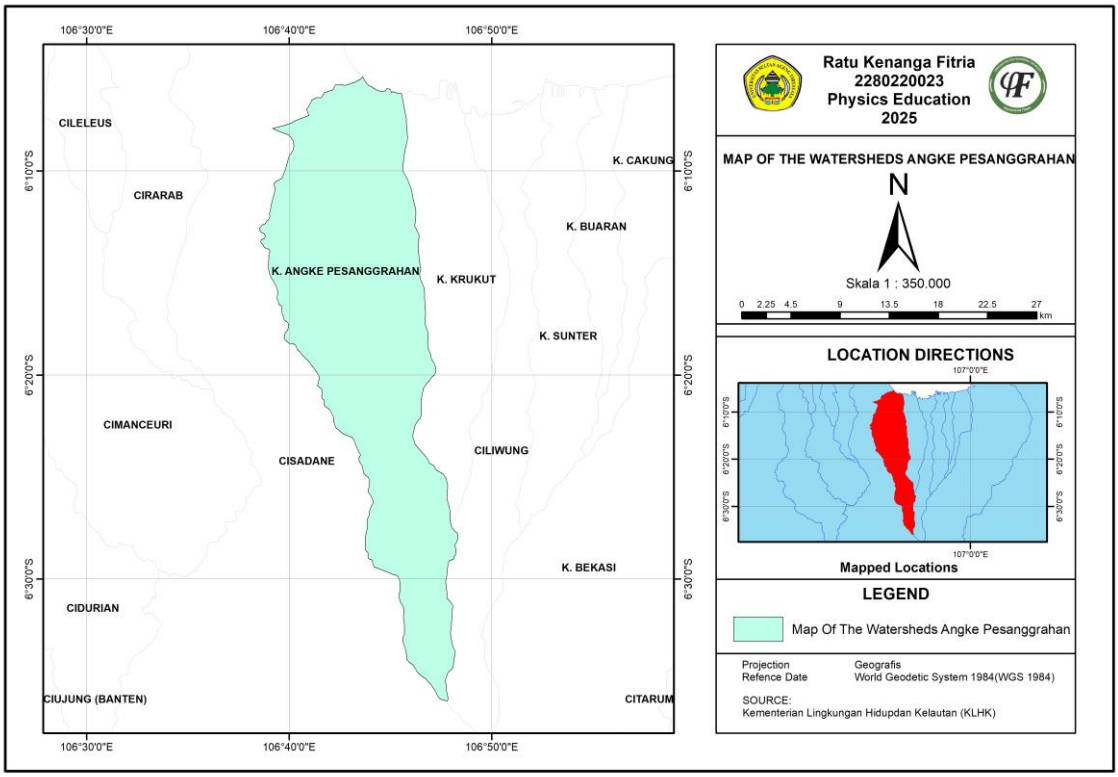

Figure 1. Angke-Pesanggrahan watersheds map.

Materials and Methods

Regional Geology and Research Area

Watersheds are vital areas for the preservation of the water cycle. Topographically, a watershed functions as a catchment area that collects and carries

rainwater runoff through river systems to lower areas or the sea (Dahlia & Fadiarman, 2020). This area is an ecological system where natural components such as soil, water, and vegetation interact with human activities, particularly in densely populated regions where land-use changes significantly affect the hydrological balance and increase flood risks (Taki & Wartaman, 2022). These characteristics significantly influence the hydrological response and flow patterns within the watershed when subjected to rainfall (Yu et al., 2025; Rhianazala et al., 2026). In tropical regions like Indonesia, atmospheric conditions often lead to high-intensity rainfall events that exceed drainage capacities. Recent spatial analyses in Greater Jakarta demonstrate that extreme rainfall intensity, coupled with topographic factors, remains a primary driver of urban flood vulnerability, often resulting in rapid surface runoff and significant hazard zones (Muhammad et al., 2025). The geographical locations of the five rainfall stations used in this study, including their coordinates, are detailed in Table 1.

Table 1. Location of Rainfall Stations in the Angke-Pesanggrahan watershed (PSDA WS Ciliwung-Cisadane, 2019).

No	Rain Station	Geographical Location	
		Latitude	Longitude
1	Sawangan	06° 18’ 54.4’’ S	106° 45’ 51.2’’ E
2	Bendung Gintung	06° 34’ 28.9’’ S	106° 52’ 58.6’’ E
3	Cengkareng Drain	06° 09’ 13.3’’ S	106° 44’ 52.6’’ E
4	Situ Parigi	06° 16’ 53.6’’ S	106° 41’ 48.3’’ E
5	Villa Pamulang	06° 20’ 34.6’’ S	106° 43’ 22.8’’ E

Data Collection

This study uses one sources of information; this secondary data came from the Ciliwung-Cisadane River Basin Management Agency and the Geospatial Information Agency. The secondary data obtained is as follows:

1.) Daily rainfall data from the Sawangan Rainfall Station, Bendung Gintung, Cengkareng, Situ Parigi, and Villa Pamulang for 15 years.
2.) Administrative boundary data West Java, DKI Jakarta, and Banten Province.
3.) Land cover data for West Java, DKI Jakarta, and Banten Province.
4.) Elevation data, land slope, soil drainage, soil texture of West Java province, DKI Jakarta, and Banten.

Analysis of Extreme Rainfall

The frequency analysis in this study was performed using the Log Pearson Type III distribution to estimate extreme rainfall events. This method is highly recommended for hydrological modelling in tropical regions due to its flexibility in handling skewed data distribution (Abdolazimi et al., 2025; Ismael & Awchi, 2023) Rainfall frequency analysis was performed using the Log Pearson Type III distribution, which is the standard approach for analyzing hydrological extreme values in tropical regions (Guo et al., 2025), as shown in Equation (1).

$$log\ \ X = \overline{LogX} + k(\overline{S\ log\ X}) \qquad (1)$$

where:
$\overline{LogX}$: mean value of log X.
k : frequency factor (found in the Pearson III table).
$\overline{S\ log\ X}$: standard deviation of log X.

Rainfall in the Region Thiessen Polygon Method

The regional average rainfall is determined by considering the spatial distribution of observation points, where the Thiessen Polygon method is applied to assign area-weighting factors to each station (Kwak et al., 2024; Rahmadani et al., 2023). The regional average rainfall was estimated by

applying the area-weighting formula shown in Equation (2). The regional average rainfall was calculated using the Thiessen Polygon spatial interpolation method to account for the uneven distribution of rain gauges (Dahlia & Fadiarman, 2020):

$$\bar{R} = \frac{A_1R_1+A_2R_2+I+A_nR_n}{A_1+A_2+I+A_n} \quad (2)$$

with:
$\bar{R}$: Average rainfall in the area (mm).
A_1, A_2, A_n : Area represented by each observation point (m^2).
R_1, R_2, R_n : Rainfall at observation location 1 (mm).

The spatial distribution and influence area of each rainfall station were determined using the Thiessen Polygon method, which ensures a representative average rainfall calculation for the entire watershed.

Debit Analysis Flood (Nakayasu HSS)

The peak flood discharge for the 50-year return period was estimated using the Nakayasu Synthetic Unit Hydrograph (SUH) method, as formulated in Equation (3). To estimate peak flood discharge, the Nakayasu SUH was applied, as it is calibrated for Indonesian watershed characteristics (Rahmadani et al., 2024).

$$Q_p = \frac{A \times R_0}{3{,}6(0{,}3T_p+T_{0,3})} \quad (3)$$

The calculation of river dimensions is based on the discharge that must be accommodated by the river (Q_s), which is greater than or equal to the planned discharge (Q_T) influenced by planned rainfall (R_T). To evaluate whether the existing river can accommodate the flood, the hydraulic capacity of the river channel was evaluated using Manning's equation to determine the threshold for overtopping during peak discharge, the cross-sectional capacity was analyzed using Equation (4) and Equation (5). One way to describe this condition is as follows (Setiyawan et al., 2022; Taki & Wartaman, 2022):

$$Q_s > Q_T \quad (4)$$

The discharge that can be accommodated by the river (Q_s) is obtained using the following formula:

$$Q_s = A_S V \quad (5)$$

Formula explanation:
A_s : Wet cross-sectional area of the river (m^2).
V : Average flow velocity according to material type (m/s).

To transform effective rainfall into flood hydrographs, the Nakayasu SUH was employed. This approach has been widely validated for urban watersheds in Indonesia to accurately predict peak discharge timing and volume (Handore et al., 2025).

Spatial Mapping Flood Vulnerability

Accuracy testing of spatial mapping was conducted using the cross-validation method by comparing ArcGIS spatial output parameters with actual accumulation data from HEC-RAS numerical modelling. The accuracy of vulnerability maps was measured based on the consistency between spatially defined 'Highly Vulnerable' zones and hydrodynamic parameters at relevant river stations.

Scoring

Vulnerability scores are calculated by multiplying the relative weight of each criterion with its corresponding rank value, a method known as Weighted Overlay Analysis (Soma et al., 2021). The scoring system for each physical parameter, such as land use, rainfall, slope, and soil characteristics, is defined in Table 2 – 7, while the assigned weights are shown in Table 8.

Table 2. Scores for land closure classes (Alif et al., 2025).

No	Class	Score
1	Rice fields, open land	9
2	Dry fields, settlements	7
3	Bushes, thickets, reeds	5
4	Plantations	3
5	Forests	1
6	Clouds and shadows	1

Table 3. Scores for rainfall classes (Alif et al., 2025).

No	Class	Score
1	> 3000 mm (very wet)	9
2	2501 – 3000 mm (wet)	7
3	2001 – 2500mm (moderately damp)	5
4	1502 – 2000 mm (dry)	3
5	< 1500mm (very dry)	1

Table 4. Score for land slope classes (Alif et al., 2025).

No	Class	Score
1	Flat (0 – 3%)	9
2	Undulating (3 – 8%)	7
3	Wavy (8 – 15%)	5
4	Small hills (15 – 30%)	3
5	Hills (30 – 45%)	1
6	Steep hills (> 45%)	0

Table 5. Scores for the upper grades (Allafta & Opp, 2021).

No	Class	Score
1	0 – 12.5m	9
2	12.5 – 25m	7
3	25 – 50m	5
4	50 – 75m	3
5	75 – 100m	1
6	> 100m	0

Table 6. Score for soil texture classes (Alif et al., 2025).

No	Class	Score
1	Very smooth	9
2	Smooth	7
3	Medium	5
4	Rough	3
5	Very rough	1

Table 7. Score for soil drainage classes (Endendijk et al., 2023).

No	Class	Score
1	Hindered	9
2	Somewhat hindered	7
3	Somewhat hindered – Moderate	5
4	Moderate	3
5	Fast	1

Table 8. Weight of parameters causing flooding (Alif et al., 2025).

No	Parameter	Weight
1	Land slope	0.2
2	Elevation class	0.1
3	Soil texture	0.2
4	Soil permeability (drainage)	0.1
5	Rainfall	0.15
6	Land use	0.15
7	River buffer	0.1

Overlay

This stage involves combining all parameters using overlay weight sum (Saad et al., 2024). The score attributes of each parameter will be overlaid to produce a new layer, thereby automatically calculating the score.

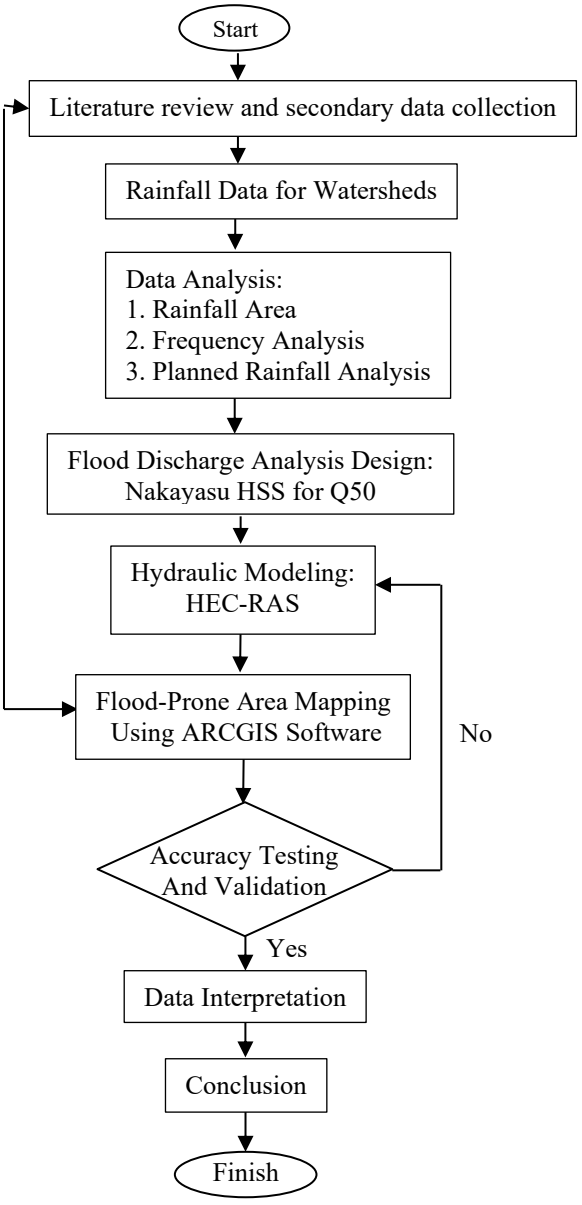

Figure 2. Flowchart of research analysis of flood vulnerability in the Angke-Pesanggrahan watershed spatial mapping and rainfall changes.

Reclassification of flood vulnerability levels

This stage involves classifying the overlay results separated into four groups of vulnerability: safe, not vulnerable, moderately vulnerable, and highly vulnerable.

The systematic workflow of this research, from data collection to final mapping, is depicted in the flowchart in Figure 2.

Results and Discussion

Rainfall Plan

Extreme price distribution

In this study, the Maximum Annual Series Method was used to ensure that there was only one data point per year, representing the maximum average rainfall value available for each period. This approach is essential for establishing a consistent dataset for flood susceptibility and vulnerability modelling (Safaei-moghadam et al., 2024). The recorded maximum daily rainfall data and the completed dataset used for further analysis are presented in Table 9 – 11.

Table 9. Maximum Daily Rainfall Data (PSDA WS Ciliwung-Cisadane, 2023).

Year	Sawangan	Bendung Gintung	Cengkareng Drain	Situ Parigi	Villa Pamulang
	Daily P (mm)				
2009	85	0	139	0	0
2010	108	0	75	0	0
2011	76	0	83	0	0
2012	83.4	0	54	0	0
2013	100	0	91	0	0
2014	100	0	105	0	0
2015	43.6	50	124	0	0
2016	105	95	120	0	0
2017	39.8	105.5	110	0	0
2018	60	67.5	83	0	0
2019	135	135	423	158	112
2020	50.7	0	156	175	94.5
2021	92	134	92.5	122.3	83.5
2022	98.4	122.5	124.5	157	85
2023	116.5	82	62	89	88

Table 10. Missing rainfall.

Year	Sawangan	Bendung Gintung	Cengkareng Drain	Situ Parigi	Villa Pamulang
	Daily P (mm)				
2009	85	0	139	0	0
2010	108	0	75	0	0
Total	1293.4	791.5	1842	701.3	463

Normal Ratio Method

The calculation used is quite simple, which is by calculating rainfall data at nearby rain stations to find the missing rainfall data at that station. The variables in this method are the daily rainfall at other stations and the total rainfall for 1 year at those other stations. For 2009, the table is on Table 10.

Table 11. Complete rainfall data (mm).

Year	Sawangan	Bendung Gintung	Cengkareng Drain	Situ Parigi	Villa Pamulang
	Daily P (mm)				
2009	85	27.9	139	30.9	25.5
2010	108	24.6	75	27.2	22.5
2011	76	20.5	83	22.8	18.8
2012	83.4	18.6	54	20.6	17
2013	100	25.1	91	27.8	22.9
2014	100	26.6	105	29.4	24.3
2015	43.6	50	124	28.8	23.8
2016	105	95	120	46.7	38.5
2017	39.8	105.5	110	39.2	32.4
2018	60	67.5	83	31	25.6
2019	135	135	423	158	112
2020	50.7	114.3	156	175	94.5
2021	92	134	92.5	122.3	83.5
2022	98.4	122.5	124.5	157	85
2023	116.5	82	62	89	88

Using the Normal Ratio formula, we get:

$$d_x = \frac{1}{n}\sum_{t=1}^{n} d_i \frac{An_x}{An_i}$$

$$d_x = \frac{1}{4}(139 \times \frac{791.5}{1842} + 85 \times \frac{791.5}{1293.5} + 0 \times \frac{791.5}{701.3} + 0 \times \frac{791.5}{463})$$

$$d_x = 27.94 \text{ mm}$$

The same applies to other years, with the following results.

Double period curve consistency test

Before collecting data, it is important to understand the nature of the data that will be used in the study. The consistency test results at each station are quite good, the reliability of the rainfall data was verified through a double-mass curve consistency test, as shown in the graphs in Figure 3.

Based on the analysis results, the validation of rainfall data feasibility for flood discharge analysis is reinforced by comprehensive statistical test findings. Furthermore, the application of double-mass curve consistency testing is a fundamental prerequisite to ensure the reliability and integrity of the hydrological

data before integrating multiple criteria into the subsequent discharge calculations and spatial analysis (Bahago et al., 2026). The results of double mass curve consistency testing show a stable and homogeneous rainfall accumulation pattern across all stations, proving that historical data is highly reliable for flood vulnerability analysis. The stability of this trend reflects the influence of regional meteorological phenomena such as La Niña, which periodically triggers extreme rainfall in the Greater Jakarta area but is still recorded consistently between stations without any systematic errors in the measuring instruments. These findings are in line with a previous study (Wigati & Wahyudin, 2013) on the characteristics of extreme rainfall in Jakarta, where spikes in accumulation on the double mass curve coincide with periods of regional climate anomalies. Thus, the consistency of this data provides an accurate climate information base for spatial mapping of flood-affected areas in the Angke-Pesanggrahan watershed.

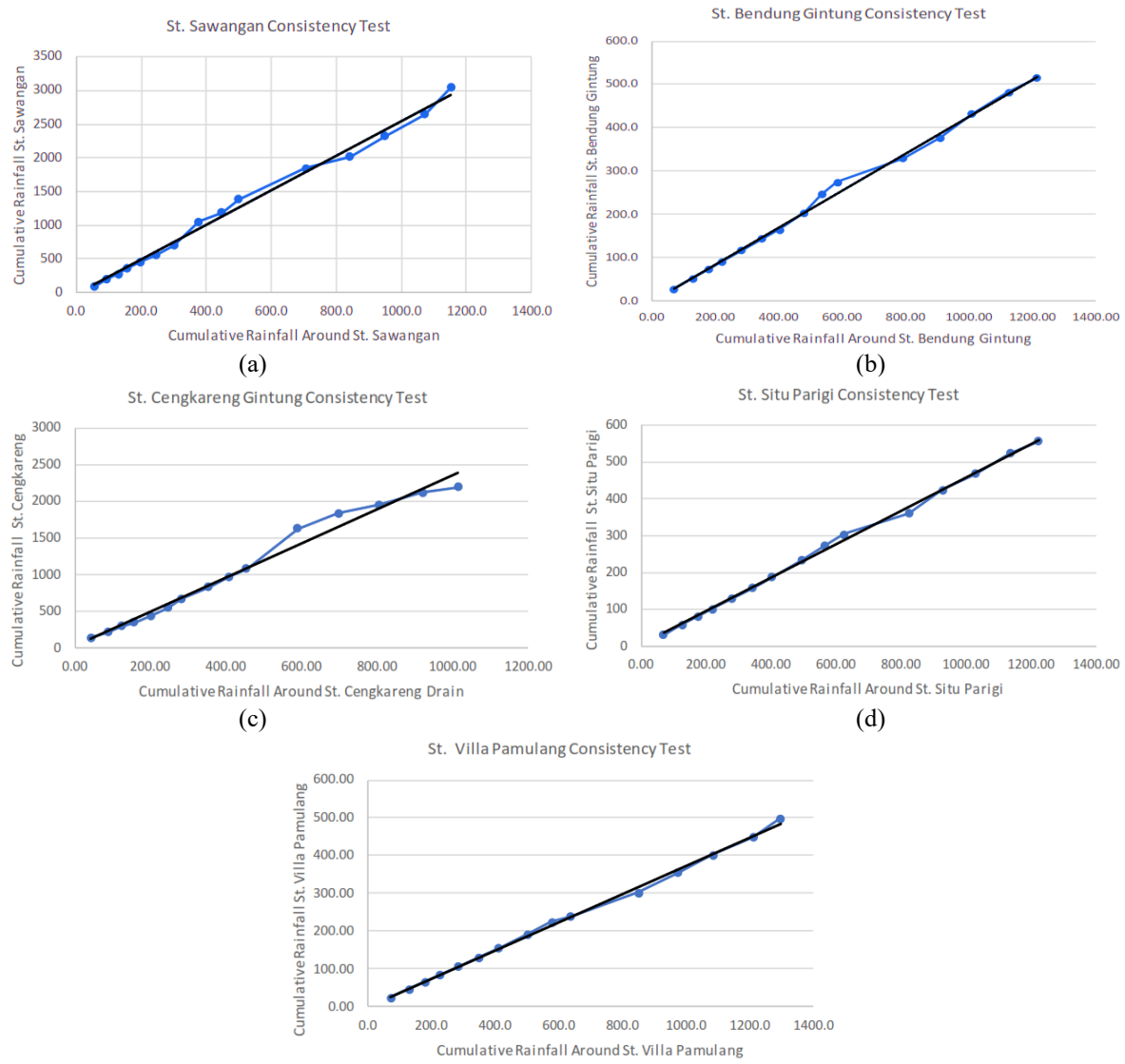

Figure 3. Data Consistency Graph (a) Sawangan Station, (b) Bendung Gintung Station, (c) Cengkareng Drain Station, (d) Situ Parigi Station, (e) Villa Pamulang Station.

Furthermore, about data stationarity, which in this study was proven through F-tests and T-tests showing variance and mean stability, is a critical assumption in

hydrological frequency analysis. Support also comes from Muhammad et al. (2025), who emphasizes that rainfall data with non-trend and non-persistent characteristics, identified through Spearman and Cox-Stuart tests, provide a valid basis for flood modelling in urban areas such as the Angke-Pesanggrahan River Basin.

The reliability of the rainfall dataset was ensured by conducting an outlier test and consistency check before the simulation. This preprocessing step is crucial to eliminate anomalies that could potentially bias the hydraulic simulation results (Carr et al., 2025; Mester et al., 2025; Saraswati et al., 2023).

Table 12. Results of rainfall data analysis calculations for the Sawangan station.

Testing	α	Zm/F/T	Zcr/Fcr/tcr	Conclusion	
Spearman Trend Absence Test	5%	-4,96	1,771	-Zcr < Z < Zcr	There is no trend
Cox and Stuart Trend Absence Test	1%	1,78	2,58	-Zcr < Z < Zcr	There is no trend
Cox and Stuart Trend Absence Test	5%	1,789	1,96	-Zcr < Z < Zcr	There is no trend
Stationarity Test (F-test)	5%	0,04	4,28	F < Fcr	Stable Variation
Stationarity Test (T-test)	5%	-24,6	1,78	-tcr < t < tcr	Stable Average
Spearman Persistence Test	5%	2,44	1,771	-tcr < t	Dependence Data

Table 13. Results of rainfall data analysis calculations for the Bendung Gintung station.

Testing	α	Zm/F/T	Zcr/Fcr/tcr	Conclusion	
Spearman Trend Absence Test	5%	-3,88	1,771	-Zcr < Z < Zcr	There is no trend
Cox and Stuart Trend Absence Test	1%	1,78	2,58	-Zcr < Z < Zcr	There is no trend
Cox and Stuart Trend Absence Test	5%	1,78	1,96	-Zcr < Z < Zcr	There is no trend
Stationarity Test (F-test)	5%	0,13	4,28	F < Fcr	Stable Variation
Stationarity Test (T-test)	5%	-33,9	1,78	-tcr < t < tcr	Stable Average
Spearman Persistence Test	5%	2,22	1,77	-tcr < t	Dependence Data

Table 14. Results of rainfall data analysis calculations for the Cengkareng station.

Testing	α	Zm/F/T	Zcr/Fcr/tcr	Conclusion	
Spearman Trend Absence Test	5%	-1,76	1,77	-Zcr < Z < Zcr	There is no trend
Cox and Stuart Trend Absence Test	1%	0.89	2,58	-Zcr < Z < Zcr	There is no trend
Cox and Stuart Trend Absence Test	5%	0,89	1,96	-Zcr < Z < Zcr	There is no trend
Stationarity Test (F-test)	5%	0,04	4,28	F < Fcr	Stable Variation
Stationarity Test (T-test)	5%	-11,2	1,78	-tcr < t < tcr	Stable Average
Spearman Persistence Test	5%	0,78	1,77	t < tcr	Random Data

Table 15. Results of rainfall data analysis calculations for the Situ Parigi station.

Testing	α	Zm/F/T	Zcr/Fcr/tcr	Conclusion	
Spearman Trend Absence Test	5%	-4,27	1,77	-Zcr < Z < Zcr	There is no trend
Cox and Stuart Trend Absence Test	1%	1,789	2,58	-Zcr < Z < Zcr	There is no trend
Cox and Stuart Trend Absence Test	5%	1,789	1,96	-Zcr < Z < Zcr	There is no trend
Stationarity Test (F-test)	5%	0,11	4,28	F < Fcr	Stable Variation
Stationarity Test (T-test)	5%	-28,9	1,78	-tcr < t < tcr	Stable Average
Spearman Persistence Test	5%	2,9	1,77	-tcr < t	Dependence Data

Table 16. Results of rainfall data analysis calculations for the Villa Pamulang station.

Testing	α	Zm/F/T	Zcr/Fcr/tcr	Conclusion	
Spearman Trend Absence Test	5%	-3,4	1,77	-Zcr < Z < Zcr	There is no trend
Cox and Stuart Trend Absence Test	1%	1,789	2,58	-Zcr < Z < Zcr	There is no trend
Cox and Stuart Trend Absence Test	5%	1,789	1,96	-Zcr < Z < Zcr	There is no trend
Stationarity Test (F-test)	5%	0,04	4,28	F < Fcr	Stable Variation
Stationarity Test (T-test)	5%	-21,3	1,78	-tcr < t < tcr	Stable Average
Spearman Persistence Test	5%	1,06	1,77	t < tcr	Random Data

The analysis of rainfall characteristics across the five stations shows varied yet statistically consistent results. Based on the data presented in Table 12, 13, and 15, the

calculated values for Sawangan, Bendung Gintung, and Situ Parigi stations exceed the critical value at α = 5%, confirming the persistent nature or serial dependence of the data. Conversely, the test results in Table 14 and 16 show that data fluctuations remain within stationary limits through F-tests and T-tests. This demonstrates that, overall, the rainfall data does not experience extreme shifts in mean or variance over time.

The data validity Is further supported by the outlier test results shown in Figure 4. Although the Saluran Cengkareng station shows data points exceeding the outlier threshold, these values are considered reasonable and hydrologically acceptable as they do not deviate significantly from historical trends. Consequently, the entire dataset is declared valid for use as input in the planned rainfall frequency analysis using the Log Pearson Type III distribution.

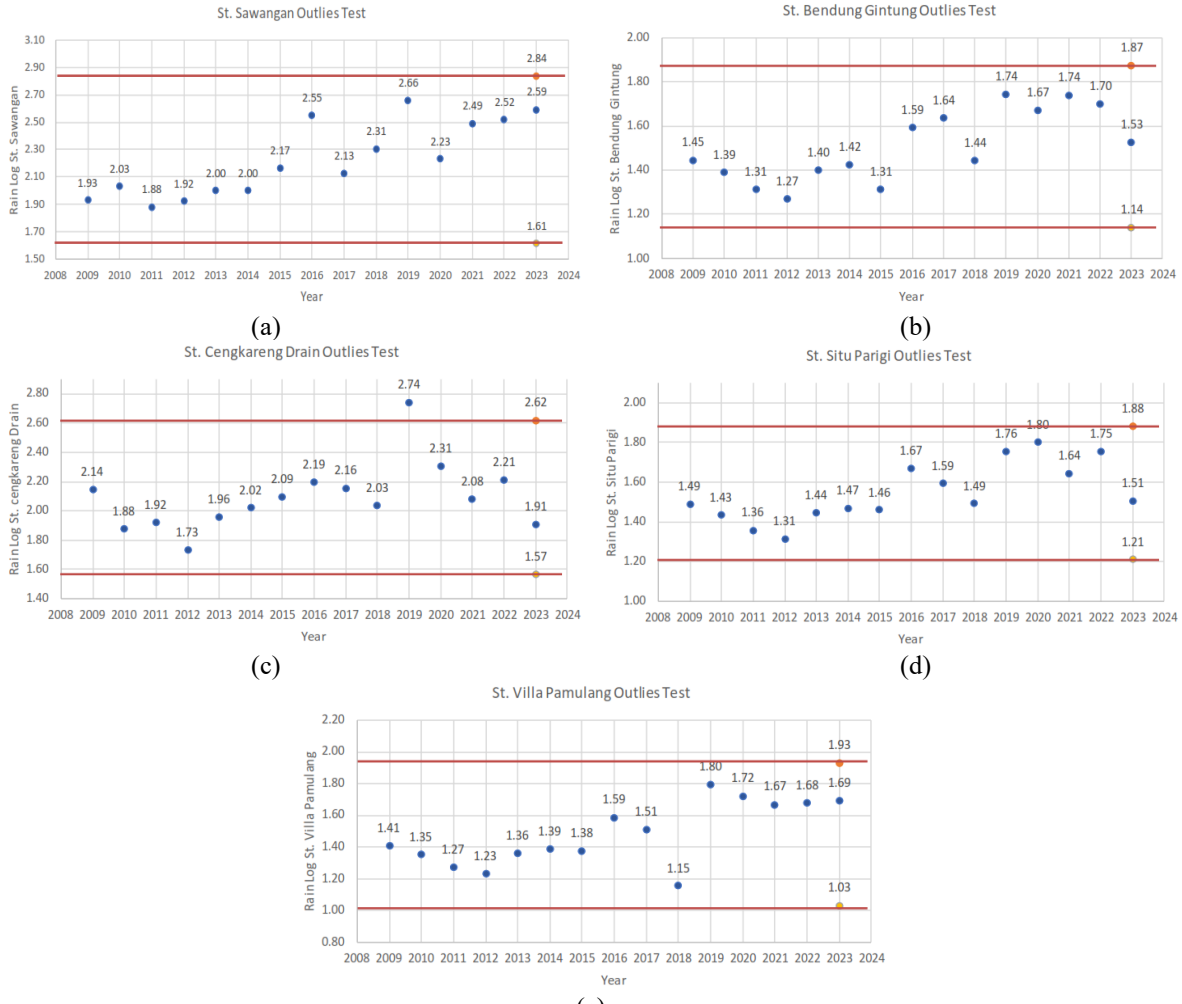

Figure 4. Outlier test graph (a) Sawangan Station, (b) Bendung Gintung Station, (c) Cengkareng Drain Station, (d) Situ Parigi Station, € Villa Pamulang Station.

The stability of data without trends reflects that despite annual fluctuations, long-term hydrological characteristics in this region remain consistent for use in modelling. In terms of regional meteorology, the absence of trends indicates that rainfall spikes are periodic, influenced by the La Niña phenomenon, which historically triggers extreme rainfall anomalies in Jakarta without permanently changing long-term distribution patterns. Compared to previous studies on extreme rainfall in the Angke-Pesanggrahan watershed, the recorded extreme values including outliers at the Cengkareng Drain Station—are representative of the high rainfall intensity

typical of regional climate anomalies and are not systematic errors. These outliers were not eliminated from the dataset because their positions were still within the main distribution threshold, in line with the approach taken by Glas et al. (2023).

The existence of stable and stationary extreme data is crucial input for HEC-RAS modelling, where the resulting design rainfall triggers a peak discharge (Q_{50}) of 1127.97 m^3/s. This figure is validated as a critical condition for river capacity, where the numerical profile shows that the water level reaches 4.15 m, which directly explains the mechanical cause behind the spatial distribution of flood vulnerability mapped through ArcGIS.

Area Rainfall

In terms of rainfall areas, rainfall stations are located in designated Watershed Areas (DAS), although they can also be found in adjacent DAS. Five rainfall stations are located within the Angke Pesanggrahan Watershed, which are Sawangan Station, Bendung Gintung Station, Situ Parigi Station, Villa Pamulang Station, and Cengkareng Drain Station. As shown in Figure 5.

Table 17 displays the Thiessen coefficient by comparing the length of the sub-DAS with the total length of the DAS. Using the Thiessen polygon method in millimeters, Table 18 displays the average rainfall of the DAS.

The coverage area represented by each rainfall station, determined through the Thiessen Polygon method, is detailed in Table 17. These area values serve as the basis for calculating the regional average rainfall for the watershed, with the final results presented in Table 18.

The method used to determine rainfall in the Angke-Pesanggrahan watershed is the Thiessen Polygon Method. This method was chosen based on the characteristics of spatial distribution, in which each rain station has a unique and non-uniform area of influence. The analysis involved five influential rainfall stations, which are Sawangan Station, Bendung Gintung, Cengkareng Drain, Situ Parigi, and Villa Pamulang.

Table 17. Influence area values for each rain station.

No	Station Name	Area (km^2)	Thiessen coefficient
1	Cengkareng Drain	139.49	0.281
2	Bendung Gintung	57.25	0.115
3	Situ Parigi	109.69	0.221
4	Villa Pamulang	56.54	0.114
5	Sawangan	133.49	0.269
	Total	496.46	1

The process of mapping the area of influence was carried out using a working map with a scale of 1:330.000. The calculation steps began with determining the watershed boundaries at the review point, then plotting the five stations based on their geographical coordinates. Based on the results of the polygon mapping, the total Thiessen polygon influence area was 496.46 km^2. The unique area of each station was then used as a weighting factor to produce accurate rainfall design input for hydrodynamic simulation.

Probability Distribution

Probability distribution tests are used to determine whether the observed probability distribution can be used to calculate the sample data's statistical distribution under analysis. The test analysis results are shown in Tables 19 and 20 below, with the most accurate distribution being the Log Pearson III distribution.

Table 18. Rainfall values in the Angke Pesanggrahan watershed area from 2009 to 2023.

Year	Rainfall Station (mm)					
	Sawangan	Bendung Gintung	Cengkareng Drain	Situ Parigi	Villa Pamulang	Rainfall
2009	85.0	27.9	139.0	30.9	25.5	74.9
2010	108.0	24.6	75.0	27.2	22.5	61.5
2011	76.0	20.5	83.0	22.8	18.8	53.3
2012	83.4	18.6	54.0	20.6	17.0	46.2
2013	100.0	25.1	91.0	27.8	22.9	64.1
2014	100.0	26.6	105.0	29.4	24.3	68.7
2015	146.8	20.6	124.0	28.8	23.8	85.7
2016	353.4	39.1	156.5	46.7	38.5	158.2
2017	134.0	43.4	143.5	39.2	32.4	93.7
2018	202.0	27.8	108.3	31.0	14.3	96.4
2019	454.4	55.5	551.7	57.0	62.5	303.3
2020	170.7	47.0	203.5	63.1	52.8	128.4
2021	309.7	55.1	120.6	44.1	46.6	138.6
2022	331.2	50.4	162.4	56.6	47.5	158.4
2023	392.1	33.7	80.9	32.1	49.1	144.7

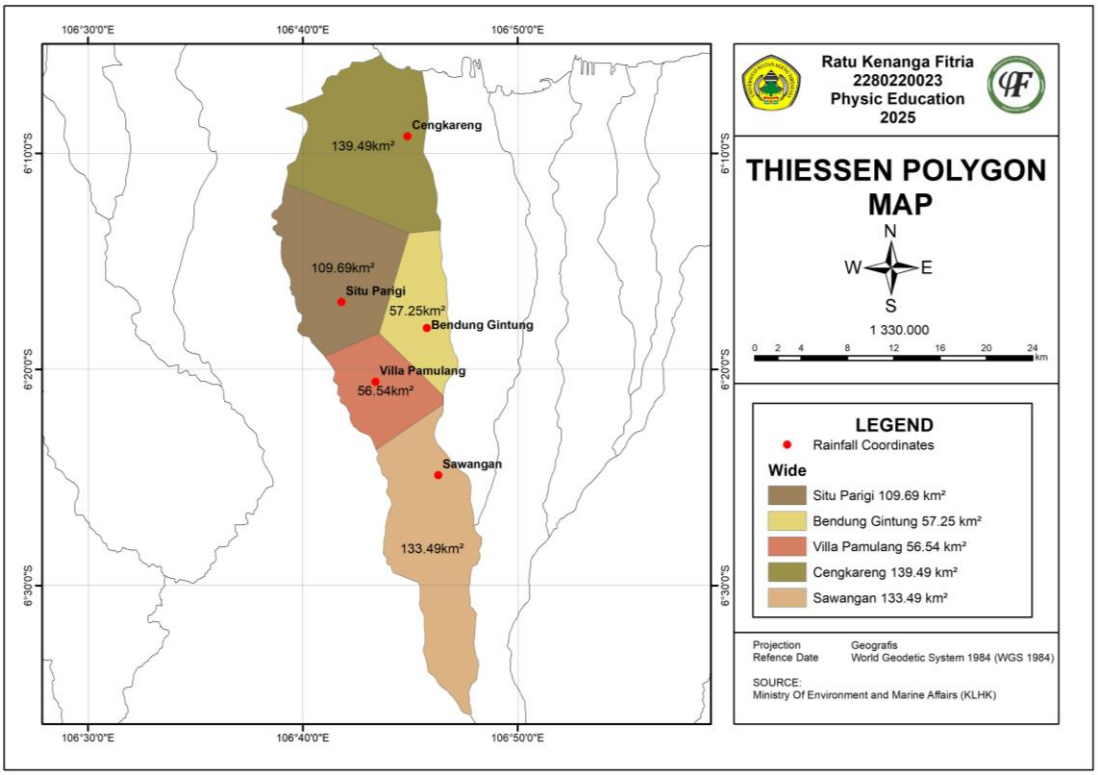

Figure 5. Map of the Angke Pesanggrahan watershed using the thiessen polygon method.

a) Chi-Square Test

Table 19. Calculation results X^2 and X^2_{cr}.

CHI-SQUARE TEST				
Description	**Distribution**			
	Gumbel	**Log Pearson**	**Normal**	**Log Normal**
X^2critis α (1%)	9.21	9.21	9.21	9.21
X^2critis α (5%)	5.991	5.991	5.991	5.991
Degrees of Freedom (DF)	2	2	2	2
X^2count	5.3	0.7	7.3	0.7
Description (1%)	Accepted	Accepted	Accepted	Accepted
Description (5%)	Accepted	Accepted	Rejected	Accepted
Difference (1%)	3.9	8.5	1.9	8.5
Difference (5%)	0.7	5.3	-1.3	5.3

b) Smirnov-Kolmogorof Test

Table 20. Distribution test calculation results using the Smirnov-Kolmogorov method.

SMIRNOV-KOLMOGOROF TEST				
Description	**Distribution**			
	Gumbel	**Log Pearson**	**Normal**	**Log Normal**
Δcritical α (1%)	0.4	0.4	0.4	0.4
Δcritical α (5%)	0.34	0.34	0.34	0.34
Large data (n)	15	15	15	15
Δcount	0.13	0.11	0.15	0.08
Description (1%)	Accepted	Accepted	Accepted	Accepted
Description (5%)	Accepted	Accepted	Accepted	Accepted
Difference (1%)	0.273	0.29	0.246	0.317
Difference (5%)	0.213	0.23	0.186	0.257

Table 21. Planned rainfall calculation results.

Repeatability [Tr] (Year)	Pr (%)	K	$K.Sd_{Log\ R}$	Log R_{design}	R_{design} (mm)
2	50	-0.141	-0.0313	1.961	88.26
5	20	0.774	0.1712	2.163	122.12
10	10	1.338	0.2960	2.288	149.20
25	4	2.008	0.4442	2.436	189.25
50	2	2.479	0.5485	2.540	223.71
100	1	2.930	0.6481	2.640	262.48
200	0.5	3.364	0.7442	2.736	306.23
1000	0.1	4.328	0.9574	2.949	431.12

Rainfall Analysis Plan

Based on the frequency analysis using Equation (1), the planned rainfall values were obtained. These results, representing the Log Pearson Type III distribution, are presented in Table 21.

Planned flood discharge

Planned flood discharge based on Equation 3 above, the planned discharge was obtained using the Nakayasu HSS method. Table 22 below shows the results obtained.

Table 22. Planned flood discharge calculation results.

No	Repeatability [Tr] (Year)	Planned Flood Discharge (m^3/s)
1	2	296.9
2	5	473.1
3	10	630.7
4	25	887.2
5	50	1128
6	100	1418.8
7	200	1770.2
8	1000	2892.3

The final estimation of peak flood discharges for various return periods, based on the integrated hydrological modelling, is summarized in Table 23. These values serve as the primary input for the subsequent flood inundation mapping.

The hydrological data used in this study consist of annual peak flood discharge records. The fluctuation and distribution of these discharge values over the observation period, which serve as the primary input for the frequency analysis, are presented in Figure 6.

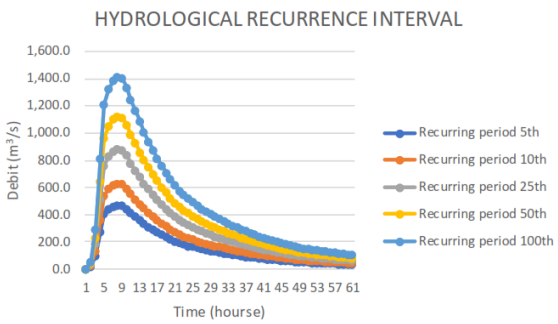

Figure 6. Total Runoff Hydrograph for 5, 10, 25, 50, and 100-year return periods, Nakayasu HSS.

Sensitivity analysis on the Nakayasu HSS model was conducted to identify the extent to which the flow coefficient (C) and peak time (T_p) parameters affect the design flood discharge in the Angke-Pesanggrahan watershed. The simulation results show that

variations in these parameter values significantly affect the hydrograph elevation, where the peak discharge (Q_{50}) produced reaches 1127.97 m^3/s. This value was then validated numerically through direct comparison with the existing storage capacity on the Cengkareng River section (Reach 4) using the HEC-RAS program. The results of ArcGIS and RAS Mapper mapping, showing the accumulation of unaccommodated discharge, are visualized in Figure 7.

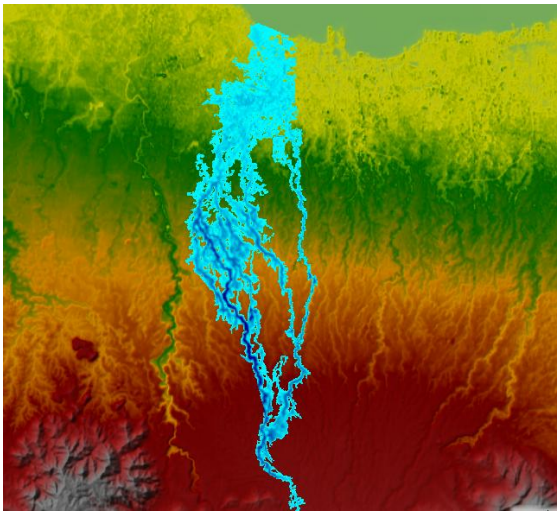

Figure 7. Results of 50-year flood modelling.

Table 23. Results of river cross-section analysis (existing) using the HEC-RAS program.

River	Location Name	Flood Discharge (m^3/s)	River Capacity (m^3/s)	Description
1	Kembangan Utara	1128	599.78	not safe
2	Kedaung Kali Angke	1128	592.12	not safe
3	Kapuk Muara	1128	565.41	not safe
4	Kamal Muara	1128	565.00	not safe
5	Cengkareng Timur	1128	596.47	not safe
6	Kedoya Utara	1128	598.54	not safe

Explanation:
Safe: flood discharge < river capacity
Not safe: flood discharge > river capacity

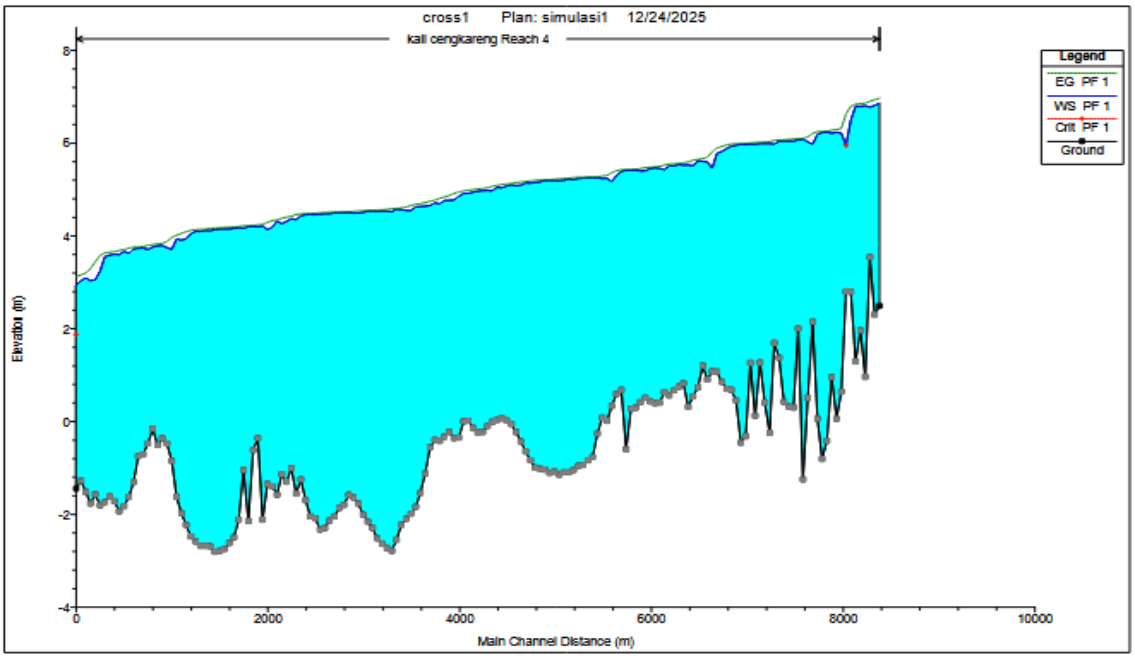

Figure 8. Longitudinal profile of the Cengkareng river.

The hydraulic simulation results for the 50-year return period (Q_{50}) are visualized through the cross-sectional profiles in Figure 8 – 11. The analysis indicates that the existing river capacity is insufficient to accommodate the peak discharge of 1.128 m^3/s. As illustrated in these figures, the water level (represented by the blue area) significantly exceeds the main channel's bank stations (marked by the red dots),

particularly in the downstream sections. This overflow confirms that the river has reached its maximum capacity, leading to extensive flooding in the surrounding areas due to the water overtopping the riverbanks.

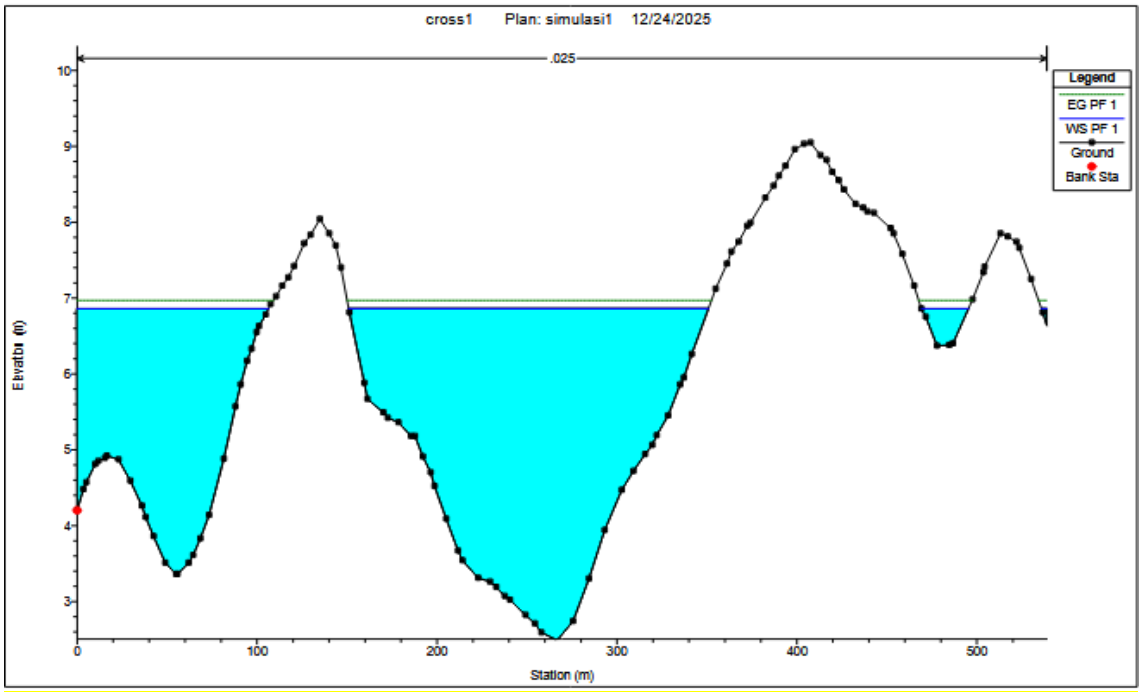

Figure 9. Cross-section of the Cengkareng river at the headwaters.

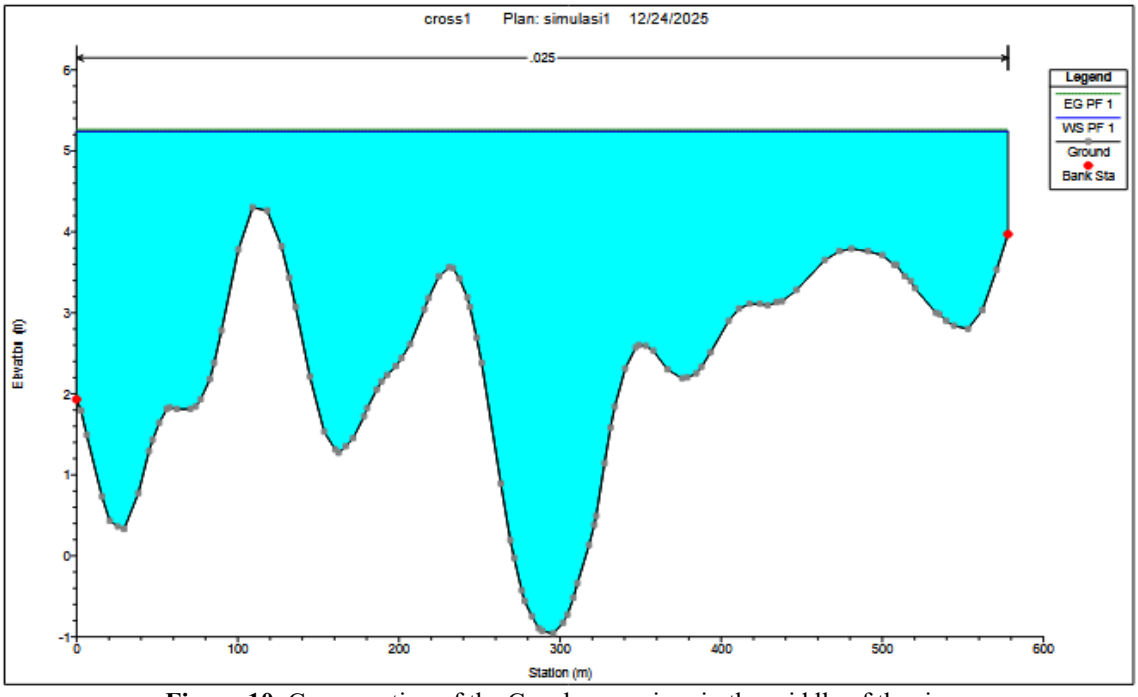

Figure 10. Cross-section of the Cengkareng river in the middle of the river.

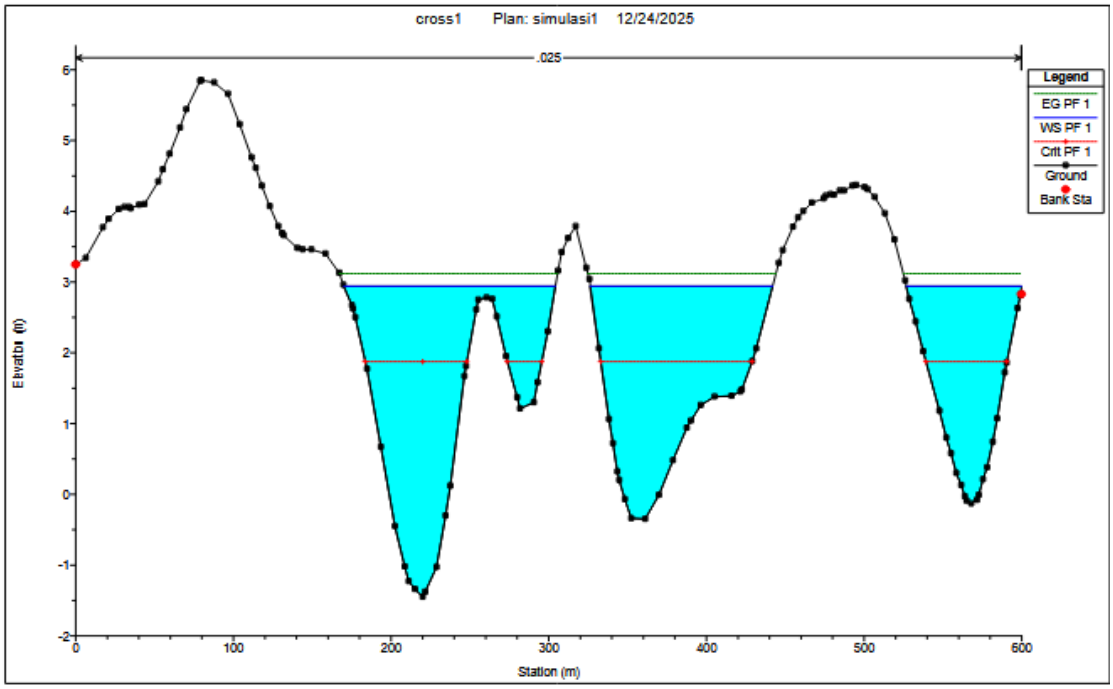

Figure 11. Cross-section of the Cengkareng river at the downstream section.

The flood vulnerability analysis in this study integrates hydrological sensitivity parameters through Nakayasu HSS method and hydrodynamic simulation using HEC-RAS 6.7. Sensitivity analysis in Nakayasu's modelling was conducted to determine the peak discharge based on various return periods. The calculation results show that for a 50-year return period (Q_{50}), the design flood discharge reaches 1128 m^3/s. This figure was validated through the Hydrological Recurrence Interval graph, which shows a very significant peak discharge surge compared to the recurrence periods below it. Numerical validation of river safety levels was carried out by comparing the design flood discharge (Q_{50}) with the river capacity at six critical locations along the Cengkareng River (Figure 8 – 11). The comparison results show that the current river capacity ranges from only 565 to 599.78 m^3/s. The comparison graph of planned discharge vs. river capacity (Figure 12) visually emphasizes the 'Not Safe' condition, where the planned flood discharge exceeds the river capacity by almost double at each observation location. This condition was confirmed technically through cross-section modelling in the upstream, middle, and downstream sections of the river. HEC-RAS simulations show that the water level at Q_{50} conditions has exceeded the elevation of the river banks (bank stations), resulting in massive flooding in the surrounding areas. Spatially, the results of ArcGIS and RAS Mapper mapping (Figure 7) show that this unaccommodated discharge accumulation spread to densely populated residential areas downstream with varying flood depths, providing strong quantitative and visual evidence for the need for immediate structural mitigation efforts.

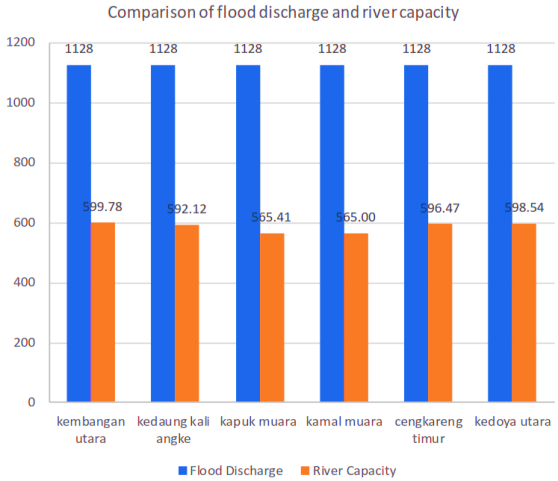

Figure 12. Comparison of flood discharge and river capacity.

Flood-Prone Areas

The analysis of flood-prone areas in the Angke-Pesanggrahan watershed was conducted through the integration of GIS technology with the overlay scoring method based on the Analytic Hierarchy Process (AHP), an approach that, according to Monir et al. (2026), is highly effective in combining multidimensional geospatial data with measurable assessment consistency through the Consistency Ratio (CR). Physical parameters of the area were validated using the pairwise comparison method and visualized in a Flood Risk Map (Figure 13), which served as a crucial validation tool to confirm the accuracy of the HEC-RAS hydrodynamic simulation results on the Cengkareng River section. The use of this hybrid model strengthens the reliability of spatial mapping, ensuring that the resulting risk zoning is in line with field conditions and can serve as a strong scientific basis in supporting disaster management policies and adaptive spatial planning.

The mapping results show a strong linear correlation with the numerical findings in the HEC-RAS model. The downstream area, particularly around the Cengkareng River, which covers the areas of Kembangan Utara, Kedaung Kali Angke, Kapuk Muara, Kamal Muara, Cengkareng Timur, and Kedoya Utara, is classified as "Vulnerable" to "Very Vulnerable." Technically, the very high vulnerability status in ArcGIS validates the field conditions where the numerical river capacity (average 596 m^3/s) proved unable to accommodate the planned flood discharge (Q_{50}) of 1128 m^3/s.

The inability of the river to accommodate the discharge caused water to accumulate and overflow the levees, which was spatially mapped as extensive flooding in densely populated settlements. Thus, this vulnerability map is not merely a statistical representation, but rather visual evidence that is synchronized with the river's hydraulic failure found in the HEC-RAS simulation. The integration of these two methods ensures that the identified flood hotspots are highly accurate because they are based on multifactorial GIS parameters and validated by extreme water flow dynamics.

From Figure 13, detailed spatial distributions for each vulnerability category, ranging from safe to highly prone areas, are shown in Figures 14 – 17.

The accuracy of this mapping was confirmed in downstream areas such as Cengkareng, Kembangan, and Kebon Jeruk (Highly Vulnerable Areas Map in Figure 17), where the water surface elevation (W.S. Elev) reached 4.15 m. These results show a high level of precision between the spatial and numerical models, the areas identified as having the highest vulnerability scores in GIS consistently coincide with the overtopping points in the HEC-RAS simulation, which have a flood width (Top Width) of up to 566.99 m.

Using the actual discharge value of 1.128 m^3/s as a validation instrument, this vulnerability map has strong scientific validity. The "Highly Vulnerable" status in coastal and downstream areas (Highly Vulnerable Map) is supported by comparative numerical data (Figure 17) showing a "Not Safe" status across all observation locations. This proves that the map produced is an accurate reflection of the physical dynamics of flooding in the field.

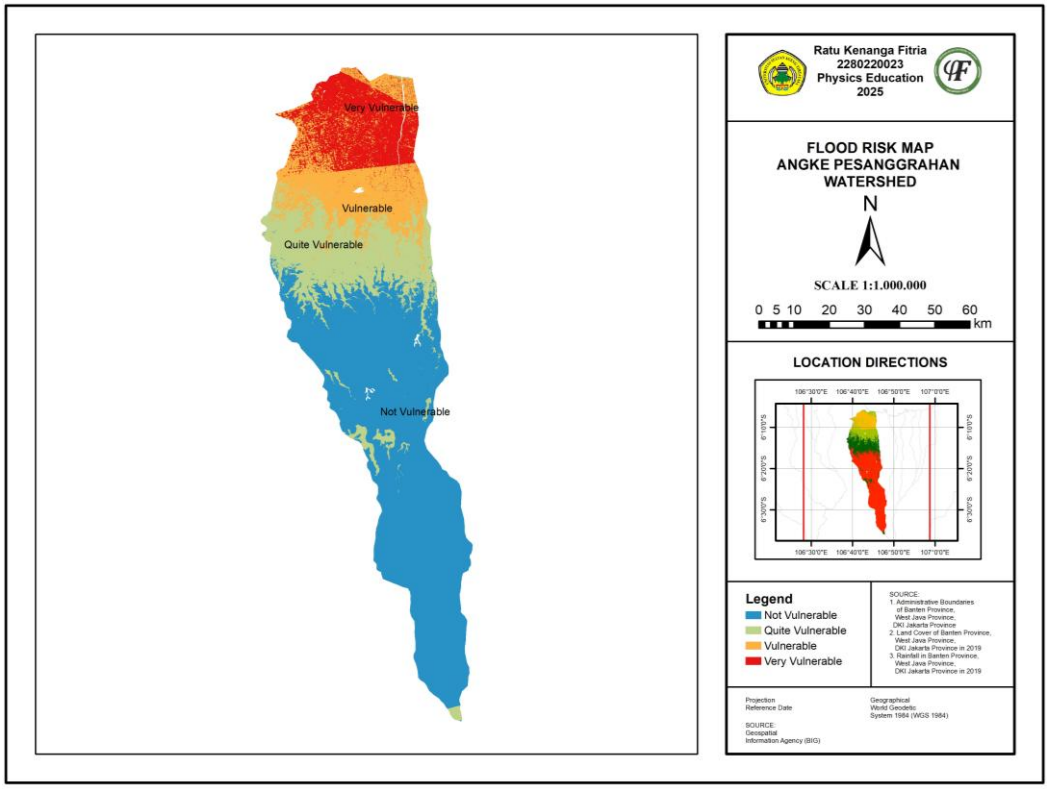

Figure 13. Angke Pesanggrahan watershed flood prone map.

The accuracy of these modeling results is strongly supported by records of actual flooding events in the downstream area of the Angke-Pesanggrahan watershed. Based on disaster reports, the areas of South Kedoya, Kebon Jeruk, and Kembangan consistently experience severe flooding when extreme rainfall hits Greater Jakarta. For example, the extreme flood event in January 2020, triggered by record-breaking rainfall intensity, caused widespread inundation across Jakarta with water levels reaching critical heights in areas such as Kembangan due to the overflow of the Pesanggrahan river system (Dahlia & Fadiarman, 2020). This incident validates the HEC-RAS simulation results in this study, which show that the water surface elevation (W.S. Elev) is at a critical level of 4.15 m and the storage capacity is 'Not Safe'.

In addition, data from the Jakarta Regional Disaster Management Agency (BPBD) (BPBD, 2021) noted that the Cengkareng and Penjaringan areas were prone to flooding with long receding times. This is in line with the 'Very Vulnerable' classification on the ArcGIS vulnerability map (Figure 13) and the spatial modeling results, which showed that the widest accumulation of flooding was in these areas. The consistency between media/field data and the results of this numerical modeling proves that the integration of the Nakayasu HSS, HEC-RAS, and GIS methods in this study has a very high level of accuracy in representing the actual flood risk in the field.

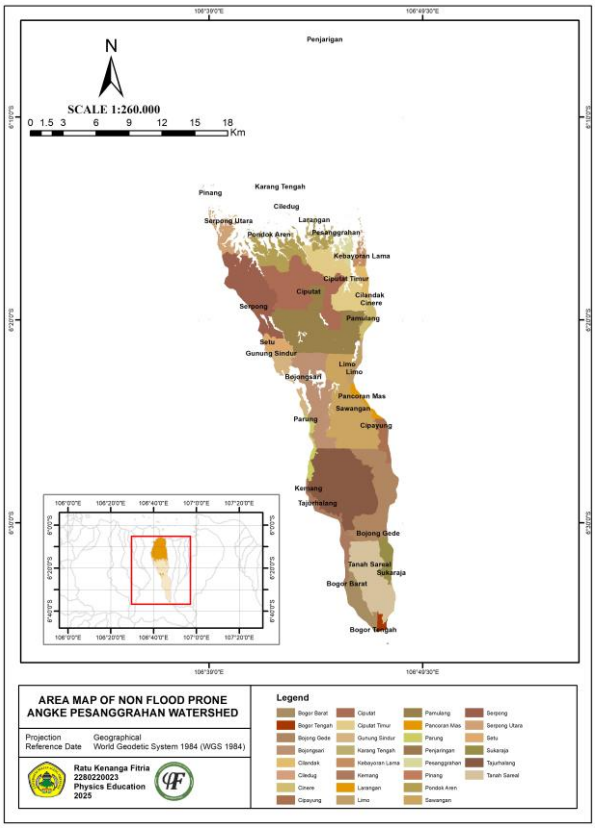

Figure 14. Map of non-flood prone areas.

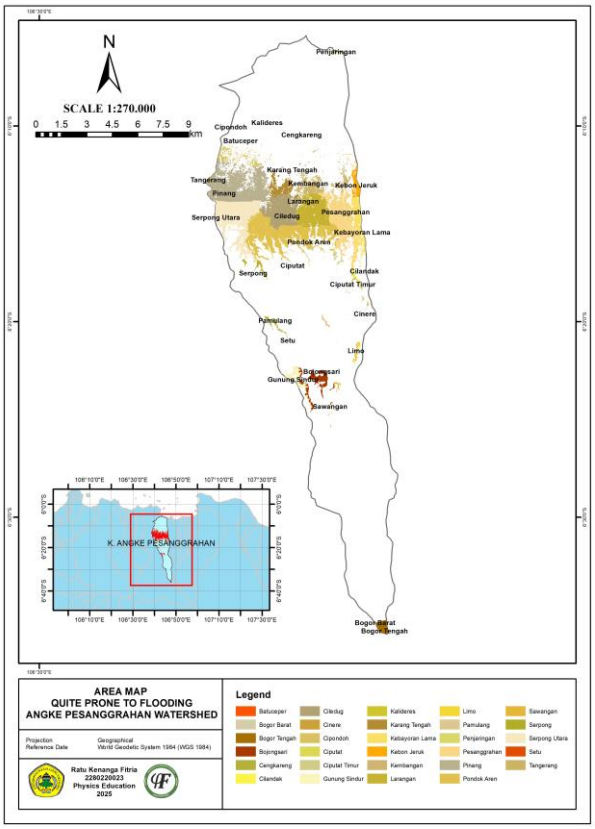

Figure 15. Map of quite prone areas.

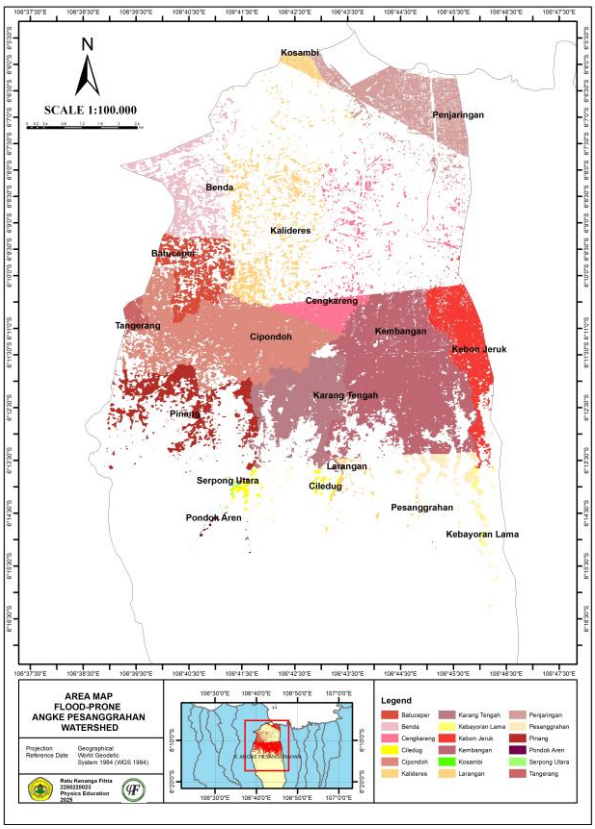

Figure 16. Map of flood-prone areas.

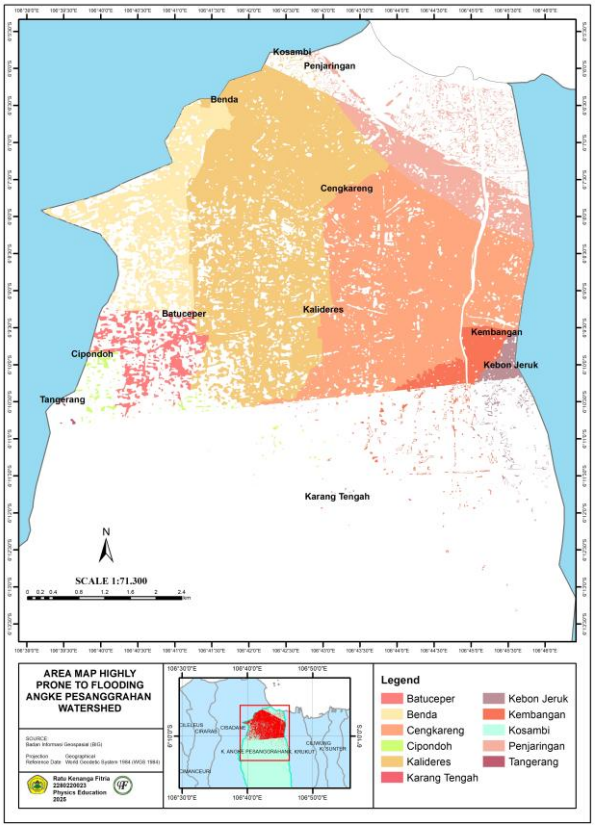

Figure 17. Map of highly prone areas.

Conclusion

Based on a series of systematic analyses using the Thiessen Polygon method, Log Pearson Type III distribution, and Nakayasu HSS, the capacity of the Cengkareng River downstream of the Angke-Pesanggrahan watershed is deemed inadequate due to its critical condition. The simulation results show that the design flood discharge (Q_{50}) reaches 1127.97 m^3/s, a figure that significantly exceeds the river's numerical storage capacity, which ranges from only 565 to 599.78 m^3/s. The inadequacy of this cross-section is validated by the HEC-RAS model with a water level elevation of 4.15 m and a flood width of 566.99 m, which spatially confirms the "Very Vulnerable" zone in the Kembangan Utara, Kedaung Kali Angke, Kapuk Muara, Kamal Muara, Cengkareng Timur, Kedoya Utara areas as mapped in ArcGIS and supported by historical flood data records.

As a mitigation measure, it is necessary to integrate short-term structural solutions in the form of normalization and elevation of embankments at critical points with a "Not Safe" status to prevent overtopping, as well as riverbank management through the relocation of residents in the "Very Vulnerable" zone. Non-structurally, long-term sustainability must be pursued through the restoration of soil infiltration functions by planting vegetation and constructing infiltration wells to reduce surface runoff. Given that this study is limited to numerical simulations, future studies are recommended to integrate inflow variables from tributaries and the impact of sedimentation, which has the potential to reduce the effective capacity of rivers more drastically.

Acknowledgements

We would like to thank the Ciliwung-Cisadane River Basin Agency (BBWS) and the Geospatial Information Agency (BIG) for providing secondary data in the research process, enabling this paper to become useful information for the community. We would also like to thank the lecturers who have provided a lot of input.

Author Contribution

Ratu Kenanga Fitria contributed to conceptualization, data curation, formal analysis, investigation, project administration, software development, visualization, writing-original draft preparration, and writing-review & editing. Yayat Ruhiat was responsible for methodology, resources, supervision, and validation. Yuvita Oktarisa contributed to supervision and validation.

Conflict of Interest

The authors declare no conflict of interest.

References

Abdolazimi, O., Sepehrifar, M., Shishebori, D., Banicescu, I., Azad, S., Pishini, K., & Ma, J. (2025). A stochastic DEA-GARMA integration for dynamic forecasting of undesirable outputs applied to the temporal efficiency analysis of water and sewerage services. *Journal of Cleaner Production*, 521(146177). https://doi.org/10.1016/j.jclepro.2025.146177

Alif, M. S. A., Marma, M-E-S., Hassan, M. N., Jahan, C. S., Howlader, R., Sarker, T., Rasel, M. I. A., Mahim, M. M. A., Roy, R., & Mazumdar, Q. H. (2025). Flash flood risk zoning in Gomti River Basin in Eastern Bangladesh and Tripura State (India) using MCDM-GIS Tool. *Safety in Extreme Environments*, 7,7. https://doi.org/10.1007/s42797-025-00120-7

Allafta, H., & Opp, C. (2021). GIS-based multi-criteria analysis for flood prone areas mapping in the trans-boundary

Shatt Al-Arab basin, Iraq-Iran. *Geomatics, Natural Hazards and Risk*, 12(1), 2087–2116. https://doi.org/10.1080/19475705.2021.1955755

Bahago, R. A., Abdulkadir, A., Yahaya, T. I., & Hassan, A. B. (2026). Geospatial Assessment of Flood Vulnerability and Its Impact on Food Security in Downstream Communities of Shiroro and Zungeru Dams, Niger. *Research Square* [Preprint], 0–23.

BPBD. (2021). *Data Titik Genangan dan Banjir Provinsi DKI Jakarta Tahun 2020-2021*. BPBD DKI Jakarta.

Carr, G., Seebauer, S., & Lun, D. (2025). Interactions Between Public and Private Flood Adaptation: Insights from a Socio – Hydrological Model. *Water Resources Research*, 61, e2025WR040502. https://doi.org/10.1029/2025WR040502

Dahlia, S., & Fadiarman. (2020). Analisis risiko banjir terhadap fasilitas pendidikan di DKI Jakarta. *Jurnal Geografi Gea*, 20(2), 185–196. https://doi.org/10.17509/gea.v20i2.24113

Endendijk, T., Botzen, W. J. W., de Moel, H., Aerts, J. C. J. H., Slager, K., & Kok, M. (2023). Flood vulnerability models and household flood damage mitigation measures: An econometric analysis of survey data. *Water Resources Research*, 59, e2022WR034192. https://doi.org/10.1029/2022WR034192

Fox, S., Agyemang, F., Hawker, L., & Neal, J. (2024). Integrating social vulnerability into high- resolution global flood risk mapping. *Nature Communications*, 15, 3155. https://doi.org/10.1038/s41467-024-47394-2

Glas, R., Hecht, J., Simonson, A., Gazoorian, C., & Schubert, C. (2023). Adjusting design floods for urbanization across groundwater-dominated watersheds of Long Island, NY. *Journal of Hydrology*, 618, 129194. https://doi.org/10.1016/j.jhydrol.2023.129194

Guo, J., Meng, Q., Du, B., & Sun, H. (2025). Probability forecasting for multivariate urban water demand using temporal convolutional network based on quantile regression and Parzen window. *Engineering Applications of Artificial Intelligence*, 162, 112528. https://doi.org/10.1016/j.engappai.2025.112528

Habibi, N. I., & Darmawan, Y. (2024). Pengendalian Banjir Pada Daerah Aliran Sungai Pesanggrahan Menggunakan Pemodelan HEC-RAS. *Jagratara: Journal of Disaster Research*, 2(2), 27–36. https://doi.org/10.36080/jjdr.v2i1.146

Handore, K. R., Patil, N., & Dangle, M. (2025). Comparative Analysis of Disaster Management Strategies in India and Indonesia. *Indonesian Journal of Geography*, 57(3), 480–494. https://doi.org/10.22146/ijg.101454

Ignes, J., & Arbaningrum, R. (2021). Analisis Debit Maksimum pada Long Storage Sungai Serua di Lingkungan Universitas Pembangunan Jaya. *Jurnal Proyek Teknik Sipil*, 4(2), 43–48. https://doi.org/10.14710/potensi.2021.11540

Ismael, Y. M., & Awchi, T. A. (2023). Meteorological Drought Analysis in Iraq using SPI and Theory of Runs for the Period 1980-2022. *IOP Conference Series: Earth and Environmental Science*, 1374, 012063. https://doi.org/10.1088/1755-1315/1374/1/012063

Kwak, J., Kim, J., Lee, H., Kim, S., Kim, S., & Seong, M. (2024). Evaluation of future flood probability in agricultural reservoir watersheds using an integrated flood simulation system. *Journal of Hydrology*, 628, 130463.

https://doi.org/10.1016/j.jhydrol.2023.130463

Limeria, A. & Saputra, R. H. (2024). Penentuan Debit Banjir Dengan HEC-HMS dan Kawasan Rawan Banjir Dipengaruhi Pasang Surut Dengan HEC-RAS 2D. *Jurnal Teknika: Jurnal Teoritis dan Terapan Bidang Keteknikan*, 7(2), 14–20. https://e-journal.upr.ac.id/index.php/JT/article/view/14077

Mester, B., Fieler, K., Korup, O., Desai, B., & Schewe, J. (2025). Socioeconomic predictors of vulnerability to flood-induced displacement. *Nature Communications*, 16, 8296. https://doi.org/10.1038/s41467-025-64015-8

Mitu, M. F., Sofia, G., & Anagnostou, E. N. (2025). Using Flood Insurance Claims in Coastal CONUS to Evaluate the Impact of Compound Flood Risk. *Water Resources Research*, 61, e2024WR039384. https://doi.org/10.1029/2024WR039384

Monir, M., Sarker, S. C., & Akhter, S. (2026). Participatory flood vulnerability assessment in the Teesta floodplain of Bangladesh using GIS-based AHP and frequency ratio models. *Next Sustainability*, 7, 100251. https://doi.org/10.1016/j.nxsust.2026.100251

Muhammad, I. N., Sarpono, S., Wibowo, A., Rachmat, S., & Kurniadi, A. (2025). Spatial Analysis of Urban Flood Vulnerability Using Weighted Overlay Technique for Identification of Hazard Zones in Greater Jakarta. *Jurnal Geografi*, 23(1), 223–238. https://doi.org/10.26740/jggp.v23n1.p223-238

Novarini, N., Harahap, A. K., Syastra, M. T., Yulia, I., Sutrisno, S., & Wijayanti, E. K. (2024). Sistem Informasi Geografis Bencana Alam Banjir Jakarta Berbasis Web dengan Metode SDLC. *Jurnal Informatika Teknologi dan Sains (Jinteks)*, 4(4), 489–495. https://doi.org/10.51401/jinteks.v4i4.4752

Noviansah, W. (2025). *Banjir 3,5 Meter Rendam Pesanggrahan Jaksel, 400 Warga Dievakuasi*. DetikNews. https://news.detik.com/berita/d-7806531/banjir-3-5-meter-rendam-pesanggrahan-jaksel-400-warga-dievakuasi

PSDA WS Ciliwung-Cisadane. (2019). *Data Curah Hujan (mm).*

PSDA WS Ciliwung-Cisadane. (2023). *Data Curah Hujan (mm).*

Rahmadani, S., Harahap, R., & Pongtuluran, E. H. (2023). Evaluasi Pola Distribusi Stasiun Hujan Kota Medan. *Jurnal Teknik Hidraulik Atau Jurnal Konstruksia*, 9(1), 10–19. https://jurnal.poltekba.ac.id/index.php/jst/article/view/1737

Rahmadani, S., Harahap, R., Yuzni, S. Z., Rani, C. M., Tinov, N., Waruwu, J. A., & Rahmadani, S. S. (2024). Hydrological Study of Deli River Flood Discharge Using the HSS Nakayasu Model. *Journal of Physics: Conference Series*, 2908, 012016. https://doi.org/10.1088/1742-6596/2908/1/012016

Rhianazala, A., Budiyanto, M. N., & Iriani, A. (2026). Analyzing the Challenges of Flood Management Policies in Bekasi City through Target Mapping Techniques. *Jurnal Pemerintahan Dan Politik*, 11(1), 108–133. https://ejournal.uigm.ac.id/index.php/PDP/article/view/5951

Saad, M. S. H., Ali, M. I., Razi, P. Z., Ramli, N. I., & Jaya, R. P. (2024). Exploring the Factors and Impacts of Flash Floods Vulnerability in Various Areas of Malaysia: A Content Analysis. *Disaster in Civil Engineering and Architecture*, 1(1), 55–82. https://doi.org/10.70028/dcea.v1i1.11

Safaei-Moghadam, A., Hosseinzadeh, A., & Minsker, B. (2024). Predicting real-time roadway pluvial flood risk: A hybrid machine learning approach

coupling a graph-based flood spreading model, historical vulnerabilities, and Waze data. *Journal of Hydrology*, 637, 131406. https://doi.org/10.1016/j.jhydrol.2024.131406

Saraswati, Y., Arifin, A., & Irsan, R. (2023). Pemetaan Sebaran Tempat Penampungan Sampah Sementara (TPS) di Kecamatan Sintang menggunakan Sistem Informasi Geografis (SIG). *Jurnal Ilmu Lingkungan*, 21(2), 238–244. https://ejournal.undip.ac.id/index.php/ilmulingkungan/article/view/45522

Setiyawan, S., Vera, W. A., Irdhiani, I., Rehana, R., Sri, H., & Hasbi, A. (2022). Testing of The Method of Gama I Synthetic Unit Hydrograph in The Analysis of The Tojo Watershed Design Flood. *IOP Conference Series: Earth and Environmental Science*, 1075, 012050. https://doi.org/10.1088/1755-1315/1075/1/012050

Sinurat, M., Mulia, A. P., & Faisal, M. (2022). Analisis spasial daerah banjir menggunakan HEC-RAS dan QGIS untuk Sub DAS Babura. *Jurnal Syntax Admiration*, 3(1), 141–162. https://doi.org/10.46799/jsa.v3i1.382

Soma, A., Arsyad, U., Nursaputra, M, Lando, A. T., Rahmat, S., Azus, F. H., & Ramadhan, M. D. R. (2021). Flood vulnerability analysis using the frequency ratio method with the watershed ecosystem in Bulukumba Regency, South Sulawesi Indonesia. *IOP Conference Series: Earth and Environmental Science*, 1230, 012044. https://doi.org/10.1088/1755-1315/1230/1/012044

Syukur, R. E. R. (2025). *Ruas jalan di Kembangan banjir akibat Kali Pesanggrahan meluap*. Antara News. https://www.antaranews.com/berita/4686793/ruas-jalan-di-kembangan-banjir-akibat-kali-pesanggrahan-meluap

Taki, H. M., & Wartaman, A. S. (2022). Study of Flood Vulnerability in Pesanggrahan District, South Jakarta. *Journal of Applied Geospatial Information*, 6(2), 647–651. https://doi.org/10.30871/jagi.v6i2.4308

Wigati, R., & Wahyudin, W. (2013). Analisis Banjir Sungai Ciliwung (Studi Kasus Ruas Sungai Lenteng Agung-Manggarai). *Fondasi : Jurnal Teknik Sipil*, 2(1), 1–9. https://doi.org/10.36055/jft.v2i1.1985

Yu, J., Wang, G., Yinglan, A., Zhu, Y., Cheng, Y., Deng, Z., Gao, R., & Duan, L. (2025). Hydrological phase-driven management in semi-arid watersheds: Linking plankton assembly dynamics and adaptive resilience strategies. *Water Research X*, 29, 100421. https://doi.org/10.1016/j.wroa.2025.100421

ISSN: 2579-5821 (Print)
ISSN: 2579-5546 (Online)
URL address: http://journal.unhas.ac.id/index.php/geocelebes
DOI: 10.70561/geocelebes.v10i1.43141

Jurnal Geocelebes Vol. 10 No. 1, April 2026, 34 – 47

Analysis of Extreme Weather in the Waters of West Kalimantan using the WRF-ARW Model (Case Study 13-14 July 2021)

Tarisya Juliana[1], Riza Adriat[1]*, Randy Ardianto[2], Andi Ihwan[1], Yuris Sutanto[3]

[1]Geophysics Study Program, Tanjungpura University, Pontianak 78124, Indonesia.
[2]Maritime Class IV Meteorology Station, Pontianak 78112, Indonesia
[3]Physics Study Program, Tanjungpura University, Pontianak 78124, Indonesia.

*Corresponding author. Email: rizaadriat@physics.untan.ac.id

Manuscript received: 6 February 2025; Received in revised form: 11 July 2025; Accepted: 7 March 2026

Abstract

On 13 July 2021, there was an extreme weather phenomenon in the waters of West Kalimantan. The extreme weather resulted in several fishing boats sinking and causing 136 casualties. This study aims to analyze atmospheric conditions during extreme weather on July 13-14, 2021. In running the WRF-ARW model, verification is carried out using the dichotomy method (Accuracy, POD, FAR) and RMSE to determine the model's accuracy in simulating extreme weather events. The RMSE verification results show an error value of 4,97. The results of the WRF-ARW model output show that the extreme weather that occurs is caused by the presence of a convergence wind zone with a maximum wind speed of 18 m/s, causing the formation of cumulonimbus clouds. OLR simulations show a low value of 122 watts/m², indicating a lot of cloud cover with the potential for rain. The emergence of this convection zone causes strong winds, which cause high waves, thus contributing to ship accidents.

Keywords: Extreme Weather; West Kalimantan; WRF.

Citation: Juliana, T., Adriat, R., Ardianto, R., Ihwan, A., & Sutanto, Y. (2026). Analysis of Extreme Weather in the Waters of West Kalimantan using the WRF-ARW Model (Case Study 13-14 July 2021). *Jurnal Geocelebes*, 10(1): 34–47, doi: 10.70561/geocelebes.v10i1.43141

Introduction

West Kalimantan's coastal and marine areas play an essential role in economic activities, transportation, and the lives of local communities. However, this region's unique geography and meteorology make it prone to a range of extreme weather events (Taufik et al., 2019). Weather is the state of the air at a particular time and in a particular area that is relatively narrow and in a short period (Puspita & Yulianti, 2016). Extreme weather is an event of natural phenomena characterized by conditions of rainfall, wind direction and speed, air temperature, air humidity, and visibility that can cause losses, especially the safety of life and property (BMKG, 2022). Many factors can influence extreme weather, one of which is climate change, which is a factor in increasing the frequency of extreme weather events such as strong winds and high waves (Nurlatifah et al., 2023). Another impact of extreme weather is the increase in wave height throughout the Indonesian Sea (Rizal et al., 2020). Changes in rainfall patterns and increases in sea surface temperature have the potential to produce large ocean waves that hurt fishermen (Afifah et al., 2024). In addition, extreme weather also impacts the smooth running of land, sea, and air transportation.

In analyzing extreme weather events, many methods can be used, one of which is numerical weather modeling. Numerical weather modeling systems are currently widely used by the world's meteorologists. One of the weather modeling systems developing in the world today is Weather Research Forecasting (WRF). WRF-ARW is a numerical weather model program that

can model atmospheric conditions in a region to help study a meteorological event better (Wisnawa et al., 2019). Research using WRF-ARW modeling was conducted by Putra & Rifani (2016), which analyzed the extreme rain that occurred on 19 August 2014. The results showed that the WRF-ARW model output had good results in showing atmospheric conditions during extreme rainfall.

In 2021, extreme weather has caused the loss of ships in the waters of West Kalimantan. As revealed by Tribunnews.com, there was bad weather that resulted in 14 boats reportedly sinking in three different locations, namely in Muara Jungkat, Muara Kubu, and Muara Pemangkat, which claimed 136 lives. Based on the analysis issued by BMKG, there have been extreme weather in the form of heavy to extreme category rain, reaching >100 mm/day on July 13, 2021, in most areas of West Kalimantan.

Based on the impact caused by extreme weather in the waters of West Kalimantan, this is the basis of the research conducted. Analyzing atmospheric conditions using the WRF-ARW model is expected to get representative results that can describe atmospheric conditions when extreme weather occurs. This research is also expected to provide preliminary information to mitigate extreme weather.

Materials and Methods

The location of this research is the waters of West Kalimantan. This research was conducted for 2 days starting from July 13-14, 2021 which is located at coordinates 5°N to 6°S and 104°BT to 112°BT. The study areas used as samples to analyze wind speed, rainfall, and Outgoing Longwave Radiation (OLR) are the Pemangkat, Jungkat, and Kubu areas because these three areas were reported as the areas where the loss of the ship occurred.

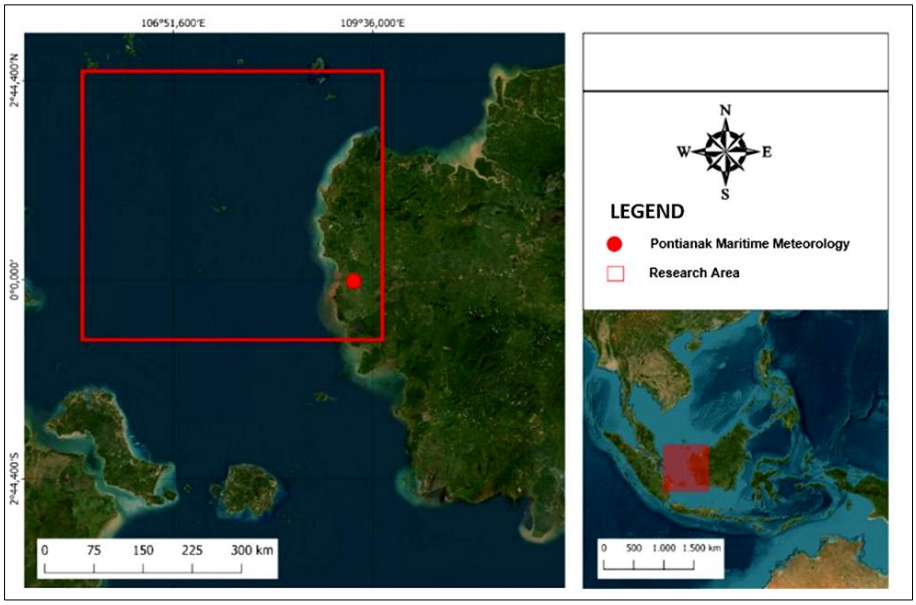

Figure 1. Study location.

Data Used

1. Data FNL (Final Global Data Assimilation System)

Initial condition data and model boundary data were used FNL (Final Global Data Assimilation System) data from 12 July 2021 at 18.00 UTC to 14 July 2021 at 18.00 UTC with a data resolution of 0.25° x 0.25° or 27.75 km x 27.75 km with a temporal resolution of 6 hours (Liu et al., 2022). The data was obtained by downloading via the link https://rda.ucar.edudatasets/ds083.3/dataaccess/.

2. Data GSMAP (Global Satellite Mapping Precipitation)
Observation data for rainfall parameters using GSMAP (Global Satellite Mapping Precipitation) data of Himawari 8 Satellite obtained from Pontianak Maritime Meteorological Station from 12 July 2021 at 18.00 UTC to 14 July 2021 at 18.00 UTC with data resolution of 0.1° x 0.1° or 11 km x 11 km (Pratama et al., 2022).

3. Wind Speed Data of Pontianak Maritime Meteorological Station
Observation data for wind speed parameters were obtained from Pontianak Maritime Meteorological Station with coordinates 0.02022° N and 109.33778° E on July 12, 2021, at 18:00 UTC to July 14, 2021, at 18:00 UTC.

Work Procedure

1. Preparation/ identification of extreme weather events
The first step is to collect information such as the date and time of the incident related to the loss of ships due to extreme weather. Next, identify suitable initial data as an identifier of extreme weather that causes the loss of vessels in West Kalimantan waters.

2. Data Collection
After identifying the event, the next step is to collect data at that time and location for analysis, model input and comparison.

3. Running Model WRF
There are several stages in the WRF model running process. The WRF model (version 4.5.1). The first stage is to carry out the downscaling and nesting process to get two domains. Downscaling is a technique to increase model resolution by downscaling the grid scale of a global model to a regional scale in the domain of interest (Maraun and Widmann, 2018). After that, the WRF Pre-Processing system (WPS) consists of three stages: running the geogrid, ungrib, and metgrid processes. At this stage, input files will be obtained, running the ./real.exe and ./wrf.exe commands to get WRF output. The results of WRF are then processed into ARWpost post-processing to produce files in .ctl and .dat formats, which are then visualized.

4. Display The Output of the WRF-ARW Model
The results of running the WRF-ARW model are then visualized. The model output results are displayed with various parameters, so a two-dimensional profile related to extreme weather parameters in the study area is obtained.

5. Conducting Accuracy Tests on the WRF-ARW Model
After obtaining the output results of the next model, a comparison with observational data is carried out. For rainfall parameters, a comparison of rainfall distribution maps between WRF-ARW model output and GSMAP data is carried out to see the accuracy of the WRF-ARW model spatially. Verification of model output also uses the dichotomy method with the contingency table in Table 1. The contingency table method is used to determine the quality of dichotomous forecast data (the result is a yes/no decision) (Sulistiyono & Fadli, 2023).

Table 1. Contingency table 2x2 (Sulistiyono & Fadli, 2023)

Frequency		**Satellite Observation (GSMAP)**		**Total Estimation Data**
		Yes	**No**	
WRF Model Output Rainfall Data	**Yes**	a (*Hits*)	c (*False Alarms*)	a + b
	No	b (*Misses*)	d (*Correct Negatives*)	c + d
	Total Observation	a + b	c + d	n = a + b + c + d

The test results of the contingency table method produce values for Probability of Detection (POD), False Alarm Ratio (FAR), and accuracy (fraction correct). POD measures the number of "YES" events correctly predicted by the satellite data, FAR calculates the forecast error of rainfall products that do not match the observed data, and accuracy indicates the proportion of correct forecasts, with values between 0 and 1, where perfect accuracy is achieved when the value is 0. The equations used to calculate these verification parameters are used in Equations 1, 2, and 3 (Mahubessy & Purnama, 2022).

$$Accuracy = \frac{Hits+Correct\ Negatives}{Total} \quad (1)$$

$$POD = \frac{Hits}{Hits+Misses} \quad (2)$$

$$FAR = \frac{False\ Alarms}{Hits+False\ Alarms} \quad (3)$$

Wind speed parameters are verified using RMSE (Root Mean Square Error). RMSE has a range of values from 0 to infinity, which depends on the error values obtained from the parameters being compared. An element of the WRF-ARW scheme results can be considered good if it has a small error value against the observed weather elements, then the RMSE value will be close to 0. The following is an equation for determining the RMSE value (Wisnawa et al., 2019).

$$RMSE = \sqrt{\frac{\Sigma(yi-\acute{y})^2}{n}} \quad (4)$$

With information, ý is the value of observation data and, *yi* is the value of model data, *n* is the amount of data.

6. Data Analysis

At this stage all the parameters that have been determined are then analyzed to obtain hypotheses that are by atmospheric conditions during extreme weather.

Results and Discussion

Validation Analysis of WRF Model and Observation Data

Rainfall verification results from the WRF-ARW model in Table 3 show three dichotomous parameters for the three ship loss regions.

Tabel 3. Rainfall verification results from the WRF-ARW model.

Statistics	Observation Area		
	Pemangkat	Jungkat	Kubu
Accuracy	0,6	0,6	0,7
POD	0,05	0,42	0,33
FAR	0,50	0,47	0,33

From Table 3, the results of the verification of WRF model data and observation data, a good accuracy value is owned by the Kubu area because the value is close to 1. The Jungkat area owns a good POD value because the value is pretty close to 1. The Kubu area owns a good FAR value because the value is close to 0. Wind speed verification has an RMSE value with an error of 4.97.

Spatial Analysis of WRF-ARW Model Rainfall

Figure 2 shows the WRF model output for 6 hours before the extreme weather occurred. During this period, it shows stable rainfall with a rainfall intensity of 3 mm/hour. Rainfall is the amount of rainwater that falls during a certain period which is measured using units of height above horizontal ground level (Ruswanti, 2020). One millimeter of rainfall means that one square meter of flat area contains one millimeter of water or one liter of water (Ajr, 2019). There was an increase in rainfall intensity at 13:00 WIB near Bangka Belitung Island, and it began to decline around 16:00 WIB. Meteorological conditions such as evaporation, humidity, wind speed, air temperature, and solar radiation intensity can affect rainfall in an area (Ramadhan, 2018; Wang & Zheng, 2022).

Figure 3 is the output of the WRF-ARW model of rainfall distribution patterns during extreme weather that is expected to occur from the 13th night until the 14th

morning. The visualization results are displayed for 10 hours, from 19:00 WIB until 04:00 WIB. At 23:00 WIB, high rainfall began to be seen in the sea near the coast of West Kalimantan with a maximum intensity reaching 27 mm/hour, then at 24:00 WIB, rainfall with high intensity began to be seen spreading in the sea near the coast of West Kalimantan. The rainfall pattern in the previous hour shows that the intensity increases within an hour, which is indicated by several areas having high rainfall. At 01.00 am, the rainfall intensity increases with a maximum intensity of 30 mm/hour with a broader range of areas. A similar pattern continues at 02:00 am, with the rainfall area moving further to the coast of West Kalimantan.

Figure 4 shows the visualization results of the WRF-ARW model output rainfall after the extreme weather event. The image is displayed in a period of 6 hours after the event. In general, the rainfall has an intensity of 3 mm/hour with a coverage area around the South China Sea and West Kalimantan Island. However, in the northern part of West Kalimantan Island, there is a high rainfall intensity with a maximum intensity of 30 mm/hour. Entering 06.00 WIB, the high rainfall intensity decreased with a maximum intensity of 21 mm/hour.

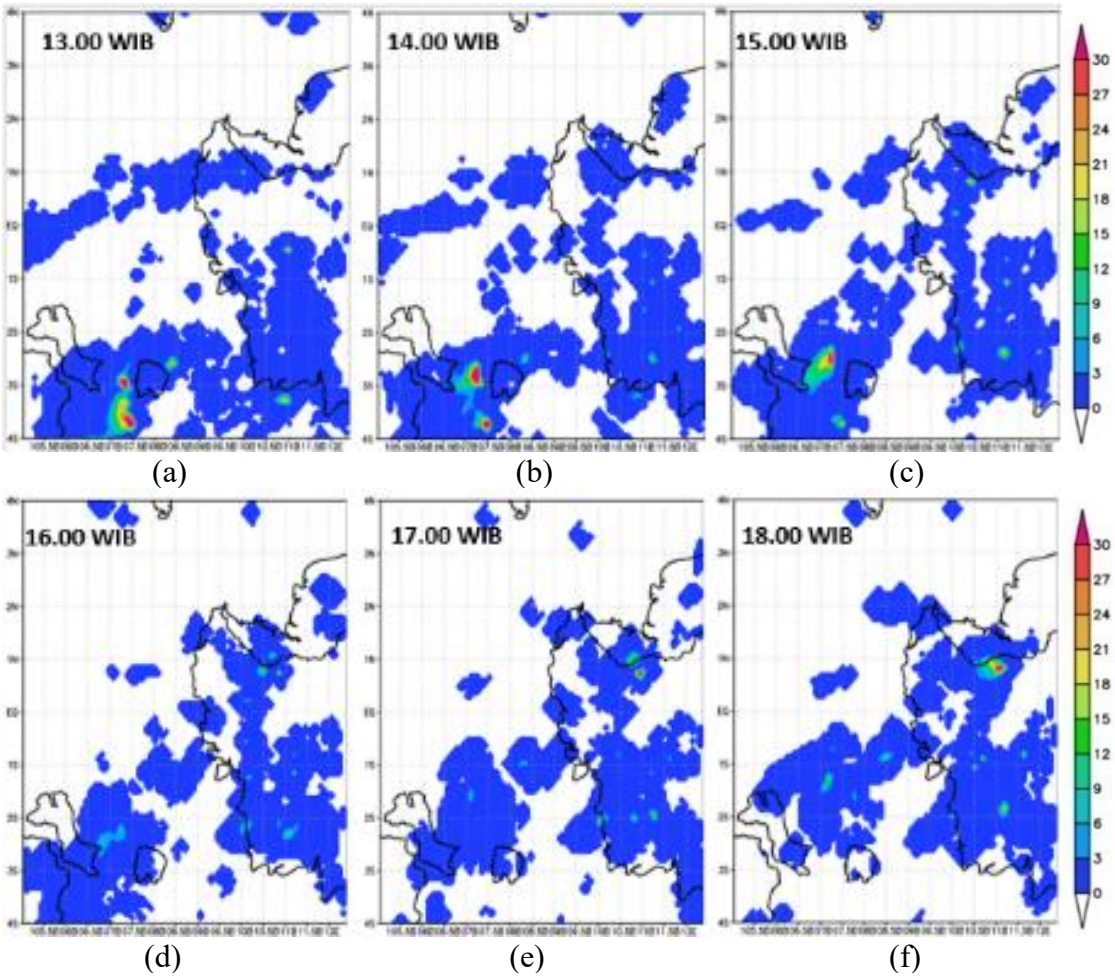

Figure 2. Rainfall distribution map before extreme weather in West Kalimantan waters on July 13, 2021 (a)13.00 WIB, (b) 14.00 WIB, (c) 15.00 WIB, (d) 16.00 WIB, (e) 17.00 WIB, (f) 18.00 WIB.

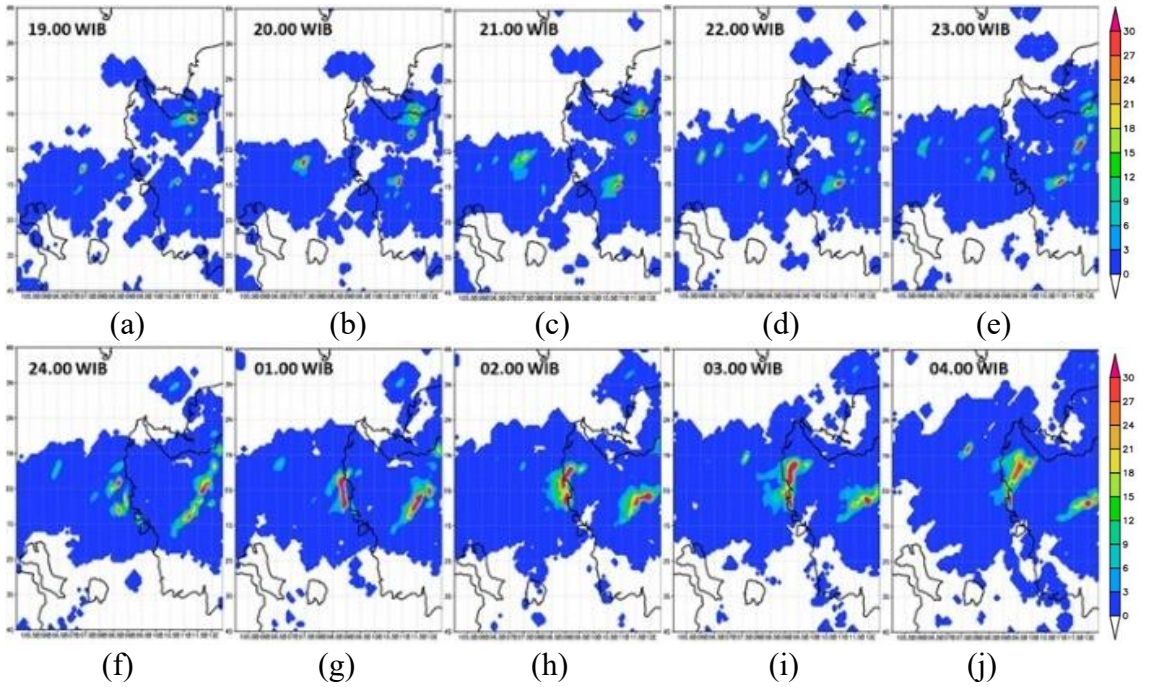

Figure 3. Rainfall distribution map during extreme weather in West Kalimantan waters on July 13-14, 2021 (a) 19.00 WIB, (b) 20.00 WIB, (c) 21.00 WIB, (d) 22.00 WIB, (e) 23.00 WIB, (f) 24.00 WIB, (g) 01.00 WIB, (h) 02.00 WIB, (i) 03.00 WIB, (j) 04.00 WIB.

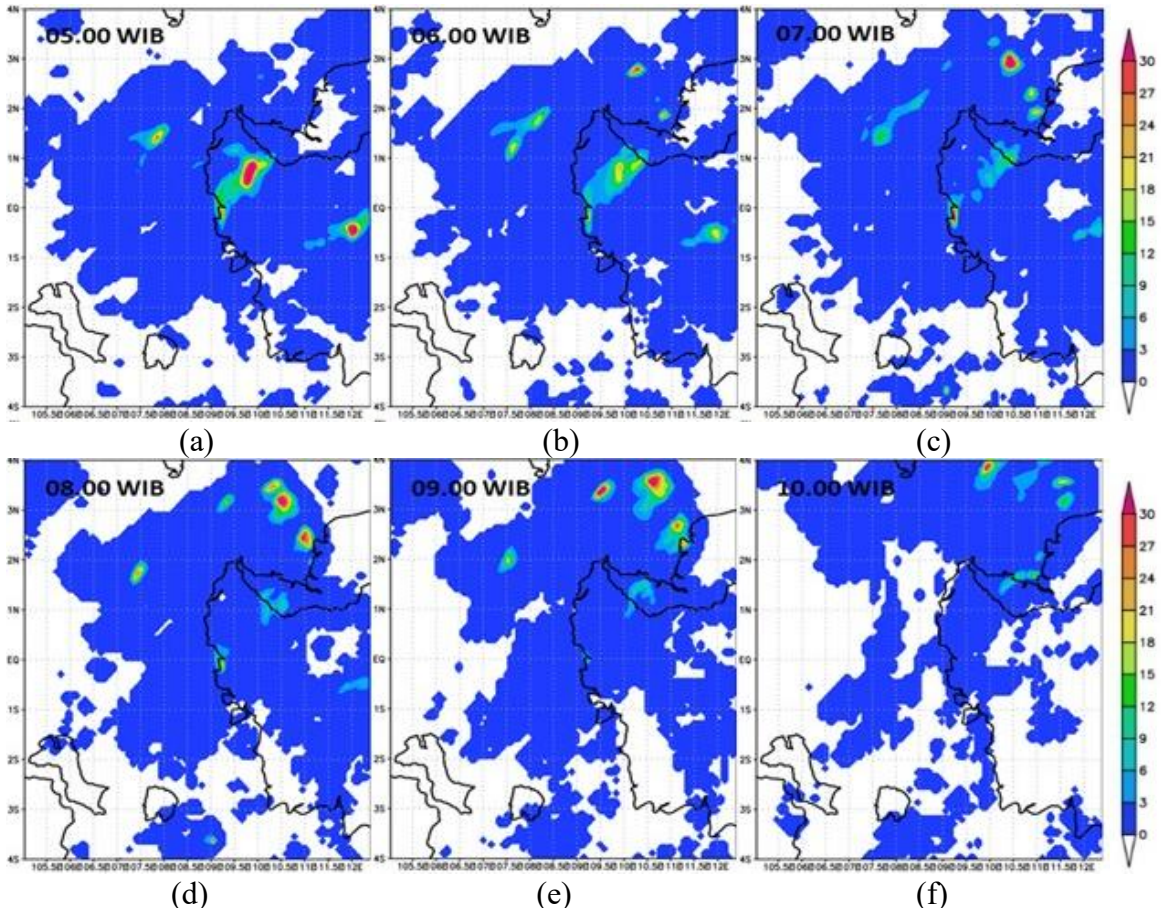

Figure 4. Rainfall distribution map after extreme weather in West Kalimantan waters on July 14, 2021 (a) 05.00 WIB, (b) 06.00 WIB, (c) 07.00 WIB, (d) 08.00 WIB, (e) 09.00 WIB, (f) 10.00 WIB.

Figure 5 displays the WRF-ARW model output for 6 hours before the extreme weather. Overall, the wind speed on the West Kalimantan coast and sea was 8 - 10 m/s. Wind speed is the speed of air moving horizontally which is influenced by the barometric gradient of the location, height, and topography of a place (Suwarti et al., 2017; Minola et al., 2024). The wind speed pattern continues to move northward from Bangka Belitung Island to Kalimantan Island. The wind movement comes from an area of high pressure to an area of low pressure (Miftahuddin, 2016; Siagian, 2022). At 18.00 WIB, the wind vector pattern shows the presence of wind convergence; the wind vector looks spread or away from one center point, which indicates convergence. Wind speed is influenced by various micro and macro factors, one of which is hurricanes, monsoons, and tornadoes can affect wind speed both regionally and locally (Abdy & Sanusi, 2020).

Figure 6 shows the wind speed and direction during extreme weather, which is expected to occur in the evening of July 13, 2021, until the early morning of 14 July 2021. The wind speed begins to increase every hour, as indicated by the pink vector in the figure as well as the wind direction shown by the wind vector; at 19.00 WIB, the wind direction pattern is already visible above Bangka Belitung Island with a maximum speed of 16 m / s, the wind vector looks increasingly spread or away from a central point indicating convergence. In this condition, the area has the potential for convective cloud growth due to the mass of air that gathers, which will allow severe weather conditions to occur (Wisnawa et al., 2019).

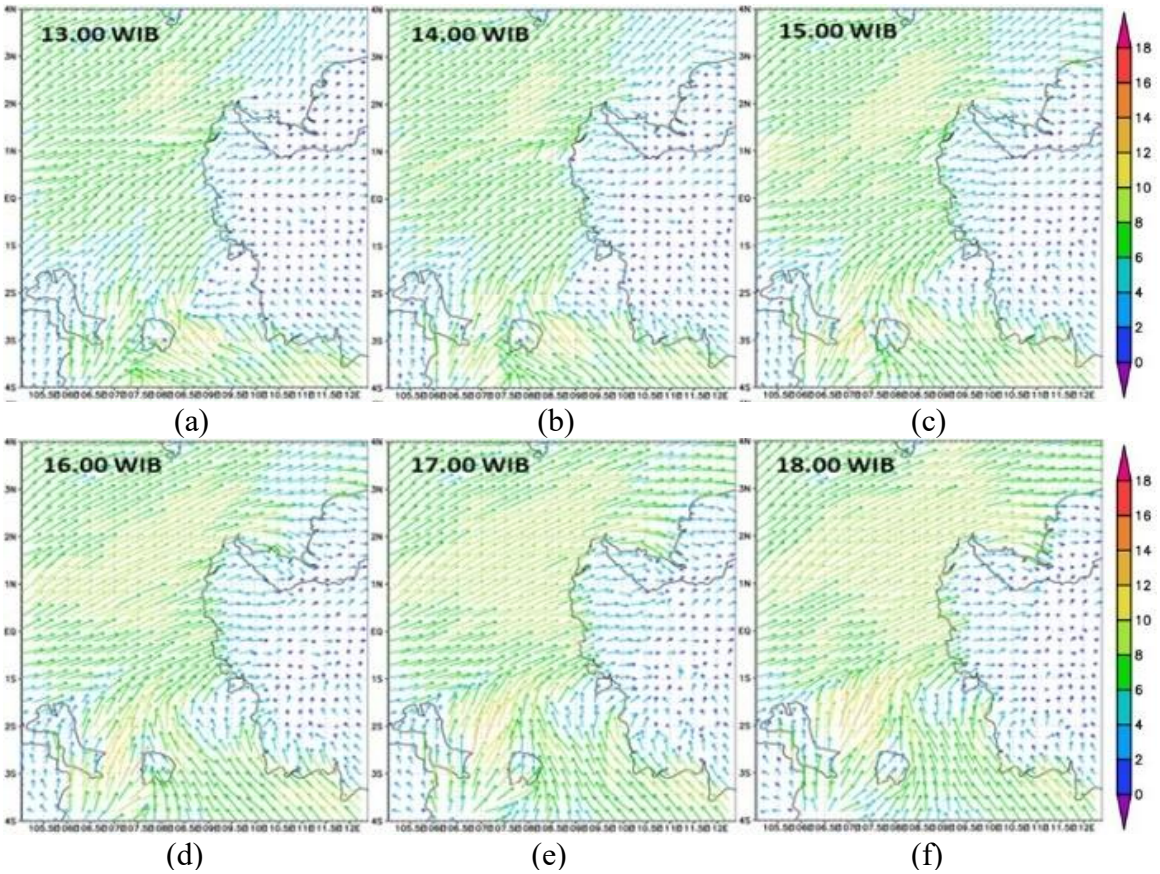

Figure 5. Spatial map of wind speed in West Kalimantan waters before extreme weather on July 13, 2021 (a) 13.00 WIB, (b) 14.00 WIB, (c) 15.00 WIB, (d) 16.00 WIB, (e) 17.00 WIB, (f) 18.00 WIB.

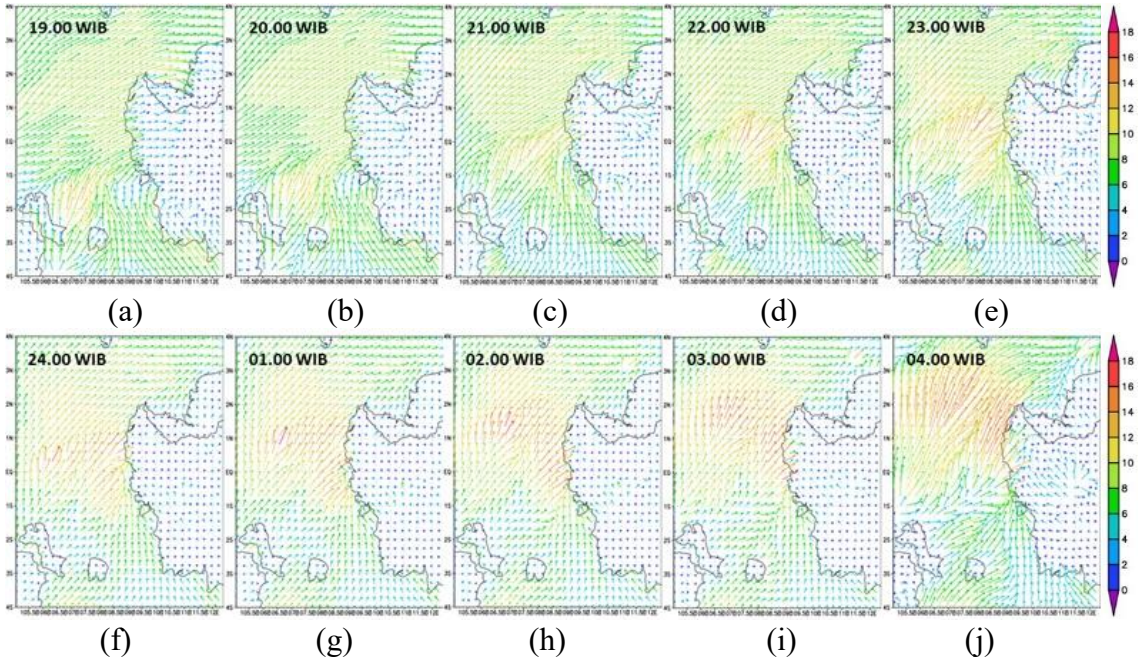

Figure 6. Spatial map of wind speed during extreme weather in West Kalimantan waters on July 13-14, 2021 (a) 19.00 WIB, (b) 20.00 WIB, (c) 21.00 WIB, (d) 22.00 WIB, (e) 23.00 WIB, (f) 24.00 WIB, (g) 01.00 WIB, (h) 02.00 WIB, (i) 03.00 WIB, (j) 04.00 WIB.

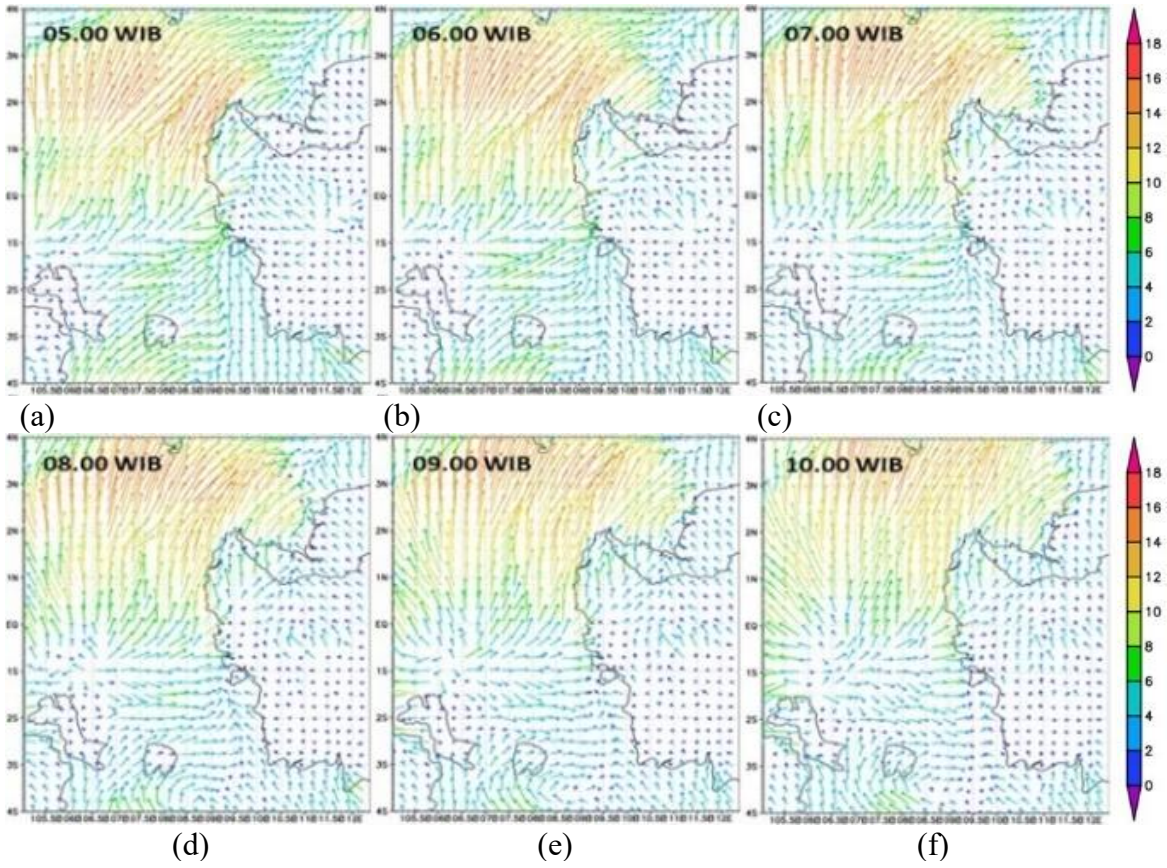

Figure 7. Spatial map of wind speed after extreme weather in West Kalimantan waters on July 14, 2021 (a) 05.00 WIB, (b) 06.00 WIB, (c) 07.00 WIB, (d) 08.00 WIB, (e) 09.00 WIB, (f) 10.00 WIB.

Figure 7 shows the wind speed for 6 hours after the extreme weather. Overall, the wind speed has decreased from 05.00 WIB to 10.00 WIB, with the direction of the wind

vector heading north or to the South China Sea. At 05.00 WIB, the wind speed on the coast of West Kalimantan, precisely in the North, has a wind speed that is still relatively high, reaching 16 - 18 m / s. The wind speed is still quite high for the coast of West Kalimantan in the lower part. The coast of West Kalimantan at the bottom of the wind speed is relatively stable, namely 4 – 8 m/s.

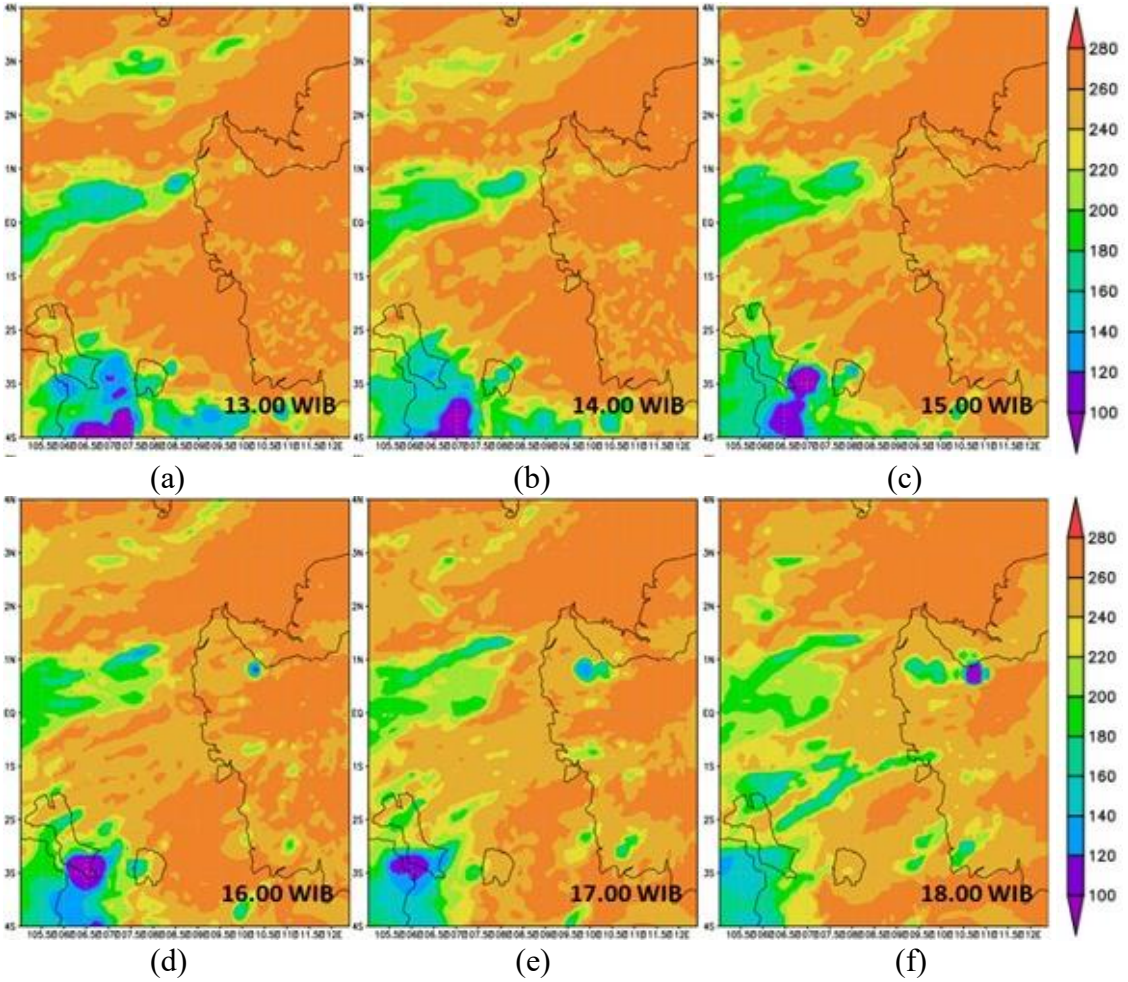

Figure 8. Spatial map of OLR in West Kalimantan waters before extreme weather on July 13, 2021 (a) 13.00 WIB, (b) 14.00 WIB, (c) 15.00 WIB, (d) 16.00 WIB, (e) 17.00 WIB, (f) 18.00 WIB.

Outgoing Longwave Radiation (OLR) is the longwave return radiation at the top of the atmosphere observed by polar-orbiting satellites in watts/meter^2 (Loeb et al., 2018). Figure 8 shows the OLR for 6 hours before the extreme weather. Overall, the OLR value on the coast of West Kalimantan Island is pretty high, at 250 – 270 Watt/m^2. However, on the North side of West Kalimantan, precisely around the Singkawang area, the OLR value looks relatively low at 13.00 WIB, around 230 - 130 Watt / m^2. From 14.00 WIB until 15.00 WIB, OLR began to move westward in West Kalimantan, as indicated by the decrease in OLR value. The low OLR value suggests that more cloud cover allows rain to occur. OLR shows the amount of cloud cover that exists; if OLR is low, then it can be indicated that many clouds are formed because the outgoing long waves are held back by the clouds and vice versa (Prayuda & Alfuadi, 2015; Schreck et al., 2018).

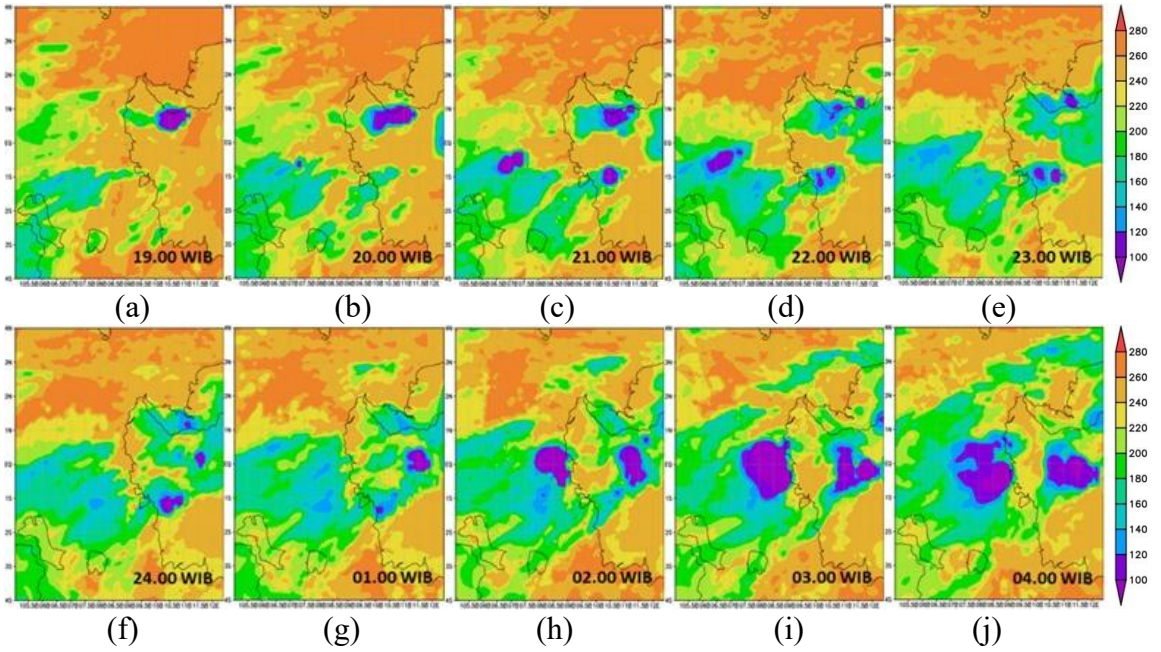

Figure 9. Spatial map of OLR during extreme weather in West Kalimantan waters on July 13-14, 2021 (a) 19.00 WIB, (b) 20.00 WIB, (c) 21.00 WIB, (d) 22.00 WIB, (e) 23.00 WIB, (f)24.00 WIB, (g) 01.00 WIB, (h) 02.00 WIB, (i) 03.00 WIB, (j) 04.00 WIB.

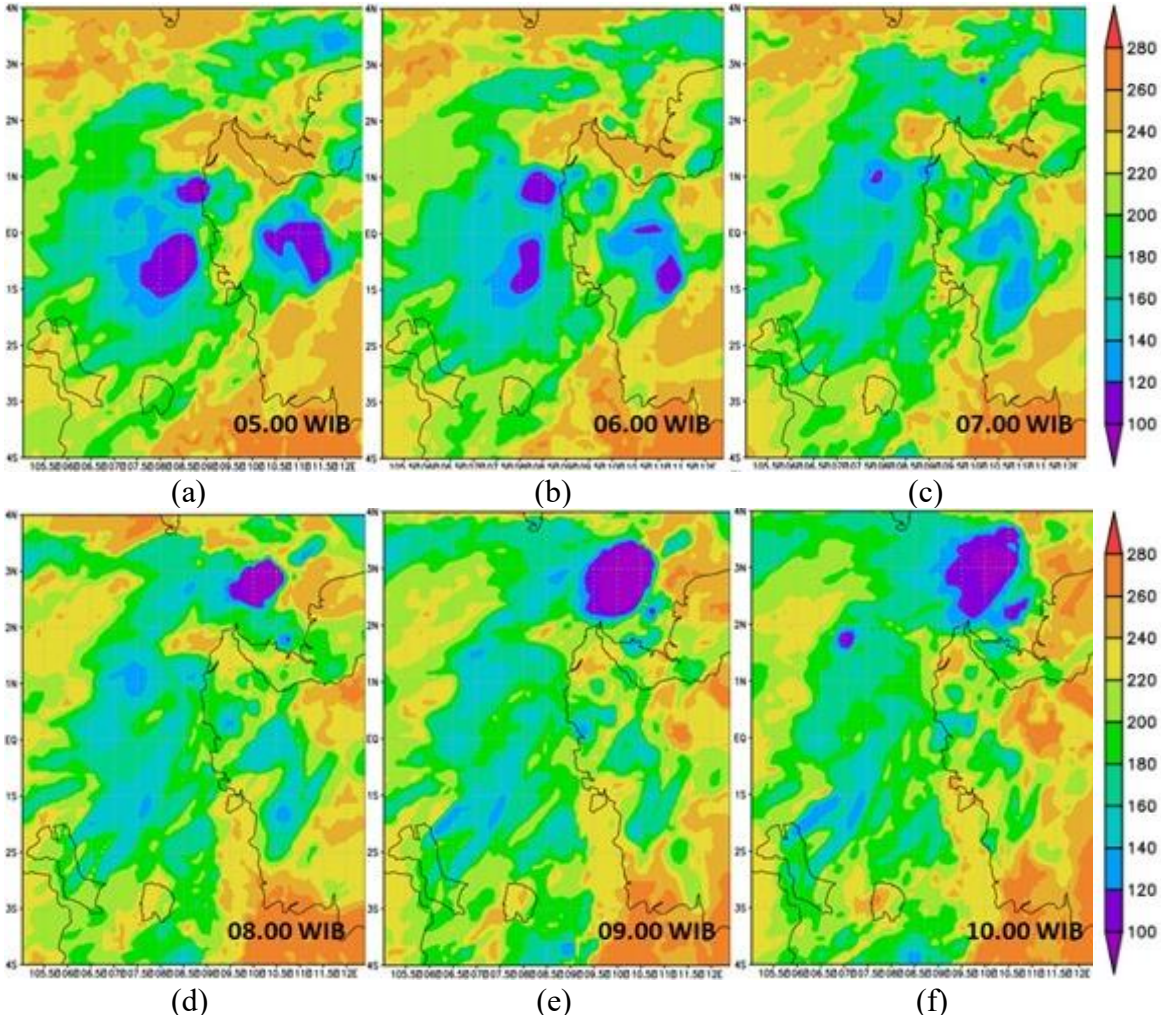

Figure 10. Spatial map of OLR after extreme weather in West Kalimantan waters on July 14, 2021 (a) 05.00 WIB, (b) 06.00 WIB, (c) 07.00 WIB, (d) 08.00 WIB, (e) 09.00 WIB, (f) 10.00 WIB.

Figure 9 shows OLR for 10 hours when extreme weather occurs. At 19:00 WIB, OLR with low values began to spread over the coast of West Kalimantan with an OLR value of around 180 Watt/m2; this continued until 20:00 WIB. At 21.00 WIB, the OLR value decreases until it reaches a value of 150 Watt / m2. It is found around the coast of West Kalimantan, but if seen in the picture, there is OLR with a minimum value of 100 Watt / m^2 on the island. This shows that there is a lot of cloud cover in the area, which makes it cooler. Low or minimum OLR values indicate cold temperatures, while high or maximum values indicate hot temperatures. (Handayani et al., 2016; Koll & Cronin, 2018). This low OLR value indicates a large cloud cover potentially containing convective clouds that can cause rain. The ORL value at the top of the Earth's atmosphere is a function of two things: the number of clouds and the temperature of the cloud surface, both of which are related to rainfall (Natasha et al., 2021). The study of the relationship between OLR and rainfall has been studied by Morrisey (1986), which states that if OLR is high, rainfall is low and vice versa (Prayuda & Alfuadi, 2015; Rasch et al., 2019). This aligns with the WRF-ARW model's output rainfall, which shows that the same time and region have high rainfall.

Figure 10 shows the OLR for 6 hours after the extreme weather. At 05.00, WIB, OLR is still at the minimum value of 100 Watt/m^2, which is located around Singkawang and in the sea near the Jungkat estuary. For coastal areas from 07.00 WIB to 10.00 WIB, it has OLR with a value of 190 - 230 Watt/m2, indicating that cloud cover in the coastal areas of West Kalimantan is not too large or small.

Conclusion

Based on the results of the research, it can be concluded that the rainfall output of the WRF-ARW model is underestimated against GSMAP data. Kubu region has the best accuracy value of 0.7, Kubu has a good prediction with a FAR value of 0.33, and Jungkat has the highest POD value of 0.42. The RMSE value shows a small error value for wind speed verification with a value of 4.97.

The WRF model output showed a low OLR value, indicating high rainfall at the time of the ship loss. High wind speeds with a maximum speed of 20 m/s and low OLR values of 100 watts/m^2 also indicate the influence of convective clouds that support high rainfall with a maximum intensity of 30 mm/hour. In a sense, meteorological conditions during extreme weather are characterized by cumulonimbus clouds formed due to wind convergence, which causes high rainfall at the study site.

Acknowledgments

The authors would like to express their sincere gratitude to the Maritime Meteorological Station Pontianak for providing the essential data used in this research. We also extend our appreciation to all parties who contributed to the completion of this study.

Author Contribution

Tarisya Juliana: conceptualized, data curation, formal analysis, visualization and writing original draft. Riza Adriat: supervision, validation, and writing review editing. Randy Ardianto: supervision, validation, and writing review editing. Andi Ihwan: supervision and visualization. Yuris Sutanto: supervision and visualization.

Conflict of Interest

The authors declare no conflict of interest.

References

Abdy, M., & Sanusi, W. (2020). Karakteristik Kategori Kecepatan Angin di Kota Majene dengan

Pendekatan Rantai Markov. *Saintifik*, 6(1), 85–90. https://doi.org/10.31605/saintifik.v6i1.305

Afifah, D., Chusni, A., Nahar, A. N., Sirojuddin, M. A., & Fatmawati, N. (2024). Persepsi Masyarakat Nelayan Dalam Menghadapi Perubahan Iklim Studi Desa Ujung Batu Kawasan Pesisir Utara Pulau Jawa (Ditinjau Aspek Sosial Ekonomi). *UTILITY: Jurnal Ilmiah Pendidikan dan Ekonomi*, *8*(1), 42–58. https://doi.org/10.30599/utility.v8i1.3107

Ajr, E. Q., & Dwirani, F. (2019). Menentukan Stasiun Hujan dan Curah Hujan dengan Metode Polygon Thiessen Daerah Kabupaten Lebak. *Jurnal Lingkungan Dan Sumberdaya Alam*, *2*(2), 139–146. https://ejournal.lppm-unbaja.ac.id/index.php/jls/article/view/674/387

Badan Meteorologi Klimatologi dan Geofisika (BMKG). (2022). *Penyediaan dan Penyebarluasan Peringatan Dini Cuaca Ekstrem*. 1–19.

Handayani, D., Asrul, A., & Nugroho, S. (2016). Analisis Angin Zonal dan Outgoing Longwave (OLR) Untuk Inisialisasi Kemunculan Fenomena Medden Julian Oscillation (MJO) di Kota Padang. *Pillar of Physics*, 8, 9–16.

Koll, D. D. B., & Cronin, T. W. (2018). Earth's outgoing longwave radiation linear due to H_2O greenhouse effect. *Proceedings of the National Academy of Sciences*, 115(41), 10293–10298. https://doi.org/10.1073/pnas.1809868115

Liu, J., Song, X., Long, W., Fu, Y., Yun, L., & Zhang, M. (2022). Structure Analysis of the Sea Breeze Based on Doppler Lidar and Its Impact on Pollutants. *Remote Sensing*, 14(2), 324. https://doi.org/10.3390/rs14020324

Loeb, N. G., Doelling, D. R., Wang, H., Su, W., Nguyen, C., Corbett, J. G., Liang, L., Mitrescu, C., Rose, F. G., & Kato, S. (2018). Clouds and the Earth's Radiant Energy System (CERES) Energy Balanced and Filled (EBAF) Top-of-Atmosphere (TOA) Edition-4.0 Data Product. *Journal of Climate*, 31(2), 895–918. https://doi.org/10.1175/JCLI-D-17-0208.1

Mahubessy, R., & Purnama, D. R. (2022). Uji Skema Parameterisasi Kumulus Untuk Prediksi Hujan Penyebab Banjir Di Kota Ambon Tanggal 11 Juli Test of Cumulus Parameterization Schemes for Prediction of Rain That Causes Floods in Ambon City on 11 July 2021. *Preprints, Open Science Framework*. https://doi.org/10.31219/osf.io/cz93f

Maraun, D., & Widmann, M. (2018). *Statistical Downscaling and Bias Correction for Climate Research*. Cambridge University Press.

Miftahuddin, M. (2016). Analisis Unsur-unsur Cuaca dan Iklim Melalui Uji Mann-Kendall Multivariat. *Jurnal Matematika, Statistika Dan Komputasi*, 13(1), 26–38. https://journal.unhas.ac.id/index.php/jmsk/article/view/3476

Minola, L., Zhang, G., Ou, T., Kukulies, J., Curio, J., Guijarro, J. A., Deng, K., Azorin-Molina, C., Shen, C., Pezzoli, A., & Chen, D. (2024). Climatology of near-surface wind speed from observational, reanalysis and high-resolution regional climate model data over the Tibetan Plateau. *Climate Dynamics*, 62, 933–953. https://doi.org/10.1007/s00382-023-06931-3

Morrissey, M. L. (1986). A Statistical Analysis of the Relationships among Rainfall, Outgoing Longwave Radiation and the Moisture Budget during January–March 1979. *Monthly Weather Review*, 114(5), 931–942. https://doi.org/10.1175/1520-

0493(1986)114<0931:ASAOTR>2.0.CO;2

Natasha, I., Putra, Y. S., & Adriat, R. (2021). Keterkaitan Outgoing Longwave Radiation dengan Intensitas Curah Hujan di Paloh Kabupaten Sambas Kalimantan Barat. *Prisma Fisika*, 9(2), 160. https://doi.org/10.26418/pf.v9i2.49490

Nurlatifah, A., Hatmaja, R. B., & Rakhman, A. A. (2023). Analisis Potensi Kejadian Curah Hujan Ekstrem di Masa Mendatang Sebagai Dampak dari Perubahan Iklim di Pulau Jawa Berbasis Model Iklim Regional CCAM. *Jurnal Ilmu Lingkungan*, 21(4), 980–986. https://doi.org/10.14710/jil.21.4.980-986

Pratama, A., Agiel, H. M., & Oktaviana, A. A. (2022). Evaluasi Satellite Precipitation Product (GSMaP, CHIRPS, dan IMERG) di Kabupaten Lampung Selatan. *Journal of Science and Applicative Technology*, 6(1), 32. https://doi.org/10.35472/jsat.v6i1.702

Prayuda, S. S., & Alfuadi, N. (2015). Pengaruh Convective Avaliable Potential Energy (CAPE) dan Outgoing Longwave Radiation (OLR) Terhadap Curah Hujan di Cengkareng. *Prosiding Seminar Nasional Fisika dan Aplikasinya*, 47–55.

Puspita, E. S., & Yulianti, L. (2016). Perancangan Sistem Peramalan Cuaca Berbasis Logika Fuzzy. *Jurnal Media Infotama*, 12(1), 1-10. https://doi.org/10.37676/jmi.v12i1.267.

Putra, R. M., & Rifani, A. (2016). Analisis Hujan Ekstrem Menggunakan Model WRF-ARW. *Prosiding Seminar Nasional Fisika Dan Pendidikan Fisika*, 105–114.

Ramadhan, F. D. (2018). *Analisis Pola Curah Hujan pada Kondisi Cuaca Ekstrem Bulan Oktober hingga Desember 2017 melalui Citra Modis Level 1B di Provinsi Jawa Timur*. Institut Teknologi Sepuluh Nopember.

Rasch, P. J., Xie, S., Ma, P-L., Lin, W., Wang, H., Tang, Q., Burrows, S. M., Caldwell, P., Zhang, K., Easter, R. C., Cameron-Smith, P., Singh, B., Wan, H., Golaz, J-C., Harrop, B. E., Roesler, B., Bacmeister, J., Larson, V. E., Evans, K. J., Qian, Y., Taylor, M., Leung, L. R., Zhang, Y., Brent, L., Branstetter, M., Hannay, C., Mahajan, S., Mametjanov, A., Neale, R., Richter, J. H., Yoon, J-H., Zender, C. S., Bader, D., Flanner, M., Foucar, J. G., Jacob, R., Keen, N., Klein, S. A., Liu, X., Salinger, A. G., Shrivastava, M., & Yang, Y. (2019). An Overview of the Atmospheric Component of the Energy Exascale Earth System Model. *Journal of Advances in Modeling Earth Systems*, 11, 2377–2411. https://doi.org/10.1029/2019MS001629.

Rizal, A. S., Widada, S., Ismanto, A., Handoyo, G., & Purwandana, A. D. P. (2020). Analysis of extreme wave heights in Indonesian waters using satellite altimetry data. *IOP Conference Series: Earth and Environmental Science*, 530(1), 012002. https://doi.org/10.1088/1755-1315/530/1/012002

Ruswanti, D. (2020). Pengukuran Performa Support Vector Machine Dan Neural Netwok Dalam Meramalkan Tingkat Curah Hujan. *Gaung Informatika*, 13(1), 66–75. https://jurnal.usahidsolo.ac.id/index.php/GI/article/view/455

Schreck, C. J., III, Lee, H.-T., & Knapp, K. R. (2018). HIRS Outgoing Longwave Radiation—Daily Climate Data Record: Application toward Identifying Tropical Subseasonal Variability. *Remote Sensing*, 10(9), 1325. https://doi.org/10.3390/rs10091325

Siagian, P. (2022). Wind Resource for Electrical Energy of Tourism and Micro Small and Medium Enterprises (MSMEs) in Coastal Areas After the

COVID-19 Pandemic. *Adpebi International Journal of Multidisciplinary Sciences*, 1(1), 175–186. https://doi.org/10.54099/aijms.v1i1.272

Sulistiyono, W., & Fadli, M. (2023). Verifikasi Produk Estimasi Curah Hujan GSMAP,GPM-IMERG, dan HIMAWARI-8 Pada Wilayah Serang, Pekanbaru, dan Ambon. *OPTIKA: Jurnal Pendidikan Fisika,* 7(2), 270–283. https://doi.org/10.37478/optika.v7i2.3119

Suwarti, S., Mulyono, M., Prasetiyo, B., Rifa'i, A., Diastiara, I. R., Indriyani, L., & Putro, W. P. (2017). Pembuatan Monitoring Kecepatan Angin Dan Arah Angin Menggunakan Mikrokontroler Arduino. *Seminar Nasional Pendidikan, Sains Dan Teknologi*, *05*(01), 56–64. https://jurnal.unimus.ac.id/index.php/psn12012010/article/view/3152

Taufik, M., Setiawan, B. I., & Van Lanen, H. A. J. (2019). Increased fire hazard in human-modified wetlands in Southeast Asia. *Ambio*, 48, 363–373. https://doi.org/10.1007/s13280-018-1082-3

Tribunnews.com (2021). *BMKG: Peringatan Cuaca Buruk Selasa 13 Juli 2021, Waspada Hujan Lebat Disertai Petir dan Angin*. Accessed on 27 January 2024. https://lombok.tribunnews.com/2021/07/12/bmkg-peringatan-cuaca-buruk-selasa-13-juli-2021-waspada-hujan-lebat-disertai-petir-dan-angin

Wang, H., & Zheng, J. (2022). Assessing the Effects of Surface Conditions on Potential Evapotranspiration in a Humid Subtropical Region of China. *Frontiers in Climate*, 4, 813787. https://doi.org/10.3389/fclim.2022.813787

Wisnawa, G. G., Utami, A. D., Prayudhi, S. A., & Sari, F. P. (2019). Pemanfaatan Model WRF-ARW untuk Simulasi Hujan Sangat Lebat di Bandara I Gusti Ngurah Rai Bali (Studi Kasus Tanggal 12 Januari 2019). *Prosiding Seminar Nasional Fisika Dan Pendidikan Fisika 2019*, 5, 56–63. https://eprints.uny.ac.id/68452/1/57-end.pdf

ISSN: 2579-5821 (Print)
ISSN: 2579-5546 (Online)
URL address: http://journal.unhas.ac.id/index.php/geocelebes
DOI: 10.70561/geocelebes.v10i1.43582

Jurnal Geocelebes Vol. 10 No. 1, April 2026, 48 – 68

Comparative Accuracy of Satellite-Derived Bathymetry Using Random Forest, Multiple Linear Regression, and Van Hengel and Spitzer Algorithm

Fathurrahman Apriliansyah[1], Muhammad Ulin Nuha[1]*, Aulia Try Atmojo[1], Kuncoro Teguh Setiawan[2], Aswar Syafnur[3]

[1]Geomatics Engineering, Faculty of Infrastructure and Regional Technology, Institut Teknologi Sumatera, Lampung 35365, Indonesia.
[2]Research Center for Geoinformatics, National Research and Innovation Agency, Cibinong 16911, Indonesia.
[3]Geophysics Department, Faculty of Mathematics and Natural Sciences, Hasanuddin University, Makassar 90245, Indonesia.

*Corresponding author. Email: muhammad.nuha@gt.itera.ac.id

Manuscript received: 23 March 2025; Received in revised form: 11 March 2026; Accepted: 26 March 2026

Abstract

Bathymetry mapping using conventional methods faces limitations in shallow waters. With the development of remote sensing technology, satellite-derived bathymetry (SDB) emerges as an alternative by utilizing wavelengths that penetrate water and capture depth information. This study compares the performance of three empirical SDB methods: Random Forest (RF), Multiple Linear Regression (MLR), and the Van Hengel and Spitzer (VHS) algorithm. SPOT 6 ORTHO-level satellite imagery and depth data from single beam echosounder measurements were used to construct the depth models. Model accuracy was evaluated using root mean square error (RMSE), mean absolute error (MAE), and total vertical uncertainty (TVU). Results show that the RF method achieves the highest accuracy across most depth ranges (1–5 m, 5–10 m, and 10–15 m), while the VHS algorithm performs best at 0–1 m. At depths beyond 15 meters, MLR shows relatively better performance compared to other methods, although overall uncertainty remains high. Based on the coefficient of determination (R^2), RF achieves the best result with a value of 0.610, followed by MLR with 0.462, and VHS with 0.313. These findings highlight the superior adaptability of the RF method in estimating bathymetry across varying depth zones using optical satellite imagery.

Keywords: Multiple Linear Regression; Random Forest; Satellite-Derived Bathymetry; Van Hengel and Spitzer Algorithm

Citation: Apriliansyah, F., Nuha, M. U., Atmojo, A. T., Setiawan, K. T., & Syafnur, A. (2026). Comparing Accuracy of Satellite-Derived Bathymetry Using Random Forest, Multiple Linear Regression, and Van Hengel and Spitzer Algoritm. *Jurnal Geocelebes*, 10(1): 48–68, doi: 10.70561/geocelebes.v10i1.43582

Introduction

Bathymetry measurement or sea depth mapping has a very crucial role in various fields, such as maritime navigation, marine resource management, and marine environmental studies. Bathymetry or sea depth is a measure of the depth of marine waters measured from the water surface to the seabed. The need for bathymetry estimation information is also driven by activities in the area around the coast such as development activities, port activities, fishing, dredging, oil mining, and aquaculture (Pushparaj & Hegde, 2017).

Bathymetry mapping continues to progress. In general, bathymetry mapping is carried out by conventional methods, which is the echosounder method. But this method has shortcomings, which is the limitations of bathymetry measurements in shallow waters which are very difficult to do because of difficulties in navigation so that the ship does not sink and the presence of coral reefs in shallow waters can cause data to be inaccurate.

Bathymetry data acquisition is increasingly experiencing development with the advent of technology. One of the methods often used to obtain bathymetry information by utilizing technology is Satellite Derived Bathymetry (SDB). Remote sensing technology in obtaining point information depth information in shallow water by utilizing wavelengths that has a good spectral response to water and can penetrate certain depths depending on the capabilities of each satellite sensor (Nugraha et al., 2017).

The basic principle behind optical satellite-derived bathymetry is that different wavelengths exhibit different attenuation rates in water, which control depth sensitivity and effective penetration range (Wei et al., 2021; IHO, 2024). The different penetration behaviors of optical wavelengths in the water column are illustrated in Figure 1.

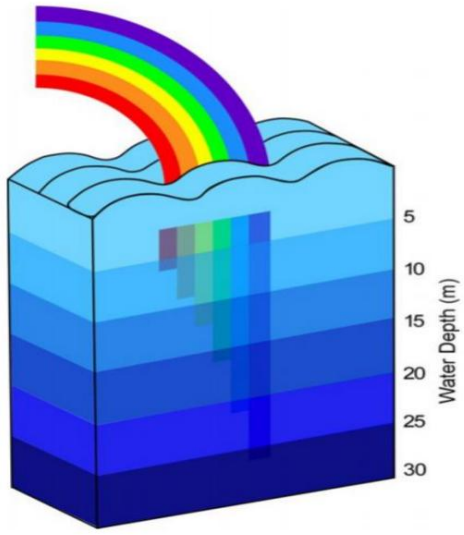

Figure 1. Wavelength penetration in water (Purkis, 2019).

Based on Figure 1 presented, the shorter the electromagnetic wavelength, the deeper the penetration of the wave. This is consistent with wavelength-dependent attenuation behavior reported in recent empirical assessments (Wei et al., 2021; IHO, 2024). The depth of penetration also depends on the level of water turbidity.

Optical penetration is limited by water turbidity and light attenuation (Kd). In clear waters, blue–green wavelengths may reach 15–20 m, but in most coastal waters, reliable SDB rarely exceeds 20–25 m (Gao, 2009; Manessa et al., 2016; Cahalane et al., 2019). Beyond this depth, bottom reflectance becomes undetectable, and depth estimates rely more on statistical extrapolation than true optical signal. Accordingly, depth estimates exceeding 20–25 m derived from optical satellite imagery should not be interpreted as true bathymetric measurements, but rather as statistical extrapolations beyond the effective optical penetration range. In the absence of detectable bottom reflectance, such estimates do not represent physically meaningful seabed depth and must be treated with caution or excluded from accuracy assessment (Caballero & Stumpf, 2020a; Cahalane et al., 2019). Recent best-practice guidance recommends that SDB products explicitly report their effective depth range and uncertainty, and that areas lacking a detectable bottom signal should be masked or excluded to avoid misleading depth interpretation (IHO, 2024).

Water quality is a critical control on the reliability of optical SDB because increasing turbidity and chlorophyll concentration reduce bottom detectability and therefore limit depth retrieval accuracy. Caballero & Stumpf (2019) emphasized that evaluating turbidity effects is essential both for selecting suitable satellite scenes and for understanding the practical limitations of SDB in optically complex waters.

Satellite-Derived Bathymetry has two methods: empirical method and analytical method. Analytical modeling of bathymetry is based on the way light propagates in water. The formation of this model requires the input of several optical properties of water, such as water coefficient, attenuation coefficient and backscattering (Gao, 2009). In empirical

modeling, the relationship between the remotely sensed radiance of a water body and the depth at the sample location is established empirically without regard to how light is transmitted in water (Gao, 2009). In this study, three methods are used to predict depth, which are the random forest (RF) method, multiple linear regression (MLR) and, the Van Hengel and Spitzer (VHS) algorithm.

Although empirical satellite-derived bathymetry models do not explicitly solve the radiative transfer equation, they implicitly approximate the physical interaction between water depth, bottom reflectance, and wavelength-dependent light attenuation in the water column. Shorter wavelengths, particularly in the blue and green spectral regions, exhibit lower attenuation coefficients and higher depth sensitivity, while longer wavelengths are rapidly absorbed. As a result, empirical models statistically approximate these optical processes without requiring direct measurements of inherent optical properties, making them suitable for shallow-water applications when bottom reflectance remains detectable (Gao, 2009; Pahlevan et al., 2017; Caballero & Stumpf, 2020a).

Recent developments in satellite-derived bathymetry have increasingly focused on the application of machine learning techniques to overcome the limitations of traditional empirical models. Recent research also shows that RF can be used not only to estimate water depth but also to automatically identify valid and invalid bathymetric pixels in satellite-derived bathymetry products, thereby improving the reliability of SDB mapping in complex coastal environments (Sharr et al., 2024). Studies employing RF, Gaussian Process Regression, and other multivariate learning approaches have demonstrated improved accuracy in capturing non-linear depth–reflectance relationships, particularly in optically complex and heterogeneous coastal waters (Ashphaq et al., 2024; Sagawa et al., 2019). Recent studies have also incorporated attention mechanisms into machine learning models to better capture spatial dependencies in multispectral imagery, leading to improved bathymetric inversion performance in optically complex coastal waters (Fang et al., 2024). Compared to earlier Indonesian case studies, this research extends previous work by systematically evaluating classical empirical models and machine learning approaches using SPOT-6 imagery, while explicitly addressing depth-dependent performance and uncertainty characteristics. Recent studies further demonstrate that RF-based SDB models benefit from the use of multi-date satellite imagery and careful image quality control, as bathymetric accuracy is strongly influenced by the quality and suitability of the input reflectance data (Mudiyanselage et al., 2022). Multi-temporal Sentinel-2 imagery has also been used to derive shallow-water bathymetry with RMSE values typically between 1.4 and 2.6 m when compared with LiDAR reference data (Evagorou et al., 2019). In addition to multispectral imagery, several recent studies have explored the integration of satellite optical data with spaceborne LiDAR measurements such as ICESat-2 to improve training data availability and enhance bathymetric prediction accuracy (Xie et al., 2023). Machine learning models combining ICESat 2 photon counting LiDAR bathymetric points with Sentinel 2 reflectance data have demonstrated high inversion accuracies for shallow water bathymetry in coastal regions, highlighting the value of hybrid active–passive data fusion approaches in SDB (Ye et al., 2024). Time-series or clean-coastal-water composite satellite imagery has been shown to improve the stability of satellite-derived bathymetry compared with single-date images, particularly when combined with RF regression and evaluated against hydrographic accuracy standards (Munawaroh et al., 2024). Recent studies

also explore iterative fusion methods that leverage active lidar photon returns and passive optical pseudo photons to enhance satellite derived bathymetry accuracy in both clear and turbid coastal waters (Hu et al., 2025).

Recent studies have shown that RF-based SDB can improve model generalization when trained using multi-temporal optical imagery rather than a single scene. The use of repeated Sentinel-2 observations also provides a practical means to improve SDB in environments with variable turbidity. Caballero and Stumpf (2020b) showed that multi-image approaches can support more routine and spatially scalable bathymetry mapping by exploiting the high revisit frequency of Sentinel-2A/B, particularly in data-poor or remote coastal regions. Sagawa et al. (2019) developed a generalized shallow-water bathymetry model using RF and 135 Landsat-8 images, reporting an RMSE of 1.41 m for depths between 0 and 20 m, which demonstrates the potential of multi-temporal machine learning approaches for improving SDB robustness across different sites.

In Indonesia, linear regression methods such as MLR are still widely used for bathymetry modeling because they are simple and easy to implement (Manessa et al., 2016). Machine learning approaches such as RF are also proven to provide high accuracy in capturing the non-linear relationship between reflectance and depth (Dewi et al., 2021). In addition, VHS spectral transformation methods have also been applied in several local studies (Nisa et al., 2023). Manessa et al. (2016) applied RF for SDB in Indonesian waters using WorldView-2 imagery. However, their study did not compare RF with MLR and the VHS algorithm using SPOT-6 imagery. Therefore, this study contributes by evaluating these three empirical methods specifically for Bawean Island using SPOT-6 data.

The principle of a RF is to create a random sample of training data with the same distribution across all trees in the forest. The MLR method forms a model that correlates the dependent and independent variables. The last method used in this research is the method with the VHS algorithm. This algorithm is a development of an algorithm previously known by Lyzenga. The principle of this algorithm is to transform the value of satellite images to obtain the relative depth of seawater using a rotational transformation matrix.

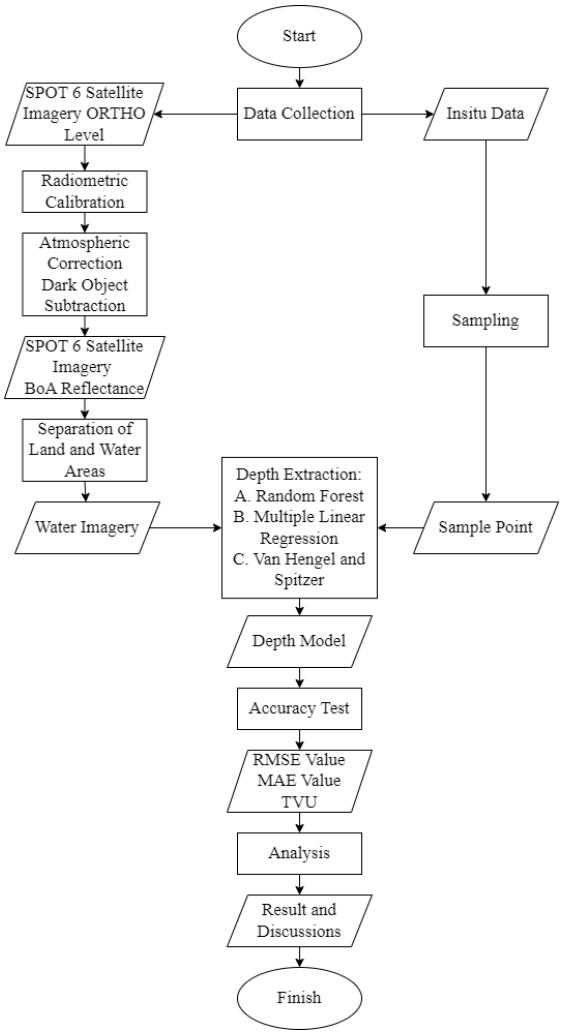

Figure 2. Flowchart.

The image used in this study is the SPOT 6 ORTHO level satellite image with a resolution of 6 meters. The image was subjected to radiometric calibration and atmospheric correction to obtain surface reflectance values. This research aims to analyze the accuracy produced by the three

methods in their ability to extract shallow water bathymetry. The overall workflow of the research process is presented in Figure 2.

Materials and Methods

The research site was located in the waters of Bawean Island, Gresik Regency, East Java. The geographical location of the study area is shown in Figure 3. The location was chosen based on the availability of data from the National Research and Innovation Agency (BRIN).

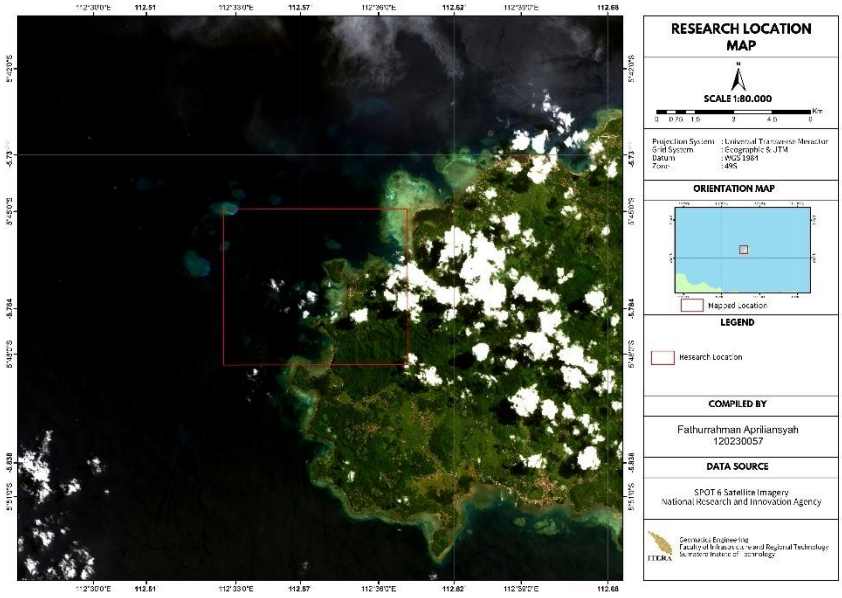

Figure 3. Research location.

Image Pre-processing

The image preprocessing stage aims to prepare the image data before further analysis. Radiometric correction is required to improve the visual quality of the image and adjust the pixel values to match the original spectral reflectance or radiance of an object. The main source of error is caused by atmospheric disturbances because it uses energy from electromagnetic radiation. Atmospheric effects alter the spectral signal recorded by satellite sensors, causing deviations between the measured reflectance and the true surface reflectance of objects. In this study, radiometric calibration and atmospheric correction processes were carried out.

To convert image data in digital number format into radians and/ or reflectance values requires a radiometric calibration stage. The radians value can also be converted to the Top of Atmosphere (ToA) reflectance value. To convert image pixel values to reflectance values, use Equation 1 (Nisa et al., 2023).

$$\rho_\lambda = \frac{\pi L_\lambda d^2}{ESUN_\lambda sin\theta} \quad (1)$$

Description:
L_λ : radians ($Wm^{-2}Sr^{-1}$)
D : earth-sun distance
$ESUN_\lambda$: solar irradiance ($Wm^{-2}\mu m$)
θ : solar elevation (°)

After the radiometric calibration process, the atmospheric correction process is then carried out. This research uses the Dark Object Subtraction (DOS) method of atmospheric correction. The DOS method converts satellite reflectance values into surface reflectance values. In the absence of atmospheric layers, dark objects such as

water and cloud shadows should have a pixel value of zero, if an object has a non-zero pixel value then the value is considered as bias (Nisa et al., 2023). The DOS method takes several samples of deep-sea pixels in each channel, and then the minimum value of the sample is used as a subtraction factor for the pixel value in each channel. The result of atmospheric correction is an image with a reflectance value below the atmosphere (Bottom of Atmosphere (BoA)). The DOS atmospheric correction calculation uses Equation 2 (Nisa et al., 2023).

$$L'_i = L_i - L_{si} \quad (2)$$

Description:
L'_i : corrected pixel value on band i
L_i : initial pixel value of band i
L_{si} : minimum pixel value of band i

Furthermore, the image masking process is used to separate land and water areas. In this research, the masking process is carried out using the Normalized Difference Vegetation Index (NDVI) method with the addition of Decision Tree rules. Satellite imagery preprocessing, including water masking and spectral filtering, is an important step in satellite-derived bathymetry workflows to ensure that depth inversion models are applied only to valid water pixels. The calculation of the NDVI method uses Equation 3 (Chybicki et al., 2023).

$$\text{NDVI} = \frac{\text{Red}-\text{NIR}}{\text{Red}+\text{NIR}} \quad (3)$$

Description:
Red : Digital Number in the red band
NIR : Digital Number in the NIR band

The Decision Tree rule is used to remove cloudy areas in the image by utilizing the NDVI value, where values less than -0.1 are considered as water.

Random Forest (RF)

RF is one of the machine learning algorithms that can be used for satellite-based bathymetry depth extraction. RF is a clustering algorithm that uses the bootstrap aggregating method by utilizing a number of decision trees to generate predictions (Bramante et al., 2013). The term “random forest” is derived from two words, the first being the word random, which refers to the random sampling of data from the original data set, and the second being forest, which refers to the construction of many decision trees from randomly sampled data (Mabula et al., 2023).

The RF model is operated by making random samples from the training data with the same distribution on all trees in the forest (Dewi et al., 2021). Mabula et al. (2023) mentioned that the RF model will automatically form a decision tree using the training data. The training data includes measured water depth and spectral values from satellite images as predictor variables (Syaiful et al., 2019). The final prediction result of RF is the average of all the results of the decision tree and will be influenced by the correlation between the trees.

Multiple Linear Regression (MLR)

Linear regression forms a model that correlates the dependent and independent variables. A linear regression will be called a simple linear regression if it only has one independent variable, while if it has more than one independent variable, it is called multiple linear regression (Dewi et al., 2021). The correlation between the dependent and independent variables is modeled by a linear function and its parameters are estimated from the data.

In this study, a MLR model was built using reflectance values from the red, green and blue channels that had been transformed using the natural logarithm. This transformation follows Lyzenga (1978), who demonstrated that the reflectance–depth relationship is exponential and must be linearized using logarithmic transformation before regression. This transformation was done because the relationship between water surface

reflectance and water depth is exponentially decreasing. Therefore, the conventional linear regression approach will only produce a less representative model if no transformation is performed. Lyzenga (1978) stated that the logarithmic transformation is used to transform the exponential relationship into a linear relationship that can be modeled statistically. The application of log transformation to reflectance is also used in various SDB studies, including by Manessa et al. (2016) who used a similar approach on WorldView-2 images in shallow waters of Indonesia.

This logarithmic transformation approach has been consistently adopted in recent empirical SDB studies to address the exponential attenuation of light in the water column. Studies have demonstrated that applying linear regression directly to raw reflectance values results in biased depth estimates, whereas log-transformed reflectance improves model stability, reduces systematic error, and preserves physical interpretability of the regression coefficients (Caballero & Stumpf, 2020a; Dewi & Rizaldy, 2021).

The MLR method performs image analysis by using multiple linear regression methods between field depth (in-situ) and multispectral images, then used to obtain regression coefficients (Nisa et al., 2023). The equation used to extract depth using the MLR method is written in Equation 4 (Manessa et al., 2016; Nisa et al., 2023).

$$Z = M_0 + M_{blue} \cdot \ln(B_{blue}) + M_{green} \cdot \ln(B_{green}) + M_{red} \cdot \ln(B_{red}) \quad (4)$$

Description:
Z : absolute depth
M_0 : constant
M_{blue} : blue channel coefficient
M_{green} : green channel coefficient
M_{red} : red channel coefficient
B_{blue} : blue channel reflectance spectral value
B_{green} : green channel reflectance spectral value
B_{red} : red channel reflectance spectral value

Van Hengel and Spitzer Algorithm (VHS)

The VHS algorithm is a development of the algorithm previously introduced by Lyzenga. The algorithm formulated by Van Hengel & Spitzer (1991) is an algorithm that transforms the value of satellite images to obtain the relative depth of seawater. The transformation process is done using a rotation transformation matrix. Van Hengel & Spitzer (1991) mentioned that water depth is directly proportional to the radiance/radiation algorithm and the relative water depth value can be obtained by performing a special transformation on the radiance value of each band. The VHS Equation 5–8 is formulated as follows (Van Hengel & Spitzer, 1991).

$$Ur = \frac{VarGreen + VarBlue}{2 * CoVarGreenBlue} \quad (5)$$

$$Us = \frac{VarRed + VarBlue}{2 * CoVarRedBlue} \quad (6)$$

$$R = \text{Arctan}(U_r + \sqrt{(Ur^2) + 1} \quad (7)$$

$$S = \text{Arctan}(U_s + \sqrt{(Us^2) + 1} \quad (8)$$

Description:
R : angle of rotation direction (Green-Blue channel)
S : angle of rotation direction (Red-Blue channel)
VarGreen : variation of 30 green channel data
VarBlue : variation of 30 blue channel data
VarRed : variation of 30 red channel data
CoVarGrenBlue : covariance of green and blue channels
CoVarRedBlue : covariance of red and blue channels

The results of the S and R angle calculation operations are then used to calculate the depth index value. The equation for

calculating the depth index is found in Equation 9 (Van Hengel & Spitzer, 1991).

$$X = (\mathrm{Cos}(R) * \mathrm{Sin}(S) * B1) + (\mathrm{Sin}(R) * \mathrm{Cos}(S) * B2) + (\mathrm{Sin}(S) * B3) \quad (9)$$

Description:
X : relative depth
B1 : reflectance value of the blue channel
B2 : reflectance value of the green channel
B3 : reflectance value of the red channel

Accuracy Test

In hydrographic contexts, vertical accuracy and uncertainty are commonly evaluated within standardized survey frameworks, such as those described in the IHO S-44 standard and satellite-derived bathymetry best-practice guidance (IHO, 2020). The field data used is the in situ depth. Based on the Regulation of the Head of the Geospatial Information Agency (Perka BIG) Number 18 of 2020 concerning Procedures for the Implementation of Geospatial Information, there are four general approaches used to conduct validation. Common approaches to test the accuracy of depth extraction results are Root mean square error (RMSE), coefficient of determination (R^2), Mean average error (MAE), and Total Vertical Uncertainty (TVU).

RMSE is the root of the average number of squares of the difference between the in situ depth value and the depth value from BBS processing using the depth algorithm (Nisa et al., 2023). The result of RMSE is the error rate of the depth extraction model. Lower RMSE values indicate higher model accuracy because they represent smaller differences between predicted and observed depths. A smaller RMSE value means that the depth extraction model is better than a larger RMSE value. The equation for evaluating the accuracy test using RMSE is as follows in Equation 10 (BIG, 2021).

$$\mathrm{RMSE}_{(\mathrm{depth})} = \sum \sqrt{\frac{(Y_i - Y'_i)^2}{N}} \quad (10)$$

Description:
Y_i : In-situ depth
Y'_i : Depth of satellite-derived bathymetry results
n : Number of depth samples used

RMSE and MAE are two standard metrics widely used in model evaluation, and reporting both is common practice because they emphasize different characteristics of model error distributions (Hodson, 2022). MAE can be operated using Equation 11 (BIG, 2021).

$$\mathrm{MAE} = \frac{1}{n}\sum_{i=1}^{n}|x_i - \hat{x}_i| \quad (11)$$

Description:
x_i : Depth of satellite-derived bathymetry results
$\hat{x}_i$: In-situ depth
n : Number of depth samples used

The coefficient of determination is between zero and one. If the R^2 value approaches one, the influence of the independent variable on the dependent variable is stronger. The equation for calculating the coefficient of determination is Equation 12 (BIG, 2021).

$$R^2 = 1 - \frac{\text{explained variance}}{\text{total variance}} \quad (12)$$

The last test performed is the calculation of Total Vertical Uncertainty (TVU). IHO standardization has an accuracy test method known as TVU. Referring to the hydrographic survey manual S-44 edition issued by IHO (2020), TVU is a component of total propagated uncertainty (TPU) calculated in vertical dimensions. TVU is a one-dimensional quantity with all vertical measurement uncertainties included. TVU can be operated using Equation 13 (BIG, 2021).

$$\mathrm{TVU}_{\max}(d) = \pm\sqrt{a^2 + (b \times d)^2} \quad (13)$$

Description:
a : Depth-independent error factor
b : Depth-dependent error factor
d : SDB model depth value
b x d : Depth-dependent uncertainty parameter

Table 1. Maximum value of TVU for 95% confidence level (IHO, 2020)

Orde	a (m)	b
Exclusive	0.15	0.0075
Special	0.25	0.0075
1a/1b	0.50	0.0130
2	1.00	0.0230

The coefficients a and b can be seen in the IHO SP-44 document in Table 1.

Results and Discussion

Radiometric and Atmospheric Correction

The images obtained are still images with pixel values in the form of digital numbers (DN). The DN value must be converted into a reflectance value so that it can be used to obtain relative depth. The value obtained from the Equation 1 is the ToA reflectance value presented in Figure 4.

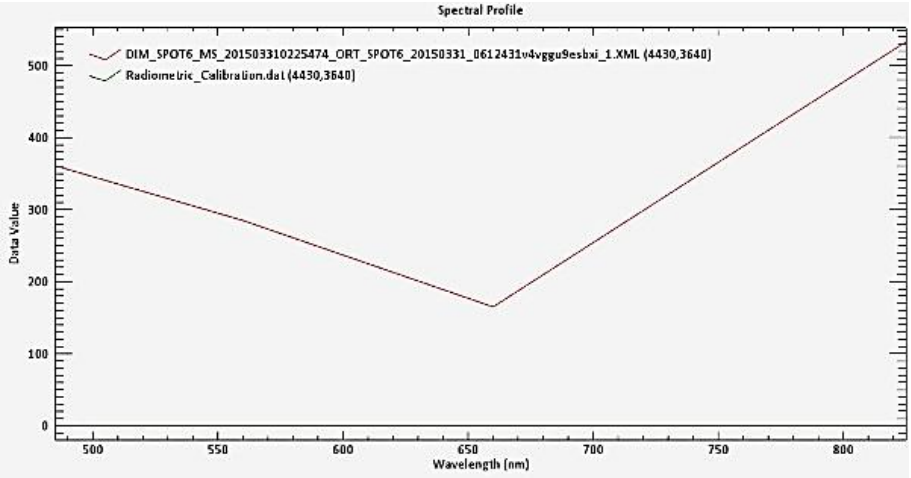

Figure 2. Pixel value of atmospheric correction image.

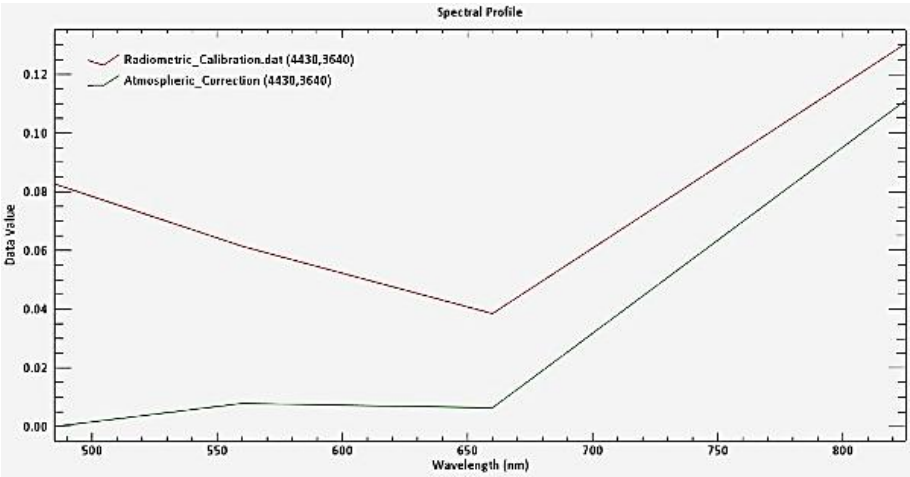

Figure 3. Pixel value of radiometric calibration image

Image pixel values that have been radiometrically calibrated range from zero to one. The pixel value of the image that has been radiometrically calibrated is the ToA reflectance value that does not represent the value of the object's reflection on the earth's surface. This is because in the process of recording from satellite imagery, there is scattering of electromagnetic waves caused by the presence of gas and dust particles in the atmosphere. A comparison of the reflectance values in the image before atmospheric correction and the image after atmospheric correction is presented in Figure 5.

Correction with the DOS method can be done because in deep water areas electromagnetic wave energy is absorbed, so the reflectance that appears from the

inside can be assumed to be atmospheric reflectance. Images that have been corrected for atmospheric effects can be used for bathymetry extraction. The corrected image is presented in Figure 6.

Image Masking

The use of water areas is necessary so that the process of extracting depth values using satellite imagery only involves spectral values present in the water. In the NDVI index value generated at the research location, cloudy areas are identified with a value range of -0.2 to -0.1. Based on this range of values, cloudy areas can be removed by providing rules on the decision tree with NDVI values less than -0.1 designated as waters. The NDVI classification results with the decision tree rule are presented in Figure 7.

Figure 4. Visual corrected image.

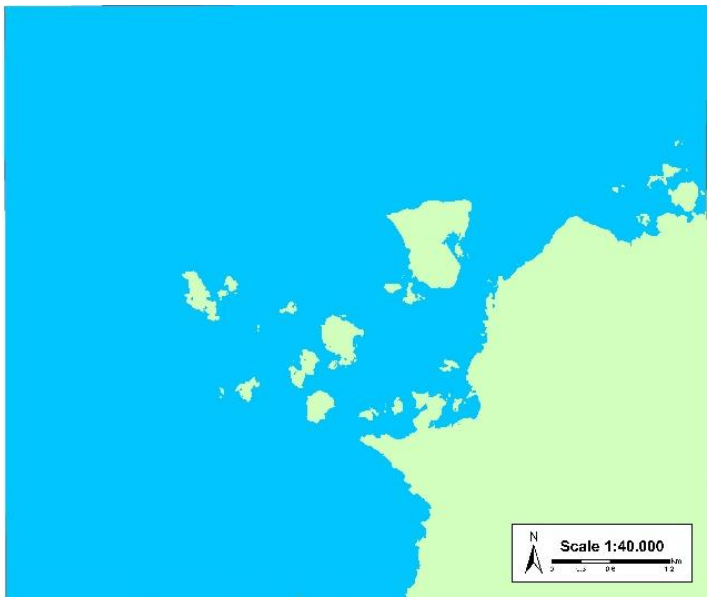

Figure 5. NDVI reclassification result.

The results of NDVI reclassification which are still in raster format become input data that will be converted into vector format. The raster data were converted into vector format through a standard conversion process in GIS software, so that the

classified water areas could be separated more clearly. The vector format classification results then removed the land part and left the water part. The data will be used for image masking in each band. The visual appearance of the extracted water area after masking is shown in Figure 8. Restricting satellite-derived bathymetry predictions to optically shallow water is essential, because accuracy decreases rapidly beyond depths where bottom reflectance is detectable; therefore, masking unsuitable pixels is required to ensure that mapped bathymetry remains fit for purpose (Richardson et al., 2025).

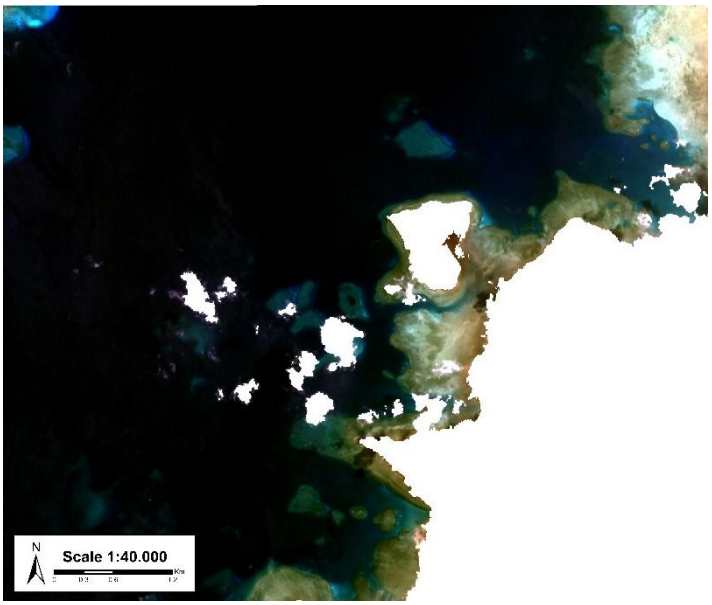

Figure 6. Visual water imagery.

Depth Extraction Results

The depth value obtained from each method produces different depths. The composite band used is the RGB band composite of the SPOT 6 satellite image. Although the RF model produced depth values up to 36.1 m, depths beyond 20–25 m likely do not represent true optical bathymetry due to light attenuation limitations. This behavior is consistent with recent studies indicating that RF-based SDB models often outperform traditional empirical approaches, while their effective depth range typically remains within approximately 10–20 m depending on water clarity and seabed conditions (Kwon et al., 2024). The results of the RF method extraction are presented in Figure 9.

There are several parameters used in processing the RF method, one of which is the variation in the number of trees (ntree). Based on Safi'i & Dewi (2020), ntree variation does not have a significant effect on the results of the SDB model, so the ntree variation used is the default setting from SDB GUI, which is 300. The train dataset is also needed in RF processing, which is 10%. A 10% training dataset was selected to avoid overfitting while still providing sufficient samples for model learning, following common practice in previous SDB studies (Safi'i & Dewi, 2020; Ashphaq et al., 2024). The remaining 90% of data were used as an independent validation set. The accuracy test process refers to horizontal and vertical accuracy with a 90% confidence level. So the training data used is 10% and the data for accuracy testing is 90%. The depth extraction results obtained using the MLR method are shown in Figure 10.

The depth extraction results obtained with the MLR method produce varied values. But there is still a depth estimation error

shown in the black part. The depth estimate obtained in the area is less than 0 meters, which means the value is negative. The negative depth result is an error because the depth value should be positive. According to Syaiful et al. (2019), depth values below 0 must be eliminated because it is a depth values with a high error rate.

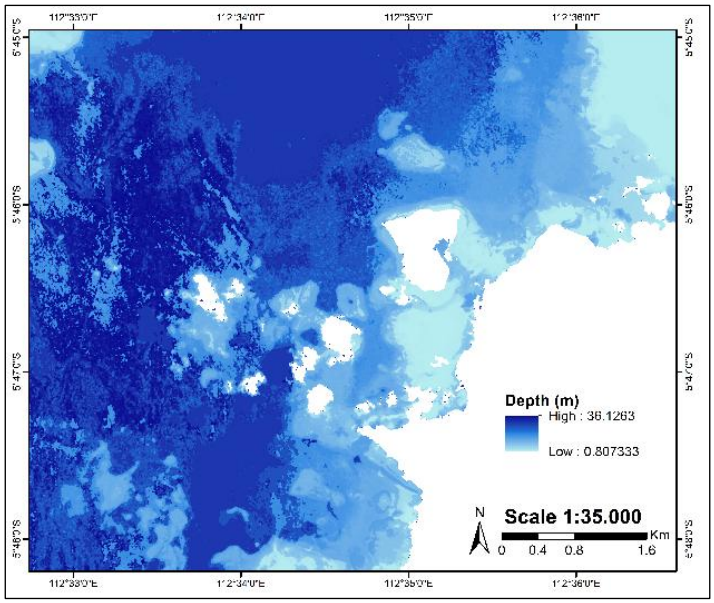

Figure 7. Results of depth extraction of RF method.

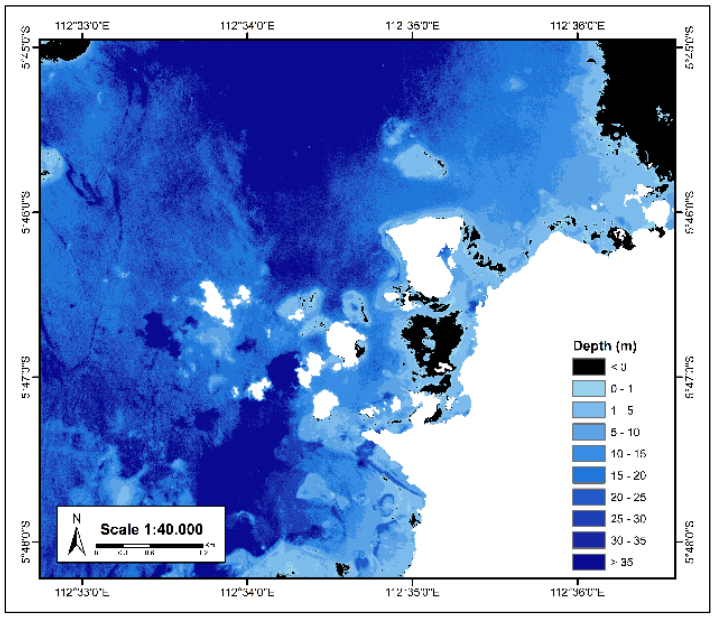

Figure 8. Depth extraction results of MLR method.

Negative depth estimates were excluded from subsequent accuracy assessment, as they are physically unrealistic and indicate model extrapolation beyond valid spectral response ranges. Similar filtering procedures have been applied in previous satellite-derived bathymetry studies to maintain physical consistency and avoid bias in model evaluation (Dewi & Rizaldy, 2021; Caballero & Stumpf, 2020a). The absolute depth results derived from the VHS algorithm are presented in Figure 11.

The absolute depth of the VHS algorithm gets a depth range of less than 0 to more than 15 meters. The maximum depth obtained from this method is 20.1 meters. The maximum depth is smaller than the

other two methods used in this study. The depth obtained also still has estimation errors in areas with black color. This is indicated by the depth of the area which is negative. This error is the same as the error obtained with the multiple linear regression method. Negative depth estimates were excluded from further analysis as they are physically unrealistic.

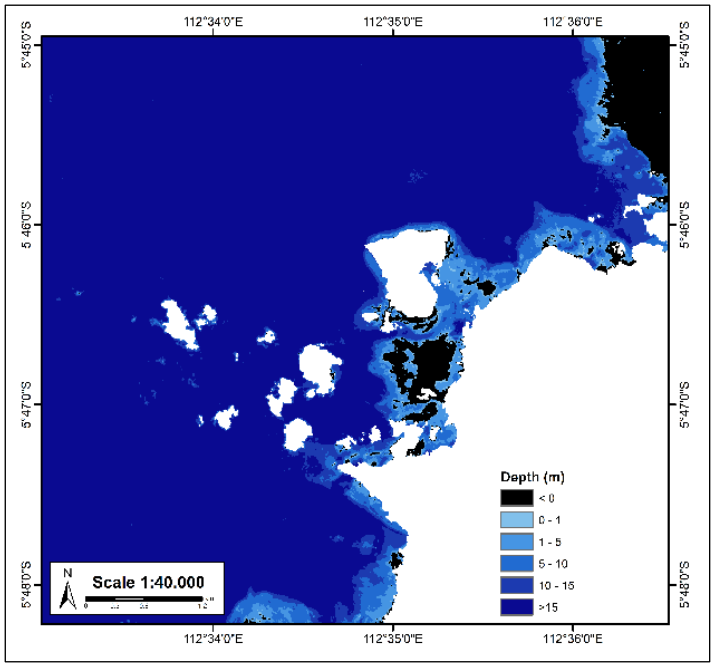

Figure 9. Absolute depth results of VHS algorithms.

Accuracy Test

The level of accuracy in the estimation model can be seen from the resulting RMSE and MAE values. The smaller the value, the higher the accuracy of the model. This study uses comparison data sourced from direct observations in the field using a single beam echosounder. The calculation of RMSE and MAE values is done per depth.

In addition to numerical accuracy metrics, scatterplots of predicted versus in-situ depths were generated for each model to visually evaluate model performance, bias, and error dispersion. Scatterplot analysis is essential to identify systematic overestimation or underestimation patterns and the presence of outliers that may not be fully captured by RMSE, MAE, or R^2 values alone (Ashphaq et al., 2024; Sagawa et al., 2019).

Based on the resulting RMSE values in Table 2 and MAE values in Table 3, the VHS algorithm produces the lowest error at a depth of 0–1 meter, with RMSE of 0.518 meters and MAE of 0.424 meters. At depths of 1–5 meters, 5–10 meters, and 10–15 meters, the RF method consistently yields the lowest errors, with RMSE values of 3.045, 6.827, and 12.491 meters respectively, and MAE values of 2.816, 6.715, and 12.417 meters. At depths exceeding 15 meters, the MLR method shows slightly better performance with RMSE of 18.120 meters and MAE of 17.900 meters. These results indicate that the RF method is the most accurate overall within the typical SDB depth range, while VHS is more suitable for very shallow areas, and MLR performs relatively better in deeper waters. Similar comparative studies in highly dynamic coastal environments report that machine learning approaches tend to reduce systematic bias relative to traditional empirical models,

although careful masking and validation remain essential to avoid overconfident extrapolation (Quang et al., 2025).

Table 2. Comparison of RMSE values.

Method	Depth (m)				
	0-1	1-5	5-10	10-15	>15
Random Forest	0.545	3.045	6.827	12.491	18.121
Multiple Linear Regression	0.613	3.221	7.703	12.325	18.120
Van Hengel and Spitzer	0.518	3.300	7.493	12.328	17.967

Table 3. Comparison of MAE values

Method	Depth (m)				
	0-1	1-5	5-10	10-15	>15
Random Forest	0.463	2.816	6.715	12.417	18.013
Multiple Linear Regression	0.545	3.009	7.576	12.244	17.900
Van Hengel and Spitzer	0.424	3.079	7.397	12.262	17.846

Table 4. Comparison of coefficient of determination

Method	R^2
Random Forest	0.687
Multiple Linear Regression	0.436
Van Hengel and Spitzer	0.444

Figure 12 presents the scatterplot of in-situ versus predicted depths for the RF model. Figure 13 presents the scatterplot of in-situ versus predicted depths for the MLR model. Figure 14 presents the scatterplot of in-situ versus predicted depths for the VHS algorithm.

Based on Table 4 presented, the highest coefficient of determination is generated by the RF method which is 0.687. Then continued by the VHS algorithm with an R^2 value of 0.444. The last is the MLR method with an R^2 value of 0.436. This indicates that the RF method has a strong correlation with insitu depth data. In contrast, the method that has the weakest correlation is produced by the MLR method.

Based on BIG Regulation No. 18 of 2021, testing of the SDB model is also carried out by calculating the total vertical uncertainty (TVU). TVU describes the total uncertainty in water depth measurement.

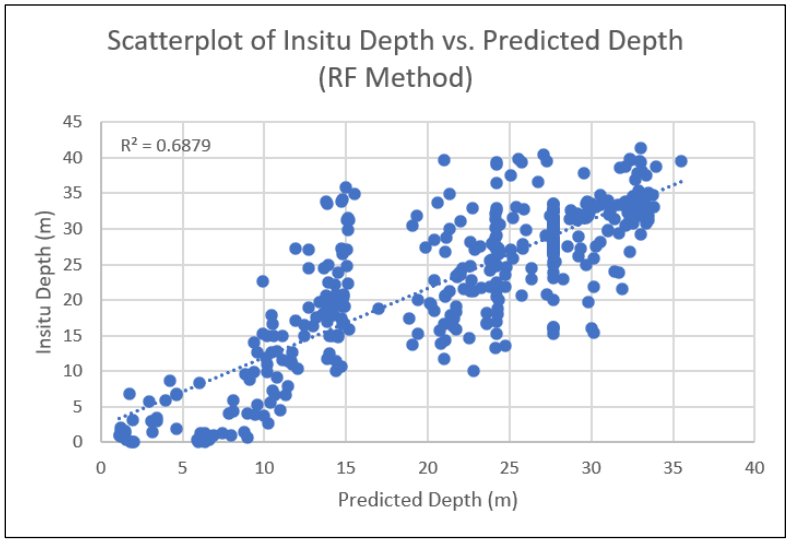

Figure 10. Scatterplot of in-situ and predicted depth (RF).

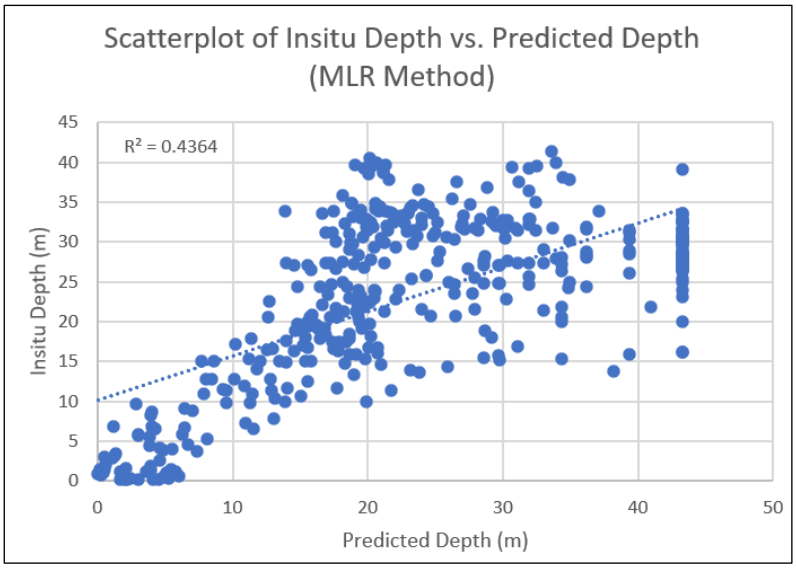

Figure 11. Scatterplot of in-situ and predicted depth (MLR).

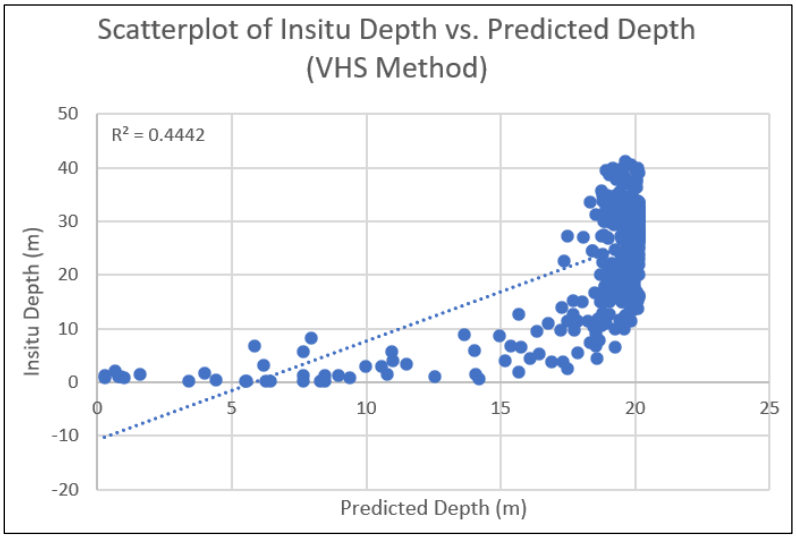

Figure 12. Scatterplot of in-situ and predicted depth (VHS).

Table 5. Random Forest method TVU testing.

Depth (m)	Inbound Data (%)				Data not entered (%)
	2	1a/1b	Special	Exclusive	
0-5	4.17	16.67	8.33	16.67	54.17
5-10	3.70	7.41	0.00	0.00	88.89
10-15	8.11	4.05	1.35	1.35	85.14
15-20	11.76	0.00	0.00	0.00	88.24
20-25	9.20	3.45	0.00	0.00	83.91
>25	12.23	6.38	2.13	2.13	71.28

Table 6. Multiple Linear Regression method TVU testing.

Depth (m)	Inbound Data (%)				Data not entered (%)
	2	1a/1b	Special	Exclusive	
0-5	18.92	5.41	0.00	0.00	75.68
5-10	0.00	13.64	0.00	0.00	86.36
10-15	3.13	3.13	0.00	3.13	90.63
15-20	6.82	3.41	0.00	2.27	87.50
20-25	1.41	1.41	0.00	1.41	95.77
>25	4.19	0.60	1.20	0.60	93.41

Table 7. Van Hengel and Spitzer method TVU testing.

Depth (m)	Inbound Data (%)				Data not entered (%)
	2	1a/1b	Special	Exclusive	
0-5	20.00	0.00	20.00	20.00	40.00
5-10	6.25	6.25	0.00	0.00	87.50
10-15	0.00	0.00	0.00	0.00	100.0
15-20	4.00	0.80	2.40	1.60	91.20
>20	0.00	0.77	0.00	1.54	97.69

Based on the TVU testing of the three SDB methods, it shows a similar trend with vertical uncertainty increasing with depth. The VHS algorithms tend to have a higher percentage of data not in any order at deeper depths, indicating a significant level of uncertainty. The RF method performed slightly better at shallower depths, with a greater percentage of data falling into the TVU order. The MLR method showed variation in its results, with some depth ranges having lower uncertainties than others, but still showing high uncertainties at deeper depths. This comparison indicates that despite variations in the accuracy of each method, vertical uncertainty remains a major challenge in depth measurement using the SDB technique, especially at deeper depths.

The TVU test results above show that the VHS algorithms perform best at shallow depths (0–5 meters) with 60% of the data falling into the TVU order, which is the highest percentage compared to other methods at the same depth range. Although vertical uncertainty remains a challenge at deeper depths, these algorithms generally show the highest level of accuracy at shallow depths compared to the RF and MLR methods. However, for deeper depths, none of the methods consistently showed a significant advantage. Each method has a high degree of uncertainty, so the selection of the best method may also depend on the depth range favored in a particular research or application.

There are several factors that can affect the accuracy of the SDB model. The bathymetry data generated from satellite image estimation has a weakness in its limited ability to penetrate waves in the water column. Penetration of light through the water column, the intensity will decrease exponentially with increasing depth (attenuation) (Prasetya et al., 2023). Organic and inorganic particles can reduce the intensity of light penetrating the water column. Cahalane et al. (2019) also said that in general the SDB model is strongly influenced by the type of sensor, water quality and other environmental conditions.

Recent studies also highlight that the accuracy of SDB is influenced not only by environmental conditions but also by how spectral input data and reference measurements are prepared prior to modeling. Lee et al. (2025) demonstrated that the configuration of spectral inputs and the spatial interpolation strategy used for reference depth data can significantly affect model performance. Their results indicate that different combinations of spectral bands, preprocessing strategies, and interpolation approaches may lead to substantial variations in predicted bathymetric accuracy, emphasizing the importance of carefully designing the input data structure when developing SDB models.

The main limitation in optical image-based bathymetry methods is the ability of light to penetrate the water column. Physics based satellite derived bathymetry methods applied to multispectral imagery, such as Landsat OLI, integrate optical water properties and bottom reflectance to optimize bottom unmixing and can achieve RMSE values mostly less than 2 m even in waters as deep as 30 m, demonstrating physical modelling as a complementary

SDB strategy (Kim et al., 2024). According to Gao (2009), the blue to green wavelengths (0.48–0.60 µm) commonly used in satellite imagery can only penetrate depths of up to 15–20 meters in clear, calm waters. Even under optimum conditions, the detectable depth rarely exceeds 20 meters and the uncertainty can reach more than 4–5 meters. Gao also emphasized that if the waters have high turbidity, the maximum detectable depth will be much shallower. In this study, the bathymetry model does not explicitly include turbidity parameters or light diffusion coefficient (Kd), so depth predictions above 25 meters need to be considered carefully as they may fall outside the effective spectral penetration range of SPOT-6 imagery. Therefore, depth estimates beyond 25 m in this study should be interpreted with caution and are not recommended for operational hydrographic use.

Recent machine learning studies also indicate that SDB accuracy is not controlled only by depth itself, but also by water-quality-dependent optical properties and by the relevance of the predictor variables used in the model. Liu et al. (2024) found that models incorporating QAA-derived inherent optical properties can match or outperform models using reflectance alone, especially in turbid waters, and they further showed that including excessive redundant bands may reduce model accuracy rather than improve it.

Conclusion

Based on the resulting RMSE and MAE values, at a depth of 0–1 meter, the VHS algorithms produce the lowest RMSE and MAE values, which are 0.518 meters and 0.424 meters. At a depth of 1–5 meters, the RF method produces the lowest values, which are RMSE of 3.045 meters and MAE of 2.816 meters. At a depth of 5–10 meters, the RF method produces the lowest value, which are RMSE of 6.827 meters and MAE of 6.715 meters. At a depth of 10–15 meters, the MLR method produces the lowest value, which are RMSE of 12.325 meters and MAE of 12.244 meters. At depths >15 meters, the VHS algorithms produce the lowest value, which are RMSE of 17.967 meters and MAE of 17.846 meters. Based on the R^2 value obtained, the RF method produces the best R^2 value of 0.687. Furthermore, the VHS algorithm with an R^2 value of 0.444 and the last is the MLR method with an R^2 value of 0.436.

Acknowledgements

The author would like to express his deepest gratitude to all those who have contributed to the making of this article so that this article can be completed.

Author Contribution

In compiling this research journal, each author is divided into several job desks. **Conceptualization**: Fathurrahman Apriliansyah, Muhammad Ulin Nuha, Aulia Try Atmojo; **Methodology**: Fathurrahman Apriliansyah, Muhammad Ulin Nuha, Aulia Try Atmojo, Kuncoro Teguh Setiawan; **Writing-Original Draft Preparation**: Fathurrahman Apriliansyah, Muhammad Ulin Nuha, Aswar Syafnur; **Writing-Review and Editing**: Fathurrahman Apriliansyah, Muhammad Ulin Nuha, Aulia Try Atmojo, Kuncoro Teguh Setiawan, Aswar Syafnur; **Visualization**: Fathurrahman Apriliansyah, Aulia Try Atmojo, Aswar Syanur. All authors have read and agreed to the published version of the manuscript.

Conflict of Interest

The author declares no financial or personal connections with any organization or parties involved in this research. Therefore, the research findings are solely the author's responsibility.

References

Ashphaq, M., Srivastava, P. K., & Mitra, D.

(2024). Satellite - Derived Bathymetry in Dynamic Coastal Geomorphological Environments Through Machine. *Earth and Space Science*, 11(7), 1–23. https://doi.org/10.1029/2024EA003554

BIG. (2021). *Peraturan Badan Informasi Geospasial Republik Indonesia Nomor 18 Tahun 2021 Tentang Tata Cara Penyelenggaraan Informasi Geospasial*. Badan Informasi Geospasial. https://peraturan.bpk.go.id/Details/217091/peraturan-big-no-18-tahun-2021

Bramante, J. F., Raju, D. K., & Sin, T. M. (2013). Multispectral derivation of bathymetry in Singapore's shallow, turbid waters. *International Journal of Remote Sensing*, 34(6), 2070–2088. https://doi.org/10.1080/01431161.2012.734934

Caballero, I., & Stumpf, R. P. (2019). Preliminary Assessment of Turbidity and Chlorophyll Impact on Bathymetry Derived from Sentinel-2A and Sentinel-3A Satellites in South Florida. *Remote Sensing*, 11(6), 645. https://doi.org/10.3390/rs11060645

Caballero, I., & Stumpf, R. P. (2020a). Atmospheric correction for satellite-derived bathymetry in the Caribbean waters : from a single image to multi-temporal approaches using Sentinel-2A/B. *Optics Express*, 28(8), 11742–11766. https://doi.org/10.1364/OE.390316

Caballero, I., & Stumpf, R. P. (2020b). Towards Routine Mapping of Shallow Bathymetry in Environments with Variable Turbidity : Contribution of Sentinel-2A/B Satellites Mission. Remote Sensing, 12(3), 451. https://doi.org/10.3390/rs12030451

Cahalane, C., Magee, A., Monteys, X., Casal, G., Hanafin, J., & Harris, P. (2019). A comparison of Landsat 8, RapidEye and Pleiades products for improving empirical predictions of satellite-derived bathymetry. *Remote Sensing of Environment*, 233, 111414. https://doi.org/10.1016/j.rse.2019.111414

Chybicki, A., Sosnowski, P., Kulawiak, M., Bieliński, T., Korlub, W., Łubniewski, Z., Kempa, M., & Parzuchowski, J. (2023). Study of various machine learning approaches for Sentinel-2 derived bathymetry. *PLoS ONE*, 18(9), e0291595. https://doi.org/10.1371/journal.pone.0291595

Dewi, R. S., & Rizaldy, A. (2021). Accuracy Assessment of Satellite Derived Bathymetry Model for Depth Extraction in Sorong Shallow Water Area Accuracy Assessment of Satellite Derived Bathymetry Model for Depth Extraction in Sorong Shallow Water Area. *IOP Conference Series: Earth and Environmental Science*, 925, 012053. https://doi.org/10.1088/1755-1315/925/1/012053

Dewi, R. S., Rizaldy, A., Hartanto, P., & Suprajaka, S. (2021). Assesing The Accuracy of Shallow Water Depth Estimation by Using Multispectral Satellite Images. *Geographia Technica*, 16(Special Issue), 180–197. http://dx.doi.org/10.21163/GT_2021.163.14

Evagorou, E., Mettas, C., Agapiou, A., Themistocleous, K., & Hadjimitsis, D. (2019). Bathymetric maps from multi-temporal analysis of Sentinel-2 data: the case study of Limassol, Cyprus. *Advances in Geosciences*, 45, 397–407, https://doi.org/10.5194/adgeo-45-397-2019

Fang, S., Wu, Z., Wu, S., Chen, Z., Shen, W., & Mao, Z. (2024). Enhancing Water depth inversion accuracy in turbid coastal environments using random forest and coordinate attention mechanisms. *Frontiers in Marine Science*, 11, 1471695. https://doi.org/10.3389/fmars.2024.1471695

Gao, J. (2009). Bathymetric mapping by

means of remote sensing: Methods, accuracy and limitations. *Progress in Physical Geography*, 33(1), 103–116. https://doi.org/10.1177/0309133309105657

Hodson, T. O. (2022). Root-mean-square error (RMSE) or mean absolute error (MAE): when to use them or not. *Geoscientific Model Development*, 15, 5481–5487. https://doi.org/10.5194/gmd-15-5481-2022

Hu, Q., Li, J., & Cheng, L. (2025). Satellite-derived bathymetry based on iterative fusion of active lidar photons and passive pseudo- photons. *International Journal of Digital Earth*, 18(1), 2543568. https://doi.org/10.1080/17538947.2025.2543568

IHO. (2020). *International Hydrographic Organization Standards for Hydrographic Surveys*. *377*.

IHO. (2024). *International Hydrographic Organization Guidance to Satellite-Derived Bathymetry © Copyright International Hydrographic Organization 2024. 377*.

Kim, M., Danielson, J., Storlazzi, C., & Park, S. (2024). Physics-Based Satellite-Derived Bathymetry (SDB) Using Landsat OLI Images. *Remote Sensing*, 16(5), 843. https://doi.org/10.3390/rs16050843

Kwon, J-Y., Shin, H-K., Kim, D-H., Lee, H-G., Bouk, J-K., Kim, J-H., & Kim, T-H. (2024). Estimation of shallow bathymetry using Sentinel-2 satellite data and random forest machine learning : a case study for Cheonsuman, Hallim, and Samcheok Coastal Seas. *Journal of Applied Remote Sensing*, 18(1), 014522. https://doi.org/10.1117/1.JRS.18.014522

Lee, S-J., Kim, H-S., Yun, H-S., & Lee, S-H. (2025). Satellite-Derived Bathymetry Using Sentinel-2 and Airborne Hyperspectral Data : A Deep Learning Approach with Adaptive Interpolation. *Remote Sensing*, 17(15), 2594. https://doi.org/10.3390/rs17152594

Liu, Z., Liu, H., Ma, Y., Ma, X., Yang, J., Jiang, Y., & Li, S. (2024). Exploring the Most Effective Information for Satellite-Derived Bathymetry Models in Different Water Qualities. *Remote Sensing*, 16(13), 2371. https://doi.org/10.3390/rs16132371

Lyzenga, D. R. (1978). Passive remote sensing techniques for mapping water depth and bottom features. *Applied Optics*, 17(3), 379–383. https://doi.org/10.1364/ao.17.000379

Mabula, M. J., Kisanga, D., & Pamba, S. (2023). Application of machine learning algorithms and Sentinel-2 satellite for improved bathymetry retrieval in Lake Victoria, Tanzania. *Egyptian Journal of Remote Sensing and Space Science*, 26(3), 619–627. https://doi.org/10.1016/j.ejrs.2023.07.003

Manessa, M. D. M., Kanno, A., Sekine, M., Haidar, M., Yamamoto, K., Imai, T., & Higuchi, T. (2016). Satellite-Derived Bathymetry Using Random Forest Algorithm and Worldview-2 Imagery. *Geoplanning: Journal of Geomatics and Planning,* 3(2), 117–126. https://doi.org/10.14710/geoplanning.3.2.117-126

Mudiyanselage, S. S. J. D., Wilkinson, B., & Lecours, V. (2022). Satellite-derived bathymetry using machine learning and optimal Sentinel-2 imagery in South- West Florida coastal waters. *GIScience & Remote Sensing*, 59(1), 1143–1158. https://doi.org/10.1080/15481603.2022.2100597

Munawaroh, M., Wicaksono, P., Farda, N. M., Lumban-Gaol, Y., Khakhim, N., & Kamal, M. (2024). Performance test of clean-coastal-water composite sentinel 2A image for shallow water bathymetry mapping. *Remote Sensing Applications: Society and*

Environment, 35, 101212. https://doi.org/10.1016/j.rsase.2024.101212

Nisa, S. Q., Karang, I. W. G. A., Putra, I. D. N. N., Setiawan, K. T., & Aziz, K. (2023). Perbandingan Akurasi Metode Empiris untuk Pemetaan Batimetri Perairan Benoa, Bali, Menggunakan Citra Satelit SPOT. *Journal of Marine Research and Technology*, 6(1), 60. https://doi.org/10.24843/jmrt.2023.v06.i01.p09

Nugraha, A. Y., Prayudha, B., Ibrahim, A. L., & Riyadi, N. (2017). Pemetaan Batimetri di Perairan Dangkal menggunakan Data Penginderaan Jauh Spot-7 (Studi Kasus Lembar-Lombok). *Jurnal Chart Datum*, 3(2), 61–80. https://doi.org/10.37875/chartdatum.v3i2.120

Pahlevan, N., Sarkar, S., Franz, B. A., Balasubramanian, S. V, & He, J. (2017). Remote Sensing of Environment Sentinel-2 MultiSpectral Instrument (MSI) data processing for aquatic science applications: Demonstrations and validations. *Remote Sensing of Environment*, 201, 47–56. https://doi.org/10.1016/j.rse.2017.08.033

Prasetya, M. I., Siregar, V. P., & Agus, S. B. (2023). Comparison of Satellite-Derived Bathymetry Algorithm Accuracy Using Sentinel-2 Multispectral Satellite Image. *Jurnal Kelautan Tropis*, 26(1), 113–125. https://doi.org/10.14710/jkt.v26i1.16050

Purkis, S. J. (2019). Remote Sensing Coral Reefs. In *Encyclopedia of Ocean Sciences, Third Edition: Volume 1-5* (3rd ed., Vols. 1–5). Elsevier Inc. https://doi.org/10.1016/B978-0-12-409548-9.10813-9

Pushparaj, J., & Hegde, A. V. (2017). Estimation of bathymetry along the coast of Mangaluru using Landsat-8 imagery. *Journal of Ocean and Climate: Science, Technology and Impacts*, 8(2), 71–83. https://doi.org/10.1177/1759313116679672

Quang, N. H., Banno, M., & Ha, N-T. (2025). Satellite derived bathymetry using empirical and machine learning approaches: a case study in the highly dynamic coastal water. *Coastal Engineering Journal*, 67(2), 232–251. https://doi.org/10.1080/21664250.2024.2445418

Richardson, G., Knudby, A., Wu, Y., & Ansari, M. (2025). A case study comparing approaches to mask satellite-derived bathymetry. *Discover Geoscience*, 3, 103. https://doi.org/10.1007/s44288-025-00219-1

Safi'i, A. N., & Dewi, R. S. (2020). Uji Akurasi Metode Berbasis Citra Satelit untuk Ekstraksi Data Batimetri. *Teknik*, 41(2), 142–151. https://doi.org/10.14710/teknik.v0i0.29516

Sagawa, T., Yamashita, Y., Okumura, T., & Yamanokuchi, T. (2019). Shallow Water Bathymetry Derived by Machine Learning and Multitemporal Satellite Images. *International Geoscience and Remote Sensing Symposium (IGARSS)*, 8222–8225. https://doi.org/10.1109/IGARSS.2019.8899043

Sharr, M. B., Parrish, C. E., & Jung, J. (2024). International Journal of Applied Earth Observation and Geoinformation Automated classification of valid and invalid satellite derived bathymetry with random forest. *International Journal of Applied Earth Observation and Geoinformation*, 129, 103796. https://doi.org/10.1016/j.jag.2024.103796

Syaiful, S. N., Helmi, M., Widada, S., Widiaratih, R., Subardjo, P., & Suryoputro, A. A. D. (2019). Analisis Digital Citra Satelit Worldview-2 untuk Ekstraksi Kedalaman Perairan

Laut di Sebagian Perairan Pulau Parang, Kepulauan Karimunjawa, Provinsi Jawa Tengah. *Indonesian Journal of Oceanography*, 1(1), 36–43. https://doi.org/10.14710/ijoce.v1i1.6262

Van Hengel, W., & Spitzer, D. (1991). Multi-temporal water depth mapping by means of landsat TM. *International Journal of Remote Sensing*, 12(4), 703–712. https://doi.org/10.1080/01431169108929687

Wei, C., Zhao, Q., Lu, Y., & Fu, D. (2021). Assessment of Empirical Algorithms for Shallow Water Bathymetry Using Multi-Spectral Imagery of Pearl River Delta Coast, China. *Remote Sensing*, 13(16), 3123. https://doi.org/10.3390/rs13163123

Xie, C., Chen, P., Zhang, Z., & Pan, D. (2023). Satellite-derived bathymetry combined with Sentinel-2 and ICESat-2 datasets using machine learning. *Frontiers in Earth Science*, 11, 1111817. https://doi.org/10.3389/feart.2023.1111817

Ye, M., Yang, C., Zhang, X., Li, S., Peng, X., Li, Y., & Chen, T. (2024). Shallow Water Bathymetry Inversion Based on Machine Learning Using ICESat-2 and Sentinel-2 Data. *Remote Sensing*, 16(23), 4603. https://doi.org/10.3390/rs16234603

ISSN: 2579-5821 (Print)
ISSN: 2579-5546 (Online)
URL address: http://journal.unhas.ac.id/index.php/geocelebes
DOI: 10.70561/geocelebes.v10i1.49005

Jurnal Geocelebes Vol. 10 No. 1, April 2026, 69 – 81

Identification of Magma Intrusion Distribution in the Sekincau Mountain Area Based on the Euler Deconvolution Method of Gravity Data

Anisa Amanda*, Rizki Buana Agustian, Aksela Dian Fista, Ilham Dani

Geophysical Engineering, University of Lampung, Bandar Lampung, 35145, Indonesia.

*Corresponding author. Email: anisaamanda2803@gmail.com

Manuscript received: 17 December 2025; Received in revised form: 26 January 2026; Accepted: 27 March 2026

Abstract

Mount Sekincau, West Lampung, is located within the active Bukit Barisan tectonic zone and exhibits geothermal potential controlled by magmatic activity and geological structures. This study aims to identify the distribution and depth of magmatic intrusions using gravity data analysis and Euler deconvolution. GGMPlus satellite gravity data were processed to generate Complete Bouguer Anomaly, regional and residual anomalies, analytical signal, Euler solutions, and three-dimensional models. The Complete Bouguer Anomaly values range from 38.05 to 58.32 mGal, with high anomalies concentrated in the central part of the study area. Positive residual anomalies ranging from 0.88 to 2.78 mGal indicate the presence of shallow high-density bodies interpreted as magmatic intrusions. Analytical signal and Euler deconvolution results with a structural index of 0 reveal clusters of shallow sources associated with fault zones. Three-dimensional modeling confirms a southeastward-oriented intrusive body. These results indicate that shallow magmatic intrusions act as the primary heat source of the Sekincau geothermal system.

Keywords: Bouguer Anomaly; Euler Deconvolution; Geothermal; Gravity; Magma Intrusion.

Citation: Amanda, A., Agustian, R. B., Fista, A. D., & Dani, I. (2026). Identification of Magma Intrusion Distribution in the Sekincau Mountain Area Based on the Euler Deconvolution Method of Gravity Data. *Jurnal Geocelebes*, 10(1): 69–81, doi: 10.70561/geocelebes.v10i1.49005

Introduction

Mount Sekincau, located in West Lampung Regency, is situated within the active Bukit Barisan tectonic belt, which is characterized by volcanic activity, active faulting, and geothermal manifestations. The complex subsurface geological conditions in this area indicate the possible presence of shallow magmatic intrusions acting as the primary heat source of the geothermal system. However, the spatial distribution and depth of these intrusions remain poorly constrained. Therefore, this study aims to identify the distribution and depth of magmatic intrusions beneath Mount Sekincau using gravity data analysis. Specifically, this research focuses on separating the Complete Bouguer Anomaly (CBA) into regional and residual components and applying the Euler deconvolution method to estimate the geometry and depth of high-density anomaly sources interpreted as magmatic intrusions.

The gravity method is highly sensitive to lateral and vertical variations in subsurface rock density (Nurul et al., 2020). Conventional gravity surveys are commonly conducted using ground-based measurements, which provide high accuracy but are spatially limited and dependent on field accessibility. In contrast, Global Gravity Models (GGMs) integrate satellite gravimetry, terrestrial gravity data, and global topographic models, enabling uniform spatial coverage and consistent resolution over large areas. As a result, GGMs are particularly suitable for regional-scale geological studies and preliminary geothermal investigations.

With advancements in data acquisition and processing techniques, gravity surveys have been widely applied not only in hydrocarbon and mineral exploration (Dianwiyono & Wiradito, 2025; Raja et al., 2025; Alfuqara et al., 2025; Karaiskos et al., 2024), but also in delineating subsurface fault structures (Farrasha et al., 2023; Dani et al., 2024), mapping sedimentary cover (Zaenudin et al., 2020; Juwita et al., 2024; Ramadhani et al., 2025), reconstructing paleovolcanic facies (Nuzula et al., 2023), assessing geothermal systems (Sugianto et al., 2017), and identifying magmatic intrusions (Hosseini et al., 2025).

The interpretation of gravity data relies on gravity anomalies that reflect variations in subsurface rock density. The key parameter commonly used in gravity studies is the CBA, which represents the difference between observed and theoretical gravity values after applying latitude, free-air, Bouguer slab, and terrain corrections. The CBA is widely used to enhance subsurface density contrasts and to minimize non-geological effects in gravity data interpretation (Syukri, 2020). Bouguer gravity anomalies reflect the combined effects of both shallow and deep geological structures (Hasanah et al., 2016; Dung et al., 2025). To distinguish deep-seated regional structures from shallow local sources, gravity anomalies are commonly separated into regional and residual components (Supriyadi et al., 2019).

High gravity anomaly values indicate the presence of dense subsurface materials, such as magmatic intrusions or compact volcanic rocks, whereas low gravity anomalies represent low-density materials, including sedimentary deposits or hydrothermally altered zones (Liana et al., 2020; Zhanakulova et al., 2025).

Euler deconvolution is a semi-automatic interpretation method used to estimate the location and depth of subsurface anomaly sources based on potential field data. The integration of gravity anomaly modeling with Euler deconvolution enhances the interpretation of subsurface structures by enabling three-dimensional analysis through both deterministic and probabilistic approaches. (Castro et al., 2020; Cao et al., 2024; Nyakundi et al., 2025). Recently, modifications within methodologies such as improved Euler solution filtering through edge detection methods, the β-Vertical Derivative of Residual (β-VDR) approach, and Euler inversion have allowed a clearer understanding of complicated potential field information (Pham et al., 2024; Uieda, 2025). Despite these methodological advances, the application of gravity-based approaches combined with Euler deconvolution in the Sekincau Mountain area remains limited. Therefore, this study aims to separate regional and residual gravity anomalies and to analyze local anomaly patterns using Euler deconvolution to estimate subsurface geological structures.

Materials and Methods

The study area is in Sekincau District, West Lampung Regency, Lampung Province, Indonesia. Geographically, it extends from 5°02′50″ S to 5°10′25″ S and from 104°16′50″ E to 104°25′50″ E. The regional geology of the study area (Figure 1) is dominated by volcanic lithologies. The Hulusimpang Formation (Tomh) consists mainly of volcanic breccia, lava, and tuff. Overlying this unit is the Ranau Formation (Qtr), which is composed predominantly of pumice breccia and volcanic tuff. Additional volcanic units associated with the Barisan Zone include Quaternary volcanic rocks (Qv), characterized by andesite–basaltic lava, volcanic tuff, and volcanic breccia. The Young Quaternary Volcanic Rocks (Qhv) comprise breccia, lava, and volcanic tuff, while the Sekincau Young Quaternary Volcanic Rock Unit (Qvs) is primarily exposed along slope areas (Amin et al., 1994).

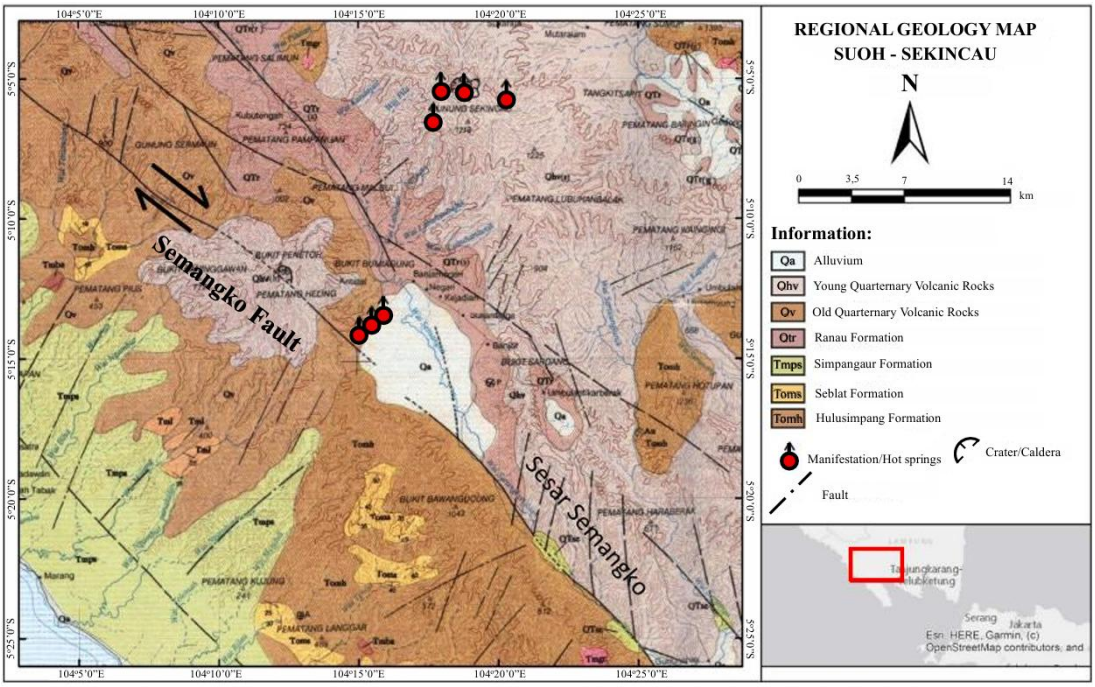

Figure 1. Geological Map of the Study Area (Iqbal & Juliarka, 2019).

The dataset used in this research is the 2013 Global Gravity Model Plus (GGMPlus) satellite gravity data with a high resolution of 7.2 arc seconds, or approximately 220 meters. The GGMPlus gravity model arose through a combination of EGM2008, gravity gradients from the European satellite mission Goce, and SRTM topography data, which allowed a short wavelength gravity signature to be detected, not accounted for in other standard satellite gravity models (Hirt et al., 2013). The SRTM topography data was used to provide a high level of topography detail to make possible accurate gravity modeling.

The first step in the processing is to compute the Bouguer anomaly using the GGMPlus gravity grid. As a prerequisite before computation, a thorough investigation is conducted on the data to remove any presence of outliers, missing data, or other numerical errors. The gravity anomaly is obtained by subtracting the theoretical gravity from the observed gravity. The observed gravity measurements are adjusted for tides and instrumental errors, and the theoretical gravity is calculated using the normal gravity model gṄ from the GRS80 ellipsoid model (Moritz, 1980). Proceeding further, corrections are applied with respect to Free Air (FAC), Bouguer (BC), and Topography (TERR). The methodology and equations employed in this study follow those outlined in Handyarso & Mauluda (2018), specifically Equations (1) through (6).

$$g_{\text{anomaly}} = g_{\text{observed}} - g_{\text{theoretical}} \quad (1)$$

$$g_{\text{observed}} = g_{read} + \text{tide} - \text{drift} \quad (2)$$

$$g_{\text{theoretical}} = g_n - \text{FAC} + \text{BC} - \text{TERR} \quad (3)$$

$$g_n = g_e \frac{1 + 0.00193185138639 \sin^2 \varphi}{\sqrt{1 - 0.00669437999013 \sin^2 \varphi}} \quad (4)$$

$$\text{FAC} = h \times \left(0.308 \frac{\text{mGal}}{\text{m}}\right) \quad (5)$$

$$\text{BC} = 2\pi \times \rho \times G \times h = 0.0419 \times \rho \times h \quad (6)$$

Description:

g_n : normal gravity value based on the World Geodetic System 1984 (mGal)

g_e : gravity at the equator (978032.67714 mGal)

g_{obs} : observed gravity value (mGal)

g_{read} : measured gravity value (mGal)
φ : latitude of measurement point (rad)
FAC : free air correction (mGal)
h : height of measurement point above mean sea level (m)
BC : bouguer correction (mGal)
TERR : field correction (mGal)
ρ : bouguer plate density (g/cm^3)
G : gravitational constant (Nm^2/kg^2)

Having obtained the Bouguer anomaly, we can separate it into a regional part and a residual part. For this separation, a moving average technique is used since it can emphasize regional characteristics with a high wavelength and suppress local variations with a short wavelength associated with shallow geology. To achieve this, a regional gravity anomaly is computed by averaging a series of consecutive gravity anomaly data points, and a residual is obtained by subtracting a regional anomaly from a Bouguer anomaly. A one-dimensional moving average can be performed using the following formula (Ramadhan & Pohan, 2024):

$$\Delta T_{reg}(i,j) = \left(\frac{1}{N}\right).\ (\Delta T(i-n, j-n) + \cdots + \Delta T(i,j) + \cdots + \Delta T(i+n, j+n) \quad (7)$$

Here, $n = (N-1)/2$, where Nmust be an odd number. ΔT_{reg}represents the magnitude of the regional anomaly, while ΔTdenotes the complete Bouguer anomaly.

Once the regional anomaly has been determined, the residual anomaly can be calculated using the following equation:

$$\Delta T_{res} = \Delta T - \Delta T_{reg} \quad (8)$$

Here, ΔT_{res} represents the magnitude of the residual anomalies. These residual anomalies are particularly useful for interpreting shallow structures, as they are more sensitive to near-surface density variations, including faults, lithological boundaries, and magmatic intrusions.

The final step in processing involves interrogating the subsurface using Euler deconvolution, which is very effective in sharpening geopotential depth anomaly features. The Second Vertical Derivative (SVD) is utilized in outlining fault regions, with Euler deconvolution used to estimate the depth of sources of both gravitational and magnetic anomalies. The Euler Equation used in this research work is presented below (Handyarso & Mauluda, 2018):

$$(x-x_0)\frac{\partial G}{\partial x} + (y-y_0)\frac{\partial G}{\partial y} + (z-z_0)\frac{\partial G}{\partial z} = N(B-G) \quad (9)$$

Here, x_0, y_0, z_0 denotes the position of the anomaly source being investigated, $N$is the structural index (SI) that characterizes the source geometry, and B represents the background field. The SI values follow the classification proposed by Reid (2014) as shown in Table 1. In this study, an SI value of 0 is applied to identify magmatic intrusions.

Table 1. Structural index values for different types of gravity anomaly sources (Reid, 2014).

N	Source Type
0	Sill / Dyke / Step
0.5	Sheet
1	Pipe
2	Sphere

Results and Discussion

The gravity data were processed from the Free-Air Anomaly to generate a CBA map, which is shown in Figure 2. The Bouguer anomaly map of the study area, derived from the GGMPlus gravity model, has values ranging from 38.05 to 58.32 mGal. Higher anomaly values, represented by red to purple, are also shown to be concentrated mostly within the central part. The zone showing the highest values is approximately located between 420,000-424,000 mE and 9,438,000-9,442,000 mN, with a shape of a circular contour pattern.

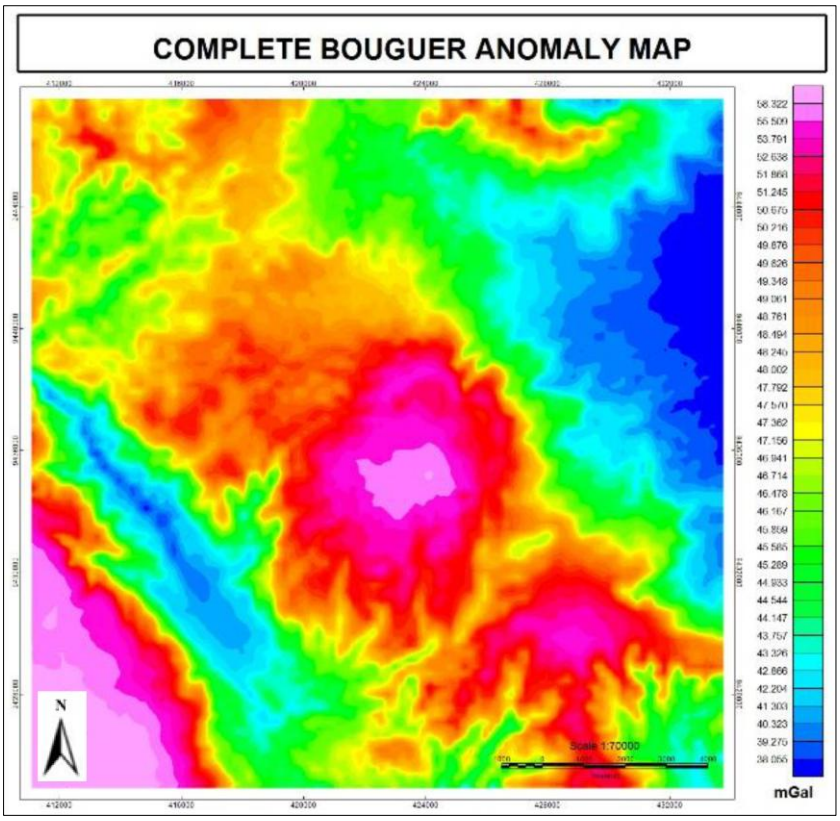

Figure 2. CBA map.

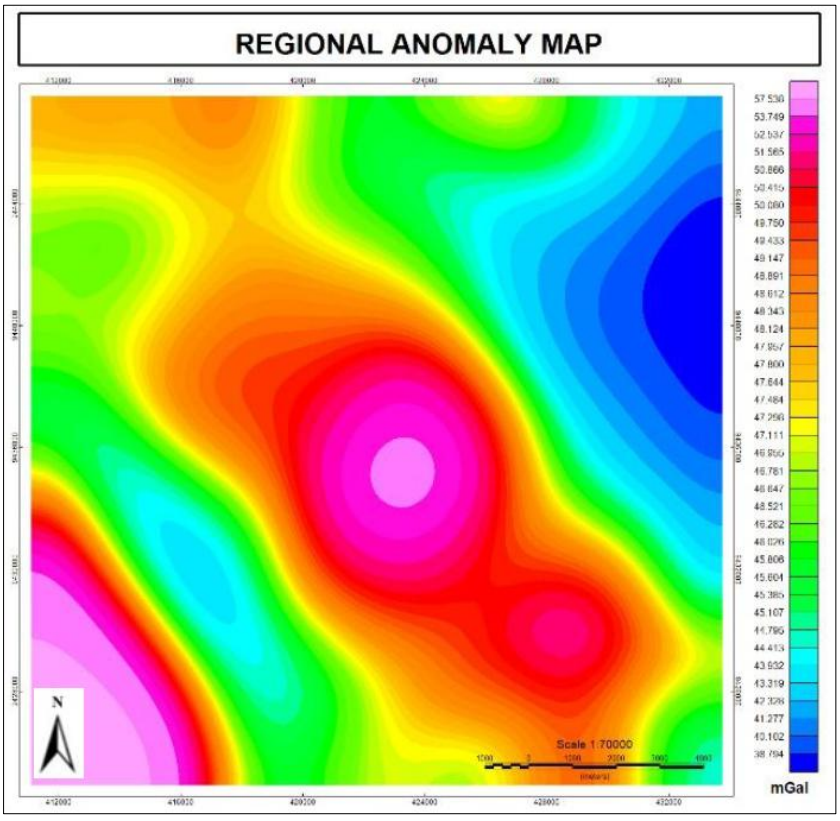

Figure 3. Regional anomaly map.

Following the creation of the CBA map, the following step is the separation of regional and residual anomalies through the moving average technique. The regional gravity

anomalies corresponding to the study area are shown in Figure 3, and these vary from 38.79 mGal to 57.53 mGal. The regional gravity anomaly maps have a NW-SE trend, which corresponds with the main geological feature of Bukit Barisan Mountains. On the other hand, in the central part of the study area, higher gravity anomaly values are also highlighted with a rather symmetrical pattern.

After identifying these regional components, the residual anomalies obtained will allow a better definition of the geological structures near the surface or rock bodies. Residual Anomaly Map of the study area is shown in Figure 4. The high positive residual in the central to southern part of the study area indicates the presence of high-density rocks in this area. Moreover, because the magnitude of these residuals is in the order of ±2 mGal, this implies that these sources are shallow.

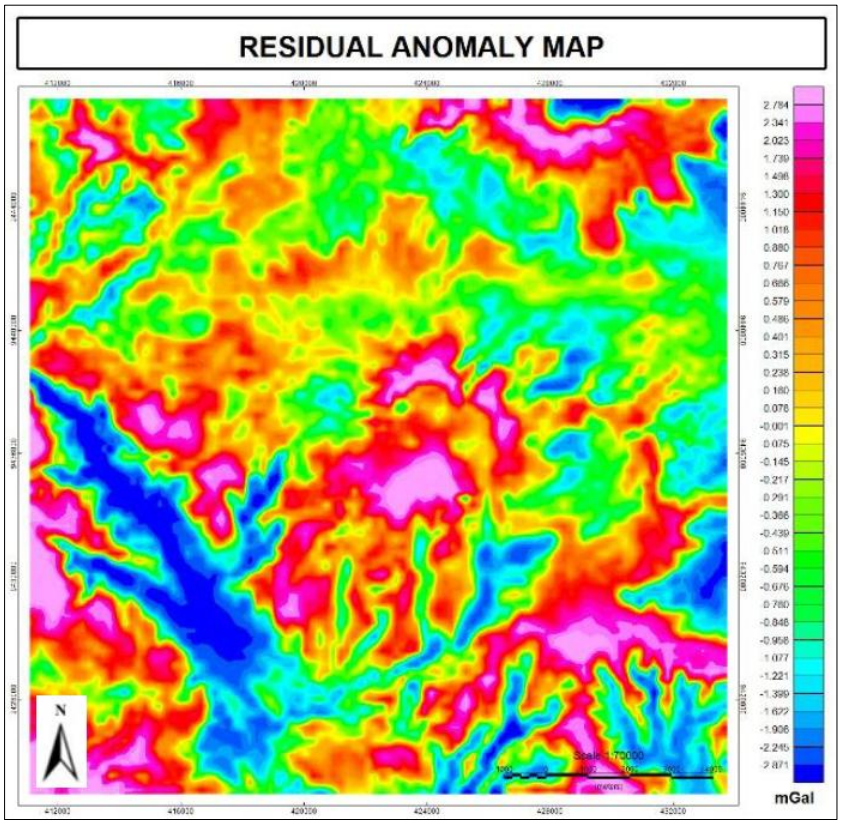

Figure 4. Residual anomaly map.

The analytical signal map of the study area is presented in Figure 5. The regions with high analytical signals are marked in red to pink colors, which indicate high analytical signals, and blue and green regions show lower analytical signals.

The Euler gravity anomaly map in Figure 6 below was used to infer the pattern of sources of these gravity anomalies, and in the intrusions of magmatic origin beneath Mount Sekincau. The Euler solution points in the map represent the regions where these sources are concentrated, especially where a large contrast in gravity anomalies is noted.

Figure 7 shows a 3D Euler deconvolution solution with a focus on a concentrated anomaly source evident around the middle of the model. The yellow/pink regions in this image represent regions of higher density, which can be attributed to magmatic intrusions.

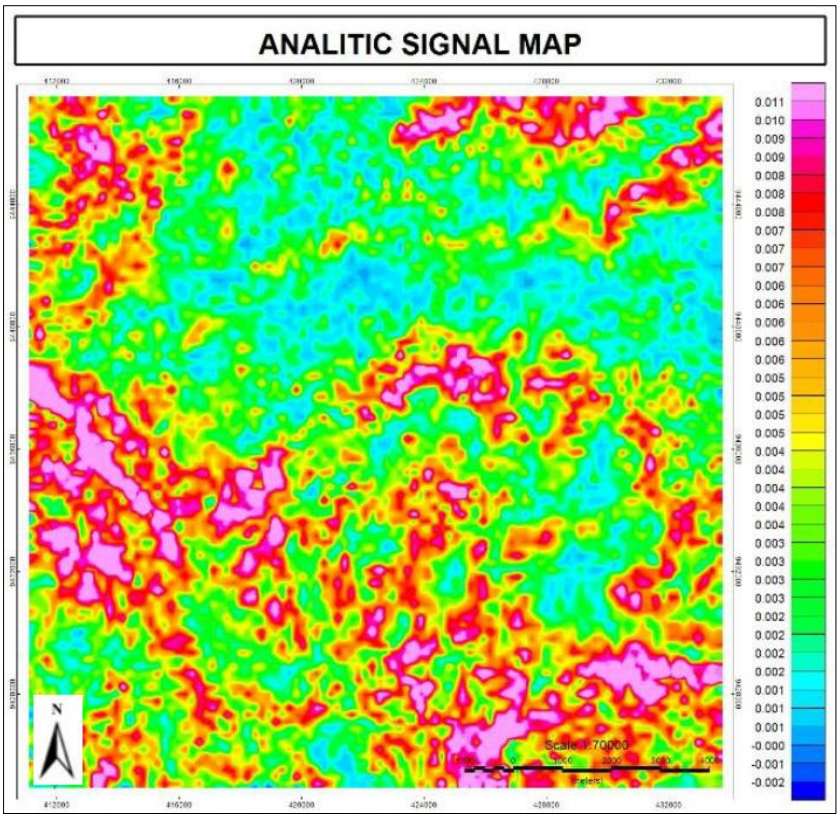

Figure 5. Analytic signal map.

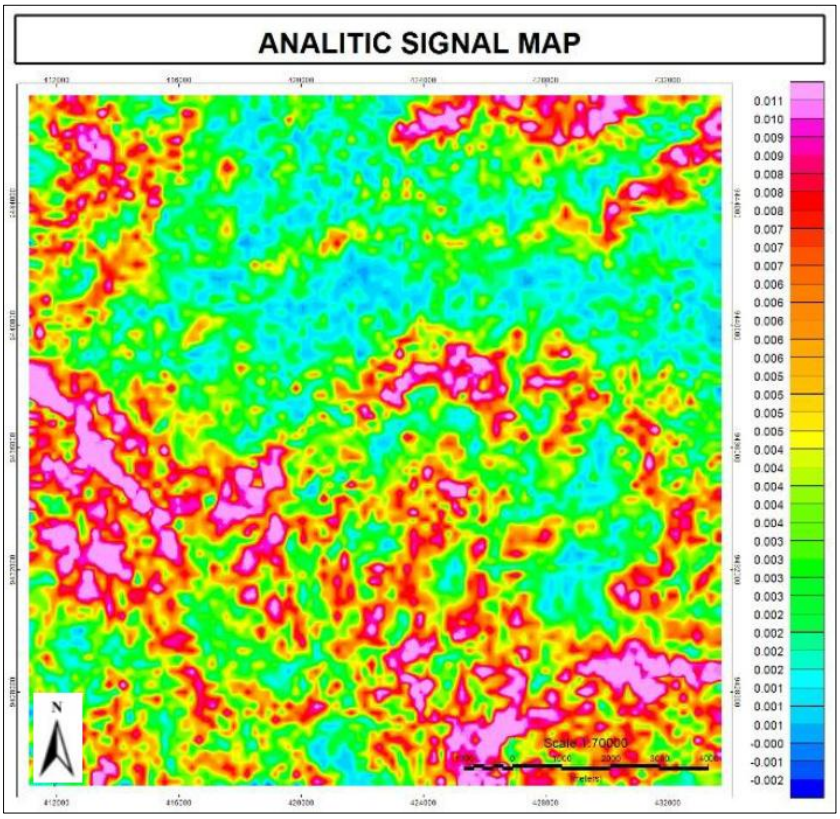

Figure 6. Euler solution map.

The gravity information obtained in the study area was processed to provide different output maps, which include a CBA Map presented in Figure 2, a regional

anomaly map presented in Figure 3, and a residual anomaly map presented in Figure 4. A series of filtered maps obtained above were used to derive additional maps, which include an analytical signal map presented in Figure 5, a localized Euler solution map presented in Figure 6, and a 3D model of intrusion distribution presented in Figure 7. The CBA Map shows gravity anomaly measurements varying from 38.05 mGal to 58.32 mGal, with higher concentrations being recorded in central-eastern portions, which suggest dense subsurface masses.

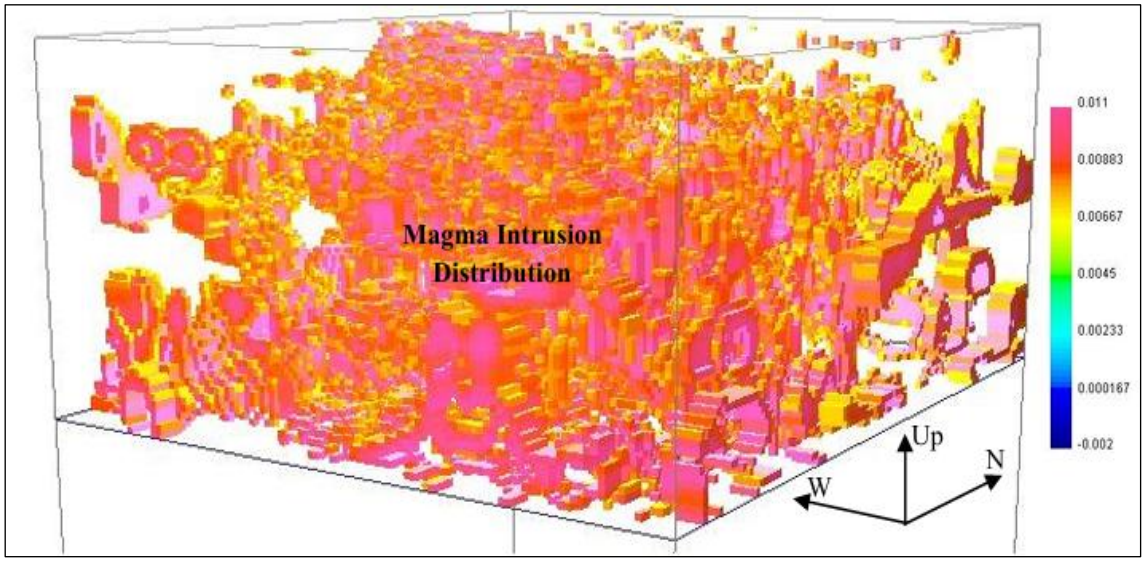

Figure 7. 3D modeling of magma intrusion distribution.

The regional anomaly map (Figure 3) and residual anomaly map (Figure 4) were derived by delineating the regional Bouguer gravity anomalies using a moving average technique. The regional anomalies are measured between 38.794 mGal and 44.413 mGal, which corresponds to deep geologic structures. However, the residual anomalies lie in the range of -2.871 mGal to 2.784 mGal, which correspond to shallow geologic structures. The positive residual gravity anomalies measured in the range of 0.880 mGal to 2.784 mGal exist in the central part of the map, which correspond to high-density masses such as intrusions in the form of shallow intrusions and magma-filled fractures. Negative gravity anomalies measured in the range of -2.871 mGal to -1.077 mGal exist in the outer part of the map, which correspond to less dense geologic materials such as altered rocks and sediment deposits. A combination of both maps shows an indication of a single major intrusion.

The Analytical Signal Map (Figure 5) marks the limits of subsurface density with the magnitude of total Bouguer gravity anomaly gradient. High-amplitude regions with a magnitude of 0.007-0.011 mGal/m, colored red to purple, delineate regions of steep density with high amplitude faulting, lithological contacts, or compacted rocks, which exist in a concentrated manner in the southern and north-central part of this study area. Conversely, low-amplitude regions of -0.002–0.003 mGal/m, colored blue to green, represent regions of gentle or more deeply sourced total density with circular regions in the central part representing basin dilation and more uniform rock masses.

The Euler deconvolutions (Figure 6) performed under a SI index set at 0, suitable for the delineation of dike targets with a depth of 100 km (Table 1) were used to depth-analyze and search for sources of gravity anomalies and possible regions of magma intrusions under Mount Sekincau.

Points of Euler concentration were noted in regions with high contrast, with blue-green shallower concentrations established in a manner surrounding but closely arrayed with peak gravity anomaly intensity, in contrast with red-yellow concentrations noted in regions west and southwest relative to principal gravity anomaly with less intensity found in lower residual gravity anomaly.

Such points were interpretable in describing a shallower dilational presence in the center relative to a dilational influence of lighter rock or rock mantle in regions on the boundary with associated dilational effects in line with observations established by Daud et al. (2019) in a delineational study relative to Blawan Ijen and a respective dilational influence in an equally parallel nature in a study by Ramadhan et al. (2017) in a delineational work relative to B24 Geothermal Field.

A separate illustration of a 3D model further clarified this influence with a magnitude indicating a peak presence of dense cubic elements in a concentrated manner in a fixed centering of this study area sustaining thence in a southeasterly angle assertive in depth disjuncture diminishing linear in a clearly observed volcanic dilation in this geothermal field sustaining a core presence in a geologically assertive manner reproductive in a fixed sustained nature in a manner theoretically evident in a first-rate nature upscale in a core sustaining nature delineative in a geologically assertive depth disjuncture in this geothermal field with a sustaining theoretical nature upscale in a volcanic dilation in this geothermal field theoretically assertive in this geologically sustained volcanic dilation core assertive in a geologically sustained.

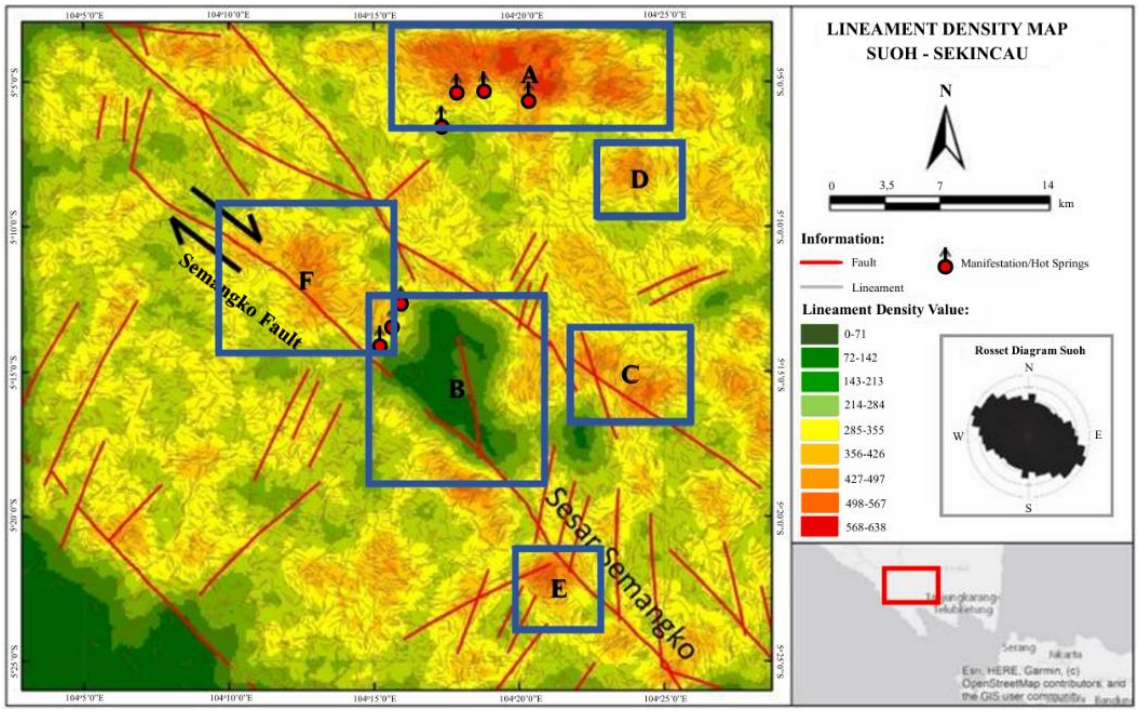

Figure 8. Lineament Density Map of the Suoh-Sekincau Geothermal Field (Iqbal & Juliarka, 2019).

The lineament density map (Figure 8) shows that Area A records the highest lineament density, which represents a region with more intensive fracturing and higher permeability channels than other regions in the study area. This can be linked to the geology of Mount Sekincau, which is primarily composed of volcanic rocks from Quaternary eruptions and is influenced by normal faults related to caldera formation,

making Mount Sekincau record a higher number of surface fractures which are evident in the form of lineaments, respectively, based on Zaenudin et al. (2021). The gravity fault line density maps show a high degree of relationship with gravity analysis studies. In this case, in Area A, where the high-density region of fault lines is recorded, it is evident that both Bouguer and Residual Anomalies are high, which show a dense body in the subsurface part interpreted to represent a shallow magmatic intrusion. Additionally, it is evident in this study that a cluster of Euler solutions in regions with high-density fault lines shows evidence of shallow bodies controlling geologic anomaly sources related to fractures in this case. Based on this information, analysis is supported by a 3D solid model, which shows an intrusive mass with a SE orientation below the region of high lineament density. Therefore, based on this information, intersection analysis related to lineament densities and gravity information shows that magmatic intrusions influence the central regions, which record a main source of geothermal energy in this case, with fractures related to normal faulting acting as critical fluid pathways in this case related to Sekincau geology.

The Euler deconvolution technique provides a quick way to estimate the positions of anomaly sources but contains some limitations because it is a noise-sensitive technique with a strongly model-dependent parameter, such as the structural index. Based on a combination of Bouguer and residual anomaly maps, field derivative maps, analytical signals, Euler solutions, and 3D modeling, a high-density mass is delineated within the central-eastern part of the area of investigation, which can be interpreted to be a magmatic intrusion, and a lower-density mass in the southwestern part. Findings are in line with expectations from regional geology and suggest a magmatic intrusion which acts as a main producer of thermal energy in Sekincau geothermal resources. For future studies, a more thorough 3D modeling technique, including geoelectric or MT, and a multi-structural index Euler analysis technique are recommended to avoid misinterpretations.

Conclusion

Gravity data analysis shows that the central area of Sekincau is characterized by a high anomaly influenced by dense subsurface bodies, interpreted as shallow intrusions. The analysis of residual anomaly maps, analytical signals, and Euler solutions each verifies the identification of this intrusive body, marked by high anomaly values and Euler solution points. In addition, a 3D model verifies this identification with a concentrated dense body in this particular area, with lower anomaly values in the Western and Southern regions, which represent less dense bodies. Based on these findings, it can be further interpreted that this central intrusive body acts as a major source of heat for this geothermal system in Sekincau. As recommendations for future studies, it is advised to integrate other geophysical analysis tools in order to improve and finalize these findings.

Acknowledgements

The authors would like to thank in earnest the Department of Geophysical Engineering, Faculty of Engineering, University of Lampung, which has provided the facilities and guidance necessary for this research to be accomplished. Moreover, they would also like to thank all supervising lecturers and friends in this research for their assistance in processing and interpreting all the data involved without which this research would not have been possible.

Author Contribution

Anisa Amanda conducted the study design and planning, as well as the main analysis. Rizki Buana Agustian assisted with the data

processing and curation. Aksela Dian Fista assisted with developing methodology, handling computer operations, interpreting results, and preparing graphics. Ilham Dani assisted with validating analysis output, providing supervision, carrying out critical reviews, and improving manuscript format. Everyone assisted in manuscript revision and approved the final form of this article.

Conflict of Interest

The author declares no conflict of interest.

References

Alfuqara, D. A., Al-E'bayat, M. S., Alsaaideh, A. S., & Al Dwairi, R. A. (2025). Sustainable exploration of critical minerals: Integrated magnetotelluric and gravity surveys for lithium pegmatite targeting. *International Journal of Environmental Sciences,* 11(24S), 1700–1713. https://theaspd.com/index.php/ijes/article/view/10353

Amin, T. C., Sidarto, S., Santosa, S., & Gunawan, W. (1994). *Geology of the Kotaagung quadrangle, Sumatera (1:250,000).* Geological Research and Development Centre.

Castro, F. R., Oliveira, S. P., de Souza, J., & Ferreira, F. J. F. (2020). Constraining Euler deconvolution solutions through combined tilt derivative filters. *Pure and Applied Geophysics,* 177(10), 4883–4895. https://doi.org/10.1007/s00024-020-02533-w

Cao, S., Deng, Y., Yang, B., Lu, G-Y., Zhu, Z., Chen, P., Xie, J., & Chen, X. (2024). 3-D probability density imaging of Euler solutions using gravity data: A case study of Mount Milligan, Canada. *Acta Geophysica,* 72(5), 3371–3391. https://doi.org/10.1007/s11600-023-01279-y

Dani, I., Zaenudin, A., Hutomo, A. I., & Yuniza, N. (2024). Analysis of Subsurface Structure of Bandar Lampung City Based on Gravity Anomalies. *Geodynamics & Tectonophysics*, 15(4), 0772. https://doi.org/10.5800/gt-2024-15-4-0772

Daud, Y., Sulistyo, A., Fahmi, F., Nuqramadha, W. A., Fitrianita, F., Sesesega, R. S., Rosid, S., Pati, G. P., Maulana, M. R., Khoiroh, M., Rahman, K. R., & Subroto, W. (2019). First horizontal derivative and Euler deconvolution in application for reconstructing structural signature over the Blawan-Ijen geothermal area. *IOP Conference Series: Earth and Environmental Science,* 254(1), 012008. https://doi.org/10.1088/1755-1315/254/1/012008

Dianwiyono, Y., & Wiradityo, D. P. (2025). Optimization of geophysical design survey priority areas for unconventional oil and gas exploration using TOPEX gravity data analysis. *Jurnal Pendidikan Indonesia,* 6(10), 4617–4633. https://doi.org/10.59141/japendi.v6i10.8697

Dung, N. K., Ebong, E. D., Gomez-Ortiz, D., Abdulrazzaq, Z. T., Al-Saady, H. A., Dung, T. T., Kha, T. V., Dai, N. B., & Duong, T. T. (2025). Novel regional–residual anomaly separation technique for evaluating Moho configuration and crustal density structure beneath the East Vietnam Sea (South China Sea). *Journal of Asian Earth Sciences: X,* 14, 100210. https://doi.org/10.1016/j.jaesx.2025.100210

Farrasha, M., Yeri, N. A., Dani, I., & Rasimeng, S. (2023). Aplikasi metode turunan kedua vertikal data gravitasi untuk interpretasi Sesar Cugenang, Jawa Barat. *Jurnal Teknik Geologi: Ilmu Pengetahuan dan Teknologi,* 6(2), 22–30. http://dx.doi.org/10.30872/jtgeo.v6i2.13534

Handyarso, A., & Mauluda, A. D. (2018). Penerapan metode dekonvolusi Euler untuk estimasi kedalaman sumber anomali. *Geomatika,* 24(1), 21–30. https://doi.org/10.24895/JIG.2018.24-1.726

Hasanah, L., Aminudin, A., Ardi, N. D., Utomo, A. S., Yuwono, H., Kamtono, K., Wardhana, D. D., Gaol, K. L., & Iryanti, M. (2016). Graben structure identification using gravity method. *IOP Conference Series: Earth and Environmental Science,* 29, 012013. https://doi.org/10.1088/1755-1315/29/1/012013

Hirt, C., Claessens, S. J., Fecher, T., Kuhn, M., Pail, R., & Rexer, M. (2013). New ultrahigh-resolution picture of Earth's gravity field. *Geophysical Research Letters,* 40(16), 4279–4283. https://doi.org/10.1002/grl.50838

Hosseini, S. H., Afshar, A., Abedi, M., Ganbarifar, S., Oskooi, B., & Moradi, S. (2025). Fixed window joint Euler deconvolution for depth estimation of magnetic and gravity data in the Shavaz region. *Scientific Reports,* 15(1), 42054. https://doi.org/10.1038/s41598-025-26220-9

Iqbal, M., & Juliarka, B. R. (2019). Analisis kerapatan kelurusan sebagai indikator tingkat permeabilitas di Lapangan Panasbumi Suoh-Sekincau, Lampung. *Journal of Science and Applicative Technology,* 3(2), 61–67 https://doi.org/10.35472/jsat.v3i2.212

Juwita, W., Juventa, J., Setiawan, A. M., Martha, A. A., Hudayat, N., & Sutejo, B. (2024). Identification of potential hydrocarbon traps using the gravity method in the Bengkulu Basin. *Iranian Journal of Geophysics,* 18(3), 69–83. https://doi.org/10.30499/IJG.2023.409882.1535

Karaiskos, D., Apostolopoulos, G., & Orfanos, C. (2024). Gravity survey for mineral exploration in Gerolekas bauxite mining site, Greece. *Mining, 5*(1), 3. https://doi.org/10.3390/mining5010003

Liana, Y. R., Wea, T. M. M., Syarifah, W., Supriyadi, S., & Khumaedi, K. (2020). Analisis anomali Bouguer data gaya berat: Studi kasus di Kota Lama Semarang. *JRST (Jurnal Riset Sains dan Teknologi),* 4(2), 63–68. https://doi.org/10.30595/jrst.v4i2.6301

Moritz, H. (1980). Geodetic reference system 1980. *Bulletin Géodésique,* 54(3), 395–405. https://doi.org/10.1007/BF02521480

Nurul, M., Rasimeng, S., Yogi, I. B. S., Yulianata, A., & Yuliantina, A. (2020). Forward modelling metode gaya berat dengan model intrusi dan patahan menggunakan Octave. *Jurnal Geocelebes,* 4(2), 111–117. https://doi.org/10.20956/geocelebes.v4i2.10112

Nuzula, J. F., & Setiahadiwibowo, A. P. (2023). Penentuan fasies sentral gunung api purba menggunakan metode gravitasi pada kawasan Gunung Ijo, Pegunungan Kulonprogo. *Jurnal Pendidikan, Sains, Geologi, Dan Geofisika (GeoScienceEd Journal),* 4(2), 32–38. https://doi.org/10.29303/goescienceed.v4i2.233

Nyakundi, D. N., Nyakundi, E. R., & Namaswa, S. (2025). Euler deconvolution of gravity data for structural mapping and heat source targeting in the Silali geothermal field, Kenya. *Journal of Geosciences and Geomatics,* 13(2), 43–51. https://doi.org/ 10.12691/jgg-13-2-2

Pham, L. T., Oliveira, S. P., Le-Huy, M., Nguyen, D. V., Nguyen-Dang, T. Q., Do, T. D., Tran, K. V., Nguyen, H-D. T., Ngo, T-N. T., & Pham, H. Q. (2024). Reliable Euler deconvolution solutions of gravity data through the β-VDR and THGED methods. *Vietnam Journal of Earth Sciences,* 46(3), 432–

448. https://doi.org/10.15625/2615-9783/21009

Raja, A., Tanesib, J., Lapono, L. A. S., & Lewerissa, R. (2025). Integrating high-resolution gravity gradients and 3D inversion modeling to delineate mineral resources in the Lewa District, East Sumba, Indonesia. *Indonesian Physical Review,* 8(3), 712–733. https://doi.org/10.29303/ipr.v8i3.501

Ramadhan, B. T., Setyawan, A., Sasongko, D. P., Raharjo, I. B., & Sastranegara, R. M. T. (2017). Pemodelan inversi gaya berat dengan panduan Euler deconvolution untuk struktur bawah permukaan di Lapangan Panas Bumi B24. *Youngster Physics Journal,* 6(2), 131–138. https://ejournal3.undip.ac.id/index.php/bfd/article/view/17116

Ramadhan, I., & Pohan, A. F. (2024). Pemisahan anomali regional dan residual metode gravitasi menggunakan moving average, upward continuation, dan polynomial. *Jurnal Fisika Unand,* 13(1), 1–7. https://jfu.fmipa.unand.ac.id/index.php/jfu/article/view/1122

Ramadhani, A., Aprina, P. U., Purba, H., Rofiq, M., Wiranatanagara, M. B., Maulin, H. B., & Prananda, A. (2025). Crustal structure modeling using regional gravity in the Tarakan Sub-Basin. In *IOP Conference Series: Earth and Environmental Science*, 1547(1), 012010. https://doi.org/10.1088/1755-1315/1547/1/012010

Reid, A. B., Allsop, J. M., Granser, H., Millett, A. J., & Somerton, I. W. (1990). Magnetic interpretation in three dimensions using Euler deconvolution. *Geophysics,* 55(1), 80–91. https://doi.org/10.1190/1.1442774

Sugianto, A., Takodama, I., & Rahadinata, T. (2017). Identifikasi struktur sistem panas bumi Pantar berdasarkan analisis gradien horizontal dan pemodelan 3D data gaya berat. *Buletin Sumber Daya Geologi,* 12(2), 135–143. https://doi.org/10.47599/bsdg.v12i2.33

Supriyadi, S., Khumaedi, K., Sugiyanto, S., & Setiaswan, F. (2019). Pemisahan anomali regional dan residual data gaya berat: Studi kasus Kota Lama Semarang. *Physics Education Research Journal,* 1(1), 29. https://doi.org/10.21580/perj.2019.1.1.3927

Syukri, M. (2020). *Pengantar Geofisika* (Edisi pertama). Syiah Kuala University Press.

Uieda, L., Souza-Junior, G. F., Uppal, I., & Oliveira Jr, V. C. (2025). Euler inversion: Locating sources of potential-field data through inversion of Euler's homogeneity equation. *Geophysical Journal International,* 241(3), 1536–1552. https://doi.org/10.1093/gji/ggaf114

Zaenudin, A., Dani, I., & Amalia, N. (2020). Delineasi Sub-Cekungan Sorong berdasarkan anomali gaya berat. *Jurnal Geocelebes,* 4(1), 14–22. https://doi.org/10.20956/geocelebes.v4i1.7976

Zaenudin, A., Karyanto, K., Kurniasih, A., & Wibowo, R. C. (2021). Analisis struktur patahan daerah Suoh menggunakan metode gaya berat dan penentuan kerapatan patahan. *Positron,* 11(2), 95–103. https://doi.org/10.26418/positron.v11i2.48461

Zhanakulova, K., Adebiyet, B., Orynbassarova, E., Yerzhankyzy, A., Kassymkanova, K-K., Abdykalykova, R., & Zakariya, M. (2025). Application of machine learning methods for gravity anomaly prediction. *Geosciences,* 15(5), 175. https://doi.org/10.3390/geosciences15050175

ISSN: 2579-5821 (Print)
ISSN: 2579-5546 (Online)
URL address: http://journal.unhas.ac.id/index.php/geocelebes
DOI: 10.70561/geocelebes.v10i1.49626

Jurnal Geocelebes Vol. 10 No. 1, April 2026, 82 – 95

Surface Ocean Current Variability Near Selayar Island During the Three El Niño-Southern Oscillation (ENSO) Phases

Andika*, Gladiva Warouw

Geophysics Department, Hasanuddin University, Makassar 90245, Indonesia.

*Corresponding author. Email: andika@unhas.ac.id

Manuscript received: 27 January 2026; Received in revised form: 25 March 2026; Accepted: 1 April 2026

Abstract

This study investigates the seasonal and interannual variability of surface ocean currents around Selayar Island, Indonesia, with a focus on differences among the three phases of the El Niño–Southern Oscillation (ENSO). Monthly surface current data from 1993 to 2020 were analyzed using climatological, composite, and anomaly approaches. The results reveal a spatially heterogeneous current structure that is dominated by seasonal variability, with domain-averaged current magnitudes ranging from approximately 0.085–0.305 ms^{-1}. Interannual variability related to ENSO is evident mainly in the magnitude of surface current anomalies, which range approximately 0.03–0.05 ms^{-1} during El Niño and increase to about 0.07–0.09 ms^{-1} during La Niña, with peak values reaching ~0.10–0.12 ms^{-1}. This indicates that ENSO primarily modulates current intensity rather than flow direction. Differences in anomaly direction are more pronounced under Neutral conditions, where anomaly patterns differ from those observed during both El Niño and La Niña phases. Overall, the results indicate that ENSO acts as an interannual modulation of surface currents, while monsoonal forcing remains the primary control on surface current dynamics in the study region.

Keywords: Anomaly; ENSO; Selayar; Surface Current; Variability,

Citation: Andika, A., & Warouw, G. (2026). Surface Ocean Current Variability Near Selayar Island During the Three El Niño-Southern Oscillation (ENSO) Phases. *Jurnal Geocelebes*, 10(1): 82–95, doi: 10.70561/geocelebes.v10i1.49626

Introduction

Sea surface currents are a key component of ocean dynamics, governing the redistribution of temperature (Gao et al., 2022; Elzahaby et al., 2021; Vijith et al., 2020), salinity (Laurindo et al., 2024; Ralston et al., 2024; Nie et al., 2023), sediments (Fu et al., 2024; Devis-Morales et al., 2021), plankton (Manral et al., 2023; Hu et al., 2021), nutrients (Li et al., 2022; Lu et al., 2020), and pollutants (Bhattacharya et al., 2026; Lefebvre et al., 2023) on daily to interannual timescales, while simultaneously defining major transport pathways for a wide range of oceanographic processes and human activities at sea. Owing to this cross-sectoral role, accurate knowledge of surface currents is increasingly recognized as a fundamental scientific and operational prerequisite for understanding ocean variability and for supporting safe and efficient maritime activities (Röhrs et al., 2021; Isern-Fontanet et al., 2017). In operational contexts, surface currents constitute a core input for drift predictions, including the tracking of drifting persons or objects (Trinanes et al., 2016), oil spill trajectory assessments (Bhattacharya et al., 2026; Keramea et al., 2021), modeling of marine debris and waste dispersion (Purba et al., 2024; Chassignet et al., 2021), and ship routing and navigation planning (Mannarini et al., 2024). In such applications, even small errors in surface current estimates can rapidly amplify into large trajectory deviations over timescales of hours to days (Röhrs et al., 2021).

The urgency of surface current research has increased in parallel with the growing demand for real-time ocean services and the rising exposure to risk in coastal and archipelagic regions. Studies in operational oceanography demonstrate that reliable surface current predictions contribute directly to the efficiency of search and rescue operations (Wang et al., 2025; Tamtare et al., 2022; Córdova & Flores, 2022; Mateus et al., 2020), the mitigation of maritime accidents (Zhu et al., 2023), and the reduction of pollution impacts (Bosi et al., 2021; Keramea et al., 2021), particularly when surface currents interact with winds and waves within the upper ocean layer (Röhrs et al., 2021).

The need for regional-scale studies is particularly pronounced in the Indonesian Archipelago, where monsoonal circulation, equatorial wave dynamics, and complex shallow deep ocean topography strongly interact (Yoneyama & Zhang, 2020; Xue et al., 2020). One of the most critical elements of this system is the Indonesian Throughflow (ITF), a large-scale transport of water masses from the Pacific to the Indian Ocean through the Indonesian seas, which plays a key role in inter-basin heat and freshwater exchange and exerts a significant influence on Indo-Pacific oceanography and climate (Feng et al., 2018). The ITF exhibits variability across seasonal to interannual timescales and is modulated by changes in monsoonal winds as well as large-scale climate modes such as the El Niño–Southern Oscillation (ENSO) and the Indian Ocean Dipole (IOD) (Zhu & Wang, 2024; Santoso et al., 2022; Feng et al., 2018). Along the primary ITF inflow pathway in the Makassar Strait, long-term observational records reveal pronounced intraseasonal, seasonal (monsoonal), and interannual fluctuations; at interannual timescales, the southward transport tends to weaken during El Niño events and strengthen during La Niña conditions (Gordon et al., 2019). This ITF–ENSO/IOD linkage underscores the potential for ENSO phase transitions to modify surface current dynamics in ITF corridors and branching regions, including the waters surrounding Selayar Island.

From an oceanographic perspective, the Selayar Slope in the southern Makassar Strait represents a confluence region where the ITF from the Makassar Strait meets the seasonally varying current system between the Java Sea and the Flores Sea, with additional influences from other regional dynamics. This setting gives rise to distinctive stratification structures and water mass characteristics (Prihatiningsih et al., 2021). Modeling evidence further indicates substantial water mass exchange within the triangle formed by the Java Sea, Makassar Strait, and Flores Sea, underscoring the strong monsoonal control and interbasin connectivity that shape regional circulation patterns (Apriansyah et al., 2024). At a more local scale, studies around the Selayar Islands have documented surface current patterns that vary in response to the monsoonal cycle and transitional seasons (Bayhaqi et al., 2017). Consequently, the waters surrounding Selayar are simultaneously influenced by monsoonal variability, ITF dynamics, and interannual climate variability, rendering surface current characteristics particularly sensitive to changes in regional ocean and atmosphere conditions.

Beyond its scientific relevance, Selayar Island and the surrounding waters are also of considerable importance for maritime safety. Ferry routes and maritime activities in this region have experienced several major accidents, including the sinking and grounding of the KMP/KM *Lestari Maju* in Selayar waters on 3 July 2018, which was widely reported by the media and authorities (Mappong, 2018), the sinking of two fishing vessels in February 2023 (Wardiyah, 2024), and the sinking of the cargo vessel KLM *Tahta Mandiri* on 10 August 2024 (Said, 2024). In this sense,

surface current research in the Selayar region carries an additional level of urgency, as it not only advances the understanding of physical oceanographic processes but also strengthens the information base for maritime safety services.

Nevertheless, existing studies in the Selayar region and its surroundings have predominantly focused on seasonal variability, stratification, and water mass connectivity (Bayhaqi et al., 2017; Prihatiningsih et al., 2021; Apriansyah et al., 2024), while a quantitative assessment of surface current responses to ENSO phases around Selayar, including changes in flow direction, current strengthening or weakening, and modifications of spatial current structure, remains relatively limited. This gap persists despite clear evidence of ENSO signals in current and transport variability within the Makassar Strait from long-term observations (Gordon et al., 2019), as well as climate modeling studies that demonstrate robust linkages between the ITF and both ENSO and the Indian Ocean Dipole (IOD) (Santoso et al., 2022). Accordingly, this study aims to quantify differences in surface ocean currents among ENSO phases (El Niño, La Niña, and Neutral) using composite and anomaly analyses of surface current speed and direction.

Data and Methods

Data

This study utilizes monthly sea surface current data obtained from the Copernicus Marine Environment Monitoring Service (CMEMS) Global Ocean Physics Reanalysis (https://doi.org/10.48670/moi-00021), produced by Mercator Ocean International (2026). The dataset consists of monthly mean fields with a horizontal resolution of 0.083° × 0.083° (approximately 1/12°), derived from the GLORYS12V1 reanalysis system based on the NEMO ocean model with assimilation of satellite observations and in-situ measurements (Jean-Michel et al., 2021). The analyzed variables include the eastward sea water velocity (u) and the northward sea water velocity (v) for the period January 1993 to December 2020. Vertically, surface currents are defined in this study as the simple average of the uppermost five model layers, spanning depths from 0.49 m to 5.08 m below the sea surface. This depth range is considered representative of near-surface ocean current dynamics. The study area is confined to waters surrounding Selayar Island and the southern Makassar Strait, covering a spatial extent of 6.92°S–5.33°S and 119.17°E–120.92°E (Figure 1). This domain is represented by a grid of 20 latitude points × 22 longitude points, which is sufficient to resolve mesoscale spatial variability of surface currents in the region.

To examine the influence of interannual climate variability, particularly ENSO, the monthly Niño-3.4 index (https://psl.noaa.gov/data/timeseries/month/DS/Nino34_CPC/) was employed and obtained from the NOAA Physical Sciences Laboratory (NOAA, 2026). The Niño-3.4 index is defined as the sea surface temperature anomaly (SSTA) averaged over the region 5°N–5°S and 170°–120°W, and is widely used as an indicator of ENSO phase and intensity (Wei, 2024; L'Heureux et al., 2024).

Methods

ENSO Phase Classification

Interannual variability is represented by the ENSO, which is classified using the monthly Niño-3.4 index. Each month during the analysis period (January 1993–December 2020) is categorized as El Niño when the Niño-3.4 SSTA is ≥ +0.5 °C, La Niña when it is ≤ −0.5 °C, and Neutral when it falls between these two thresholds (L'Heureux et al., 2024; Halide et al., 2024). Based on these criteria, a total of 336 months is classified into Neutral (N = 156), El Niño (N = 76), and La Niña (N = 104),

which are subsequently used in the composite analyses.

Surface Current Processing

In this study, surface currents are represented as a simple vertical average of the uppermost five model layers (0.49, 1.54, 2.65, 3.82, and 5.08 m) at each grid point and time step. This approach is used to characterize current dynamics within the near-surface ocean layer that is most relevant to surface oceanographic processes.

Surface currents are represented as two-dimensional vectors, and their magnitude is calculated using standard vector formulations (Stewart, 2008; Emery & Thomson, 2001). The climatological mean and anomalies are computed following standard statistical approaches (Wilks, 2011; Hartmann, 2016), while composite analysis is applied to extract ENSO-related variability (Boschat et al., 2016; Li & Dolman, 2023).

The notation (x, y, t) is used to denote the spatial and temporal dependence of the variables, where x and y represent longitude and latitude coordinates, respectively, and t denotes the monthly time index. The zonal and meridional components of the surface current velocity are expressed as $u(x, y, t)$ and $v(x, y, t)$, respectively.

Surface currents are represented as two-dimensional vectors, as shown in Equation (1):

$$\vec{U}(x, y, t) = \big(u(x, y, t), v(x, y, t)\big) \qquad (1)$$

The current speed (current magnitude) is calculated using the Equation (2):

$$\left|\vec{U}(x, y, t)\right| = \sqrt{u(x, y, t)^2 + v(x, y, t)^2} \qquad (2)$$

This magnitude is used to describe the intensity of the surface current, while current direction is assessed qualitatively based on the orientation of the current vectors.

Composite Analysis of Surface Currents

Composite analysis is employed to identify the mean surface current patterns associated with each ENSO phase. Composite methods are widely used in the geosciences to extract the typical characteristics of a given condition by averaging events that belong to a specific category (Li & Dolman, 2023; Boschat et al., 2016).

After the monthly data are grouped into El Niño, La Niña, and Neutral phases, surface current composites are calculated by averaging the zonal and meridional current components for each phase. For a given ENSO phase c with a total of N_c months, the composite current components are given by Equation (3) and (4):

$$u_c(x, y) = \frac{1}{N_c} \sum_{t \in c} u(x, y, t) \qquad (3)$$

$$v_c(x, y) = \frac{1}{N_c} \sum_{t \in c} v(x, y, t) \qquad (4)$$

The composite current magnitude is then calculated from the composite current components using the same formulation as for the individual data. This analysis is intended to highlight interannual variability signals associated with ENSO while suppressing short-term, random fluctuations.

Composite Analysis of Surface Currents Anomalies

Surface current anomaly analysis is conducted to examine deviations of the currents from their mean state. The mean zonal and meridional current components are calculated as time averages at each grid point over the entire analysis period and are denoted as $\bar{u}(x, y)$ and $\bar{v}(x, y)$, respectively.

The anomalies of the current components are given by Equation (5) and (6):

$$u'(x, y, t) = u(x, y, t) - \bar{u}(x, y) \qquad (5)$$

$$v'(x, y, t) = v(x, y, t) - \bar{v}(x, y) \qquad (6)$$

This approach computes anomalies as the difference between the raw current values and their corresponding mean values, calculated separately for the zonal and meridional components. The magnitude of the surface current anomaly vector is then calculated using the Equation (7):

$$\left|\vec{U}'(x,y,t)\right| = \sqrt{u'(x,y,t)^2 + v'(x,y,t)^2} \quad (7)$$

Composite anomalies for each ENSO phase are obtained by averaging the anomaly component values over all months belonging to the respective phase. This approach allows spatial patterns of surface current intensification or weakening relative to the long-term mean state to be consistently analyzed within a vector framework.

It should be noted that the magnitude of the surface current anomaly vector is always non-negative. This is a direct consequence of defining vector magnitude as the square root of the sum of squared zonal and meridional anomaly components. Although the anomaly components $u'$and v'may take either positive or negative values, the vector magnitude represents only the absolute strength of the deviation from the mean state and does not convey information on sign or direction. Accordingly, changes in current direction are interpreted based on the orientation of the anomaly vectors, whereas the anomaly magnitude is used to assess the intensity of surface current variability.

Results and Discussion

To describe the dynamics of surface currents around Selayar Island, the results are organized based on analyses of the long-term mean (climatological mean), monthly variability, and differences among the ENSO phases. The long-term mean pattern of surface currents in the study area is obtained by averaging the data over the period 1993–2020 and is used to provide a general depiction of surface current conditions (Figure 1).

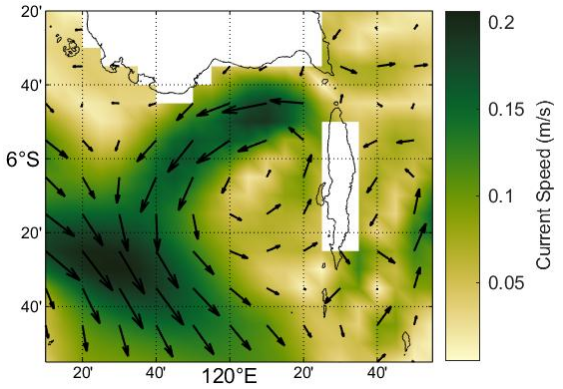

Figure 1. Long-term climatological mean (1993–2020) of sea surface currents around Selayar Island. Shading indicates the mean current speed (magnitude), while arrows represent the direction of the mean current vectors.

The long-term mean reveals a well-defined current corridor in the northwestern sector of Selayar Island that converges toward the main current pathway, representing a branch of the ITF extending toward the southwestern part of the domain, along with relatively weaker currents in the vicinity of the island. Within the main corridor, the flow direction is relatively uniform, whereas greater directional variability around Selayar Island reflects the influence of local topography on surface circulation. This spatial variability is consistent with the characteristics of the Selayar Slope region, which is shaped by shelf–slope topography and regional water mass interactions (Prihatiningsih et al., 2021).

Figure 2 presents the monthly climatology of surface currents, calculated as the mean for each month over the period 1993–2020. Compared to the 27-year long-term mean (Figure 1), the monthly climatology indicates that surface currents exhibit a pronounced seasonal cycle in both intensity and direction. Quantitatively, the domain-averaged monthly current magnitude ranges from 0.085 to 0.305 ms^{-1}. The highest domain-mean current speeds occur in January (~0.305 ms^{-1}), followed by February (~0.281 ms^{-1}) and December (~0.257 ms^{-1}). In contrast, the lowest domain-mean current speeds are observed in April (~0.085 ms^{-1}) and remain relatively

weak again in October (~0.093 ms^{-1}), coinciding with the seasonal transition periods. At the spatial scale, the maximum current magnitude within the domain reaches approximately 0.64–0.66 ms^{-1} during June–August as well as in January, indicating the presence of intensified current cores during specific months.

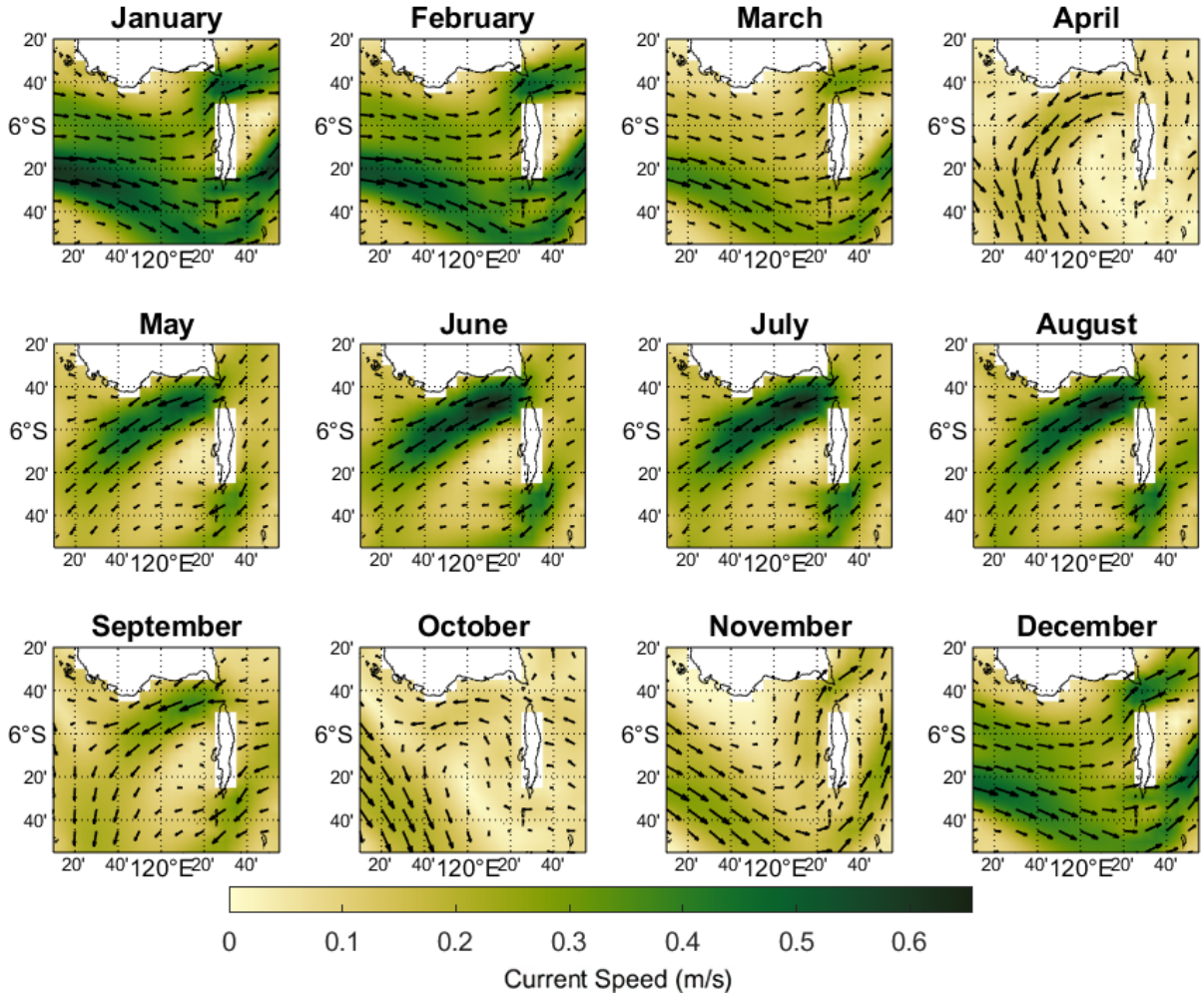

Figure 2. Monthly climatology of sea surface currents around Selayar Island based on the 27-year mean (1993–2020). Each panel shows the current speed magnitude (shading) and the direction of current vectors (arrows) for each month.

Seasonal changes in current direction are also clearly evident. Domain-averaged results show that during January–March and November–December, the mean zonal component tends to be eastward (positive *u*), whereas during May–September the mean zonal component is predominantly westward (negative *u*), accompanied by a generally southward mean meridional component (negative *v*). April and October are characterized by weaker current conditions and directional tendencies that differ from those observed during the peak monsoon months. This seasonal pattern is consistent with previous findings showing that surface currents around the Selayar Islands vary in response to the monsoonal cycle and transitional seasons (Bayhaqi et al., 2017), and it further reflects the strong monsoonal control and inter-basin connectivity that characterize circulation within the Indonesian Archipelago (Yoneyama & Zhang, 2020; Xue et al., 2020; Apriansyah et al., 2024).

Figure 3 presents the composite mean surface currents for the three ENSO phases based on the Niño-3.4 index: Neutral (N = 156 months), El Niño (N = 76 months), and La Niña (N = 104 months). The Niño-3.4

time series for the period 1993–2020 includes strong ENSO events, with peak positive anomalies reaching +2.72 °C in November 2015 and minimum anomalies reaching −1.77 °C in January 2000 (NOAA, 2026). Accordingly, the resulting composites represent an aggregation of weak to strong events within each ENSO phase.

Overall, all three ENSO phases preserve the primary spatial structure of surface currents around Selayar Island, but exhibit differences in mean intensity and vector configuration across several sectors of the domain. As shown in Figure 3, Neutral conditions are characterized by a relatively strong current flowing from the Selayar Strait toward the southwest and merging with the main current corridor. This feature is not observed during El Niño and La Niña phases, during which currents west of Selayar Island undergo deflection and form vortex-like circulation patterns, indicating the presence of localized circulation arising from current–topography interactions. In addition, during Neutral conditions, currents within the main corridor in the southwestern sector of the domain tend to be oriented predominantly in the north–south direction. In contrast, during El Niño and La Niña phases, the orientation of currents in the main corridor is more similar to the long-term climatological pattern, flowing from the northwest toward the southeast. Nevertheless, during La Niña conditions, currents within this corridor appear slightly stronger than those observed during El Niño.

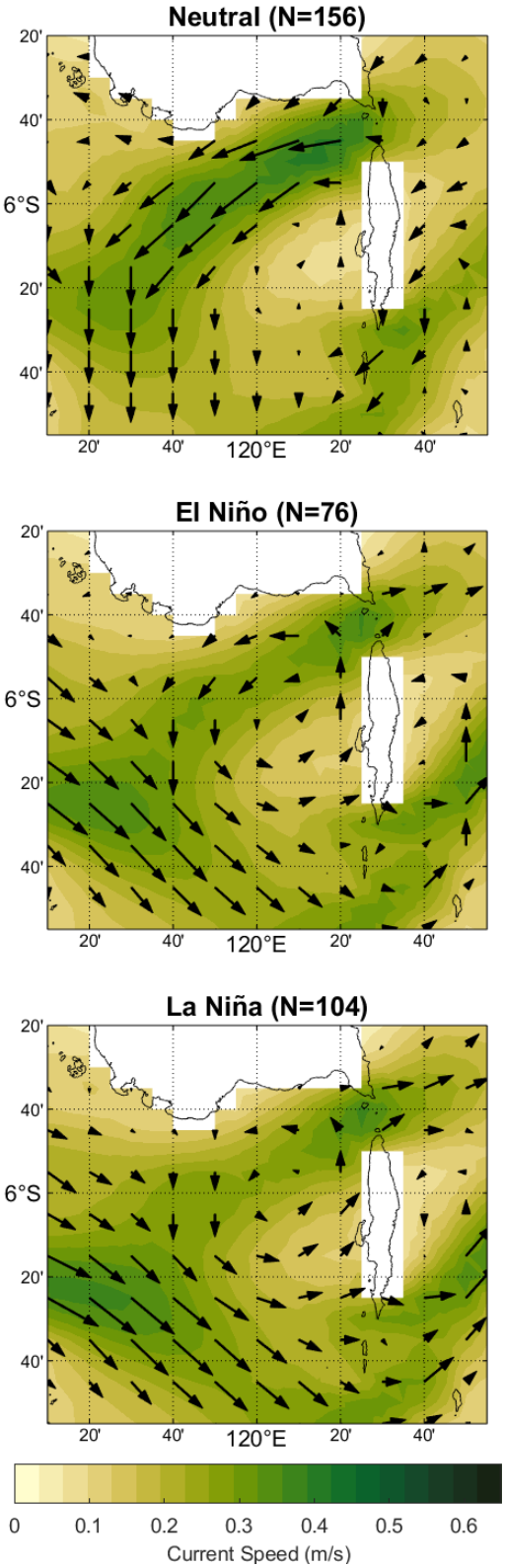

Figure 3. Composite mean sea surface currents for the three ENSO phases: Neutral, El Niño, and La Niña. Shading indicates the composite current speed magnitude, while arrows represent the direction of the composite current vectors. The composites are calculated by averaging the current components over the months corresponding to each ENSO phase.

To assess the extent to which surface current patterns under different ENSO phases deviate from the long-term mean state, the analysis is further focused on composite surface current anomalies. The composite anomaly results are shown in Figure 4. The direction of anomaly currents crossing the Selayar Strait exhibits clear differences among ENSO phases. Under Neutral conditions, current anomalies display a northeast-to-southwest flow crossing the Selayar Strait and extending into the southern part of Selayar Island. In contrast, during El Niño and La Niña phases, anomaly currents show opposite directions when crossing the Selayar Strait and the waters south of the island. In addition, the intensity of current anomalies during El Niño conditions appears weaker than that observed during La Niña conditions.

The composite anomaly patterns further reveal clear quantitative differences between the two phases. Domain averaged anomaly magnitudes are estimated to range from approximately 0.03–0.05 ms^{-1} during El Niño and increase to about 0.07–0.09 ms^{-1} during La Niña. The maximum anomaly magnitudes further highlight this contrast. During La Niña, peak anomaly values reach approximately 0.10–0.12 ms^{-1}, whereas during El Niño the maximum anomalies are generally limited to around 0.04–0.08 ms^{-1}. This indicates that surface current anomalies during La Niña are stronger by approximately 0.03–0.06 ms^{-1} compared to those during El Niño. Spatially, regions with relatively high anomaly magnitudes (>0.08 ms^{-1}) are more extensive during La Niña, while anomalies during El Niño tend to be weaker.

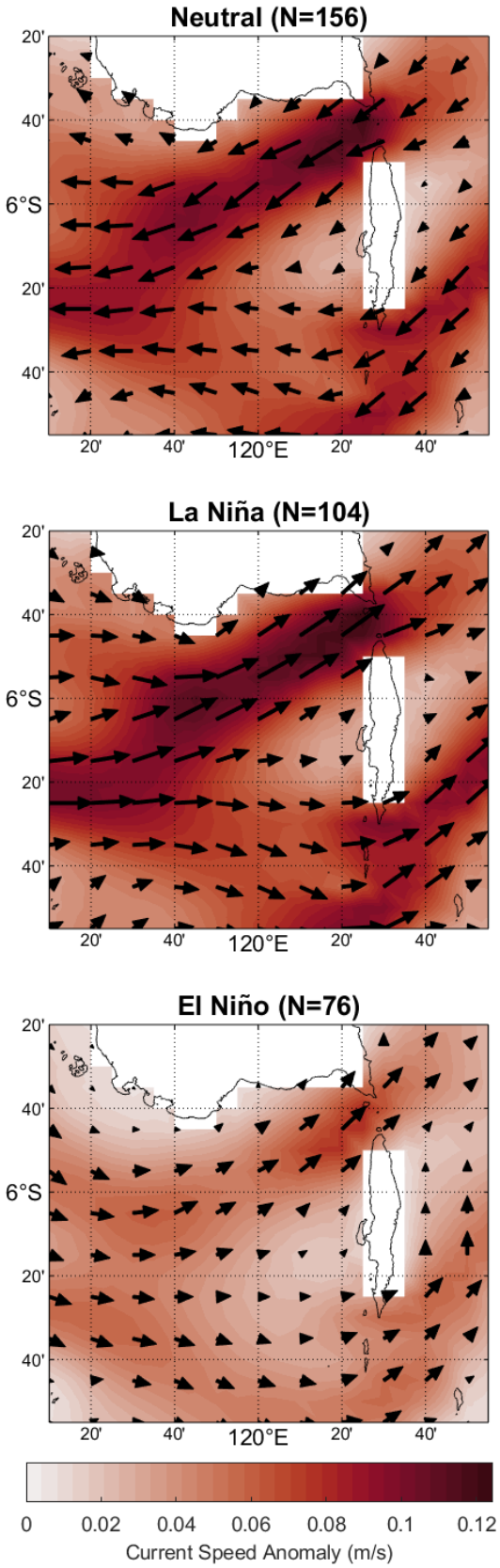

Figure 4. Same as Figure 3, but for composite sea surface current anomalies.

These results indicate that ENSO exerts a measurable influence on surface current

variability in the study region, with La Niña conditions enhancing current anomalies more effectively than El Niño. This asymmetry is consistent with previous studies indicating that La Niña is associated with strengthened large-scale circulation and increased ITF transport, which can amplify regional current variability (Feng et al., 2018; Gordon et al., 2019; Santoso et al., 2022).

In addition to these interannual differences, the results are further examined in the context of seasonal variability. The dominance of seasonal variability in the monthly climatological results confirms that monsoonal circulation is the primary driver of surface currents around Selayar Island. Changes in monsoon phases and transitional periods modulate both current intensity and direction, consistent with the characteristics of the Indonesian Archipelago, which is embedded within the coupled ocean and atmosphere system of the Maritime Continent (Yoneyama & Zhang, 2020; Xue et al., 2020).

Furthermore, the spatial heterogeneity evident in both the long-term climatological mean and the monthly climatology reflects the influence of local topography, particularly the Selayar Slope and island geometry, in modifying surface flow structures (Bayhaqi et al., 2017; Prihatiningsih et al., 2021). The inter-phase differences identified in the current composites and anomaly patterns indicate that ENSO acts as an interannual modulation of surface current dynamics in the study region. Nevertheless, the influence of ENSO on surface currents around Selayar Island appears to be weaker than that of seasonal variability, confirming that monsoonal forcing remains the dominant control on surface current dynamics in the region.

Several limitations should be considered when interpreting the results of this study. First, ENSO phase–based composites may be subject to seasonal sampling bias because the distribution of El Niño, La Niña, and Neutral months is not uniform throughout the year, while surface currents in the study region are strongly influenced by monsoonal variability. Second, the surface current data are derived from a reanalysis product; although this product assimilates a wide range of observations, the results remain dependent on the underlying model configuration and data assimilation schemes. Third, defining surface currents as an average over the upper layers (approximately 0.49–5 m) may limit the representation of very shallow processes or those strongly influenced by instantaneous wind forcing.

Conclusion

This study demonstrates that surface currents around Selayar Island exhibit a spatially heterogeneous structure and are primarily controlled by seasonal variability. Both the long-term climatological mean and the monthly climatology confirm the dominant role of monsoonal circulation in modulating the intensity and direction of surface currents. Seasonal variability produces larger changes in current direction and strength than interannual variability, indicating that monsoonal dynamics constitute the primary control on surface currents in the study region.

Interannual variability associated with ENSO is also evident, particularly in the magnitude of surface current anomalies. Quantitatively, surface current anomalies during El Niño range from approximately 0.03–0.05 ms^{-1} while anomalies during La Niña increase to about 0.07–0.09 ms^{-1}, with peak values reaching ~0.10–0.12 ms^{-1}. This indicates that anomalies during La Niña are stronger by approximately 0.03–0.06 ms^{-1} compared to those during El Niño. Notably, differences in the direction of surface current anomalies are more pronounced under Neutral conditions, where anomaly directions differ markedly from those

observed during both El Niño and La Niña phases.

Overall, these results indicate that ENSO acts as an interannual modulation of surface current intensity, superimposed on dominant seasonal forcing and local topographic influences. Despite this modulation, the influence of ENSO remains secondary to the strong control exerted by monsoonal circulation.

Acknowledgements

The authors would like to express their sincere gratitude to the editor and the anonymous reviewers for their constructive comments and suggestions that helped improve the quality and clarity of this manuscript. The authors also thank Fakhira Raisha for her support during the preparation of this study. No specific funding was received for this research.

Author Contribution

Andika**:** Conceptualization, Methodology, Data curation, Formal analysis, Visualization, Writing original draft, Writing-review & editing. Gladiva Warouw: Data collection, Reference collection, English language editing.

Conflict of Interest

The author declares no conflict of interest.

References

Apriansyah, A., Atmadipoera, A. S., Natih, N. M. N., Nugroho, D., Zuraida, R., Hartanto, M. T., & Syahdan, M. (2024). Water mass exchange in triangle seas of the Java-Makassar-Flores (JMF): A modeling study. *Continental Shelf Research*, 275, 105225. https://doi.org/10.1016/j.csr.2024.105225

Bayhaqi, A., Iskandar, M. R., & Surinati, D. (2017). Surface current pattern and physics condition of waters around Selayar Island in the first transitional and southeast monsoons. *Journal Oseanologi dan Limnologi di Indonesia*, 2(1), 83–95. https://doi.org/10.14203/oldi.2017.v2i1.71

Bhattacharya, B., Hossain, S. K. A., & Ghosh, M. (2026). Leveraging cloud-based SAR remote sensing and GNOME numerical simulation for modeling oil spill trajectory in the Black Sea. *Marine Pollution Bulletin*, 224, 119166. https://doi.org/10.1016/j.marpolbul.2025.119166

Boschat, G., Simmonds, I., Purich, A., Cowan, T., & Pezza, A. B. (2016). On the use of composite analyses to form physical hypotheses: An example from heat wave–SST associations. *Scientific Reports*, 6(1), 29599. https://doi.org/10.1038/srep29599

Bosi, S., Broström, G., & Roquet, F. (2021). The role of Stokes drift in the dispersal of North Atlantic surface marine debris. *Frontiers in Marine Science*, 8, 697430. https://doi.org/10.3389/fmars.2021.697430

Chassignet, E. P., Xu, X., & Zavala-Romero, O. (2021). Tracking marine litter with a global ocean model: where does it go? Where does it come from?. *Frontiers in Marine Science*, 8, 667591. https://doi.org/10.3389/fmars.2021.667591

Córdova, P., & Flores, R. P. (2022). Hydrodynamic and Particle Drift Modeling as a Support System for Maritime Search and Rescue (SAR) Emergencies: Application to the C-212 Aircraft Accident on 2 September, 2011, in the Juan Fernández Archipelago, Chile. *Journal of Marine Science and Engineering*, 10(11), 1649. https://doi.org/10.3390/jmse10111649

Devis-Morales, A., Rodríguez-Rubio, E., & Montoya-Sánchez, R. A. (2021). Modelling the transport of sediment discharged by Colombian rivers to the southern Caribbean Sea. *Ocean Dynamics*, 71(2), 251–277. https://doi.org/10.1007/s10236-020-01431-y

Elzahaby, Y., Schaeffer, A., Roughan, M., & Delaux, S. (2021). Oceanic circulation drives the deepest and longest marine heatwaves in the East Australian Current system. *Geophysical Research Letters*, 48(17), e2021GL094785. https://doi.org/10.1029/2021GL094785

Emery, W. J., & Thomson, R. E. (2001). *Data analysis methods in physical oceanography* (2nd ed.). Elsevier.

Feng, M., Zhang, N., Liu, Q., & Wijffels, S. (2018). The Indonesian throughflow, its variability and centennial change. *Geoscience Letters*, 5(1), 3. https://doi.org/10.1186/s40562-018-0102-2

Fu, Y., Wang, Z., Zhao, M., Song, X., Jia, Y., & Song, Z. (2024). Factors influencing the variation of the Sepik-Ramu River system's sediment plume off the north coast of New Guinea. *Estuarine, Coastal and Shelf Science*, 303, 108782. https://doi.org/10.1016/j.ecss.2024.108782

Gao, Y., Kamenkovich, I., Perlin, N., & Kirtman, B. (2022). Oceanic advection controls mesoscale mixed layer heat budget and air–sea heat exchange in the southern ocean. *Journal of Physical Oceanography*, 52(4), 537–555. https://doi.org/10.1175/JPO-D-21-0063.1

Gordon, A. L., Napitu, A., Huber, B. A., Gruenburg, L. K., Pujiana, K., Agustiadi, T., Kuswardani, A., Mbay, N., & Setiawan, A. (2019). Makassar Strait throughflow seasonal and interannual variability: An overview. *Journal of Geophysical Research: Oceans*, 124(6), 3724–3736. https://doi.org/10.1029/2018JC014502

Halide, H., Wulandari, P., & Andika, A. (2024). New metrics for distinguishing the skill of long-range ENSO forecasting models. *AIP Conference Proceedings*, 2774(1), 050005. https://doi.org/10.1063/5.0164472

Hartmann, D. L. (2016). *Global physical climatology* (2nd ed.). Elsevier.

Hu, Q., Chen, X., Huang, W., & Zhou, F. (2021). Phytoplankton bloom triggered by eddy-wind interaction in the upwelling region east of Hainan Island. *Journal of Marine Systems*, 214, 103470. https://doi.org/10.1016/j.jmarsys.2020.103470

Isern-Fontanet, J., Ballabrera-Poy, J., Turiel, A., & García-Ladona, E. (2017). Remote sensing of ocean surface currents: A review of what is being observed and what is being assimilated. *Nonlinear Processes in Geophysics*, 24(4), 613–643. https://doi.org/10.5194/npg-24-613-2017

Jean-Michel, L., Eric, G., Romain, B-B., Gilles, G., Angélique, M., Marie, D., Clément, B., Mathieu, H., Olivier, L. G., Charly, R., Tony, C., Charles-Emmanuel, T., Florent, G., Giovanni, R., Mounir, B., Yann, D., & Pierre-Yves, L. T. (2021). The Copernicus global 1/12 oceanic and sea ice GLORYS12 reanalysis. *Frontiers in Earth Science*, 9, 698876. https://doi.org/10.3389/feart.2021.698876

Keramea, P., Spanoudaki, K., Zodiatis, G., Gikas, G., & Sylaios, G. (2021). Oil spill modeling: A critical review on current trends, perspectives, and challenges. *Journal of Marine Science and Engineering*, 9(2), 181. https://doi.org/10.3390/jmse9020181

L'Heureux, M. L., Tippett, M. K., Wheeler,

M. C., Nguyen, H., Narsey, S., Johnson, N., Hu, Z., Watkins, A. B., Lucas, C., Ganter, C., Becker, E., Wang, W., & Di Liberto, T. (2024). A relative sea surface temperature index for classifying ENSO events in a changing climate. *Journal of Climate*, 37(4), 1197–1211. https://doi.org/10.1175/JCLI-D-23-0406.1

Laurindo, L. C., Siqueira, L., Small, R. J., Thompson, L., & Kirtman, B. P. (2024). Quantifying the contribution of ocean advection and surface flux to the upper-ocean salinity variability resolved by climate model simulations. *Geophysical Research Letters*, 51(3), e2023GL106354. https://doi.org/10.1029/2023GL106354

Lefebvre, C., Le Bihanic, F., Jalón-Rojas, I., Dusacre, E., Chassaigne--Viscaïno, L., Bichon, J., Clérandeau, C., Morin, B., Lecomte, S., & Cachot, J. (2023). Spatial distribution of anthropogenic particles and microplastics in a meso-tidal lagoon (Arcachon Bay, France): A multi-compartment approach. *Science of The Total Environment*, 898, 165460. https://doi.org/10.1016/j.scitotenv.2023.165460

Li, L., & Dolman, A. J. (2023). On the reliability of composite analysis: an example of wet summers in North China. *Atmospheric Research*, 292, 106881. https://doi.org/10.1016/j.atmosres.2023.106881

Li, S., Zhang, Z., Zhou, M., Wang, C., Wu, H., & Zhong, Y. (2022). The role of fronts in horizontal transports of the Changjiang River plume in summer and the implications for phytoplankton blooms. *Journal of Geophysical Research: Oceans*, 127(8), e2022JC018541. https://doi.org/10.1029/2022JC018541

Lu, Z., Gan, J., Dai, M., Zhao, X., & Hui, C. R. (2020). Nutrient transport and dynamics in the South China Sea: A modeling study. *Progress in Oceanography*, 183, 102308. https://doi.org/10.1016/j.pocean.2020.102308

Mannarini, G., Salinas, M. L., Carelli, L., Petacco, N., & Orović, J. (2024). VISIR-2: Ship weather routing in Python. *Geoscientific Model Development*, 17(10), 4355–4382. https://doi.org/10.5194/gmd-17-4355-2024

Manral, D., Iovino, D., Jaillon, O., Masina, S., Sarmento, H., Iudicone, D., Amaral-Zettler, L., & van Sebille, E. (2023). Computing marine plankton connectivity under thermal constraints. *Frontiers in Marine Science*, 10, 1066050. https://doi.org/10.3389/fmars.2023.1066050

Mappong, S. (2018, 3 Juli). *KM Lestari Maju tujuan Selayar tenggelam*. ANTARA News. https://www.antaranews.com/berita/723622/km-lestari-maju-tujuan-selayar-tenggelam?

Mateus, M., Canelas, R., Pinto, L., & Vaz, N. (2020). When tragedy strikes: potential contributions from ocean observation to search and rescue operations after drowning accidents. *Frontiers in Marine Science*, 7, 00055. https://doi.org/10.3389/fmars.2020.00055

Mercator Ocean International. (2026). Global Ocean Physics Reanalysis [Data set]. Copernicus Marine Service (CMEMS). https://doi.org/10.48670/moi-00021

Nie, X., Liu, H., Xu, T., & Wei, Z. (2023). Influence of the El Niño-Southern Oscillation on upper-ocean salinity changes in the southeast Indian ocean. *Frontiers in Marine Science*, 10, 1181278. https://doi.org/10.3389/fmars.2023.1181278

NOAA (2026). *Niño 3.4 monthly time-*

series dataset [Data set]. NOAA Physical Sciences Laboratory. https://psl.noaa.gov/data/timeseries/month/DS/Nino34_CPC/

Prihatiningsih, I., Jaya, I., Atmadipoera, A. S., & Zuraida, R. (2021). Stratification and characteristic of water masses in Selayar Slope-Southern Makassar Strait. *Omni-Akuatika*, 17(1), 27–36. http://dx.doi.org/10.20884/1.oa.2021.17.1.620

Purba, N. P., Faizal, I., Christie, D., Pratama, M. B., Valino, D. A., Martasuganda, M. K., Herawati, T., Wulandari, A., Utami, S. T., Aryanto, N. C. D., Ilmi, M. H., Alfarez R. R., & Pasaribu, B. (2024). Mapping the sources and strands of marine debris via particle modelling and In-situ sampling approaches in archipelagic countries. *Scientific Reports*, 14(1), 25804. https://doi.org/10.1038/s41598-024-73373-0

Ralston, D. K., Geyer, W. R., Wackerman, C. C., Dzwonkowski, B., Honegger, D. A., & Haller, M. C. (2024). Interacting influences of diurnal tides, winds, and river discharge on a large coastal plume. *Journal of Geophysical Research: Oceans*, 129(9), e2024JC021288. https://doi.org/10.1029/2024JC021288

Röhrs, J., Sutherland, G., Jeans, G., Bedington, M., Sperrevik, A. K., Dagestad, K. F., Gusdal Y., Mauritzen, C., Dale A., & LaCasce, J. H. (2023). Surface currents in operational oceanography: Key applications, mechanisms, and methods. *Journal of Operational Oceanography*, 16(1), 60–88. https://doi.org/10.1080/1755876X.2021.1903221

Said, N. H. (2024, 11 Agustus). *Kapal muat 5.000 sak semen tenggelam di Selayar, 8 ABK-penumpang selamat*. https://www.detik.com/sulsel/berita/d-7483896/kapal-muat-5-000-sak-semen-tenggelam-di-selayar-8-abk-penumpang-selamat?

Santoso, A., England, M. H., Kajtar, J. B., & Cai, W. (2022). Indonesian Throughflow variability and linkage to ENSO and IOD in an ensemble of CMIP5 models. *Journal of Climate*, 35(10), 3161–3178. https://doi.org/10.1175/JCLI-D-21-0485.1

Stewart, R. H. (2008). *Introduction to physical oceanography*. Texas A&M University.

Tamtare, T., Dumont, D., & Chavanne, C. (2022). The Stokes drift in ocean surface drift prediction. *Journal of Operational Oceanography*, 15(3), 156–168. https://doi.org/10.1080/1755876X.2021.1872229

Trinanes, J. A., Olascoaga, M. J., Goni, G. J., Maximenko, N. A., Griffin, D. A., & Hafner, J. (2016). Analysis of flight MH370 potential debris trajectories using ocean observations and numerical model results. *Journal of Operational Oceanography*, 9(2), 126–138. https://doi.org/10.1080/1755876X.2016.1248149

Vijith, V., Vinayachandran, P. N., Webber, B. G., Matthews, A. J., George, J. V., Kannaujia, V. K., Lotliker, A. A., & Amol, P. (2020). Closing the sea surface mixed layer temperature budget from in situ observations alone: Operation Advection during BoBBLE. *Scientific reports*, 10(1), 7062. https://doi.org/10.1038/s41598-020-63320-0

Wang, J., Qin, H., Wang, D., Li, Z., Li, B., Su, H., Liu, C., Qin, L., Tu, H., & Mu, L. (2025). Research on drift trajectories of typical marine search and rescue objects based on wind-wave-current coupled experiments. *Applied Ocean Research*, 165, 104827. https://doi.org/10.1016/j.apor.2025.104827

Wardiyah, N. S. (2024, 8 Januari). *Bupati Selayar salurkan santunan ke ahli waris korban kapal tenggelam*. ANTARA News. https://www.antaranews.com/berita/3905547/bupati-selayar-salurkan-santunan-ke-ahli-waris-korban-kapal-tenggelam?

Wei, L. (2024). Summary of Commonly Used ENSO Indices. *Highlights in Science, Engineering and Technology*, 88, 687-694. https://doi.org/10.54097/vndv3190

Wilks, D. S. (2011). *Statistical methods in the atmospheric sciences* (3rd ed.). Academic Press.

Xue, P., Malanotte-Rizzoli, P., Wei, J., & Eltahir, E. A. B. (2020). Coupled ocean-atmosphere modeling over the Maritime Continent: A review. *Journal of Geophysical Research: Oceans*, 125(6), e2019JC014978. https://doi.org/10.1029/2019JC014978

Yoneyama, K., & Zhang, C. (2020). Years of the maritime continent. *Geophysical Research Letters*, 47(12), e2020GL087182. https://doi.org/10.1029/2020GL087182

Zhu, K., Mu, L., Yu, R., Xia, X., & Tu, H. (2023). Probabilistic modelling of surface drift prediction in marine disasters based on the NN–GA and ARMA model. *Ocean Engineering*, 281, 114804. https://doi.org/10.1016/j.oceaneng.2023.114804

Zhu, Q., & Wang, C. (2024). Contributions of Indo-Pacific forcings to interannual variability of the Indonesian Throughflow in the upper and lower layers. *Journal of Geophysical Research: Oceans*, 129(1), e2023JC020306. https://doi.org/10.1029/2023JC020306

ISSN: 2579-5821 (Print)
ISSN: 2579-5546 (Online)
URL address: http://journal.unhas.ac.id/index.php/geocelebes
DOI: 10.70561/geocelebes.v10i1.47264

Jurnal Geocelebes Vol. 10 No. 1, April 2026, 96 – 107

Stratigraphy and Paleoenvironment of the Kuaro Formation, Muru River, Kutai Basin: A Paleontological Approach

Iwan Prabowo*, Fathony Akbar Pratikno, Efrina Chandra Agusti Putri, Jamaluddin, Eliza Putri Andrean, Imanuel Kaunang

Geological Engineering Study Program, Sekolah Tinggi Teknologi Migas, Jl. KM.8, Karang Joang, Balikpapan, Kalimantan Timur, 76127, Indonesia.

*Corresponding author. Email: iwan.prabowo@sttmigas.ac.id

Manuscript received: 23 September 2025; Received in revised form: 3 October 2025; Accepted: 9 April 2026

Abstract

The southern margin of the Kutai Basin remains poorly constrained regarding its Paleogene history compared to the well-studied northern depocenter. This research investigates the stratigraphic characteristics, relative ages, and depositional environments of the Kuaro Formation along the Muru River, Paser Regency. The study integrates a detailed measuring section with biostratigraphic analyses of Larger Benthic Foraminifera (LBF), calcareous nannofossils, and palynology to reconstruct the paleoenvironmental evolution. The results reveal a continuous stratigraphic succession spanning from the Late Eocene to the Late Oligocene. The lower interval comprises coal-bearing siliciclastics deposited in a coastal swamp environment, marking the initial terrestrial influence. This unit transitions upward into massive *Pellatispira* and *Discocyclina*-bearing rudstones, indicating the development of a stable shallow-marine carbonate platform during the Late Eocene. The sequence culminates in Late Oligocene fine-grained calcareous claystones yielding *Reticulofenestra bisecta* and *Reticulofenestra lockeri*, deposited in a lower-energy inner shelf setting. This vertical stacking pattern records a major transgressive phase, evolving from terrestrial-influenced environments to open marine conditions. These findings provide significant insights into the Eocene–Oligocene transition in the southern Kutai Basin, distinguishing its retrogradational stratigraphic architecture from the progradational deltaic cycles typical of the younger Neogene sequences in the northern basin.

Keywords: Biostratigraphy; Carbonate Platform; East Kalimantan.

Citation: Prabowo, I., Pratikno, F.A., Putri, E.C.A., Jamaluddin, J. Andrean, E.P., & Kaunang, I. (2026). Depositional Environments and Rock Ages Interpretation of Muru River, Kuaro District, Paser Regency using Stratigraphic Evidence and Paleontological Approaches. *Jurnal Geocelebes*, 10(1): 96–107, doi: 10.70561/geocelebes.v10i1.47264

Introduction

The Kutai Basin in East Kalimantan represents one of the most significant Tertiary sedimentary basins in Indonesia, characterized by sedimentary thicknesses reaching up to 15 km and containing prolific hydrocarbon systems (Winarno et al., 2018). Geochemical assessments of the Lower Kutai Basin's younger sequences have verified its high organic content, primarily driven by deltaic deposition settings, which significantly contributes to its regional hydrocarbon potential (Jamaluddin et al., 2025). The structural framework and tectonic rotation of the Kutai Basin have been extensively studied (Advokaat et al., 2018; Irawati et al., 2022), while recent sedimentological and biostratigraphic studies have increasingly emphasized the complexity of deposition-al systems and facies heterogeneity within the Kutai Basin.

Recent studies on the Balikpapan Formation demonstrate that deltaic sys-tems in the Kutai Basin exhibit complex facies architecture, stacking patterns, and reservoir heterogeneity, which can be ef-fectively analyzed through integrated out-

crop and digital modeling approaches (Rohmana et al., 2019). Additionally, integrated micropaleontological approaches have successfully reconstructed Neogene paleoenvironments in the northern Kutai Basin (Darman, 2023; Jambak et al., 2024; Nisa et al., 2024). However, these existing studies largely focus on Miocene to Pleistocene sequences or rely heavily on subsurface data from the northern depocenters. Consequently, the high-resolution stratigraphic architec-ture and environmental evolution of the southern basin margin specifically during the Paleogene remain less understood, with limited published outcrop data that integrates multiple fossil groups to constrain the complex Eocene–Oligocene transition.

In the Muru River, Kuaro District, Paser Regency – geographically situated within the southern segment of the Kutai Basin – the sedimentary record is expected to preserve comparable paleoenvironmental and stratigraphic signatures. This selection is supported by recent regional studies indicating that Eocene clastics and Oligocene carbonates are significantly better preserved in the southern margin compared to other parts of the Kutai Basin (Darman, 2023). Complementing this, Sehah et al. (2024) recently modeled the coal-bearing formations in the adjacent North Penajam Paser Regency using satellite gravity data, further highlighting the structural significance and distribution of these sequences in the southern basin margin and mapped basaltic intrusions (Sopan et al., 2024). Against this backdrop of diverse regional geology, this study focuses on the detailed biostratigraphic and facies analysis of the Kuaro Formation to refine the sedimentary evolution of the area. Previous work in the Sangatta area demonstrated that assemblages of calcareous nannofossils such as *Catinaster coalitus*, *Discoaster spp.,* and *Coronocyclus nitescens* define zonations NN6–NN11 (Middle to Late Miocene), while benthic foraminifera such as *Trochamina* and *Haplophragmoides* provide constraints on bathymetry ranging from tidal flats to prodelta–shelf environments (Jambak et al., 2024).

This research addresses this stratigraphic gap by presenting a detailed multi-proxy analysis of the Kuaro Formation exposed along the Muru River in the southern Kutai Basin. Unlike previous regional assessments that often generalize the southern margin's geology, this study integrates larger benthic foraminifera, calcareous nannofossils, and palynology to provide precise age control and paleoenvironmental reconstruction. By documenting the specific transition from carbonate platform facies to siliciclastic deltaic systems, this work offers new insights into the tectono-stratigraphic development of the southern Kutai Basin, distinguishing it from the well-documented northern trends and establishing a key reference section for Paleogene correlation in the region. The basin has long been the focus of stratigraphic studies where microfossils, particularly foraminifera and calcareous nannofossils, have been utilized to refine age determinations and reconstruct depositional environments.

Palynological and foraminiferal studies from northern offshore Kutai Ba-sin wells (e.g., FN O-1) demonstrate that pollen, spores, and mangrove-derived palynomorphs serve as reliable indicators of terrestrial input into the Kutai Basin. When integrated with planktonic–benthic foraminiferal ratios, these biotic assemblages provide valuable insights into sequence stratigraphic system tracts, including the Transgressive System Tract (TST), Highstand System Tract (HST), and Falling Stage System Tract (FSST) during the Late Miocene to Pleistocene. This integrative, multi-proxy approach has been further validated by Nisa et al. (2024), who showed that combining small foraminifera with palynomorph data is highly effective

for reconstructing dy-namic changes in depositional environ-ments within the Kutai Basin. Therefore, such a biostratigraphic framework high-lights the importance of integrating mul-tiple fossil groups to achieve a more comprehensive understanding of basin evolution. Palynomorph assemblages are widely used to reconstruct depositional environments during sea-level fluctua-tions, particularly transgressive phases, where an increase in palynomorph abun-dance is commonly observed (Senduk et al., 2021).

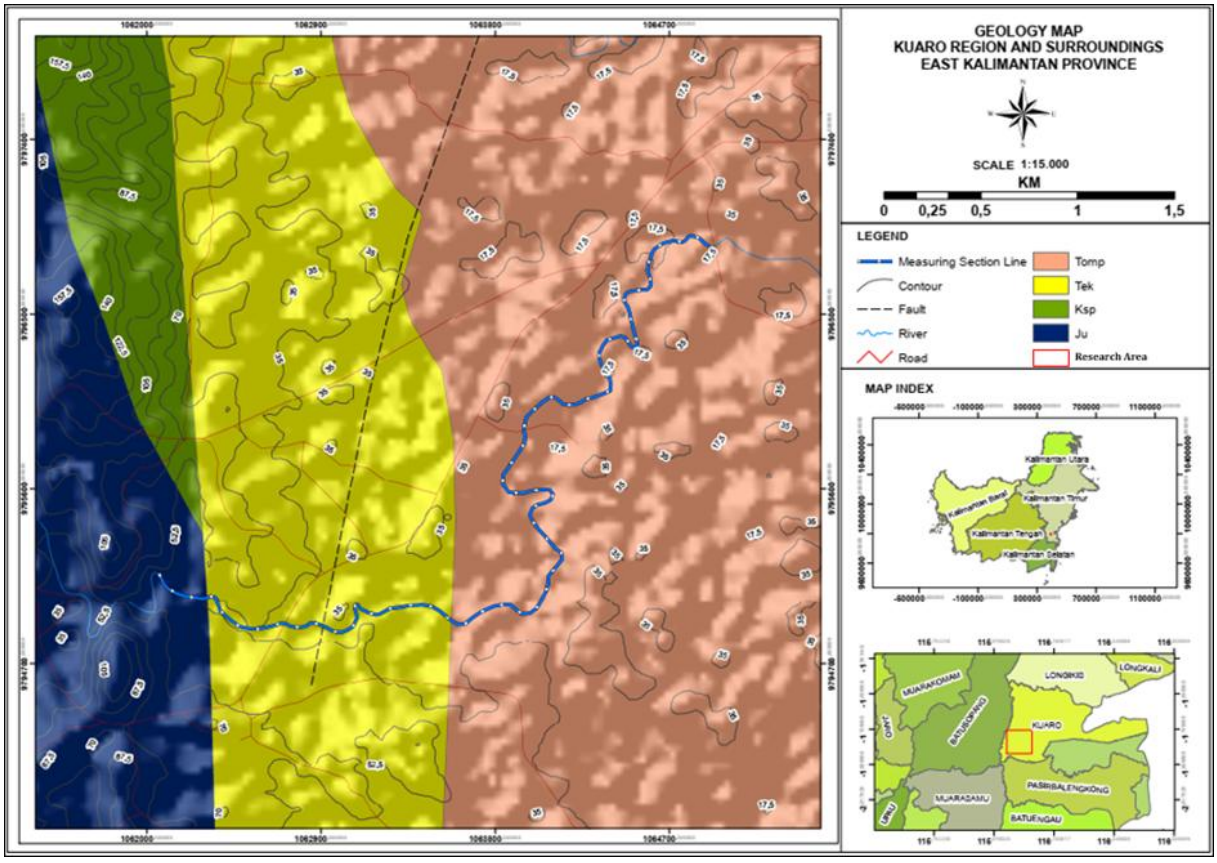

Figure 1. The Measuring Section (MS) route map of the Muru River overlaid on the regional geological map.

In terms of biostratigraphic zonation, three fossil groups provide complementary resolution: (1) larger benthic foraminifera (e.g., *Nummulites*, *Lepidocyclina*, *Miogypsina*) are particularly useful for shallow-marine carbonates and often define Eocene–Miocene shallow-marine zones; (2) pollen and spores enable correlation with terrestrial depositional phases and provide insights into vegetation and paleoclimate, especially in deltaic to coastal plain settings; and (3) calcareous nannofossils such as *Discoaster*, *Sphenolithus*, and *Catinaster* form the basis of the Martini (1971) zonation (NN zones), which remains the standard for Miocene–Pliocene sequences. The integration of these datasets with measured stratigraphic sections provides a robust tool for relative age determination and depositional environment interpretation.

Accordingly, the objectives of this study are: (i) to determine the relative ages of the Muru River rock units using integrated biostratigraphy of larger foraminifera, pollen–spores, and calcareous nannofossils; (ii) to reconstruct the depositional environments from fluvial–deltaic to shallow-marine settings through facies and fossil evidence. This study is expected to provide new insights into regional geological development and contribute to the geological inventory supporting geotourism development as

previously identified by Adha et al. (2023) and further emphasized by Putri et al. (2025) regarding the strategic value of Paser geosites, as well as serving as a reference for academic and applied geological studies in East Kalimantan.

Materials and Methods

This study employed a comprehensive approach integrating field measurements and laboratory analyses. Fieldwork involved detailed stratigraphic logging along the Muru River to record lithological variations, sedimentary structures, and fossil content (Figure 2). For laboratory analysis, representative rock samples were selected based on lithological characteristics. Carbonate samples were prepared as petrographic thin sections to identify microfacies and Larger Benthic Foraminifera (LBF) assemblages following the classification of BouDagher-Fadel (2018). Meanwhile, fine-grained clastic samples (marl and claystone) were processed for calcareous nannofossils using the standard smear slide technique. The preparation involved scraping fresh rock surfaces and suspending the sediment in distilled water without centrifugation to preserve the original assemblage composition. Nannofossil identification was conducted using a polarizing microscope at 1000x magnification, with taxonomic identification referring to Martini (1971) zonation.

Results and Discussion

Lithological Characteristics

The measured stratigraphic section along the Muru River outcrop exhibits a heterogeneous lithological succession indicative of transitional depositional environments (Figure 2).

The excellent exposure of these rock units along the river does not only provide stratigraphic data but also serves as a potential object for edu-geotourism, as identified by Battu et al. (2023). Regionally, the development of these carbonate units during the Oligocene aligns with the stable platform conditions known as the Barito Platform, which extends offshore to the Paternoster Platform, allowing for extensive carbonate growth in the southern basin margin (Darman, 2023). The limestone intraparticle and fenestral porosity, and sparite cements with meniscus and drusy morphologies (Figure 3).

These features indicate deposition under warm, clear, shallow-marine conditions. Overlying marl beds contain higher clay fractions, suggesting increased terrigenous input from the hinterland. The rock has an allochthonous material composition, with material sizes ranging from < 0.1 mm to 9 mm, more than 10% material measuring > 2 mm, a massive, closed-packed structure with skeletal components, intersecting grains, and intraparticle and fenestral porosity, with sparite morphology, meniscus and drusy. The composition of this rock is 60% allochem (Alc), 35% micrite (Mc), 4% sparite (Spr), and 1% oxide minerals (Ox). Microfacies analysis identifies this in-terval as a bioclastic rudstone, character-ized by a consist primarily of abundant Larger Benthic Foraminifera (LBF). Grain supported texture dominated by large skeletal grains (> 2 mm).

Large benthic Foraminifera (LBF)

Paleontological analysis of limestone samples revealed abundant larger benthic foraminifera (LBF), dominated by *Discocyclina* and *Pellatispira*, with a little *Miliolids* (Figure 4).

Discocyclina, characterized by flat to elongated morphologies, indicates deposition within the oligophotic zone, reflecting slightly deeper marine settings within the photic zone. Petrographic thin sections show evidence of bioerosion and micritization, with skeletal grains partly

replaced by dark micrite. The occurrence of *Pellatispira* provides a robust biostratigraphic marker for the Late Eocene, confirming the age of the lower limestone unit. This aligns with the global evolutionary framework established by BouDagher-Fadel (2018), which identifies the stratigraphic range of the genus Pellatispira as being restricted to the Late Eocene (Priabonian), particularly within the Tethyan and Indo-Pacific realms. The composition of this assemblage contrasts sharply with the younger Miocene LBF faunas common to the Northern Kutai Basin, confirming that this interval belongs to an older Eocene sequence.

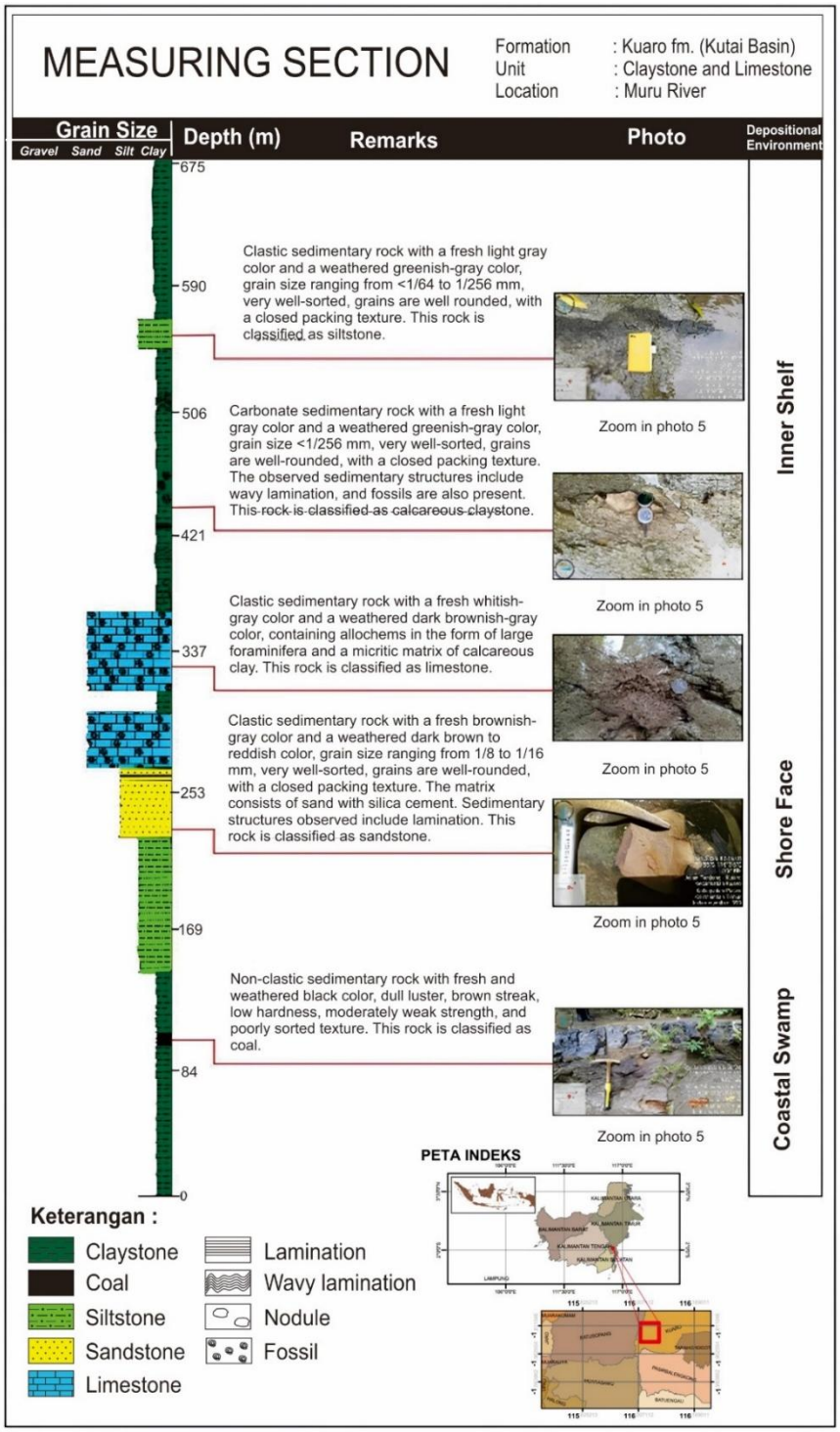

Figure 2. Measuring stratigraphic section of Muru River showing lithology and interpreted depositional environments.

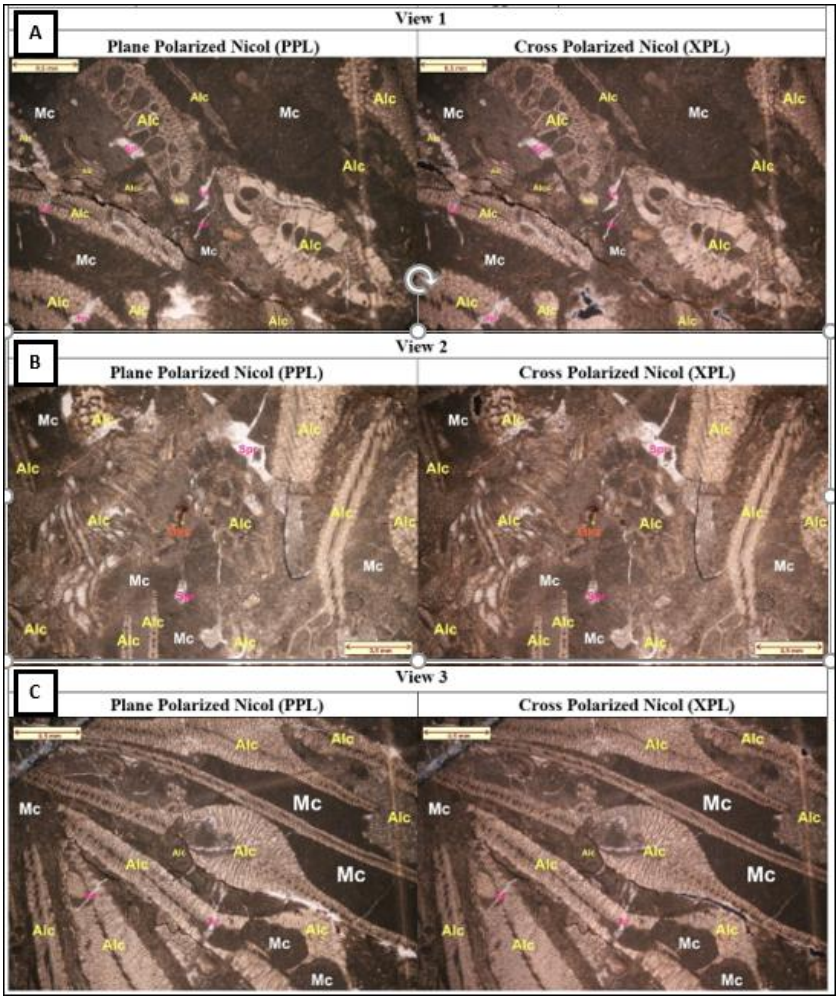

Figure 3. Thin-section photomicrographs of rudstone limestone (ALC : Allochem; MC : Micrite; SPR : Sparite).

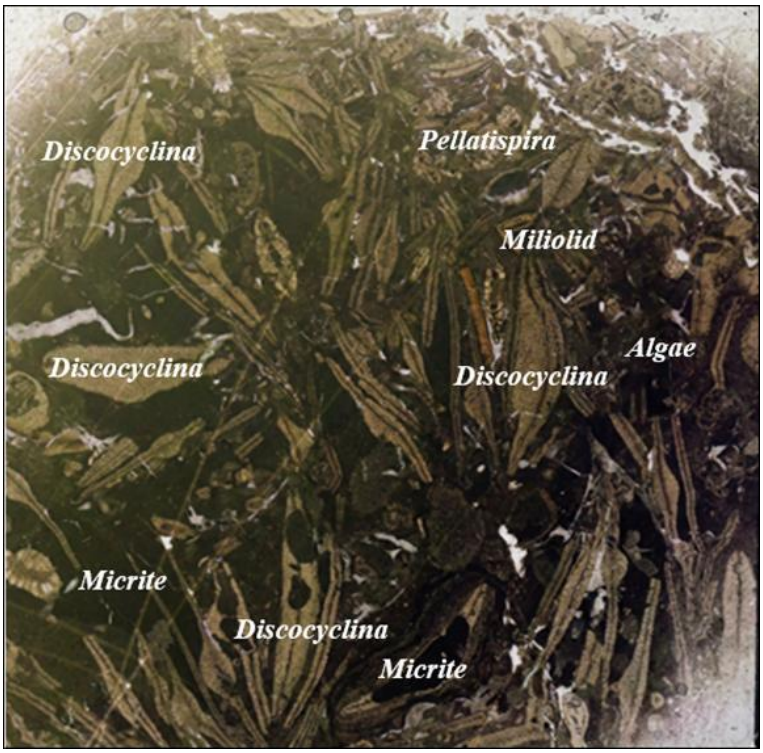

Figure 4. thin section of rock illustrating the distribution of large foraminifera in rudstone.

Calcareous Nannofossil Assemblages

Nannofossil analyses from marl and shale horizons yielded diverse assemblages, including *Cyclicargolithus floridanus*, *Reticulofenestra dictyoda*, *Reticulofenestra lockeri*, *Reticulofenestra bisecta*, *Helicosphaera mediterranea*, and *Braarudosphaera bigelowii*. Key species such as *Reticulofenestra bisecta* and *Reticulofenestra lockeri* are diagnostic of the Late Oligocene, thereby extending the stratigraphic range beyond the Late Eocene age indicated by the foraminiferal assemblages. While Jambak et al. (2024) utilized nannofossils to successfully define Miocene zonations (NN6–NN11) in the Kutai Basin, and Jamaluddin et al. (2024a) recently demonstrated the effectiveness of integrating nannofossils with sedimentological data to reconstruct depositional environments in the overlying Balikpapan Formation, our study confirms that nannofossil biostratigraphy remains a reliable tool for constraining the older Late Oligocene sequences as well. The identification of diagnostic markers in our samples validates the utility of this multi-proxy approach across different stratigraphic intervals of the basin. These results suggest that the section records a transition from the Late Eocene to the Late Oligocene, with overlapping fossil evidence reflecting temporal changes in depositional environments.

Coal and Shale Intervals

The section is generally dominated by interbedded limestone and calcareous claystone but transitions into a lower interval of thick shale with siltstone and coal intercalations (Figure 6), indicating a significant environmental shift. These characteristics strongly suggest deposition within a coastal swamp environment. The presence of coal confirms a regime of high organic productivity coupled with anoxic conditions, which are necessary for the preservation of organic matter (peat accumulation). The dull luster specifically points to a specific depositional setting within the swamp, likely indicating a slightly higher mineral content or 'ash' influx—possibly due to periodic flooding from nearby fluvial channels—or the accumulation of more decomposed plant material in a stagnant, low-energy mire. The poorly sorted texture further supports an autochthonous or hypo-autochthonous origin, implying that the vegetative matter accumulated in situ with minimal transport or winnowing by water currents. The coal indicates deposition in a coastal swamp or deltaic environment (lower delta plain), while the associated shale is interpreted as representing shore face or intertidal conditions (Figure 6).

This environmental interpretation aligns with the regional geochemical characterization by Winarno et al. (2018), who demonstrated that the specific properties of Kutai Basin coals are genetically linked to their formation in terrestrial-dominated deltaic and coastal swamp settings. In a broader context, recent evaluations by Jamaluddin et al. (2023; 2024b) further corroborate that such organic enrichment is strongly controlled by depositional conditions fluctuating between humid and arid periods within these swampy systems. Comparative studies in the adjacent Barito Basin by Fikri et al. (2022) further characterize these tropical peat systems as 'Kerapah' type peats, which represent a transitional environment crucial for understanding the organic matter preservation in this region. The dominance of terrestrial organic matter observed in the Kuaro Formation is characteristic of the Kutai Basin's deltaic systems. A similar trend is observed in the overlying Miocene Balikpapan Formation, where organic petrology analysis reveals a predominance of vitrinite macerals derived from higher plants deposited in delta plain to delta front environments, indicating a consistent supply of terrigenous material throughout the basin's history (Permana et al., 2018) Sedimentary structures such as

parallel bedding within these intervals further support their interpretation as shallow, regressive, and transitional depositional environments.

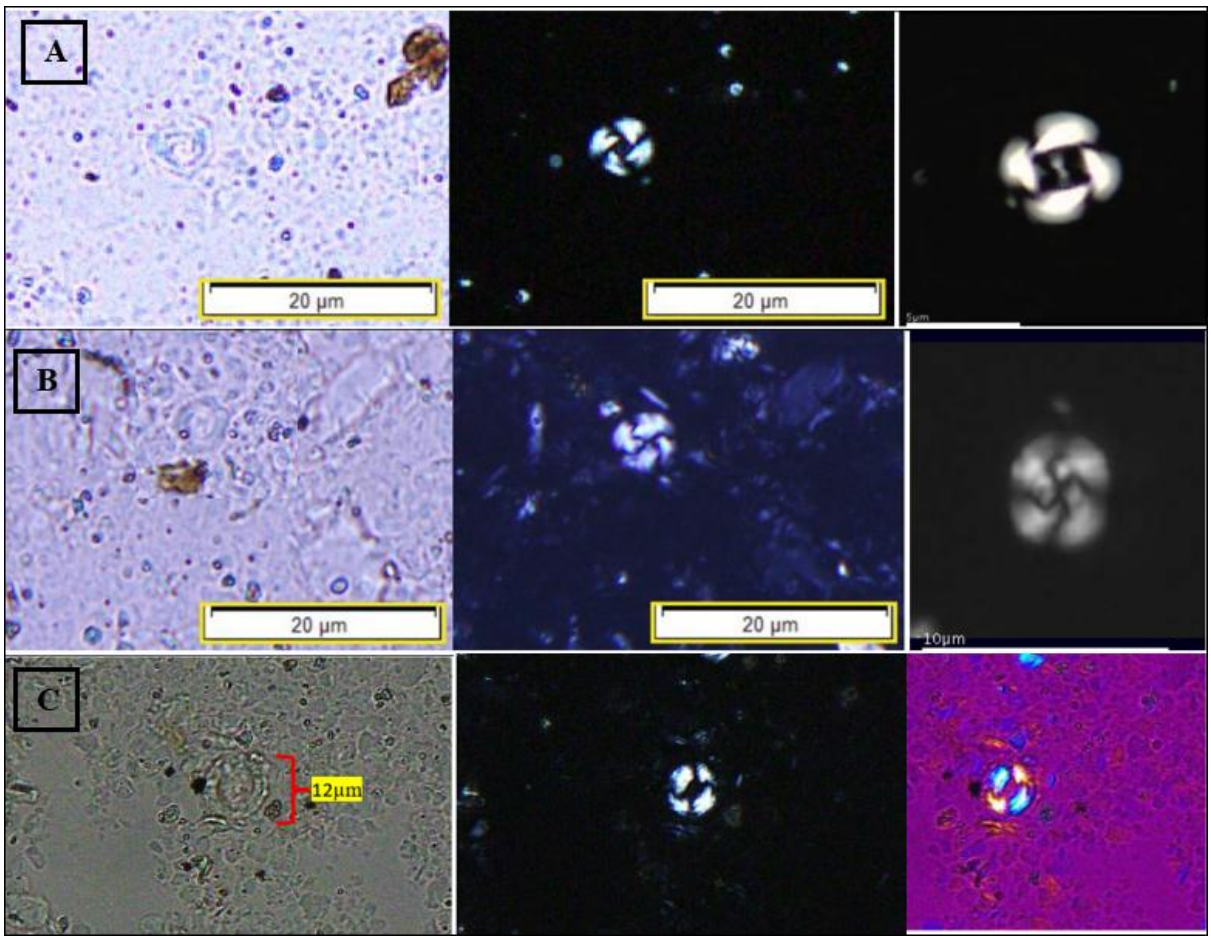

Figure 5. (A) *Reticulofenestra locker*; (B) *Reticulofenestra bisecta*, *Reticulofenestra dictyoda*.

Figure 6. A layer that shows a continuous layer of coal above a layer of shale and siltstone.

Stratigraphic Succession

This stratigraphic evolution reflects sustained relative sea-level fall, likely driven by a combination of eustatic and tectonic controls within the Kutai Basin margin. The stratigraphic succession records a distinct transgressive sequence, characterized by a transition from terrestrial-influenced deposits to open marine sediments. The depositional history commenced in a coastal swamp setting, evidenced by the accumulation of coal seams. The dull luster and poorly sorted texture of the coal imply a stagnant, low-energy, and anoxic mire environment where organic matter was preserved in situ. Following a relative rise in sea level, the environment evolved into a high-energy Shoreface to Shallow Marine zone. This transition is initially marked by the deposition of fine-grained sandstone exhibiting high textural maturity (very well-sorted and rounded grains). These characteristics indicate a regime dominated by wave action, effectively winnowing fine, clay-sized particles. Crucially, this interval is intercalated with bioclastic rudstones, characterized by a grain-supported texture and abundant Larger Benthic Foraminifera (LBF). The assemblage is dominated by *Discocyclina* and *Pellatispira*, with minor *Miliolids*. The presence of *Discocyclina* typically indicates deposition within the oligophotic zone (lower photic zone), while the rudstone texture implies that these skeletal grains were reworked by high-energy currents or waves. This development of a carbonate factory signifies a period of reduced terrigenous clastic input and warm, clear water conditions during the ongoing transgression. Finally, continued deepening of the environment.

The lithology fines upward into cal-careous claystone and siltstone, reflect-ing a significant reduction in flow energy as the depositional surface submerged below the fair-weather wave base. The presence of marine fossils and wavy lam-ination within these fine-grained units confirms a quiet, open marine setting dominated by suspension settling and weak bottom currents. This interpretation further supports the development of a ret-rogradational system controlled by re-duced sediment supply and increasing accommodation space during the Paleo-gene.

Conclusion

Based on the analysis, the measured stratigraphic section along the Muru River indicates a progressive and continuous marine transgression, an interpretation supported by both lithological changes and paleontological evidence. Initially, the Late Eocene depositional environment represented a warm, clear shallow marine setting, evidenced by massive rudstone limestone and confirmed by the presence of larger benthic foraminifera such as *Pellatispira* and *Discocyclina*. Subsequently, the section records an increase in clastic sediment input from the hinterland during the Eocene–Oligocene transition, characterized by alternating limestone and marl layers; although the coexistence of Eocene foraminifera and Late Oligocene nannofossils (*Reticulofenestra bisecta*) suggests potential fossil mixing or sam-pling variations, the overall succession confirms the section spans this transitional period. As the sequence progresses into the Late Oligocene and Early Miocene, a major environmental shift occurred to-ward transitional terrestrial, such as coastal swamps or deltaic systems, marked by the deposition of thick shale and coal layers to marine environments. This study provides one of the first integrated outcrop-based multi-proxy bio-stratigraphic frameworks for the Paleo-gene succession in the southern Kutai Basin. Ultimately, the stratigraphic succession records a progressive marine transgression, highlighting the transition from terrestrial to fully marine conditions and providing

important implications for understanding Paleogene basin evolution in the Southern Kutai Basin.

Acknowledgements

We sincerely appreciate everyone who contributed to the successful completion of this research. The author would like to express his deepest gratitude to the Head of the Sekolah Tinggi Teknologi Migas Balikpapan for the research grant provided through the LPPM which made this research possible. The author would also like to thank the editors of the Geocelebes Journal, the editors, and the reviewers for their assistance in completing and publishing this paper.

Author Contribution

Conceptualization, I.P.; methodology I.P., E.C.A.P.; validation, J., F.A.P.; Investigation and data curation, E.P.A., I.K.; writing-original draft presentation, J., E.C.A.P.; writing-review and editing, I.P. All authors have read and agreed to the published version of the manuscript.

Conflict of Interest

The authors declare no conflict of interest.

References

Adha, I., Utama, P. P., Eriyanto, M. I., Burhan, A. S., Opang, J. Y., Taslim, A. I., & Rhendo, A. Y. (2023). Identification and Analysis of Geoheritage Potential in Paser Regency as Supporter of the Geotourism Development in East Kalimantan. *Jurnal Ilmu Geologi Pangea*, 10(2), 51–60. https://doi.org/10.31315/jigp.v10i2.11183

Advokaat, E. L., Marshall, N. T., Li, S., Spakman, W., Krijgsman, W., & van Hinsbergen, D. J. J. (2018). Cenozoic Rotation History of Borneo and Sundaland, SE Asia Revealed by Paleomagnetism, Seismic Tomography, and Kinematic Reconstruction. *Tectonics*, 37(8), 2486–2512. https://doi.org/10.1029/2018TC005010

Battu, D. P., Adha, I., Kurniawan, T., Ryka, H., & Eriyanto, M. I. (2023). Potensi Geowisata di Kabupaten Paser, Kalimantan Timur. *Petrogas: Journal of Energy and Technology*, 5(1), 59–71. https://doi.org/10.58267/petrogas.v5i1.122

BouDagher-Fadel, M.K. (2018). *Evolution and geological significance of larger benthic foraminifera*. London: UCL Press. https://doi.org/10.14324/111.9781911576938

Darman, H. (2023). Paleogene paleogeographic reconstructions of the Kutai Basin: Refinement based on outcrop and subsurface data. *Berita Sedimentologi*, 49(1), 25–52. https://doi.org/10.51835/bsed.2023.49.1.397

Fikri, H. N., Sachsenhofer, R. F., Bechtel, A., & Groß, D. (2022). Organic geochemistry and petrography in Miocene coals in the Barito Basin (Tutupan Mine, Indonesia): Evidence for astronomic forcing in kerapah type peats. *International Journal of Coal Geology*, 256, 103997. https://doi.org/10.1016/j.coal.2022.103997

Irawati, S. M., Hidayat, H., Wijanarko, E., & Grandis, H. (2022). Integrated Magnetotelluric (MT), Gravity and Seismic Study of Lower Kutai Basin Configuration. *Journal of Engineering and Technological Sciences*, 54(1), 220103. https://doi.org/10.5614/j.eng.technol.sci.2022.54.1.3

Jamaluddin, J., Wagreich, M., Gier, S., Schöpfer, K., & Battu, D. P. (2023). Sedimentary Environments and Paleoclimate Control of the Middle

Miocene Balikpapan Group, Lower Kutai Basin (Indonesia): Implications for Evaluation of the Hydrocarbon Potential. *Minerals*, 13(10), 1259. https://doi.org/10.3390/min13101259

Jamaluddin, J., Wagreich, M., Schöpfer, K., Sachsenhofer, R. F., Maria, M., Rahmawati, D. (2024a). Hydrocarbon potential and depositional environment of the Middle Miocene Balikpapan Formation, lower Kutai Basin, Indonesia: Sedimentology, calcareous nannofossil, organic geochemistry, and organic petrography integrated approach. *International Journal of Coal Geology*, 293, 104591. https://doi.org/10.1016/j.coal.2024.104591

Jamaluddin, J., Wagreich, M., Schöpfer, K., Maria, M., Gier, S., Fathy, D. (2024b). Effect of Depositional Environment and Climate on Organic Matter Enrichment in Sediments of the Upper Miocene—Pliocene Kampungbaru Formation, Lower Kutai Basin, Indonesia. *Geosciences*, 14(6), 164. https://doi.org/10.3390/geosciences14060164

Jamaluddin, J., Jamaludin, S. N. F., Massinai, M. A., Zhang, S., Mansor, H. E., & Oscar, A. W. (2025). Paleoenvironmental Influences Evaluation on Sedimentary Organic Matter of the Kampungbaru Formation, Lower Kutai Basin: Organic and Inorganic Geochemical Approaches. *Journal of Geoscience, Engineering, Environment and Technology*, 10(4), 574–586. https://journal.uir.ac.id/index.php/JGEET/article/view/24526

Jambak, M. A., Deny, D., Rendy, R., & Syavitri, D. (2024). Miocene Paleogeographic Reconstruction in the Sangatta Area, East Kalimantan Based on Calcareous Nannofossil Biostratigraphy and Benthonic Foraminiferal Analysis. *Bulletin of the Marine Geology*, 39(2), 105–122. http://dx.doi.org/10.32693/bomg.39.2.2024.869

Martini, E. (1971). Standard Tertiary and Quaternary calcareous nannoplankton zonation. *Proceedings of the Second Planktonic Conference* (Rome, 1970), 2, 739–785.

Nisa, F. A., Jurnaliah, L., Winantris, W., & Nugrahanto, K. (2024). Environmental changes during the late Miocene to Pleistocene using small foraminifera and palynomorphs in the Kutai Basin, East Kalimantan. *Bulletin of the Marine Geology*, 39(2), 97–110. http://dx.doi.org/10.32693/bomg.39.2.2024.855

Permana, A. K., Sendjadja, Y. A., Panggabean, H., & Fauzely, L. (2018). Depositional Environment and Source Rocks Potential of the Miocene Organic Rich Sediments, Balikpapan Formation, East Kutai Sub Basin, Kalimantan. *Jurnal Geologi dan Sumberdaya Mineral*, 19(3), 171–186. https://jgsm.geologi.esdm.go.id/index.php/JGSM/article/view/407

Putri, E. C. A., Ryka, H., & Prabowo, I. (2025). Identifikasi dan Analisis Potensi Geosite sebagai Pendukung Pengembangan Kawasan Geowisata Daerah Paser, Kalimantan Timur. *Jurnal Teknik Geologi: Jurnal Ilmu Pengetahuan dan Teknologi*, 8(1), 20–27. http://dx.doi.org/10.30872/jtgeo.v8i1.15858

Rohmana, R. C., Fardiansyah, I., Taufani, L., & Harishidayat, D. (2019). Depositional processes and facies architec-ture of Balikpapan sandstone formation: Application of 3D digital outcrop model (DOM) to identify reservoir geometry and distribution in deltaic system. *Scientific Contributions Oil and Gas*, 42(1), 35–42. https://doi.org/10.29017/SCOG.42.1.379

Sehah, S., Rizqi, N. S., & Abdullatif, R. F. (2024). Modeling of Coal-Bearing

Rock Formations in The Kutai Basin, North Panajam Paser Regency, Kalimantan Based on Satellite Gravity Anomaly Data. *Earth Sciences Malaysia*, 8(2), 91–97. http://doi.org/10.26480/esmy.02.2024.91.97

Senduk, K. G., Jambak, M. A., Heriadi, R. R. S. A., & Syaifullah, K. A. (2021). Biostratigraphic analysis and age determination, depositional environment and paleoclimate at well X-section of the Kutai Basin, East Kalimantan region. *AIP Conference Proceedings*, 2363(1), 040016. http://dx.doi.org/10.1063/5.0063270

Sopan, L. E. P., Agustin, E., Kuncoro, K. H. A., Sarkowi, M., Kuswanto, A., Kumalasari, I. N., & Mulyasari, R. (2024). Identification of Basalt Rock Distribution Using Resistivity Geoelectric Method in The National Capital City (IKN), Paser, East Kalimantan. *Eksplorium*, 45(2), 91–98. https://doi.org/10.55981/eksplorium.2024.7081

Winarno, A., Amijaya, D. H., & Harijoko, A. (2018). Geochemical characterization of Kutai Basin coals using proximate and ultimate analysis. *IOP Conference Series: Earth and Environmental Science*, 212, 012033. https://doi.org/10.1088/1755-1315/212/1/012033

ISSN: 2579-5821 (Print)
ISSN: 2579-5546 (Online)
URL address: http://journal.unhas.ac.id/index.php/geocelebes
DOI: 10.70561/geocelebes.v10i1.50204

Jurnal Geocelebes Vol. 10 No. 1, April 2026, 108 – 120

Hypocenter Relocation using Teleseismic Double Difference Method (Case Study: West Sulawesi, Indonesia)

Harmita Lestari[1]*, Pepen Supendi[2], Andri Dian Nugraha[3], Wira Hadi Kusuma[1]

[1]Civil Engineering, State University of Makassar, Makassar, 90224, Indonesia
[2]Meteorology, Climatology and Geophysics Agency (BMKG), Jakarta, 10610, Indonesia
[3]Geophysics Engineering, Bandung Institute of Technology, Bandung, 40132, Indonesia

*Corresponding author. Email: harmita.lestari@unm.ac.id

Manuscript received: 8 March 2026; Received in revised form: 23 April 2026; Accepted: 28 April 2026

Abstract

This study analyzes seismicity in West Sulawesi through earthquake hypocenter relocation using the teleseismic double-difference (TeletomoDD) method. P-wave arrival times recorded by local, regional, and teleseismic stations from the Meteorology, Climatology, and Geophysics Agency (BMKG) were analyzed for the period January 2017 to January 2021. The hypocenter relocation results show a significant reduction in residual time, with most values concentrated between −10 and 10 before relocation and more than 50% near zero after relocation. The epicenters shifted toward the northwest and southeast, driven by the complex tectonic conditions and the presence of shallow faults, particularly along the Mamuju–Mamasa at depths of 5 km to 10 km. The average horizontal hypocenter shift was approximately 4.9 km relative to the routine BMKG catalog, with maximum corrections reaching approximately 17.7 km, and roughly 37.5% of events showing shifts 4–5 km, indicating a substantial improvement in the spatial accuracy of the original catalog. The seismicity analysis results indicated that the fault area was dominated by shallow earthquakes with an average earthquake magnitude of M > 4. The local tectonic regime, mainly controlled by an active shallow crustal thrust fault, suggests that the majority of seismic events are related to local faulting, although some mechanisms remain uncertain. The relocated hypocenter distribution obtained in this study indicates relatively high seismicity in the region. These findings provide improved constraints on seismicity patterns and fault geometry in West Sulawesi, which are important for understanding regional tectonics in more detailed.

Keywords: double difference; hypocenter relocation; Mamasa; Seismicity; West Sulawesi.

Citation: Lestari, H., Supendi, P., Nugraha, A.D., & Kusuma, W.H. (2026). Hypocenter Relocation using Teleseismic Double Difference Method (Case Study: West Sulawesi, Indonesia). *Jurnal Geocelebes*, 10(1): 108–120. https://doi.org/10.70561/geocelebes.v10i1.50204

Introduction

The tectonic setting of the southern arm of Sulawesi is characterized by two major groups: the Makassar Strait Thrust (MST) to the west and the Walanae Fault System (WFS) to the south (Jaya et al., 2023; Serhalawan & Chen, 2024). In the West Sulawesi, tectonic deformation had identified as a fold-and-thrust belt affecting Pliocene-aged rock units located offshore to the west of Mamuju (Brackenridge et al., 2020). This fold-and-thrust belt is interpreted to consist of a series of imbricated synthetic thrust faults, commonly referred to as the floor thrust (Yan et al., 2016). This structural system propagates westward and is bounded by the MST, which is subdivided into four distinct segments: Mamuju (MSTM), Central (MSTC), and North (MSTN), including a newly identified segment between the northern and central parts of the Makassar Strait Thrust (MST Central-North) (Hutchings & Mooney, 2021).

In the southern arm of Sulawesi (approximately 2°S to 4.5°S), seismic activity has increased following the 2018

Palu earthquake (Supendi et al. 2019), particularly in the Mamasa region, where earthquake swarm activity has been observed. This swarm is characterized by a sequence of clustered earthquakes with relatively small magnitudes (M < 5) (Figure 1). Between 2017 and 2021, earthquake data from the Meteorology, Climatology, and Geophysics Agency (BMKG) further indicate that West Sulawesi exhibits relatively high seismicity, especially along the Mamuju–Mamasa region (Figure 1).

The potential for a major destructive earthquake remains a significant threat to the Sulawesi region, which is charac-terized by an extensive network of active faults and a high prevalence of tra-ditional structures with limited seismic resistance (Widiyanto et al., 2019; Omira et al., 2019; Pasari et al., 2021). This concern is further supported by geophysical and geodetic evidence highlighting the region's complex tec-tonic setting. Tectonic complexity is evidenced by a three-dimensional shear-wave velocity model showing pro-nounced depth-dependent lateral heter-ogeneities, including a shallow low-velocity zone (≤ 14 km) and a high-velocity anomaly at depths of 20–30 km beneath the North Makassar Strait (Heryandoko et al., 2024). Moreover, interseismic GPS data indicate elevated crustal strain rates in the Mamuju and Majene regions compared to adjacent areas, suggesting heightened seismic vulnerability (Meilano et al., 2023). Additionally, Zenonos et al. (2020) identify Sulawesi as a transition zone with high Vp/Vs anomalies, re-flecting fluid-rich mantle conditions that promote mechanical weakening and strain localization, as evidenced by clustered seismicity in the region.

Over the last five decades, two significant and destructive earthquakes have occurred in the Mamuju–Majene region (indicated by red stars in Figure 1). Several destructive earthquakes have been historically recorded in the West Sulawesi region, including the Mw 7.0 event on 23 February 1969, the Mw 7.0 earthquake on 8 January 1984 (Supendi et al, 2021), and the more recent Mw 6.2 event on 14 January 2021 (Figure 1) in West Sulawesi, caused extensive building damage within approximately 30 km of the epicenter and was associated with a partial rupture of an east-dipping offshore fault west of Mamuju (Meilano et al., 2023). This indicates that extensive seismicity studies are needed to understand the earthquake patterns in West Sulawesi. To characterize seismic activity in Sulawesi, it is essential to analyze hypocenter relocation data in the context of the tectonic region and active fault systems.

Previous relocation studies in Sulawesi have demonstrated the importance of improving hypocenter accuracy for understanding local fault systems using the BMKG network data. For example, in Poso, Central Sulawesi (Supendi et al., 2018), Palu and Mamasa (Supendi et al., 2019), Palu Koro Fault (Ismullah et al., 2017), Mamuju-Majene (Supendi et al., 2021), Mamasa (Rosid et al., 2022), Central Sulawesi (Jayadi et al., 2023), which still uses a 1D velocity model. In contrast, the implementation of 3-D velocity models significantly reduces travel-time residuals and improves the resolution of subsurface structures, particularly in subduction and active faults. (Nugraha et al., 2018).

Previous studies on hypocenter relocation using the teleseismic double-difference (TeletomoDD) method have been conducted in entire Indonesia including West Sulawesi (Nugraha et al., 2019), Palu earthquake sequences (Supendi et al., 2020), and also in East Sulawesi (Lestari et al., 2022). However, previous studies have not provided detailed hy-pocenter relocation focusing on the Mamuju-Mamasa region using a

3D ve-locity model integrated with teleseismic observations, limiting the resolution of local fault geometry.

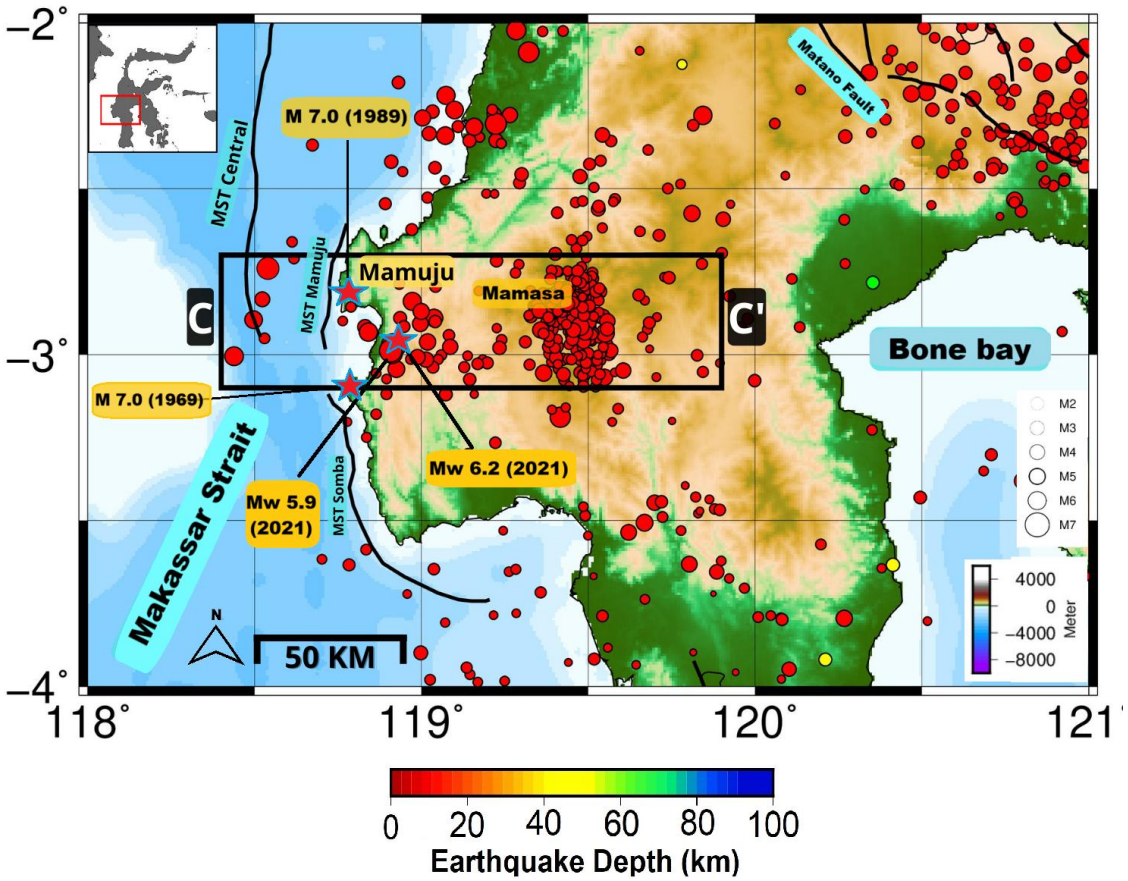

Figure 1. Seismicity map of Sulawesi (earthquake period: January 2017-January 2021 from the BMKG catalog). Earthquake data of M 7.0 in 1970 and M 7.0 in 1969 were taken from Supendi et al. (2021).

The teleseismic double-difference (TeletomoDD) method was proposed by Pesicek et al. (2010) to improve earthquake location accuracy and subsurface imaging. The advantage of this method is its ability to improve earthquake locations by jointly utilizing body-wave arrival times and differential time data observed at various distances (Pesicek et al., 2014). Hypocenter relocation using the TeletomoDD method improves the accuracy of earthquake locations and provides a clearer delineation of regional tectonic structures along the Sunda Arc (Nugraha et al., 2018).

Therefore, this study aims to improve the precise of earthquake hypocenter locations in West Sulawesi and delineate the spatial distribution of seismicity in relation to active fault systems using a 3D velocity model. In addition, this study evaluates the uncertainty of relocated hypocenters to ensure that the results can be interpreted within a robust tectonic framework.

Materials and Methods

Data used

The data used in this study are the arrival times of earthquakes from Indonesian Agency of Meteorology, Climatology, and Geophysics (BMKG) catalog from January 2017 to January 2021. The spatial extent of the study area covers approximately 118°E to 121°E in longitude and 4°S to 2°S in latitude, focusing on the Mamuju–Mamasa region and using earthquake data in those areas.

The earthquake data were then selected based on a minimum of six P-phases to reduce mis-location errors during the relocation process, resulting in 427 events. The S-wave phase was excluded from this study because most events were characterized by fewer than six recorded phases, which is insufficient to satisfy the minimum observational requirements for obtaining a stable and well-constrained hypocenter solution.

Teleseismic Double Difference

The basic equation of the double-difference method relates the residuals between the observed and predicted phase differences of travel times, dr_k^{ij}, for a pair of earthquakes i and j observed at the same station, k, to the change in the vector connecting the two hypocenters through the partial derivative of the travel time t, for each earthquake event with respect to the unknown model parameter, **m**, which is written in Equation 1 (Waldhauser & Ellsworth, 2000):

$$\frac{\partial t_k^i}{\partial \boldsymbol{m}} \Delta m_i - \frac{\partial t_k^j}{\partial \boldsymbol{m}} \Delta m_j = dr_k^{ij} \quad (1)$$

Similar to the local scale double-difference tomography method, the teleseismic double-difference method (Pesicek et al, 2010) can represent its extension to teleseismic distances using the following equation:

$$r_k^i = \sum_{l=1}^{3} \frac{\partial T_k^i}{\partial x_l^i} \Delta x_l^i + \Delta\tau^i + \sum_{n\epsilon G} w_n^G \delta u_n^G + \sum_{n\epsilon L} w_n^L \delta u_n^L + S_k \quad (2)$$

Where, r_k^i and r_k^j is residual arrival times for earthquakes i and j at station k, dr_k^{ij} is residual from *double-difference*, $\Delta\tau^i$ is the perturbation of the origin time for earthquakes i, $\Delta x_l^i (l = 1,2,3)$ is a location perturbation in three coordinate directions, δu_n^G and δu_n^L are slowness perturbations for global (G) and local (L) models. w_n^G and w_n^L is the ray lengths with respect to the global and local model nodes (n), S_k is a station correction.

The velocity models used in this study are the 3-D velocity model for Indonesia (Widiyantoro & van der Hilst, 1997) and the 1-D global velocity model AK135 (Kennett et al., 1995) for areas outside Indonesia, following previous studies (Nugraha et al., 2019). The background velocity model comprises 72 × 36 × 18 grid nodes along longitude, latitude, and depth, respectively, spanning global spherical coordinates from −180° to 180° longitude and −90° to 90° latitude, with depth nodes ranging from −50 km to 6000 km. This setup enables consistent ray tracing for phases from regional to teleseismic distances. Ray paths were calculated using the spherical pseudo-bending method, which incorporates Earth curvature and 3D velocity heterogeneity.

One of the important parameters that needs to be considered in the TeletomoDD inversion process is damping. The attenuation parameters depend on the amount of data and the condition number (CND). In this study, the CND value used was between 65 and 80 to balance data misfit reduction and model stability. The inversion adopts an L2-norm (least-squares) formulation, minimizing the squared residuals between observed and calculated travel times. This approach ensures stable convergence and produces a smooth model, although it may be sensitive to outliers in the data.

The inversion solver with three sequential iteration sets, resulting 11 iterations. The inversion process exhibits a rapid and consistent convergence, as indicated by the reduction of weighted RMS from an initial value of 0.955 s to approximately 0.62–0.65 s in iterations (1–3), followed by a more pronounced decrease to ~0.07 s in iterations (4–7). This represents an overall reduction of more than 90%, demonstrating a substantial improvement in the fit between observed and calculated travel times, where

early iterations correct major inconsistencies in the initial model.

The stations used in the relocation process are 284 seismic stations spread across and outside Indonesia, including teleseismic stations (Figure 2). In addition to local and regional data, this study utilizes teleseismic stations, defined as stations located at large epicentral distances from the earthquake source. The seismic stations used in this study are distributed across Southeast Asia and surrounding regions, approximately within 11°S to 11°N and 105°E to 132°E, ensuring broad azimuthal coverage. This wide distribution of stations enhances the stability and resolution of hypocenter relocation using the TeletomoDD method.

This study is limited to hypocenter relocation based on seismic travel-time data. The analysis is therefore focused on improving earthquake location accuracy and interpreting regional seismicity patterns.

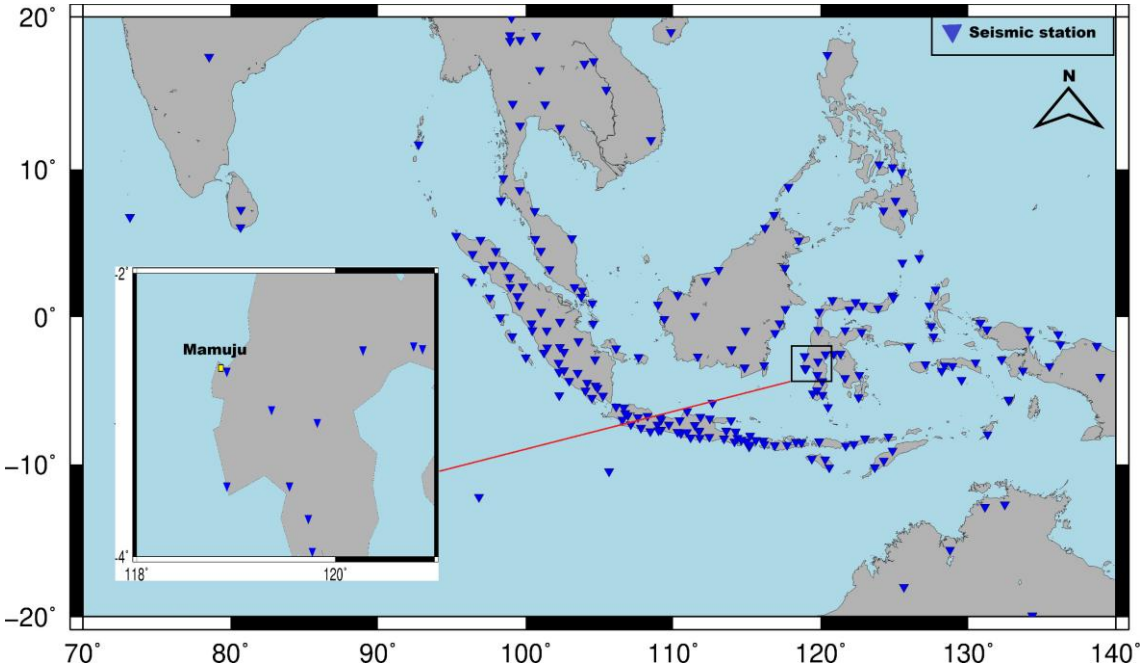

Figure 2. The distribution of seismic stations used in hypocenter relocation within and outside Indonesia, shown by the blue inverted triangles, and the black box, is the study area. Teleseismic stations are distributed over a distance of >1.000 km from the study area.

Results and Discussion

The mean of hypocenter shift is initially on the order of 4–5 km, reflecting substantial corrections to the initial catalog locations. This value progressively decreases to less than 1 m in the final iteration, suggesting a stable and well-constrained solution.

Figure 3 shows that the dominant direction of the relocation vectors is northwest-southeast, with some vectors oriented northeast-southwest. This is consistent with the orientation of the Makassar Strait Thrust, which generally trends northwest-southeast, as also mentioned in Meilano (2023).

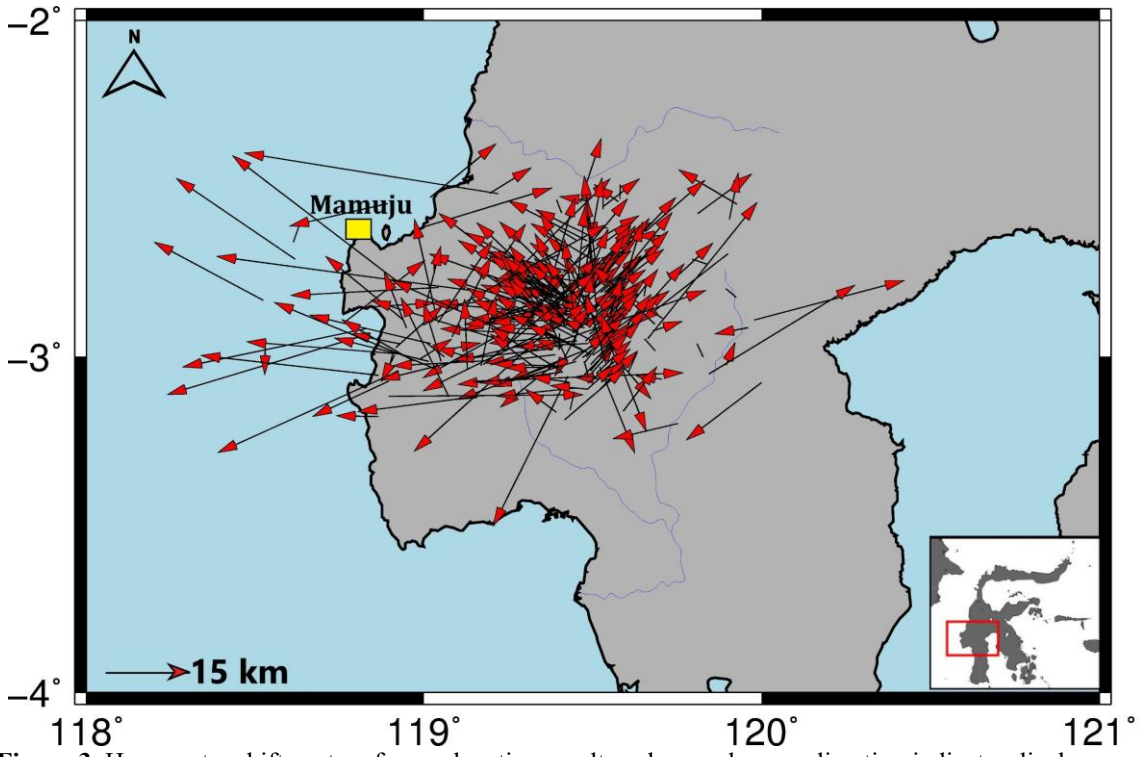

Figure 3. Hypocenter shift vectors from relocation results, where red arrow direction indicates displacement orientation and arrow length represents the magnitude of the shift, highlighting systematic corrections from initial to improved earthquake locations.

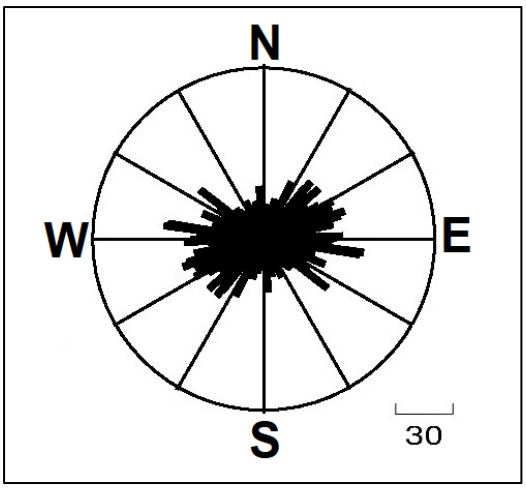

Figure 4. Rose diagram of epicenter shifts resulting from relocation in the Sulawesi region. It appears that direction of epicenter shifts is predominantly northwest and southeast due to the greater distribution of stations in the southeastern and western parts of Sulawesi.

The rose diagram analysis (Figure 4) further supports these findings, showing that the dominant earthquake directions are within ±20° of E–W. It appears that the earthquake epicenters predominantly moved toward the northwest and southeast. This pattern is likely controlled by the uneven station distribution in the southeastern and western parts of Sulawesi and the complex tectonic conditions in these areas. This is also due to the fact that earthquakes in Sulawesi are generally caused by land faults and are shallow earthquakes.

From Figure 5, the residual travel time obtained from the TeletomoDD results shows a significant reduction. In the TeletomoDD, the distance between the earthquake hypocenters is smaller than the distance between the earthquake and the station, so the raypaths of the two earthquakes can be considered the same. This can reduce the difference in residual travel times between the two earthquakes. The relocation results can be considered satisfactory if the residual time value approaches zero.

The depth distribution before relocation (Figure 6a) shows a relatively broad range of earthquake depths, with events extending to approximately 50 km and a peak at approximately 8–15 km. This

wide distribution likely reflects uncertainties in the initial hypocenter locations. After relocation (Figure 6b), the depth distribution becomes more concentrated at shallow depths (< 20 km), with a significant reduction in deeper events. This indicates an improvement in hypocenter accuracy and suggests that seismicity in the study area is dominated by shallow crustal earthquakes.

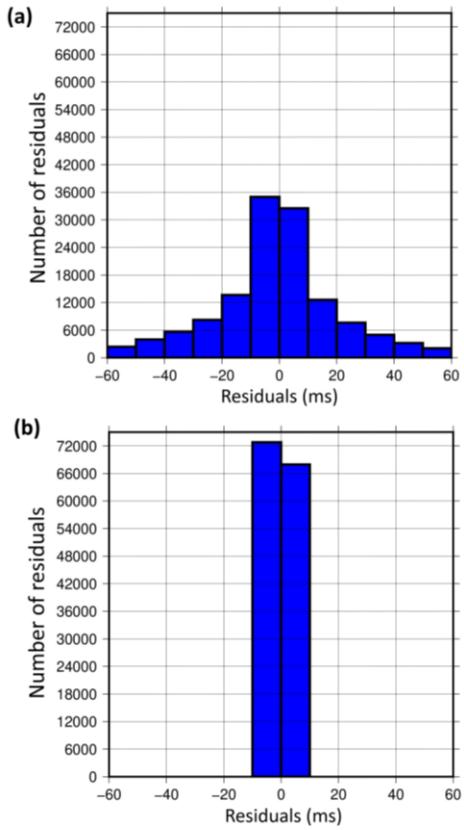

Figure 5. Residual time before (a) and after relocation (b) using the program TeletomoDD in the Sulawesi region. The relocation results show residual values approaching zero.

The horizontal distribution of hypocenters (Figure 7) shows a dominance of shallow crustal earthquakes (< 50 km). The distribution of earthquakes forms a cluster around Mamuju–Mamasa and follows the structure of active faults, including the Makassar Strait Fault, which reflects tectonic control of seismic activity. In this study, the Mamasa earthquake swarm is interpreted to be associated with a previously unidentified local fault system, as its relatively large distance from the MSTM suggests limited direct stress interaction. Previous studies indicate that the swarm is related to a shallow thrust fault mechanism and likely controlled by local fault activity, while also potentially influenced by subsurface fluid migration or hydrothermal processes (Supendi et al., 2019; Rosid et al., 2022; Serhalawan & Chen, 2024).

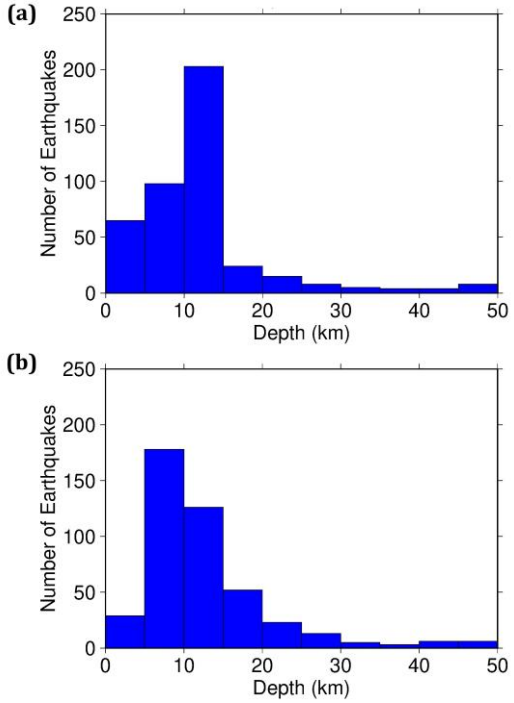

Figure 6. Histogram of the distribution of earthquake depth against the number of events, where panel (a) shows data before relocation, while panel (b) after hypocenter relocation.

In addition, beneath the MSTM (Figure 8b), two earthquakes with M>5 occurred on January 14, 2021 (Mw 5.9) and January 15, 2021 (Mw 6.2). Based on the hypocenter relocation results from this study, Figure 8b shows that Mw 6.2 events occurred beneath the MSTM. Analysis of the focal mechanism solutions (Supendi et al., 2021) indicates that the event was most likely related to activity within the Majene-Mamuju fold and thrust belt system. This interpretation is in line with previous findings from Gunawan et al. (2022), where the Mw 6.2 earthquake occurred along the bending

fault plane of MSTM, although this conclusion is based on geodetic inversion and stress analysis.

There were more than 10 earthquake events with magnitude ≥ M4 that occurred along the MSTM at depths of 5–15 km. These earthquakes form a southeastward alignment, indicating the direction of the MSTM, consistent with the findings of Supendi et al. (2019). This condition warrants attention due to the high seismicity in this shallow-depth region.

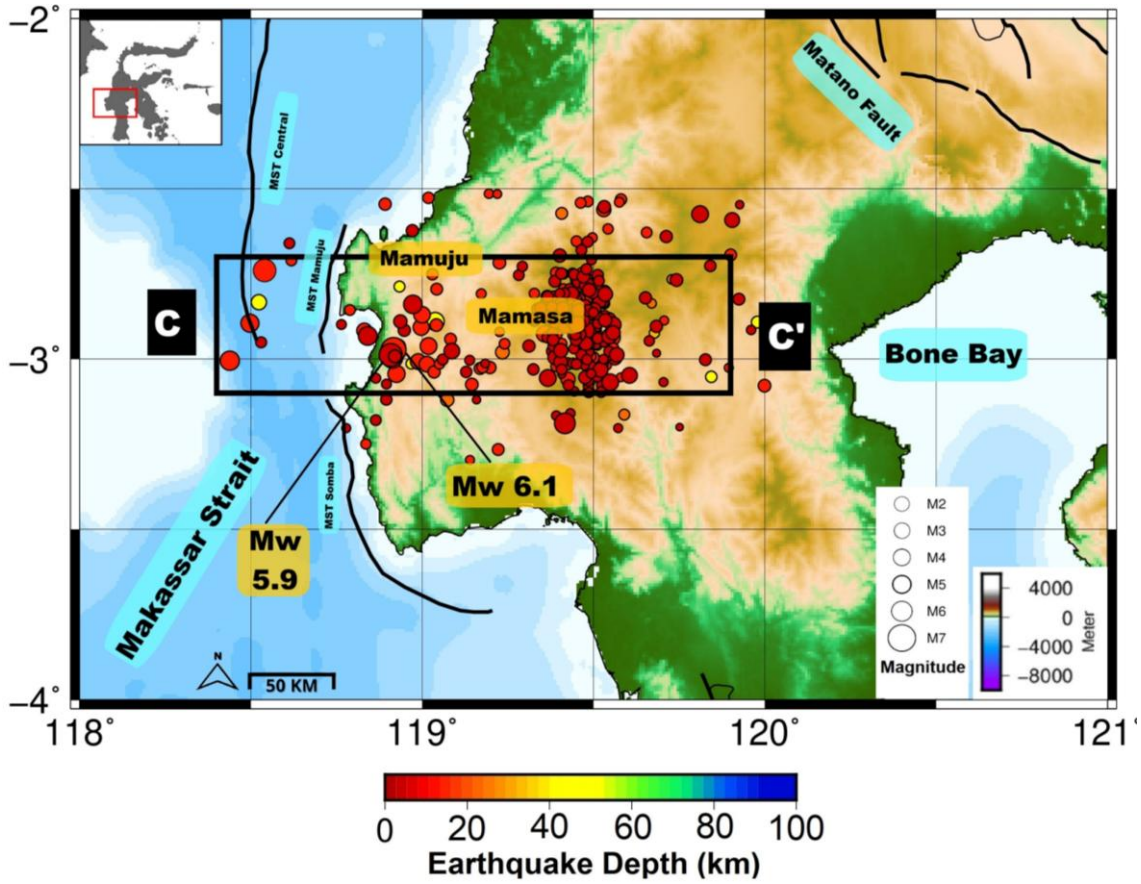

Figure 7. The seismicity map of West Sulawesi shows the distribution of earthquake hypocenters represented by circle symbols, with color indicating depth (±0–100 km). Significant earthquake events (M 5.9, and M 6.2). The horizontal cross-section (C–C') line indicates the location of the cross-section for depth distribution analysis. Black box is the area that is the focus of interpretation. The black lines are faults lines from the Geological Agency.

In addition, an earthquake swarm (Figure 7) is observed as a distinct cluster located approximately 30–40 km from the main seismic activity, with events predominantly characterized by magnitudes of M 3–4 and occurring at shallow depths of 0–10 km beneath Mamasa Regency. This cluster is therefore identified as the Mamasa earthquake swarm. The swarm, which persisted for approximately 30 days (Supendi et al., 2019), is consistent with the interpretation of Sallarès & Ranero (2019) that shallow seismicity often exhibits prolonged duration and low-frequency radiation, indicating sustained rupture processes within the shallow crust. In this context, direct dynamic triggering from distant seismic sources (~230 km) is unlikely, as it exceeds the typical timescale of dynamic stress transfer (O'Malley et al., 2018).

Figure 8b shows the distribution of hypocenters is dominated by shallow to intermediate depths (±5–25 km), with a

main cluster identified in the eastern part (~100–130 km) and a secondary cluster in the central part (~50–80 km). The presence of scattered shallow earthquakes and several outliers at greater depths reflects the uncertainty of the location before the relocation process.

Figure 8b shows the epicenter locations in West Sulawesi, specifically in Mamuju and Majene. It appears that some earthquake epicenters are located around the MSTM. However, focal mechanism calculations using the global CMT (Ekström et al., 2012), available at https://www.globalcmt.org, indicate that these events are predominantly characterized by a thrust faulting mechanism. This finding suggests a strong association between the observed seismicity and the Mamuju Thrust, which is known to exhibit a thrust fault-ing mechanism.

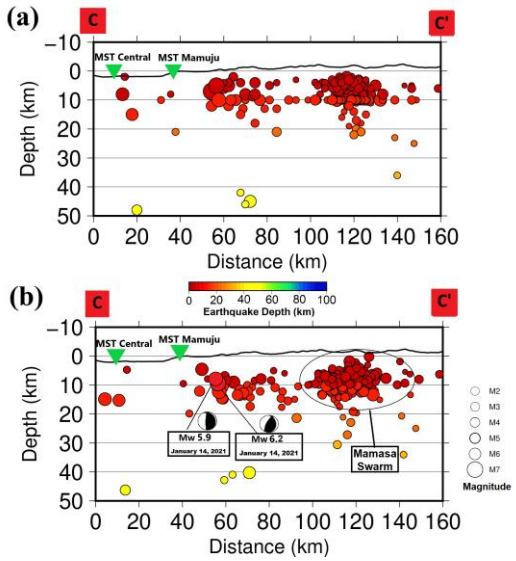

Figure 8. The vertical cross-section of seismicity along the C–C' (west–east) before hypocenter relocation (a) and after relocation (b) shows the distribution of earthquakes with respect to depth (0–50 km) and horizontal distance. Each circle represents an earthquake event, with the size of the symbol indicating the magnitude (M2–M7) and colors indicating depth variations.

The results of the earthquake relocation show that the earthquake hypocenter depth ranges from 5 to 10 km, with the hypocenter becoming deeper as it moves farther west, reaching 40 km (Figure. 8b). The dominant seismicity cluster was identified at shallow to intermediate depths (±10–30 km), particularly in the eastern part (~100–130 km), known as the "Mamasa swarm" zone. Significant earthquake events (Mw 5.9; and Mw 6.2) occurred. The more focused distribution pattern compared to before the relocation indicates a clearer earthquake source geometry.

The shallow earthquakes along the Mamuju-Mamasa area indicate that the source of the earthquakes originates from shallow crustal faulting. Analysis of the hypocenter relocation performance using the TeletomoDD method (shows significant results, where the fixed-depth issue (Figure 8a) was resolved (Figure 8b), and provide a new description about the sequence of earthquakes along the MSTM and MSTC.

Conclusion

relocation was performed using TeletomoDD method applied to the BMKG catalog for the period January 2017 to January 2021, resulting in 465 relocated events in West Sulawesi. The relocation results demonstrate a significant reduction in travel-time residuals and produce a more coherent clustering of seismic events that better correlates with known geological structures. Earthquakes in Mamuju are dominated by shallow crustal earthquakes. Earthquakes occurring along the Mamuju-Mamasa region are likely associated with the MSTM. The Mamasa swarm indicates stress redistribution rather than activity on a single fault plane as in the Mamuju earthquakes.

Acknowledgements

We thank the Meteorology, Climatology, and Geophysics Agency (BMKG), Re-

gion IV Makassar, Indonesia, which provides the catalog data. All map figures in this study were made using Generic Mapping Tools (GMT) (Wessel et al., 2019) which is available online at www.soest.hawaii.edu/gmt.

Author Contribution

Harmita Lestari: Conceptualization, Methodology, Data curation, Formal analysis, Software, Visualization, Writing original draft.
Pepen Supendi: Supervision, Methodology, Validation, Writing - review and editing.
Andri Dian Nugraha: Investigation, Resources, Validation.
Wira Hadi Kusuma: Data curation, Visualization, Software.

Conflict of Interest

The authors declare that there is no conflict of interest regarding the publication of this paper.

References

Brackenridge, R. E., Nicholson, U., Sapiie, B., Stow, D., & Tappin, D. R. (2020). Indonesian Throughflow as a preconditioning mechanism for submarine land-slides in the Makassar Strait. *Geological Society, London, Special Publications*, 500, 195–217. https://doi.org/10.1144/SP500-2019-171

Ekström, G., Nettles, M., & Dziewonski, A. M. (2012). The global CMT project 2004–2010: Centroid-moment tensors for 13,017 earthquakes. *Physics of the Earth and Planetary Interiors*, 200–201, 1–9. https://doi.org/10.1016/j.pepi.2012.04.002

Gunawan, E., Kholil, M., & Widiyantoro, S. (2022). Coseismic slip distribution of the 14 January 2021 Mamuju–Majene, Sulawesi, earthquake derived from GPS data. *Natural Hazards*, 111(1), 939–948. https://doi.org/10.1007/s11069-021-05084-y

Heryandoko, N., Nugraha, A. D., Zulfakriza, Z., Rosalia, S., Yudistira, T., Rohadi, S., Daryono, D., Supendi, P., Nurpujiono, N., Yusuf, F., Fauzi, F., Lesmana, A., Husni, Y. M., Prayitno, B. S., Triyono, R., Adi, S. P., Karnawati, D., Greenfield, T., Rawlinson, N., & Widiyantoro, S. (2024). Crustal structure of Borneo, Makassar Strait and Sulawesi from ambient noise tomography. *Geophysical Journal International*, 237(2), 949–964. https://doi.org/10.1093/gji/ggae085

Hutchings, S. J., & Mooney, W. D. (2021). The seismicity of Indone-sia and tectonic implications. Geochemistry, *Geophysics, Geosystems*, 22(9), e2021GC009812. https://doi.org/10.1029/2021GC009812

Ismullah, M. F., Nugraha, A. D., Ramdhan, M., & Wandono, W. (2017). Precise hypocenter determination around Palu Koro fault: A preliminary result. *IOP Conference Series: Earth and Environmental Science*, 62, 012056. https://doi.org/10.1088/1755-1315/62/1/012056

Jaya, A., Nishikawa, O., & Jumadil, S. (2023). Paleoseismic analysis of the Walanae Fault Zone in South Sulawesi, Indonesia. *Indonesian Journal on Geoscience*, 10(2), 215–227. https://doi.org/10.17014/ijog.10.2.215-227

Jayadi, H., Janat, N. R., Santosa, B. J., Warnana, D. D., Nugraha, A. D., Leopatty, H., Asyhar, I. F., Meidji, I. U., Fitriana, T., & Ninasafitri. (2023). Hypocenter relocation of local earthquake using double dif-ference method in Central Sula-wesi from BMKG network data: Time

periods of July 26–August 18, 2021. *IOP Conference Series: Earth and Environmental Science*, 1157(1), 012023. https://doi.org/10.1088/1755-1315/1157/1/012023

Kennett, B. L. N., Engdahl, E. R., & Buland, R. (1995). Constraints on seismic velocities in the Earth from traveltimes. *Geophysical Journal International*, 122(1), 108–124. https://doi.org/10.1111/j.1365-246X.1995.tb03540.x

Lestari, H., Nugraha, A. D., Supendi, P., & Ismullah, M. F. (2022). Preliminary results: Application of teleseismic double-difference method for earthquake hypocenter relocation and seismicity analysis in East Sulawesi region using a 3D seismic velocity model. *Proceedings of the 47th Annual Scientific Meeting of the Himpunan Ahli Geofisika Indonesia* (Malang, Indonesia, October 10–13, 2022).

Meilano, I., Salman, R., Susilo, S., Ash Shiddiqi, H., Supendi, P., Lythgoe, K., Tay, C., Bradley, K., Rahmadani, S., Kristyawan, S., & Yun, S.-H. (2023). The 2021 Mw 6.2 Mamuju, West Sulawesi, Indonesia earthquake: Partial rupture of the Makassar Strait thrust. *Geophysical Journal International,* 233(3), 1694–1707. https://doi.org/10.1093/gji/ggac512

Nugraha, A. D., Shiddiqi, H. A., Widiyantoro, S., Thurber, C. H., Pesicek, J. D., Zhang, H., Wiyono, S. H., Ramdhan, M., Wandono, W., & Irsyam, M. (2018). Hypocenter relocation along the Sunda arc in Indonesia, using a 3D seismic-velocity model. *Seismological Research Letters*, 89(2A), 603–612. https://doi.org/10.1785/0220170107

Nugraha, A. D., Rosalia, S., Widiyantoro, S., Supendi, P., Wiyono, S., & Daryono, D. (2019). Updating hypocenter relocation in Indonesia using 3D seismic velocity model: Period of April 2009–March 2018. *IOP Conference Series: Earth and Environmental Science,* 318(1), 012048. https://doi.org/10.1088/1755-1315/318/1/012048

O'Malley, R. T., Mondal, D., Goldfinger, C., & Behrenfeld, M. J. (2018). Evidence of systematic triggering at teleseismic distances following large earthquakes. *Scientific Reports*, 8, 11611. https://doi.org/10.1038/s41598-018-30019-2

Omira, R., Dogan, G. G., Hidayat, R., Husrin, S., Prasetya, G., & Annunziato, A. (2019). The September 28th, 2018 tsunami in Palu, Sulawesi, Indonesia: A post-event field survey. *Pure and Applied Geophysics*, 176, 1379–1395. https://doi.org/10.1007/s00024-019-02145-z

Pasari, S., Simanjuntak, A. V. H., Neha, N., & Sharma, Y. (2021). Nowcasting earthquakes in Sulawesi Island, Indonesia. *Geoscience Letter*s, 8, 23. https://doi.org/10.1186/s40562-021-00197-5

Pesicek, J. D., Thurber, C. H., Widiyantoro, S., Zhang, H., DeShon, H. R., & Engdahl, E. R. (2010). Teleseismic double-difference relocation of earthquakes along the Sumatra–Andaman subduction zone using a 3-D model. *Journal of Geophysical Research: Solid Earth,* 115(B10), B10303. https://doi.org/10.1029/2010JB007443

Pesicek, J. D., Zhang, H., & Thurber, C. H. (2014). Multiscale seismic tomography and earthquake relocation incorporating differential time data: Application to the Maule subduction zone, Chile. *Bulletin of the Seismological Society of America*, 104(2), 1–16.

https://doi.org/10.1785/0120130121

Rosid, M. S., Ali, Y. H., & Ramdhan, M. (2022). Characterization of the Mamasa earthquake source based on hypocenter relocation and gravity derivative data analysis. *International Journal of GEOMATE,* 23(97), 220–227. https://doi.org/10.21660/2022.97.j2375

Sallarès, V., & Ranero, C. R. (2019). Upper-plate rigidity determines depth-varying rupture behaviour of megathrust earthquakes. *Nature*, 576(7785), 96–101. https://doi.org/10.1038/s41586-019-1784-0

Serhalawan, Y., & Chen, P.-F. (2024). Seismotectonics of Sulawesi, Indonesia. *Tectonophysics*, 883, 230366. https://doi.org/10.1016/j.tecto.2024.230366

Supendi, P., Nugraha, A. D., Puspito, N. T., Widiyantoro, S., Daryono, & Wiyono, S. H. (2018). Identification of active faults in West Java, Indonesia, based on earthquake hypocenter determination, relocation, and focal mechanism analy-sis. *Geoscience Letters*. https://doi.org/10.1186/s40562-018-0130-y

Supendi, P., Nugraha, A. D., Widiyantoro, S., Abdullah, C. I., Puspito, N. T., Palgunadi, K. H., Daryono, D., & Wiyono, S. H. (2019). Hypocenter relocation of the aftershocks of the Mw 7.5 Palu earthquake (September 28, 2018) and swarm earthquakes of Mamasa, Sulawesi, Indonesia, using the BMKG network data. *Geoscience Letters*, 6(1), 18. https://doi.org/10.1186/s40562-019-0148-9

Supendi, P., Nugraha, A. D., Widiyantoro, S., Pesicek, J. D., Thurber, C. H., Abdullah, C. I., Daryono, D., Wiyono, S. H., Shiddiqi, H. A., & Rosalia, S. (2020). Relocated aftershocks and background seismicity in eastern Indonesia shed light on the 2018 Lombok and Palu earthquake sequences. *Geophysical Journal International*, 221(3), 1845–1855. https://doi.org/10.1093/gji/ggaa118

Supendi, P., Nugraha, A. D., Widiyantoro, S., Abdullah, C. I., Puspito, N. T., Daryono, D., & Wiyono, S. H. (2021). Foreshock–mainshock–aftershock sequence analysis of the 14 January 2021 (Mw 6.2) Mamuju–Majene (West Sulawesi, Indonesia) earthquake. *Geoscience Letters*, 8, 1–13. https://doi.org/10.1186/s40623-021-01436-x

Waldhauser, F., & Ellsworth, W. L. (2000). A double-difference earthquake location algorithm:Method and application to the Northern Hayward fault, California. *Bulletin of the Seismological Society of America*, 90, 1353–1368. https://doi.org/10.1785/0120000006

Wessel, P., Luis, J. F., Uieda, L., Scharroo, R., Wobbe, F., Smith, W. H. F., & Tian, D. (2019). The Generic Mapping Tools version 6. *Geochemistry, Geophysics, Geosystems*, 20(11), 5556–5564. https://doi.org/10.1029/2019GC008515

Widiyanto, W., Santoso, P. B., Hsiao, S.-C., & Imananta, R. T. (2019). Post-event field survey of the 28 September 2018 Sulawesi earth-quake and tsunami. *Natural Hazards and Earth System Sciences*, 19, 2781–2794. https://doi.org/10.5194/nhess-19-2781-2019

Widiyantoro, S., & Van Der Hilst, R. D. (1997). Mantle structure beneath Indonesia inferred from high-resolution tomographic imaging. *Geophysical Journal International,*

130(1), 167–182. https://doi.org/10.1111/j.1365-246X.1997.tb00996.x

Yan, D.-P., Xu, Y.-B., Dong, Z.-B., Qiu, L., Zhang, S., & Wells, M. (2016). Fault-related fold styles and progressions in fold-thrust belts: Insights from sandbox modeling. *Journal of Geophysical Research: Solid Earth*, 121, 2087–2111. https://doi.org/10.1002/2015JB012397

Zenonos, A., De Siena, L., Widiyantoro, S., & Rawlinson, N. (2020). Direct inversion of S–P differential arrival times for Vp/Vs ratio in SE Asia. *Journal of Geophysical Research: Solid Earth*, 125(4), e2019JB019152. https://doi.org/10.1029/2019JB019152

ISSN: 2579-5821 (Print)
ISSN: 2579-5546 (Online)
URL address: http://journal.unhas.ac.id/index.php/geocelebes
DOI: 10.70561/geocelebes.v10i1.20270

Jurnal Geocelebes Vol. 10 No. 1, April 2026, 121 – 132

Determination of Weak Zone using Wenner Configuration in Jendral Sudirman Street Section Muara Bulian, Batang Hari

Fitriyanti Retno Siwi[1], Linda Handayani[1], Buhaira[2]*

[1]Study Program of Geophysical Engineering, Faculty of Science and Technology, Jambi University, Jambi-Muara Bulian Street Km 15, Jambi, 36361, Indonesia.
[2]Study Program of Agroecotechnology, Faculty of Agriculture, Jambi University, Jambi-Muara Bulian Street Km 15, Jambi, 36361, Indonesia.

*Corresponding author. Email: boy_buhaira@unja.ac.id

Manuscript received: 8 March 2022; Received in revised form: 1 May 2022; Accepted: 13 September 2022

Abstract

Jenderal Sudirman road is an alternative road used to avoid traffic congestion located on the National Causeway in Muara Bulian District, Batang Hari, Jambi. The road has a weak zone so that the purpose of this study, determines the subsurface structure and distribution of the weak zone on Jenderal Sudirman roads, Muara Bulian, Batang Hari, Jambi. The weak zone, namely the soil, decreases due to a large load so that there is ablaze on the road. Road damage one of which is damaged edges can result in accidents. Determination of weak zones using Wenner Configuration Geoelectric Method and DCPT data. Lines 1 and 2 are in the alluvial area (Qa) and Line 3 and 4 in the Kasai Formation (QTk). The first line of the weak zone at 17 – 44 m with a thickness of 3 – 10 m is located near the surface and below the surface at 45 – 95 m is estimated at a depth of 3 – 10 m with a thickness of 8 m with fine sandstone lithology. The weak zone on line 2 is near the surface at 20 – 28 m is estimated to be 6 m thick and at 40 – 77 m it is estimated at a depth of 3 – 5 m with a thickness of 2 – 6 m located under the surface of the clay periphery to a layer of fine sand saturated with water. The weak zone on line 3 is located at 20 – 56 m with a depth of 8 m and a thickness of 6 m located below the surface. The weak zone on track 4 is located at 35 – 87.5 m with a depth of 3 m and a thickness of 3 – 10 m. DCPT results from Robertson's 1986 chart and sondir graph obtained a weak zone at a depth of 0 m to 10.60 m with a conus pressure below 20 kPa.

Keywords: DCPT; weak zone; Wenner configuration.

Citation: Siwi, F. R., Handayani, L., & Buhaira, B. (2023). Determination of Weak Zone using Wenner Configuration in Jendral Sudirman Street Section Muara Bulian, Batang Hari. *Jurnal Geocelebes* 10(1): 121–132, doi: 10.70561/geocelebes.v10i1.20270

Introduction

Background

Economic growth is getting higher and the population is increasing. This has an impact on traffic density, especially national roads that connect between cities. In addition, economic activities are also increasing, such as the opening of mining areas, oil palm plantations are increasingly widespread, demanding dense mobilization and can occur congestion due to accidents or cars stopping because they are damaged due to too large car loads. The car load of coal trucks and palm oil tanks, if it continues to increase, will cause subsidence and even collapse due to weak zones that can cause the road to deteriorate quickly. even due to road compaction there are accidents that cause deaths.

The congestion of the National Cross Road has caused several vehicles to switch to using alternative roads, one of which is the Jendral Sudirman Road, Muara Bulian Village, Muara Bulian District, Batang Hari Regency, Jambi. However, this road also has a weak zone that at any time within a

certain period of time will cause road damage. The threat of road damage due to subsurface weak zones will result in natural disasters, such as liquefaction, the level of soil layer density is very loose and the geological area consists of sandstones and sedimentary deposits as shown in Figure 1. (Yudiana et al., 2020).

Figure 1. Sighting of the Jendral Sudirman Road, Muara Bulian, Batang Hari.

This research also contains data from the Dutch Cone Penetration Test (DCPT), which is an effective method to determine the soil in situ, especially in areas with unconsolidated rock and soil layers, soft materials, organic materials and materials that have the potential for liquefaction. (Pranantya et al., 2018).

Weak zones are zones in rocks that have low resistivity values and high porosity and have very loose soil density. This zone will collapse if exposed to continuous loads. One of the geophysical methods that can be used to investigate rock weak zones is the geoelectric method (Makmur et al., 2016). This research is intended to determine the subsurface structure and determine the distribution of weak zones based on the Wenner configuration geoelectric method located on Jendral Sudirman Road, Muara Bulian, Batang Hari.

Regional Geology

The Jendral Sudirman Road, Muara Bulian, Batang Hari crosses 2 formations, which are the alluvial formation (Qa), and the kasai formation (QTk) based on the Regional Geological Map of Muara Bungo Sheet (Appendix 1-2).

Physiographically, the Batang Hari area is located in the western part of the South Sumatra Basin, which is a lowland area in eastern Sumatra, bounded by the Semangko Fault and Bukit Barisan to the southwest, the Sunda Shelf to the northeast, the Lampung Plateau to the southeast separating the basin from the Sunda Basin, and the Twelve Mountains and Thirty Mountains to the northwest separating the South Sumatra Basin from the Central Sumatra Basin (Wisnu & Nazirman, 1997).

Basic Theory

1. Weak Zone

A weak zone is an area of soil or rock with lower soil mechanics than the surrounding rock mass. Weak zones are defined as

subsurface layers of highly susceptible materials, including wet clay, dry clay, dry sand, water and subsurface air voids. Weak zones can be fault zones, shear zones, weak layers or materials (Ramadianti et al., 2019).

The weak zone can be associated with liquefaction, which is the phenomenon of soil masses experiencing a loss of shear resistance value due to conditions that are monotonous, repetitive, cyclic (dynamic) and shock loading so that the soil is like a liquid that flows until the shear stress that occurs in the soil mass has a value as low as the shear resistance value (Sladen et al., 1985).

The weak zone can also be seen from the road collapse event which shows that the stability of the supporting rock below the road surface has decreased due to disruption of the continuity of rock strength in the subsurface structure (Soedarsono, 2006). One of the methods to identify weak zones in roads is the geoelectric method, which is the first step to investigate the subsurface geological structure (Akinlalu et al., 2016).

2. Geoelectric Method

The basic concept of the geo-metric method is Ohm's Law. In 1826 George Simon Ohm conducted research that determined the relationship between the voltage (V) on the conductor and the current (I) through the conductor within the limits of the characteristic parameters of the conductor. This parameter is called resistance R, which is defined as the quotient of voltage (V) and current (I), so it is written as:

$$R = \frac{V}{I} \; or \; V = IR \qquad (1)$$

The earth is assumed to be an isotropic homogeneous medium but in reality it is a nonhomogeneous medium consisting of many layers with different resistivity values, so that the measured resistivity value is not the true resistivity value but the apparent resistivity value. The apparent resistivity value is formulated as follows:

$$\rho_a = K\frac{\Delta V}{I} \qquad (2)$$

with ρ_a is the apparent resistivity value, ΔV is the potential value and I is the current value. The value of K depends on the type of configuration to be used.

Mapping is the collection of data in the form of changes in subsurface resistivity in the lateral (horizontal) direction. acquisition of data collection with fixed current and voltage electrode spacing, the measuring point is moved or shifted horizontally. The electrode configuration commonly used is the Wenner configuration.

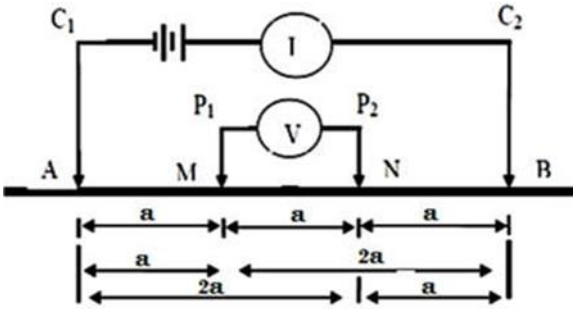

Figure 2. Wenner Configuration Electrode Arrays (Loke and Barker, 1996).

The Wenner configuration is one of the configurations in geophysical exploration with electrode arrays located in a line symmetrical to the center point. The Wenner electrode configuration has good vertical resolution, high sensitivity to lateral changes but weak current penetration to depth. The electrode arrays of the Wenner configuration can be seen in Figure 2.

The distance between electrodes in the Wenner configuration is the same as shown in Figure 2. The value of each electrode distance is substituted into Equation (2), then the value of K Wenner configuration is obtained, as follows:

$$K_S = 2\pi a \qquad (3)$$

then the apparent rho equation is obtained

$$\rho_a = 2\pi a \frac{\Delta V}{I} \quad (4)$$

where ρ_a is apparent resistivity, I is current strength, a is electrode distance, and ΔV is potential.

Resistivity states the typical properties of a material, which is the amount of resistance of a material that has a certain length and cross-sectional area with units of ohmmeter (Ωm). if a material with the same constituent minerals but the ratio is different, the resistivity will be different. By considering geological conditions, the value of the resistivity of several types of rocks that have been known based on the classification of Telford et al. (1990) in Table 1.

Table 1. Resistivity value constant according to Telford et al. (1990).

No.	Material	Resistivity (Ωm)
1.	Air	~
2.	Limestone	500-10000
3.	Sandstone	200-8000
4.	Slate	20-2000
5.	Marls	3-70
6.	Clays	7 - 30
7.	Alluvium	10-800
8.	Gravel	100-600

3. DCPT (*The Dutch Cone Penetration Test)*

DCPT (*The Dutch Cone Penetration Test)* is known as the sondir test which is widely used in Indonesia. DCPT is a test to calculate the bearing capacity of soil. The values of static cone resistance or conus resistance (qc) obtained from the field can be directly correlated with the bearing capacity of the soil (Hardiyatmo, 1992).

In 1986 Robertson developed a chart with twelve soil types (Figure 3). The use of these charts can be done in the field using the qt-Fr soil type zones shown in Table 2 (Robertson et al., 1986).

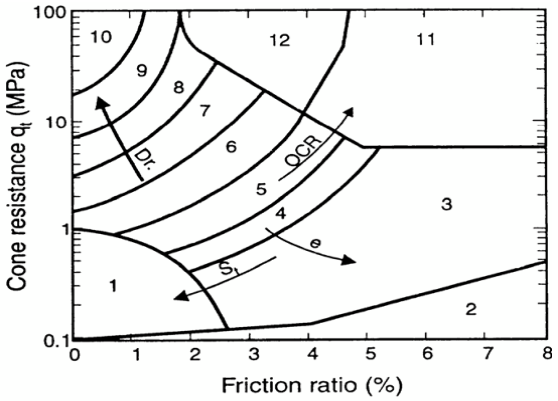

Figure 1. Soil type zone qt-Fr (Robertson et al., 1986).

Table 2. Soil type zone qt-Fr (Robertson et al., 1986).

Zone	Soil Behavior Test
1	Sensitive fine grain
2	Organic
3	Clays
4	Silty clay to clay
5	Clayey silt to silty clay
6	Partially drained sandy silt to clayey silt
7	Silty sand to sandy silt
8	Sand to silty sand
9	Sand
10	Gravelly sand to sand
11	Fine to stiff grain
12	Sand to clayey sand

Research Method

This research was conducted on Jenderal Sudirman Road, Muara Baulian, Batang Hari, Jambi using the Wenner configuration geoelectric method as many as 4 lines and a line length of 100 m and the electrode spacing distance is 5 m based on the acquisition map which can be seen in Figure 4. The results obtained from the acquisition of geoelectric data are the current value (I) in units of Ampere (A) and potential difference (V) in units of millivolts (mV). These values are used to obtain Apparent Rho (ρa) through Microsoft Excel Software calculations. after that is the next stage to obtain a 2D subsurface cross section using Res2DInv Software. This 2D cross section is interpreted based on Table 2.

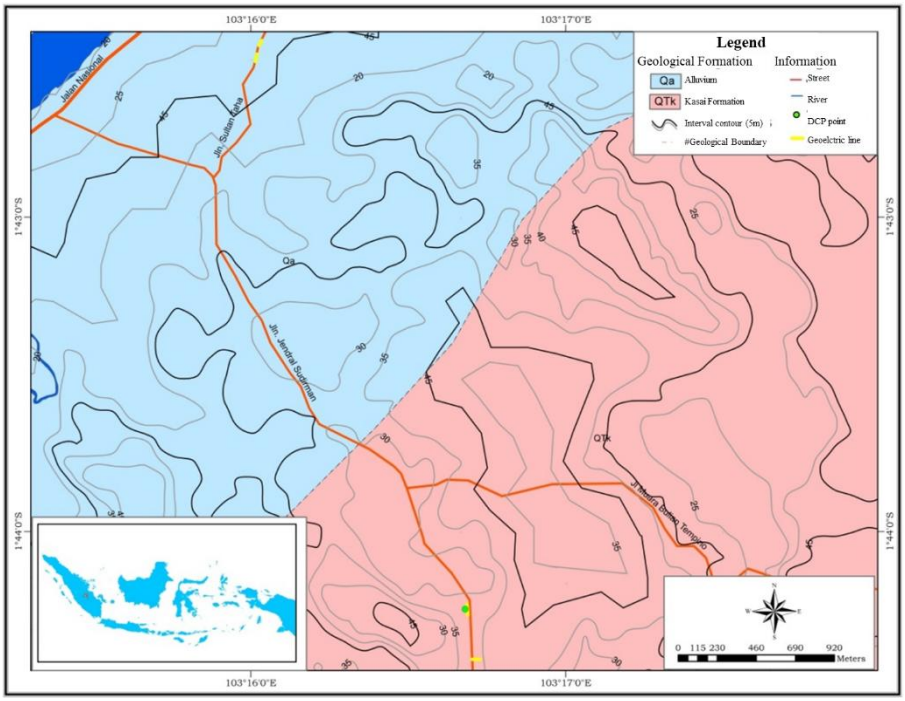

Figure 2. Wenner configuration geoelectric acquisition design (modified from Badan Informasi Geospasial, 2017).

Tools and Materials

1. *Resistivity meter* as a data measurement tool such as current strength (I) and potential value (V).
2. Electrodes 4 pieces as a conductor to channel electric current.
3. Cable 4 pieces as a connection between the power source and the electrode.
4. Accu/ Battery as a source of electric current.
5. Hammer used to stick the current and potential electrodes.
6. Tape measure used to measure the length of the line.
7. GPS, used to determine the position at each research point.
8. Microsoft Excel 2010 software, used for geoelectric data processing to obtain apparent resistivity (ρa) and DCPT data processing to obtain conus value (qc).
9. Res2DInv software, used for processing the results of the apparent resistivity (ρa) to obtain a two-dimensional subsurface cross section.

Results and Discussion

Processing of Wenner configuration geoelectric data obtained in the field then through the calculation stage and the inversion process the results obtained 2D cross section on line 1 to 4 which has a color image in the form of blue, green, yellow, orange, red to purple color groups that represent the resistivity value of a subsurface material / rock with a vulnerable value of 8.35 – 453 Ωm and a depth of 16.6m.

Table 3. Resistivity values obtained in the field.

No.	Color Scale	Rho (Ωm)	Materials
1		4.54 – 20.2	Fine sandstone, sand
2		50.4 – 74.9	Clay, claystone
3		91.3 – 175	Siltstone, silty clay
4		399 – 579	Sandstone, swamp

2D geoelectric cross-sections produce different color images to interpret subsurface rock types. Based on Table 3 to determine the weak zone, there are layers of water-saturated sand, clay, silt clay because in the area there are 2 formations, which are alluvial and Kasai Formation.

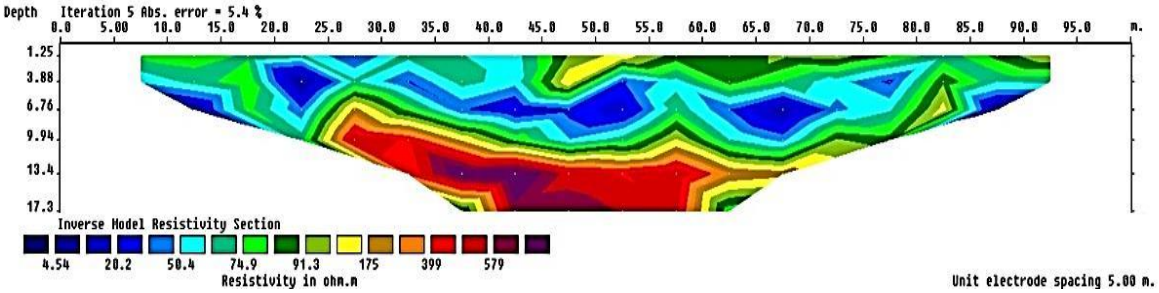

Figure 5. 2D Subsurface Cross Section Line 1.

Line 1 (Figure 5) was taken in an alluvial area (Qa), the area is close to swamps and rivers. The presence of lithology is indicated by rock resistivity values from 4.54 - 20.2 Ωm, these rocks are interpreted as water-saturated fine sand represented by blue color. The resistivity value of 50.4 - 74.9 Ωm is interpreted as semi-permeable sandy clay sedimentary rock represented in green. The resistivity value of 91.3 - 175 Ωm is interpreted as mudstone sedimentary rock, represented by dark green to yellow color. The red to orange color has a resistivity value of 399 - 661 Ωm estimated as sandstone. The presence of weak zones almost along Line 1 is because the area is near swamps and rivers. There are 2 parts of the weak zone, which are near the surface and below the ground surface. The weak zone on the ground surface is located at a distance of 17 - 44 m with a thickness of 3 - 10 m. The second part of the weak zone is located below the ground surface. The second part of the weak zone is found in the subsurface at a distance of 45 - 95 m, estimated at a depth of 2 - 10 m with a thickness of 8 m. The weak zone is estimated to be dominated by water-saturated fine sand shown in blue along the 100 m track.

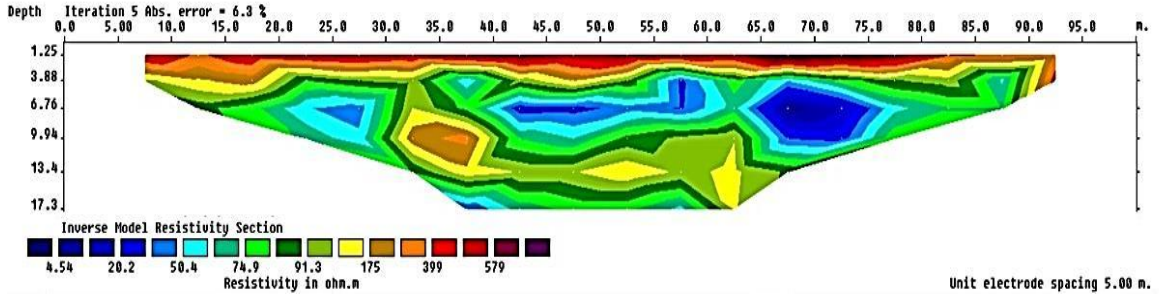

Figure 6. 2D Subsurface Cross Section Line 2.

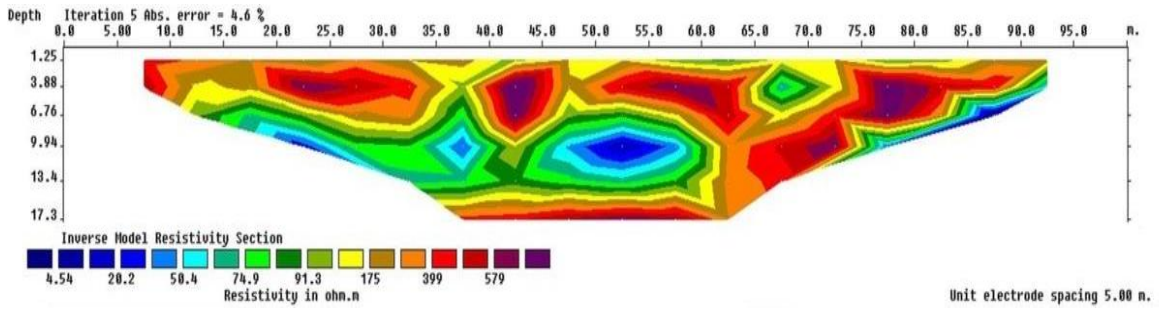

Figure 7. 2D Subsurface Cross Section Line 3.

Line 2 was taken in the Alluvial area (Qa) which can be seen in Figure 6. The presence of lithology is indicated by rock resistivity values from 4.54 – 20.2 Ωm, these rocks are interpreted as water-saturated sand represented in blue. The resistivity value of 50.4 – 74.9 Ωm is interpreted as passive clay sedimentary rock represented with

green color, 91.3 – 175 Ωm is interpreted as clay, represented with dark green to yellow color. While the presence of a layer of soil with a high resistivity value of 399 – 661 Ωm is represented by black to orange color which is thought to be fill soil because the road is adjacent to the swamp. The weak zone on line 2 is in the subsurface at a distance of 20 – 28 m estimated to be at a depth of 4 m with a thickness of 6 m and part 2 at a distance of 40 – 77 m estimated at a depth of 2 – 5 m with a thickness of 2 – 6 m. This weak zone is of clay lithology. This weak zone is lithologically clay to water-saturated fine sand layers. According to Yudiana et al. (2018) the weak zone is caused by the arrangement of the overlying rock layers of sandy clay to dense sand which is buried into a layer of water-saturated sand and silty clay so that it is impermeable and has high porosity, above this layer there is sand that can pass water so that it has the potential for liquefaction.

Line 3 was taken in the Kasai Formation (QTk) which can be seen in Figure 7. The presence of lithology is indicated by rock resistivity values from 4.54 – 20.2 Ωm interpreted as water-saturated fine sand represented in blue. The resistivity value of 50.4 – 74.9 Ωm is interpreted as passive clay sedimentary rock represented in green. The resistivity value of 91.3 – 175 Ωm is interpreted as clay or mudstone represented by dark green to yellow color. While the presence of lithologies with high resistivity values of 399 – 661 Ωm is represented by red to orange colors which are interpreted as sand and sandstone. The weak zone in line 3 is located at a distance of 20 – 56 m with a depth of 8 m and a thickness of 6 m. This line is not dangerous for buildings above. This line is not dangerous for the building above it because it has a strong and very compact soil layer with dense sand lithology and there are no weak zones close to the surface.

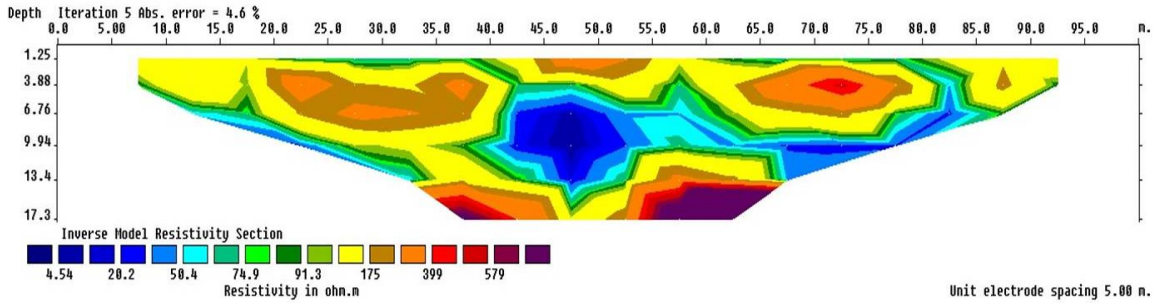

Figure 8. 2D Subsurface Cross Section Line 4.

Line 4 was taken in the Kasai Formation (QTk) which can be seen in Figure 8. The presence of lithology is indicated by rock resistivity values from 4.54 – 20.2 Ωm, these rocks are interpreted as water-saturated fine sand represented in blue. The resistivity value of 50.4 – 74.9 Ωm is interpreted as semi-permeable sandy clay sedimentary rock represented in green. The resistivity value of 91.3 – 175 Ωm is interpreted as sand sedimentary rock, represented by dark green to yellow color. While the presence of lithology with a high resistivity value of 399 – 579 Ωm is represented by red to orange color which is interpreted as sandstone. The weak zone on line 4 is located at a distance of 35 – 87.5 m with a depth of 3 m and a thickness of 3 – 10 m. According to Yudiana et al. (2018) the existence of a weak zone is due to the rock layers arranged undergoing burial, namely a layer of water-saturated passive to dense clay, silt clay is immobile and has high porosity and is overlain by sandstones that can pass water so that it has the potential for liquefaction.

The value of conus resistance (qc) at a depth of 0.00 m – 7.20 m from the ground surface is 196 kPa to 1,176 kPa (1 kPa = 0.0102 kg/cm^2) as shown in Figure 9. At a depth of 7.40 m to 10.60 m the conus

pressure decreases to a conus value of 196 kPa. At a depth of 10.80 m to a depth of 11.60 m the conus pressure continues to increase reaching hard soil with a conus value of 14,700 kPa. Shear resistance (fs) values range from 0.13 – 1.67 kg/cm^2. The total shear value (TF), which is the ability of the soil to withstand loads, increased to a value of 328 kg/cm^2 at a depth of 11.6 m from the ground surface. The friction ratio (Rf) value with a value of >1% can be said to be a cohesive soil. A groundwater table was found at a depth of 8 m. The presence of weak zones is estimated at a depth of 0 – 10.60 m as shown in Figure 10.

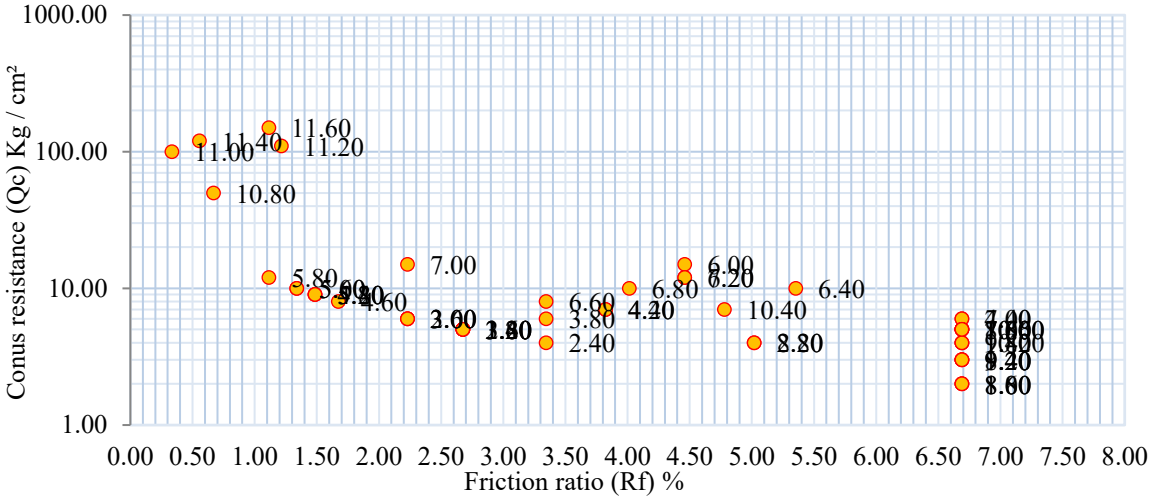

Figure 9. Robertson's 1986 graph (Robertson et al., 1986).

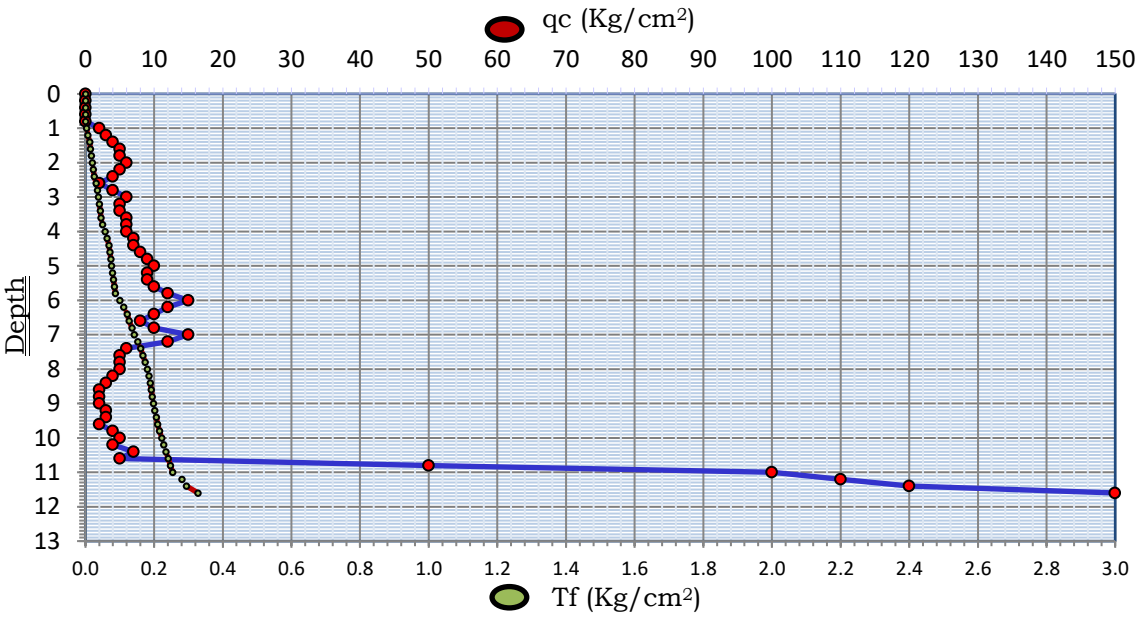

Figure 3. Sondir Test Graphics.

Conclusion

Research on the determination of weak zones using the Wenner configuration geoelectric method was conducted at Jenderal Sudirman Road, Muara Bulian, Batang Hari, Jambi. The acquisition has been carried out in two formations which are alluvial (Qa) and Kasai Formation (QTk), each formation has 2 lines. Based on the results of the study, the resistivity value variation of the subsurface layer consisting of fine sand to fine sandstone with a resistivity value of 4.54 - 20.2 Ωm, clay to

mudstone with a resistivity value of 50.4 - 74.9 Ωm swamp soil with a resistivity value of 399 - 579 Ωm and siltstone has a resistivity value of 91.3 - 175 Ωm.

The results prove that on Jenderal Sudirman Road, Muara Bulian, Batang Hari, Jambi, there is a weak zone with a water-saturated fine sand to fine sandstone lithology. Based on the interpretation of 2D subsurface geo-electrical cross-section of Line 1 and Line 2, there is a weak zone in the subsurface and close to the surface, line 3 weak zone is far below the surface so it is possible that there is no collapse, while line 4 is almost all a weak zone estimated to be up to 10 m deep. The weak zone in traverse 4 is found in the sondir/ DCPT test with the result that the depth of 0 - 10.6 m is a weak zone because the conus value (qc) is below 20 kPa.

The weak zones found in the study area are interpreted as soft and non-compact rocks that are unable to withstand loads, and can cause road damage.

Acknowledgements

The author would like to thank the parties involved, which are the Department of Public Works and Spatial Planning, Batang Hari Regency, Geophysical Engineering lecturers and friends who helped complete this research.

References

Akinlalu, A. A., Adegbuyiro, A., & Obore, A. A. (2016). Application of Electrical Resistivity Method in Designing a Structural Model for a Proposed Filling Station Site, Akure, Southwestern Nigeria. *Global Journal of Science Frontier Research*, 16(6), 21–34. https://journalofscience.org/index.php/GJSFR/article/view/1884

Badan Informasi Geospasial. (2017). InaCORS BIG. *Satu Referensi Pemetaan Indonesia*. Pusat Jaring Kontrol Geodesi dan Geodinamika Badan Informasi Geospasial. https://srgi.big.go.id/

Hardiyatmo, H. C. (1992). *Mekanika Tanah I*. Jakarta: PT. Gramedia Pustaka Utama.

Loke, M. & Barker, R. (1996). Rapid least-squares inversion of apparent resistivity pseudosections by a quasi-Newton method. *Geophysical Prospecting*, 44, 131–152. https://doi.org/10.1111/j.1365-2478.1996.tb00142.x

Makmur. S., Sehah. S., & Sugito, S. (2016). Analisis Zona Lemah (Amblesan) di Kawasan Jalan Raya Gunung Tugel Kabupaten Banyumas Berdasarkan Survei Geolistrik Konfigurasi Wenner. *Jurnal Techno*, 17(2), 111–121. http://jurnalnasional.ump.ac.id/index.php/Techno/article/view/1404

Pranantya, P. A., Sukiyah, E., Utomo, E. P., & Hendrawan, H. (2018). Korelasi Nilai Sondir Terhadap Parameter Geoteknik dan Rembesan pada Pondasi Tanggul Fase E, Kalibaru, Jakarta Utara. *Jurnal Sumber Daya Air*, 14(2), 78–86. https://doi.org/10.32679/jsda.v14i2.177

Ramadianti. N., Wardana, A. P., Nababan, R. N., & Saragih, D. A. (2020). *Identifikasi Zona Lemah di Area X Kab Blora*. PT. Abhinaya Mappindo Bumitala. https://www.abhinaya-mb.com/wp-content/uploads/2020/06/Survey-Geolistrik-Identifikasi-Zona-Lemah-di-Area-%E2%80%9CX%E2%80%9D-Kab.-Blora.pdf

Robertson, P. K., Campanella, R. G., Gillespie, D., & Greig, J. (1986). Use of Piezometer Cone Data. *Proceedings of American Society of Civil Engineers, ASCE*. In-Situ 86 Specialty Conference, Blacksburg, 23-25 June 1986, 1263-1280.

Sladen, J. A., D'Hollander, R. D., & Krahn, J. (1985). The liquefaction of sands, a collapse surface approach. *Canadian Geotechnical Journal*, 22(4), 564–578. https://doi.org/10.1139/t85-076

Soedarsono. (2006). Analisis Amblesan Tanah Akibat Pembebanan Pada Akuifer Bebas dan Pengaruh Terhadap Lingkungan di Sebagian Kota Semarang. *Jurnal Pondasi*, 12(1), 76 – 85.

Telford, W. M., Geldart, L. P., & Sheriff, R. E. (1990). *Applied Geophysics*. 2nd Edition. New York: Cambridge University Press.

Wisnu, W. & Nazirman, N. 1997. *Geologi Regional Sumatra Selatan*. Pusat Survey Geologi. Badan Geologi Kementrian ESDM, Bandung.

Yudiana, R., Alaydrus, A. T., & Suhayat, M. (2020). Korelasi Hambatan Jenis dan Hambatan Konus untuk Identifikasi Zona Lemah di Desa Sekotong Barat, Kecamatan Sekotong, Kabupaten Lombok Barat. *Jurnal Penelitian dan Pembelajaran Fisika Indonesia*, 2(2), 38–44. https://jpfis.unram.ac.id/index.php/jppfi/article/view/73

*this article followed the template in use at the time of its acceptance.

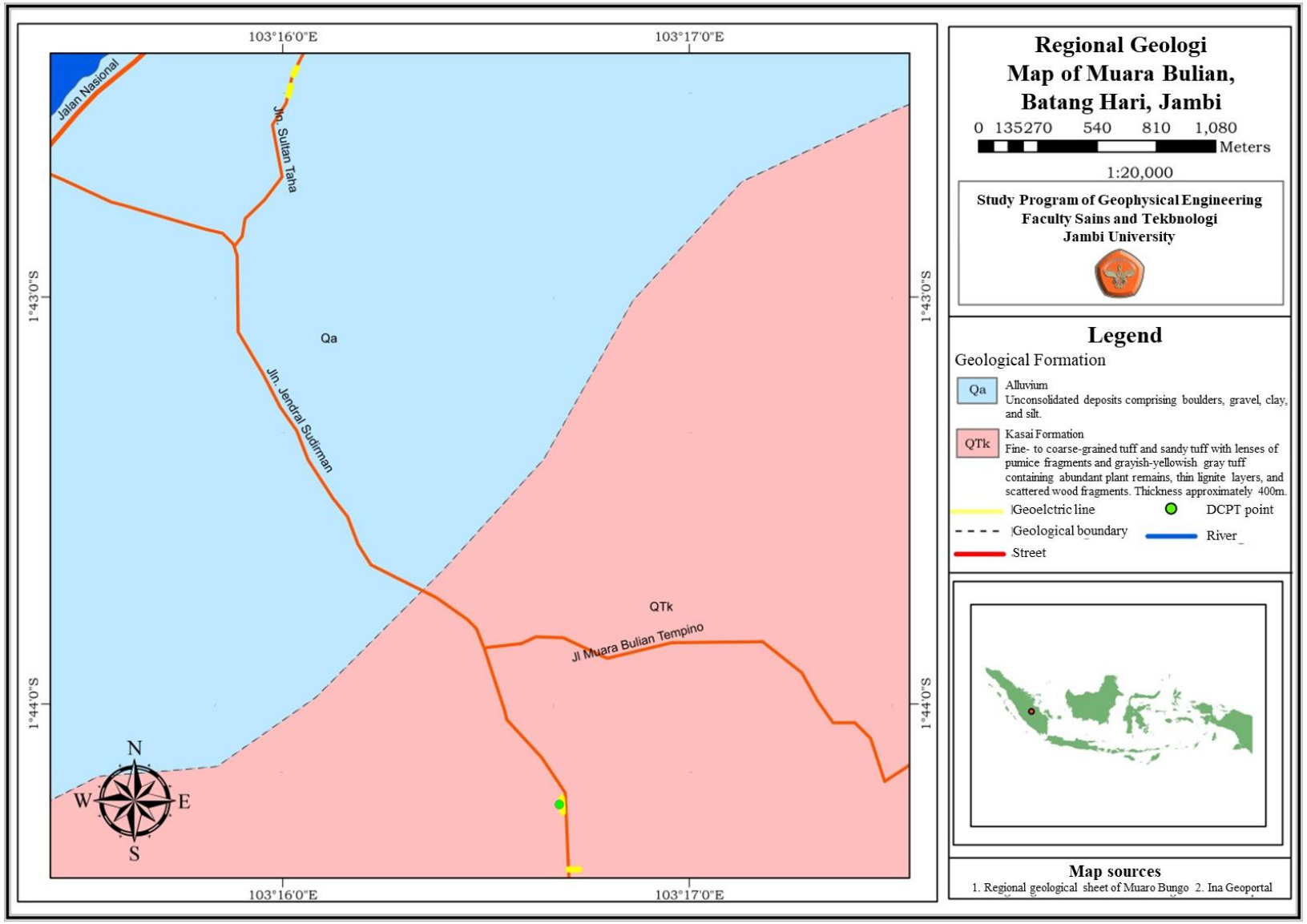

Appendix 4. Regional geology map of Muara Bulian, Batang Hari.

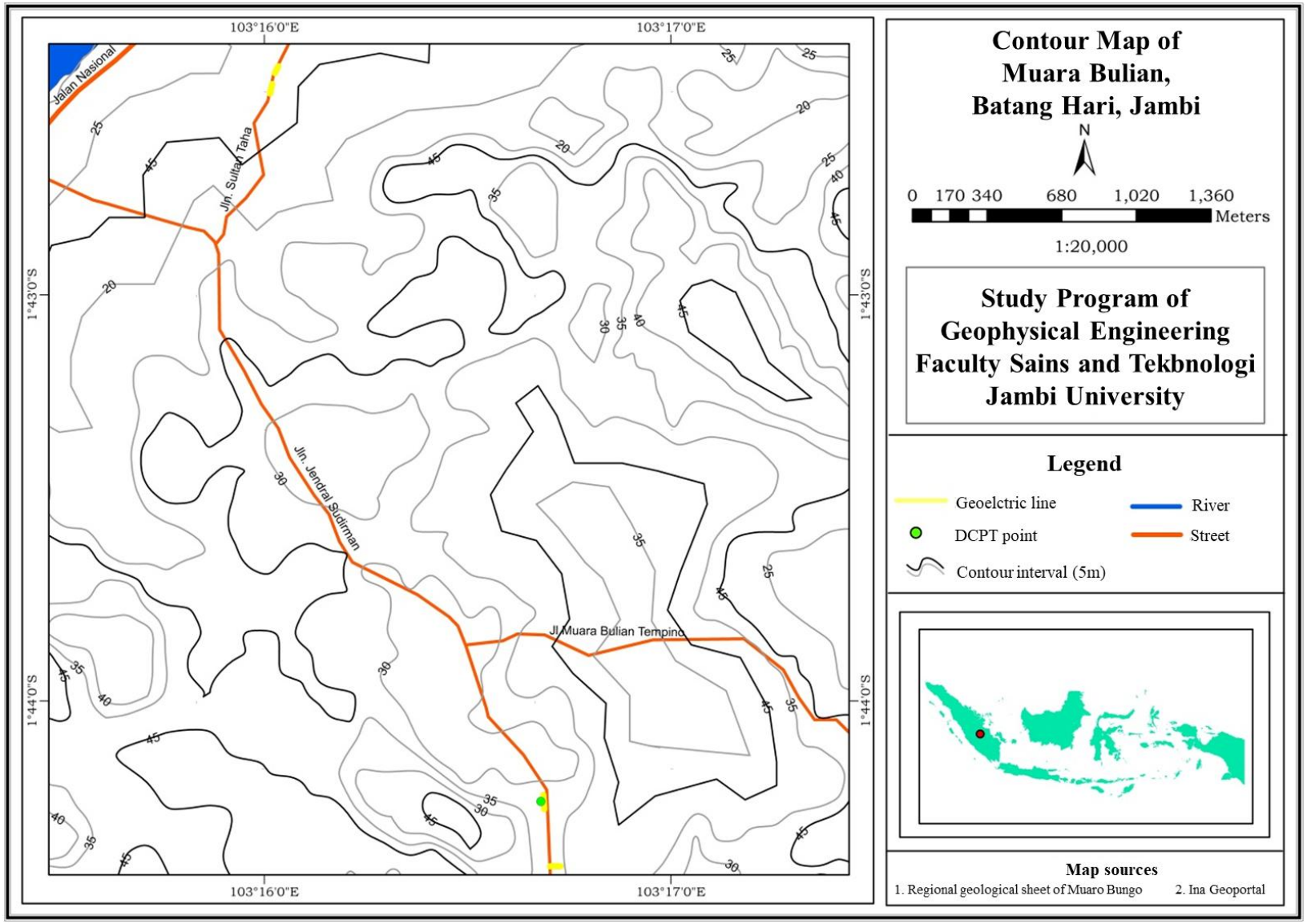

Appendix 5. Contour map of Muara Bulian, Batang Hari.

Indexing and Abstracting

GEOFISIKA
UNIVERSITAS HASANUDDIN

ISSN 2579-5546